Disorder, Geometric Frustration and the Dipolar Interaction in Rare Earth Magnets

by

Jeffrey Andrew Quilliam

A thesis
presented to the University of Waterloo
in fulfilment of the
thesis requirement for the degree of
Doctor of Philosophy
in
Physics

Waterloo, Ontario, Canada, 2010

I hereby declare that I am the sole author of this thesis. This is a true copy of the thesis, including any required final revisions, as accepted by my examiners.

I understand that my thesis may be made electronically available to the public.

Abstract

This thesis will present research that studies the role of disorder, geometric frustration and the long-range dipolar interaction on the collective behaviour of several insulating, rare earth magnets. Experiments were performed at low temperatures to measure the specific heat and magnetic susceptibility of several materials. Susceptibility was measured with a SQUID magnetometer that has been designed and constructed primarily for the study of slow dynamics in glassy systems. Specifically, this thesis will discuss three distinct topics.

The first is the series of materials $LiHo_xY_{1-x}F_4$, which are manifestations of the dilute, dipolar coupled Ising model. The low-x portion of the phase diagram has become a rather contentious issue in recent years with both theoretical and experimental groups disagreeing on the existence of a spin glass freezing transition and one experimental group arguing for the existence of an exotic "antiglass" or spin liquid state resulting from quantum entanglement at $x = 0.045$. We present specific heat and dynamical susceptibility measurements on four stoichiometries in this series: $x = 0.018$, 0.045, 0.080 and 0.012. No evidence of an unusual antiglass state is observed. Instead, our results show evidence, at all dilution levels studied, of a spin glass freezing transition. Interpretation of experimental data is found to be complicated by the anomalously slow dynamics in these materials. The relaxation time scales are found to increase as the concentration of Ho^{3+} ions is reduced, an effect which can be attributed to single-ion physics and the importance of the nuclear hyperfine coupling in this system.

A second set of materials studied here is a series of several Gd garnet materials, the most famous of which is $Gd_3Ga_5O_{12}$ (GGG), a material previously argued to be a disorder-free spin glass. Our specific heat experiments reproduce previous experiments on GGG and show that the homologous Gd garnets $Gd_3Te_2Li_3O_{12}$ and $Ga_3Al_5O_{12}$ do not share the same glassy physics but exhibit sharp ordering features. By experimenting with the introduction of random site dilution, it is concluded that a 1-2% off-stoichiometry inherent in GGG is likely a special kind of disorder that is particularly effective in inducing random frustration and the formation of a spin glass.

Finally, specific heat measurements on the pyrochlore antiferromagnet $Gd_2Sn_2O_7$ (GSO) are presented. While GSO has generally been found to be a well behaved and well understood model magnet, with long range order developing at around 1 K, like many other geometrically frustrated magnets, it has been discovered to possess persistent spin dynamics down to very low temperatures as measured by μSR and Mössbauer spectroscopy. Measurement of the low temperature limit of the specific heat when compared with linear spin-wave theory, however, presents a consistent picture of gapped magnon excitations that freeze out at low temperatures and make the existence of the proposed dynamic ground state unlikely.

Acknowledgements

First and foremost, I would like to thank my supervisor Jan Kycia. Jan possesses an unparalleled and infectious passion for experimental low temperature physics and working in his laboratory has been a tremendous experience. His seemingly limitless technical know-how and diverse interests make him an excellent and inspiring advisor, respectively. It goes without saying, that this thesis could not have been achieved without him, but in fact, there is so much more that I have learned in working with Jan than is contained in this document. I know that the knowledge and skills that I have acquired in Kycia lab, will stand me in good stead through the rest of my career.

Michel Gingras, almost a co-supervisor at times, has provided the theoretical background and inspiration for my work at Waterloo, which has often been connected to his own research. He has been an invaluable resource for learning about geometrically frustrated and disordered magnetic systems and is always available to talk about physics. It has been a pleasure to collaborate with him on a number of subjects which are discussed in this thesis.

Thanks are owed to many other people who have directly contributed to the experimental work contained in this thesis. Chas Mugford provided a myriad of technical assistance, essential helium liquefaction and was the person who made work the cryostat on which all of this research was performed. Thanks to Shuchao Meng, who has been my cryogenic "partner in crime" for the last several years, sharing the responsibilities of looking after our battle hardened dilution refrigerator. Thanks to Luke Yaraskevitch who has taken on that role in recent months. Kate Ross played an important part in our work on $Gd_2Sn_2O_7$ and it has been a pleasure to collaborate with her again now that she has moved on to McMaster.

The work on $Gd_2Sn_2O_7$ would not have been the same without the theory of Adrian del Maestro and Michel Gingras. Thanks to Linton Corruccini and Oleg Petrenko for providing us with several of the materials studied in this work. Thanks to Stefan Kycia, Ariel Gomez and Jim Britten for assistance with characterization of our Ho:YLF samples. It has also been a pleasure to work with Graeme Luke, Jose Rodriguez, Sarah Dunsiger, Greg MacDougall, Adam Aczel and others on the $LiHo_xY_{1-x}F_4$ project and to accompany them to a μSR beamline experiment at TRIUMF. I am grateful for additional collaborations with professors Bruce Gaulin and John Greedan.

Thanks to Lauren Persaud and Nat Persaud who both contributed a lot to the lab and have always been great friends. Thanks to Jeff Mason, Jeff Hill and many other graduate and undergraduate students with whom it has been a pleasure to work in the lab. I owe thanks to Steve Johnston for having pushed me through several courses and simply for being a kindred spirit in graduate school. I have met so many other close friends in

Waterloo, too numerous to list, through physics or otherwise, who have made me feel very much at home here.

I have had very valuable conversations with several other graduate students and post-docs in the physics department, particularly Ali Tabei, Ka-Ming Tam and Taras Yavors'kii. Thanks also to Moshe Schechter and Patrik Henelius for informative conversations regarding the $LiHo_xY_{1-x}F_4$ series of materials. Thanks to Rob Hill and Roger Melko for patiently listening to me talk about my research at committee meetings and giving valuable feedback. A further thanks goes to Rob Hill, Michel Gingras and my other examiners Thorsten Hesjedal and Peter Schiffer for a detailed reading of this thesis.

Finally, I would like to thank those people who are most important in my life. I am forever indebted to my loving parents of course, not only for having helped to support me through many years of post-secondary education, but also for having encouraged me to go into science and go as far as obtaining a PhD in physics. Last, but not least, to my wonderful girlfriend Fabienne: thank you for always being there for me and for providing some badly needed light in dark times.

Dedication

I would like to dedicate this thesis to the memory of Chas Mugford. As a fellow graduate student in the same research group and as one of my closest friends, Chas has had a tremendous impact on my life during the years I have spent in Waterloo. His creativity, intelligence, patience, technical abilities in the lab and elsewhere, sense of humour and kindness were an inspiration to all. Sadly Chas passed away in 2009 leaving myself and many others feeling incomplete at best. My deepest sympathies go out to Chas's wife Allison, his daughter Ella, his parents Chuck and Heather and his brother and sister, Ashleigh and Adele.

I miss Chas deeply now and always will. But I will also never forget the good things that he and his friendship have brought to my life.

Contents

List of Tables

List of Figures

Chapter 1

Introduction

The work of physicists might be divided into two main categories or approaches to the solving of physical problems. In one, perhaps the one most commonly associated with the field of physics, the aim is to discover the underlying physical principles on which nature is based. Essentially a 'top-down' approach, one aims to describe the building blocks of a physical system. From the discovery of the atom to the development of quantum mechanics and further down to the development of the standard model, this approach has dominated the more historically famous discoveries in physics. The goal is always to find the simplest and most beautiful theories to describe the basic elements of the world around us.

Another broad segment of physics, however, recognizes that even if nature, at its roots, is described by the simplest most elegant of laws, the resulting behaviour of a collection of millions of building blocks can be incredibly complex or can demonstrate its own set of elegant physical laws. It is this part of physics, that realizes that more can be different [1]. The assembly of a mole of atoms or more can take on many forms, from the complexity of life to the elegant universality of phase transitions.

Condensed matter is typically a fusion of these two ideas. One uses the material properties of a sample to deduce a valid description of the material's underlying model. Or, one uses the assumed model of a material to predict what critical behaviour or many-body physics may result. Magnetic systems have long been used as the purest exemplar of the bottom-up approach to condensed matter physics. Simple magnetic models, such as the Ising, XY and Heisenberg models, have allowed theorists to study what otherwise could be an immensely complex system. With certain select materials, so-called 'model magnets', those theoretical predictions can be tested, with relative confidence that the systems are representative of the theoretical models. Through the universality of critical behaviour, for example, one can then easily use these model magnets as analogies for very different physical systems.

Compared to many condensed matter systems, insulating magnets have easily defined effective Hamiltonians that can often be summed up in a concise set of equations. As a counter example, consider the exhaustively studied high temperature superconductors, the cuprates, where one must consider the dopant impurities, band structure, itinerant magnetism and phonons as a starting point for simulations. Magnetic systems allow us, as physicists, to study many-body physics and complexity in their cleanest realizations. Later, we can hope to extend these discoveries to understanding the more convoluted systems which show more promise for direct applications. As a specific example, the superconductivity of the cuprates is thought to result, at least partly, from magnetic excitations, and possibly exotic spin-1/2 excitations known as spinons [2]. But without (at least until very recently [3]) a clean example of a quantum spin liquid with spinon excitations that is not masked by superconductivity and plagued by sample quality issues, how can physicists hope to fully understand the inner-workings of the cuprates?

Insulating rare earth magnets (as opposed to those containing magnetic transition metal ions) are arguably the best kind of model magnets. The spin-orbit interaction creates states of total angular momentum $|J\, m_J\rangle$ (rather than decoupled orbital angular momentum and spin), often with large values of J. The crystal electric field can then mould these magnets into a variety of magnetic species such as Ising, Heisenberg and XY models. The lack of conduction electrons greatly simplifies the physics, making the consideration of band structure and other complexities unnecessary. The same crystal structure can often accommodate a number of different rare earth ions, so different magnetic species, without a significant change to the unit cell, and these magnetic R^{3+} ions can often be replaced, randomly, with non-magnetic Y^{3+} (or sometimes Lu^{3+} ions) to test the effects of random site dilution.

However, not all is straightforward with such systems. The small magnitude of the simple, isotropic exchange interactions tends to expose other more complicated effects. In particular, one of the more unique aspects of rare earth magnets is the importance and sometimes dominance, therein, of the dipolar interaction. The dipolar interaction adds complexity to these systems since it is both anisotropic and long range ($1/r^3$) in nature.

Subsequent to a general introduction and a chapter discussing our experimental apparatus, this thesis will describe the study of three main, distinct magnetic rare earth systems. These subjects will touch on three general themes, which are currently quite important in the field of magnetism: disorder, geometric frustration and the dipolar interaction.

The first system to discuss and the largest component of this work, is the series of materials $LiHo_xY_{1-x}F_4$. Thought to be a good realization of the dilute, dipolar Ising model, this material has seen a great deal of attention over the past two decades and much controversy in recent years. We will concentrate here on the low x end of the phase diagram and the question of the existence of a dipolar spin glass state versus the notion of

an exotic quantum "antiglass" state, observed by one research group [4, 5]. Experiments have been performed measuring the specific heat and ac magnetic susceptibility of several stoichiometries in this series.

Following that, we will turn to the material $Gd_2Sn_2O_7$: a geometrically frustrated, isotropic magnet on the pyrochlore lattice. Our aim was to investigate the low temperature spin excitations of this material with specific heat to better understand some unexplained results seen in studies of the spin dynamics [6]. Once again, the dipolar interaction is seen to be crucial to the physics of this system and to understanding the results of our experiments.

Finally, we combine all three themes with the study of the exotic material $Gd_3Ga_5O_{12}$ or GGG and a series of similar materials. The unusual physics of this geometrically frustrated garnet material, including spin glass properties [7], extended short range order [8] and persistent spin dynamics [9], has evaded explanation for many years. Through specific heat measurements on a set of homologous Gd garnets, we address the question of whether the glassiness observed in GGG is the result of sensitivity to small levels of disorder or whether there is an inherent competition between the local, frustrated exchange interactions and the long range dipolar interaction that results in an intrinsic glass-like state.

1.1 Hamiltonian of Insulating, Rare Earth Magnets

1.1.1 Hund's Rules for Rare Earth Ions

In the rare earth ions, generally R^{3+}, the $4f$ states are typically the valence electrons and therefore are the most physically important electrons to be considered [10]. Through much of this discussion, we will use the example of the Ho^{3+} ion which has the electronic configuration [Xe].$4f^{10}$. To understand the structure of the electronic states, we turn to Hund's rules or more formally, to the Russel-Saunders angular momentum coupling scheme [11]. Essentially, one has n valence electrons with orbital angular momentum $l = 3$ and spin $s = 1/2$ in states $|m_l\, m_s\rangle$ that are coupled to form an n-electron wavefunction. Naturally, the Pauli exclusion principle demands that these electrons not all exist in the same state, but that they occupy the n lowest energy levels and form a properly anti-symmetrized wavefunction. The Russel-Saunders coupling scheme involves the following intra-atomic interactions, in order of importance: the spin-spin coupling $\mathcal{H}_{SS}$, the orbital-orbital coupling $\mathcal{H}_{OO}$ and then the spin-orbit coupling $\mathcal{H}_{SO}$. These three interactions correspond to Hund's three rules for deciding the n-electron angular momentum state.

The spin-spin coupling is strongest and is driven by the exchange interaction between the electrons. It is found that the state of maximum multiplicity or the state with the

highest total spin S is the lowest energy state. This can be qualitatively attributed to the Coulomb interaction and the cost of overlapping wavefunctions. If the electrons are all in different orbital angular momentum states, and therefore have maximal multiplicity, there will be less overlap of the spatial wavefunctions. For the case of Ho^{3+}, this gives us a total spin of $S = 2$.

The orbit-orbit coupling or Hund's second rule, demands that one should maximize the total orbital angular momentum. Loosely speaking, this rule is derived from the logic that if all the electrons are orbiting in the same direction, they will meet less often and again, there will be less overlap of wavefunctions, thus less Coulomb repulsion. For the case of the Ho^{3+} ion, this results in $L = 6$.

For free ions, the next most important term in the Hamiltonian is certainly the spin-orbit coupling

$$\mathcal{H}_{SO} = \zeta \mathbf{L} \cdot \mathbf{S}. \tag{1.1}$$

This is a relativistic effect that is more pronounced in heavier, higher-Z elements. In fact, in some very heavy elements it can become comparable to or even more important than the spin-spin and orbit-orbit couplings resulting in so-called jj-coupling [10]. In that situation, each electron's spin and orbital angular moment are coupled first to create states $|j\, m_j\rangle$ and these are then coupled together by $\mathcal{H}_{SS}$ and $\mathcal{H}_{OO}$. This jj-coupling or intra-orbital spin-orbit coupling may not be dominant but can be an important correction as will be discussed in the case of Gd^{3+} ions.

On the other hand, in the transition metal ions, the spin-orbit coupling can be less important than the crystal field energy [11]. In rare earths, with which we are dealing in this work, relativistic effects are important and the $4f$ electrons are tightly bound so do not interact as strongly with the surrounding ions in a crystal structure. Thus it is generally accurate to make spin-orbit coupling the next most important interaction and obey Hund's third rule [12]. The result is a state of total angular momentum so that the good eigenstates with which to work are

$$|L\, S\, J\, m_J\rangle$$

states. The sign of ζ depends on whether the $4f$ shell is more or less than half filled. If under half-filled, J should be minimized and we should have $J = |L - S|$. If over half-filled, J should be maximized and $J = L + S$. Ho^{3+} falls into the latter category so $J = L + S = 8$. In spectroscopic notation, we can write the state of Ho^{3+} as ${}^5I_8$ and it can be roughly illustrated as follows:

$\uparrow\downarrow$	$\uparrow\downarrow$	$\uparrow\downarrow$	$\uparrow$	$\uparrow$	$\uparrow$	$\uparrow$
-3	-2	-1	0	1	2	3

though obviously the actual wavefunction is a properly antisymmetrized combination of different single-electron combinations.

Another rare earth ion to be studied in this thesis is the Gd^{3+} ion which possesses a [Xe].$4f^7$ electronic configuration. This is an exactly half filled shell. Maximizing the multiplicity or the spin leads to a configuration with one electron in each orbital angular momentum state and $S = 7/2$. This forces the angular momentum to add up to $L = 0$. The spin-orbit coupling then tells us simply that $J = S = 7/2$ or that the ground states of Gd^{3+} are ${}^8S_{7/2}$ states.

$\uparrow$	$\uparrow$	$\uparrow$	$\uparrow$	$\uparrow$	$\uparrow$	$\uparrow$
-3	-2	-1	0	1	2	3

As a final example, the Yb^{3+} ion, with electronic configuration [Xe].$4f^{13}$, will have $S = 1/2$, $L = 3$. The ground state of the spin-orbit coupling will then be a ${}^2F_{7/2}$ state, or $J = 7/2$.

$\uparrow\downarrow$	$\uparrow\downarrow$	$\uparrow\downarrow$	$\uparrow\downarrow$	$\uparrow\downarrow$	$\uparrow\downarrow$	$\uparrow$
-3	-2	-1	0	1	2	3

Once we have the relevant angular momentum states $|L\,S\,J\,m_J\rangle$ for the rare earth ions, we can move to lower energies and discuss their interaction with surrounding ions or external magnetic field. Since many interactions will be based on the operators $\boldsymbol{L}$ or $\boldsymbol{S}$ or some combination thereof and not directly connected to $\boldsymbol{J}$, the Wigner-Eckardt theorem becomes quite useful [12]. For the interaction with an external magnetic field, one has the Zeeman energy

$$\mathcal{H}_Z = \mu_B \boldsymbol{H} \cdot (\boldsymbol{L} + 2\boldsymbol{S}) \tag{1.2}$$

where the gyromagnetic ratio of the electron spin is taken to be exactly 2, a very good approximation. But if we are treating the Zeeman energy as a perturbation to the good J states of the spin-orbit interaction, we should use the Wigner-Eckardt theorem to write

$$\langle L\,S\,J\,m_J|\boldsymbol{L} + 2\boldsymbol{S}|L\,S\,J\,m'_J\rangle = g_J\langle J\,m_J|\boldsymbol{J}|J\,m'_J\rangle \tag{1.3}$$

where the Landé g-factor is given by

$$g_J = 1 + \frac{J(J+1) - L(L+1) + S(S+1)}{2J(J+1)} \tag{1.4}$$

Then the Zeeman term in the magnetic Hamiltonian will simply be written as

$$\mathcal{H}_Z = -\mu_B g_J \boldsymbol{H} \cdot \boldsymbol{J} \tag{1.5}$$

thus making it energetically favourable for the magnetic moments to align with the external magnetic field.

1.1.2 Crystal Field

Following the spin-spin, orbit-orbit and spin-orbit interactions, the next most important energy in rare earth ions is typically the crystal field Hamiltonian [11]. The crystal field is simply an electrostatic interaction with the surrounding ions and has a symmetry dependent on the crystal structure of the material in which the magnetic ion is situated. In the absence of a crystal field, there are $2J+1$ states described as $|L\,S\,J\,m_J\rangle$ all degenerate in energy. However, removing the spherical symmetry of the problem with a crystalline electric field splits those $2J+1$ states in energy. The most important effect of the crystal field is to introduce anisotropy, be it easy-axis or easy-plane anisotropy.

To first order, the crystal field can be approximated by assuming that the surrounding ions (labeled with index i) are point charges. Then the potential is given as

$$V(\mathbf{r}) = \sum_i \frac{q_i}{|\mathbf{R}_i - \mathbf{r}|} \tag{1.6}$$

The energy contribution can be evaluated by performing integrals in cartesian coordinates, but it is much more convenient to expand this crystal field in spherical harmonics [12]:

$$V(r,\theta,\phi) = \sum_{n=0}^{\infty}\sum_{\alpha} r^n \gamma_{n\alpha} Z_{n\alpha}(\theta,\phi) \tag{1.7}$$

where

$$\gamma_{n\alpha} = \sum_i \frac{4\pi q}{(2n+1)} \frac{Z_{n\alpha}(\theta_i,\phi_i)}{R_i^{n+1}} \tag{1.8}$$

and the $Z_{n\alpha}$'s are the tesseral harmonics – spherical harmonics containing $\sin\phi$ or $\cos\phi$. Thus relative to the usual spherical harmonics, the tesseral harmonics are defined as

$$\begin{aligned} Z_{n0} &= Y_n^0 \\ Z_{n\alpha}^C &= \frac{1}{\sqrt{2}}\left[Y_n^{-\alpha} + (-1)^\alpha Y_n^\alpha\right] \\ Z_{n\alpha}^S &= \frac{1}{\sqrt{2}}\left[Y_n^{-\alpha} - (-1)^\alpha Y_n^\alpha\right] \end{aligned} \tag{1.9}$$

To get the crystal field Hamiltonian, one must sum this energy over all of the valence electrons of the rare earth ions (labeled with index j) so

$$\mathcal{H}_{\mathrm{CF}} = -e\sum_j V(\mathbf{r}_j) = -e\sum_{ij} \frac{q_i}{|\boldsymbol{R}_i - \boldsymbol{r}_j|}. \tag{1.10}$$

or

$$\mathcal{H}_{\mathrm{CF}} = -e \sum_j \sum_{n\alpha} r_j^n \gamma_{n\alpha} Z_{n\alpha}(\theta_j, \phi_j) \tag{1.11}$$

This calculation is best accomplished by using the Stevens' operator equivalents O_n^α [12, 13], defined as

$$\sum_j r_j^n Z_{n\alpha}(x_j, y_j, z_j) \equiv c_{n\alpha} \theta_n \langle r^n \rangle O_n^\alpha. \tag{1.12}$$

so that, after taking a radial integral, one has

$$\mathcal{H}_{\mathrm{CF}} = -e \sum_{n=0}^{\infty} \sum_{\alpha} \gamma_{n\alpha} c_{n\alpha} \theta_n \langle r^n \rangle O_n^\alpha. \tag{1.13}$$

Here $c_{n\alpha}$ is a constant which is contained in $Z_{n\alpha}$. $\theta_2 \equiv \alpha_J$, $\theta_4 \equiv \beta_J$ and $\theta_6 \equiv \gamma_J$ are reduced matrix elements. In the case of transition metal ions, the crystal field energy is often more significant than the spin-orbit coupling, thus the operator equivalents are expressed in terms of the orbital angular momentum operators L_z, L_+ and L_-. In the rare earth ions, the appropriate states are states of total angular momentum, yet the crystal field affects only the orbital momentum, not the spin. Nevertheless, applying the Wigner-Eckart theorem, the Stevens' operators can be written in terms of the total angular momentum operators J_z, J_+ and J_-, in the same way provided the reduced matrix elements θ_n are included [12]. These reduced matrix elements can be derived or found in tables, for example in Ref. [12]. For Ho^{3+}, for example, $\alpha_J = -1/(2 \cdot 3^2 \cdot 5^2)$, $\beta_J = -1/(2 \cdot 3 \cdot 5 \cdot 7 \cdot 11 \cdot 13)$ and $\gamma_J = -5/(3^3 \cdot 7 \cdot 11^2 \cdot 13^2)$.

The crystal field Hamiltonian can finally be expressed in terms of Steven's crystal field operators [13] as

$$\mathcal{H}_{CF} = \sum_{n\alpha} B_n^\alpha O_n^\alpha. \tag{1.14}$$

The summation should include both the $O_n^{\alpha C}$ (containing $\cos\phi$) and $O_n^{\alpha S}$ (containing $\sin\phi$) operators. Certain operators will be disallowed by symmetry. For example, the crystal field surrounding Ho^{3+} ions in $LiHoF_4$ has S_4 symmetry and will have the following non-zero terms (after an arbitrary rotation in the ab-plane) [14]:

$$\mathcal{H}_{CF} = B_2^0 O_2^0 + B_4^0 O_4^0 + B_4^{4C} O_4^{4C} + B_6^0 O_6^0 + B_6^{4C} O_6^{4C} + B_6^{4S} O_6^{4S}. \tag{1.15}$$

The B_n^α coefficients are defined (in the point charge model) as

$$B_n^\alpha = -eq\theta_n \gamma_{n\alpha} c_{n\alpha} \langle r^n \rangle \tag{1.16}$$

These could be easily calculated except for q and the radial integral[1] $\langle r^n \rangle$ which present more of a challenge and are often left as fitting parameters. Thus the symmetry of the potential determines which operators are not present, but the relevant crystal field parameters must be determined experimentally. In principle, they can be calculated, though in practice the results are highly unreliable [16, 17].

Those relevant operator equivalents for $LiHoF_4$ are given in terms of angular momentum operators (J_z, J_+, J_-, J^2) by [18]

$$\begin{aligned}
O_2^0 &= 3J_z^2 - J^2 \\
O_4^0 &= 35Jz^4 - 30J^2J_z^2 + 25J_z^2 - 6J^2 + 3J^4 \\
O_4^{4C} &= \frac{1}{2}(J_+^4 + J_-^4) \\
O_4^{4S} &= \frac{i}{2}(J_+^4 - J_-^4) \\
O_6^0 &= 231J_z^6 - 315J^2J_z^4 + 735J_z^4 + 105J^4J_z^2 - 525J^2J_z^2 + 294J_z^2 - 5J^6 + 40J^4 - 60J^2 \\
O_6^{4C} &= \frac{1}{4}(J_+^4 + J_-^4)(11J_z^2 - J^2 - 38) + \frac{1}{4}(11J_z^2 - J^2 - 38)(J_+^4 + J_-^4) \\
O_6^{4S} &= \frac{1}{4i}(J_+^4 - J_-^4)(11J_z^2 - J^2 - 38) + \frac{1}{4}(11J_z^2 - J^2 - 38)(J_+^4 - J_-^4)
\end{aligned} \tag{1.17}$$

The use of operator equivalents and symmetry arguments gives us an understanding of what energy splittings will occur and, most importantly, what single-ion anisotropies may result. The single-ion anisotropy can tell us whether we should be dealing with an Ising (spins up or down along an axis), XY (spins confined to a plane) or Heisenberg (isotropic) magnet. The energy splittings can tell us in what temperature range or to what strength of perturbation does the single-ion anisotropy hold. One of the exciting prospects of studying rare earth magnets is the freedom to create many different kinds of magnetic species, and study them in the same geometric structure.

According to Kramers' theorem, rare earth ions that have an odd number of valence electrons, such as Dy^{3+}, Er^{3+} and Yb^{3+}, must be split, at most, into doublets, until a magnetic field breaks time-reversal symmetry [19]. Non-Kramers ions, including Ho^{3+}, on the other hand, are able to split into a collection of doublets or singlets, depending on the crystalline environment [20]. Ho^{3+} in the $LiYF_4$ lattice, for example, does form a ground state doublet. However, introduction of a small lattice strain, for example, will split this doublet in energy.

In some non-Kramers ions, the crystal field can result in singlets as the lowest energy eigenstates. Since $\langle J^\mu \rangle = 0$ for each singlet energy level, in that case there is no magnetic

[1]The radial integrals $\langle r^n \rangle$ can in principle be calculated accurately, at least for free rare earth ions [15]

moment in the ground state [21, 22]. This means that at the single-ion level, there will be no magnetism. However, interactions between the magnetic moments of sufficient strength in such a "singlet-singlet" magnet can induce a magnetic moment by mixing the the two lowest lying energy levels. There will be a critical value of the interaction strength between the ions above which magnetism will be found and below which one will observe van Vleck paramagnetism [22]. An important example of such behaviour is the magnetic ion Tb^{3+} in the $LiYF_4$ lattice [23]. Despite a singlet-singlet ground state, $LiTbF_4$ orders ferromagnetically as a result of an induced moment. In $LiTb_xY_{1-x}F_4$, there is found to be a critical concentration at $x = x_C$ below which the interactions are no longer strong enough to induce magnetism and the material ceases to order. A similar case occurs in the material Pr_3Tl for example [22].

1.1.3 Exchange and Dipolar Interactions

As with most magnetic systems, in rare earth magnets there are usually exchange interactions

$$\mathcal{H}_{\text{Ex}} = \sum_{\langle i,j \rangle} \mathcal{J}_{ij} \boldsymbol{J}_i \cdot \boldsymbol{J}_j \tag{1.18}$$

with neighbouring spins. In this convention, a positive value of $\mathcal{J}_{ij}$ is an antiferromagnetic interaction and a negative value of $\mathcal{J}_{ij}$ is ferromagnetic. In some cases the nearest-neighbour interaction $\mathcal{J}_1$ may be sufficient to describe the magnetic behaviour and in others, more distant exchange interactions must be considered. Because of the tightly bound nature of the $4f$ electrons, the exchange interactions can be quite small in rare earth magnets (relative to most transition metal magnets). For example, in $LiHoF_4$, the nearest-neighbour exchange is only about 0.1 K in strength [24]. This lowers the temperature of relevance. In the materials studied in this thesis, all of the important physics occurs below 2 K.

This small exchange interaction, as well as the large magnetic moments, then expose the dipole-dipole interaction, which would otherwise be much less significant. The dipolar interaction is quite simple in fact: each dipole moment creates a magnetic field around it which is 'felt' by other magnetic dipoles. However the form of the interaction is more complicated than isotropic exchange and is given by

$$\mathcal{H}_D = \sum_{\langle i,j \rangle} \mathcal{D}_{ij}^{\alpha\beta} J_i^\alpha J_j^\beta = \sum_{\langle i,j \rangle} \frac{\mu_0}{4\pi} g_J^2 \mu_B^2 \left[\frac{\mathbf{J}_i \cdot \mathbf{J}_j}{r_{ij}^3} - \frac{3(\mathbf{J}_i \cdot \mathbf{r}_{ij})(\mathbf{J}_j \cdot \mathbf{r}_{ij})}{r_{ij}^5} \right]. \tag{1.19}$$

In certain rare earth magnets, this dipolar interaction is just as important as the nearest-neighbour exchange (for example in $Gd_2Sn_2O_7$ and $Gd_3Ga_5O_{12}$ to be discussed in Chapters

4 and 5). In $LiHo_xY_{1-x}F_4$, it turns out that the dipolar interaction is overwhelmingly dominant (as will be discussed in Chapter 3). An energetically significant dipolar interaction has several important implications.

First, it is important to note that the dipolar interaction is anisotropic. It can be antiferromagnetic (positive) or ferromagnetic (negative) depending on the orientation of the spins relative to the vector connecting the spins. For example, if one considers Ising spins that are on top of each other along the Ising axis, they will be found to be ferromagnetically coupled by the dipolar interaction. If they reside in the same plane perpendicular to the Ising axis, however, they will be antiferromagnetically coupled. Thus, depending on the lattice in question, the dipolar interaction could favour either ferromagnetism or antiferromagnetism.

Furthermore, dipolar systems have inherent frustration – an inability to minimize all pairwise interactions – due to the inevitable competition between ferromagnetic and antiferromagnetic dipolar interactions. In a pure crystalline lattice, either ferromagnetism or antiferromagnetism will be energetically favourable. However, if the system is diluted, as in the case of $LiHo_xY_{1-x}F_4$, this competition can be exposed as random frustration. This random frustration is one of the key ingredients for a spin glass state [25, 26] and is what is thought to give rise to a spin glass state in dilute $LiHo_xY_{1-x}F_4$. This will be explained in more detail in Chapter 3.

In otherwise isotropic Heisenberg systems, the dipolar interaction plays an important role by creating an anisotropy. As a simple example, imagine a linear chain of Heisenberg spins with the length of the chain along x. If the interactions are completely isotropic, all that matters is the relative orientation of the spins. Let us assume that they are ferromagnetically coupled by nearest-neighbour exchange. They all want to point in the same direction, but that could be any arbitrary direction. However, if we introduce the dipolar interaction, things change appreciably. With all the spins pointing perpendicular to the x-axis, only the first term of Equation 1.19 will play a role and the dipolar energy will be a positive

$$E_D \propto +\frac{1}{4}\sum_{\langle i,j\rangle}\frac{1}{r_{ij}^3}. \tag{1.20}$$

If the spins are, on the other hand, all pointing along the length of the chain, the dipolar energy becomes

$$E_D \propto \left(+\frac{1}{4}-\frac{3}{4}\right)\sum_{\langle i,j\rangle}\frac{1}{r_{ij}^3} = -\frac{1}{2}\sum_{\langle i,j\rangle}\frac{1}{r_{ij}^3}. \tag{1.21}$$

Thus it is clearly energetically favourable for the moments to lie along the x-axis. This creates an anisotropy energy. Even if the dipolar interaction is not strong enough to alter

the ordering wavevector which is selected by stronger interactions, it will certainly affect the low energy spin excitations, in particular by introducing an anisotropy gap [27]. The nature of this anisotropy is much more complicated in a 3-dimensional antiferromagnet, than in the simple example above. Such an effect on $Gd_2Sn_2O_7$ will be discussed extensively in Chapter 4.

We also note that the dipolar interaction is long range. Whereas exchange interactions beyond third nearest neighbour are rarely important, the dipolar interaction drops off only as $1/r_{ij}^3$, which means that it can have very unique effects. As we mentioned above, in $LiHo_xY_{1-x}F_4$, dilution of the dipole moments introduces random frustration which may result in a spin glass transition. What happens as we continue to dilute the system by removing Ho and lowering x? If the system were dominated by short range interactions, we would eventually hit a percolation threshold x_C. This critical concentration would be the point at which our system was no longer fully connected by exchange interactions. Below that point, the system could be subdivided into many smaller, isolated subsystems. In such instances, the thermodynamic limit is lost and a true thermodynamic phase transition becomes impossible [28].

In a dipolar system, however, there is no percolation threshold [29]. Certainly the average interaction strength in the system will become smaller as x is decreased, but the system can never be subdivided into smaller isolated pieces at some critical x_C. Only at $x = 0$ should the spin glass temperature drop to 0 [29]. This effect is central to our discussion of $LiHo_xY_{1-x}\ F_4$ in Chapter 3.

The long range nature of the dipolar interaction is also predicted to have an impact on the critical behaviour of a continuous phase transition. For a magnetic system coupled with short range interactions, it is found that $d = 4$ is the upper critical dimension meaning that for dimensions higher than 4, such a system will exhibit mean-field critical exponents [30]. In dimensions less than 4, one will find critical behaviour but with non-mean-field critical exponents. Precisely at $d = d^* = 4$, one should expect to find mean-field critical behaviour with logarithmic corrections [31]. However, when the interactions become long range, like the dipolar interaction, this can shift the upper critical dimension. For the dipolar coupled Ising ferromagnet, theory predicts that the upper critical dimension will be $d^* = 3$ [31, 32]. This allows for the possibility of observing mean-field critical behaviour with logarithmic corrections in a realistic system. Several experimental [33, 34, 35, 36] and numerical [37, 38] studies have shown evidence of such behaviour. For dipolar antiferromagnets, however, it is not expected [39] or observed [40, 41] that the critical behaviour close to the transition is altered from that of a short range model.

Finally, we note that the dipolar interaction, owing to its long range nature, can make the pursuit of a theoretical description of a system rather challenging. Truncating calculations to a finite distance, for example, can have disastrous effects on the accuracy of the

theoretical results. Thus complex methods such as Ewald summation must be employed to properly include the dipolar interaction [27].

1.1.4 Hyperfine Interactions

Hyperfine interactions with nuclear moments are rarely important to the collective behaviour exhibited by the electronic moments in a system. The dipole moment of a nucleus is a great deal smaller than the dipole moment of an electronic spin thus nuclear ordering generally only takes place at very low temperatures, often 100 μK or lower [42]. Nuclear hyperfine interactions are, however, frequently important for the interpretation of certain experimental results. Generally the important nuclear moments to consider are the magnetic dipole moment and the electric quadrupole moment [20].

The nuclear dipole moment interacts with the electronic magnetic moments via what is usually just referred to as the hyperfine interaction. It is usually taken to be an isotropic interaction

$$\mathcal{H}_{HF} = A\boldsymbol{I}\cdot\boldsymbol{J}. \tag{1.22}$$

In principle, this hyperfine coupling can affect the electronic moments. However, the energy of interaction is generally so tiny (several mK) that it becomes completely irrelevant. Holmium is a rare exception and as we will see in Chapter 3, the nuclear hyperfine interaction is so large (relatively speaking) that it can influence the collective magnetic behaviour of the electronic moments in the system!

The nuclear electric quadrupole moment, on the other hand, interacts with the electric field gradient. This Hamiltonian is given by

$$\mathcal{H}_Q = P\left[I_z^2 - \frac{1}{3}I(I+1) + \frac{1}{3}\eta(I_x^2 - I_y^2)\right] \tag{1.23}$$

where

$$P = \frac{3eQ}{4I(2I-1)}\left(\frac{\partial^2 V}{\partial z^2}\right). \tag{1.24}$$

The electric field gradient at the nucleus $\partial^2 V/\partial z^2$ has contributions from the crystal field and from the electronic valence orbitals. For axially symmetric systems, $\eta = 0$ [43]. This is the case for the materials in this thesis for which we will want to consider the nuclear electric quadrupole interaction.

Most often, nuclear hyperfine interactions are at a low enough energy that they have a negligible effect on the collective behaviour of the electronic magnetic moments in a system. These hyperfine interactions can, however, frequently be observed with various experimental methods. The specific heat of a material, for example, will show a Schottky

anomaly[2] as a result of the nuclear hyperfine interaction. Often, since this interaction happens at very low temperature, one observes only the tail of the anomaly which has a $1/T^2$ dependence. In nuclear magnetic resonance (NMR) [44] and Mössbauer [45] experiments, one often directly observes the nuclear moments and the corresponding hyperfine energy levels. Thus one can essentially be studying the electronic magnetism through hyperfine interactions.

1.2 Spin Glasses

In a nutshell, a spin glass is a magnetic analog to a real, structural glass, like amorphous SiO_2 for example. An antiferromagnet or ferromagnet is, in the same way, analogous to a crystalline material (like quartz or crystalline SiO_2 for example). Loosely speaking, a spin glass state is a magnetic "solid" where the spins are largely frozen, but that is "amorphous" in that it has no long range periodic order and the spins are seemingly randomly oriented.

More precisely, though, a spin glass is thought to have a thermodynamic transition [25]. In fact, much of the research into spin glasses (and into structural glasses) has aimed at determining whether there is a sharp (spin) glass phase transition at some finite temperature T_g. While it is clear that some materials relax very slowly at low temperatures and are unable to find an ordered state, are they truly frozen at some precise, non-zero temperature or is this merely a failure to obtain equilibrium measurements in experiment? The current consensus is that there is indeed, in some materials, a strange second-order phase transition at a temperature T_g to a random but largely "frozen" state where any remaining dynamics are irreversible [25].

The prevailing picture of spin glasses is one of a complicated free-energy landscape with many energy barriers and energetically favourable valleys. As one approaches the glass transition at T_g, the energy barriers diverge, leaving the system trapped in a particular valley with a random configuration of spins. While some dynamics remain, as the system is allowed to explore that particular valley, ergodicity is lost and the system is not able to explore all possible states [26].

It is found that rather diverse physical systems, for example dilute magnetic alloys such as CuMn [46] as well as magnetic insulators such as $Eu_xSr_{1-x}S$ [47], show very similar spin glass behaviour. This suggests a degree of "universality", in that the details of the magnetic interactions seem not to be so important to the end result, that is collective spin glass behaviour [25].

[2] A Schottky anomaly is the specific heat form resulting from a single energy level splitting ϵ, given by $C/k_B = (\beta\epsilon)^2 e^{-\beta\epsilon}/(1+e^{-\beta\epsilon})^2$. Often times, a Schottky-like feature results, as a result of several, evenly spaced energy levels.

The view at this time, is that there are two principal ingredients that are necessary to give rise to a spin glass state. First, the system must have a sufficient level of quenched randomness or disorder and second, there must be competing interactions between pairs of spins, otherwise known as frustration. These ingredients can be generated in a variety of ways, often through either random dilution of the magnetic moments, or through random interactions between the moments, or some combination thereof.

Spin glass theory is an extremely complex and numerically intensive subject and the experimental side of this subject also presents many technical and interpretive challenges. The body of research on spin glasses is absolutely enormous so this section of the thesis will attempt only to summarize some of the more important aspects of the topic and will concentrate especially on the phenomenology associated with spin glass systems.

1.2.1 Phenomenology

The discovery of spin glasses came about while studying a dilute alloy of magnetic manganese (Mn) in copper (Cu). It was initially noticed that at low temperatures, there was an anomalously large linear component to the specific heat [46]. It was suggested by Anderson [48] that this low-temperature linear specific heat could be resulting from a distribution of two level systems (TLSs) coming from a random ordering of the magnetic moments. This randomly frozen ground state begat the term 'spin glass', an analogy for structural glasses which are a solid (frozen) state of matter without conventional long range order. Otherwise, the spin glass specific heat showed a broad feature which did not seem to indicate a phase transition of any kind [49]. Much of the history of spin glasses has involved and still involves, the question of weather there is a sharp, finite temperature spin glass transition of some kind.

Initial measurements of the ac magnetic susceptibility noted a relatively sharp peak, suggestive of a phase transition [50, 51]. This peak was later found to be somewhat rounded and frequency dependent (see Figure 1.1) with the position of the peak or freezing temperature (T_f) shifting to lower temperatures with lower frequencies of measurement [52, 53, 54]. In some cases [55] it is obvious that the limit of $\omega = 0$ gives a non-zero freezing temperature which can be thought of as a true transition temperature or glass temperature which we will call T_g throughout this thesis.

As the in-phase component of the susceptibility χ' is freezing out and dropping at T_f, the out-of-phase component or dissipation χ'' becomes relevant as well, showing that the magnetic moments are lagging or phase shifted relative to the oscillating magnetic field. Studies of the frequency dependence of $\chi' - i\chi''$ find an exceptionally broad maximum in $\chi''(\omega)$ with a peak position that shifts to lower frequencies with lower temperatures [56, 57, 58]. This wide absorption spectrum is indicative of a broad distribution of time scales

in the system.

In measuring the 'dc' susceptibility or magnetization, a divergence between the field-cooled (FC) susceptibility and the zero-field-cooled (ZFC) susceptibility is encountered in the vicinity of T_g [59]. Of course there is no such thing as a truly 'dc' measurement. This is particularly important in glassy systems possessing sharply diverging time scales. However, in most spin glasses, there is a fairly well defined point at which FC and ZFC susceptibility diverge on the time scale of a typical experiment.

Critical slowing down, or a diverging time constant, also takes place in more conventional magnetic systems such as ferromagnets and antiferromagnets. However, the time scales are generally much shorter until very close to the transition temperature and the dynamical critical exponent z is smaller. For example, $z = 2$ for an anisotropic FM and $z = 5/2$ for a Heisenberg FM [60], as compared with $z > 5$ often observed in spin glasses [61]. This leads to a much less dramatic effect that is not easily observed with ac magnetic susceptibility measurements. Studies of critical slowing down in antiferromagnets and ferromagnets have employed faster experimental techniques such as neutron scattering, electron spin resonance (ESR) and nuclear magnetic resonance (NMR) [62, 60]. There are also other reasons why the peak in χ of a ferromagnet might also be rounded including demagnetization and disorder.

While for many years, the idea of a true spin glass transition was debated, this debate is currently mostly settled, in large part due to the discovery (theoretical [63] and experimental [64]) that the nonlinear susceptibility χ_3 diverges at T_g, as shown in Figure 1.1(c). The magnetization can be written as a Taylor series in the applied magnetic field H as

$$M(H) = \chi H + \chi_3 H^3 + \chi_5 H^5 + \dots \tag{1.25}$$

There are various ways to then extract χ_3. If one has a measurement, such as a SQUID magnetometer, capable of measuring the magnetization rather than the susceptibility, one can directly measure $M(H)$ to extract χ_3. Often the nonlinear susceptibility is simply defined [65] as

$$\chi_{nl} = -(M/H - \chi) \tag{1.26}$$

leaving a quantity that is, at least, dominated by $-\chi_3$ and diverges at the transition temperature. Alternatively [66], with a susceptometer, one can apply a constant magnetic field plus a sinusoidal magnetic field $H_0 + h\cos(\omega t)$. Then the signal observed in the susceptometer at frequency ω will be proportional to

$$\chi + 2H_0^2\chi_3 + \dots \tag{1.27}$$

A final method is to use a large oscillating magnetic field and to observe the 3rd harmonic of the magnetization, which will be proportional to the nonlinear susceptibility

χ_3 [61]. Even though χ_3 diverges in spin glass materials, it is quite small at temperatures far away from T_g and inevitably, the transition is rounded by dynamical effects [61], thus a larger ac magnetic field is often required to measure the nonlinear susceptibility than the linear susceptibility. In Ref. [61], the balance of the susceptometer is deliberately spoiled in order to cancel some of the linear susceptibility and therefore make χ_3 more easily apparent.

Below the spin glass transition temperature, the system is not in fact completely frozen and one can still observe dynamics and fluctuations. However, the dynamics are highly irreversible as there are significant energy barriers to relaxation. If, for example, the sample is field cooled below the transition and the field is turned off, the magnetization will quickly fall to what is known as the thermo-remanent magnetization (TRM) which will very slowly decay towards, but never reach, zero magnetization [44]. There is also significant history dependence and hysteresis in the magnetization below T_g as either the temperature or the magnetic field is changed [44]. Ocio *et al.* [67], among others, have observed $1/f$ fluctuations in the spin glass state. The often linear (or close to linear) variation of the specific heat below T_g has been interpreted as resulting from quantum tunneling of a collection of nearly degenerate two-level systems, as is also seen in structural glasses [48]. Alternatively, it has been suggested that the linear specific heat can be explained with delocalized modes, not unlike spin waves, at least in Heisenberg spin glasses [68].

There are several other measurements that can be used to identify a spin glass material [44]. In dilute magnetic alloys like Cu*Mn*, the resistivity shows an anomaly near the spin glass transition. Clearly such a measurement would not be applicable to insulating spin glasses, however. In neutron scattering experiments, the structure factor $S(\omega, \boldsymbol{q})$ can be broken up into a static part $S_S(\omega, \boldsymbol{q})$ and a dynamic part $S_D(\omega, \boldsymbol{q})$. The static part provides at least a null result – magnetic Bragg peaks will not be seen in a spin glass, thereby ruling out a conventionally long range ordered state. The dynamic part of the structure factor permits the observation of spin relaxation, though on a rather short time scale $\sim 10^{-7}$ to 10^{-8} s [44]. Longer time scales (smaller energy) can be probed with neutron spin echo (NSE) experiments.

The local probe muon spin resonance or μSR (also known as muon spin rotation or relaxation) is also quite useful in spin glass measurements [44]. As a dynamical tool, it is able to interpolate between high frequency neutron scattering experiments and low frequency ac susceptibility measurements. This technique also probes low enough frequencies to track the critical slowing down of the system, to a certain point. Alternatively, μSR can provide information about the distribution of internal fields in the material [44].

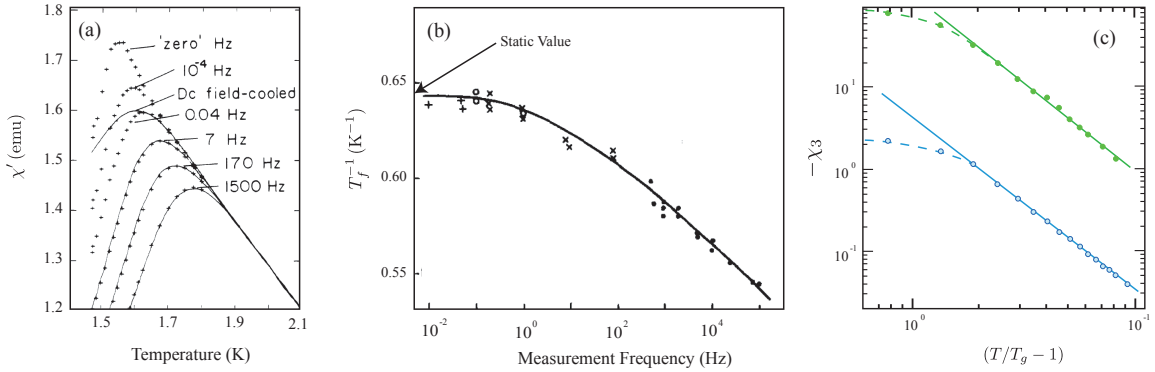

Figure 1.1: (a) Linear susceptibility χ' of $Eu_xSr_{1-x}S$ ($x = 0.4$) for different measurement frequencies [55]. (b) The corresponding location of the maximum in χ' or T_f as a function of frequency showing a transition temperature in the static limit. (c) The nonlinear susceptibility of Cu*Mn* showing critical behaviour with an exponent $\gamma = 2.3$ in zero field (open blue circles) and in 90 G (closed green circles) [61].

1.2.2 Spin Glass Materials

The first spin glasses to be studied were dilute magnetic alloys such as Cu*Mn*, Ag*Mn* and Au*Fe*.[3] The magnetic ions in these materials interact via the Ruderman-Kittel-Kasuya-Yosida (RKKY) interaction

$$J_{ij} = J_0 \frac{\cos(2k_F r_{ij} + \phi)}{(2k_F r_{ij})^3}. \tag{1.28}$$

where k_F is the Fermi wavevector and r_{ij} is the distance between the magnetic moments i and j. This interaction is a result of magnetic impurities creating a damped oscillation in the susceptibility of the conduction electrons and a corresponding interaction between the impurities [44]. Most importantly, the oscillation causes a sign change in the interaction depending on the distance r_{ij} between spins. This creates competing interactions or frustration, since some interactions will be ferromagnetic and others will be antiferromagnetic.

While initially study of spin glasses was confined to dilute magnetic alloys, later very different types of spin glasses were discovered. $Eu_xSr_{1-x}S$ is the first insulating magnetic material to exhibit spin glass physics (see for example Refs. [69, 47, 70]). In this site-disordered system, the nearest-neighbour (n.n.) interaction J_1 is ferromagnetic whereas the next-nearest-neighbour (n.n.n.) interaction J_2 is antiferromagnetic. At high concentration

[3]The elements in italics are the dilute sites on which magnetic moments are found.

of Eu, this material is a ferromagnet. Dilution of the magnetic moments, however, exposes random competition between J_1 and J_2, leading to a spin glass state. The discovery of spin glass ordering in $Eu_xSr_{1-x}S$ with many of the same properties as the dilute magnetic alloys suggested that spin glass physics possesses a certain level of "universality" and can manifest itself in a similar way in very diverse physical systems.

Another class of materials to consider is one where the individual spins are replaced by much larger magnetic moments. These can take on various forms and may be referred to by different names, including mictomagnets, cluster glasses [44] and superspin glasses [71]. Mictomagnetism (cluster glasses) may take place in the vicinity of ferromagnetism, where large ferromagnetic clusters form. These clusters then act like very large magnetic moments and interact with each other in such a way that they develop glassy physics and may freeze at a glass transition. Cluster glasses may be at the heart of the counterintuitive idea of spin glass reentrance, where certain systems seem to order ferromagnetically and then, at lower temperatures, give way to a spin glass state.

Superspin glasses are collections of nanomagnets, that by virtue of their disordered positioning and therefore random interactions, mimic the behaviour of spin glasses [71]. These systems are found to generally have a much longer overall, intrinsic time constant τ_0 than most spin glasses, perhaps because the larger magnetic moments have significant internal barriers to spin reversal.

A related concept that is important to mention is superparamagnetism [44]. Superparamagnets are related in that they demonstrate similar 'glassy' behaviour, characterized by slow relaxation in the susceptibility for example. However, superparamagnets, often consisting of magnetic clusters, do not have a freezing transition. The individual moments or clusters have significant random anisotropy barriers to spin flipping and therefore relaxation. This results in a very slow response at low temperatures and so seemingly glassy dynamics. However, the clusters in a superparamagnet are largely non-interacting. Thus the anisotropy energies are temperature independent. The dynamics of the system are therefore thermally activated and the time scales generally follow an Arrhenius law

$$\tau = \tau_0 e^{-E_a/k_B T} \tag{1.29}$$

In a spin glass, the energy barriers to relaxation are highly temperature dependent, leading to diverging time scales at the spin glass transition temperature T_g.

1.2.3 Theory of Spin Glasses

The theory of spin glasses is challenging indeed, exemplified by the difficulties in establishing even a simple mean-field, toy model of spin glass behaviour! Some of the ideas that go into forming such a mean-field theory are discussed here.

The starting point for such a theory must, of course, be a model that is simple enough to work with and extract some meaningful results. We have discussed several different examples of real spin glasses that seemed to have very little in common. What does seem to be (almost) universal in spin glasses is the requirement of randomness and frustration. A set of very simple models which provide those requirements are known as Edwards-Anderson (EA) models [72]. Such models consist of spins on a regular lattice in some dimension, interacting with other spins by J_{ij} where the J_{ij}'s are random variables with probability distribution $P(J_{ij})$. This probability distribution might, to be more realistic, depend on the vector between spins $\boldsymbol{R}_{ij}$. The distribution is often chosen to be either Gaussian or a double δ-function distribution (taking on values $+J_{ij}$ or $-J_{ij}$) [26].

The Sherrington-Kirkpatrick (SK) model [73] is a particularly simple version of the EA model. The interactions are taken to be independent of distance. Thus it is equivalent to an infinite-dimensional model. The concept of a lattice becomes completely irrelevant since every spin is interacting with every other spin with a common probability distribution. That distribution is again often taken to be Gaussian, centred about J_0/N with variance J^2/N. Thus

$$P(J_{ij}) = \sqrt{\frac{N}{2\pi J^2}} \exp\left[-\frac{N(J_{ij} - J_0/N)^2}{2J^2}\right] \tag{1.30}$$

The normalization by N must be taken to ensure that quantities such as the average internal energy do not diverge in the thermodynamic limit [26].

In addition to a simple Hamiltonian with which to model spin glass behaviour, it is also important to have in mind a concise description of spin glass ordering in the form of an order parameter. The order in a ferromagnet, for example, is easily described with an order parameter m, the magnetization. The magnetization on each site is obtained through the thermal or statistical average of the spin: $m_i = \langle S_i \rangle$. The order parameter m is then the average magnetization across the whole sample $m = [m_i]_{av}$. For an antiferromagnet it is also straightforward to define an order parameter, taking a staggered magnetization instead. For a spin glass, it is less clear what the order parameter should be. How does one characterize a state that is randomly frozen? A strong contender is the Edwards-Anderson order parameter q_{EA} [72] given by

$$q_{EA} = \lim_{t\to\infty} \lim_{N\to\infty} [\langle S_i(t_0) S_i(t_0 + t)\rangle]_{av} \tag{1.31}$$

This order parameter essentially characterizes the ergodicity of the system. If the system is ergodic, it will visit all possible states and clearly q_{EA} will be zero. One can imagine a very complicated free-energy landscape in the space of the m_i's resulting from the disorder in the system, which can have many local valleys in which the system would prefer to reside. The notion of a spin glass transition, is the point where the mountains in the energy

landscape become infinitely high and the system is 'stuck' in one of the valleys. At this point it will no longer be ergodic as it is restricted to exploring a single valley and not the entire phase space. There is broken ergodicity in ferromagnets as well, though of a simpler variety. In that situation, the system finds itself magnetized and to change the direction of the magnetization requires the traversal of an energy barrier that is proportional to the size of the sample, hence the time to surpass that barrier diverges in the thermodynamic limit. In spin glasses, one has broken ergodicity where the restricted phase space is not simply related to a broken symmetry of the Hamiltonian [25].

Much of the challenge in developing a coherent theory of the spin glass transition comes from the difficulties associated with averaging over disorder [26]. In normal statistical mechanics, one performs weighted averages over all the possible states of a system to form a partition function $\mathcal{Z}$. Now, if this partition function

$$\mathcal{Z}[J] = \mathrm{Tr}_S \exp\left\{-\beta \mathcal{H}[S, J]\right\} \tag{1.32}$$

depends on some random configuration of bonds J_{ij}, we must somehow average over different possible configurations of such bonds, symbolized by $[\,]_{av}$. But $[\mathcal{Z}]_{av}$ is not the appropriate average to perform, since this would be equivalent to annealing out the disorder rather than quenching in the disorder [26]. Instead, one should average the free energy with $[F]_{av}$ or equivalently average the logarithm of the partition function $[\ln \mathcal{Z}]_{av}$. This average turns out to be a difficult one to perform, a problem that commonly arises in studying disordered systems.

A method commonly used to get around this problem is known as the replica trick. It uses the identity

$$\ln \mathcal{Z} = \lim_{n \to 0} \frac{\mathcal{Z}^n - 1}{n} \tag{1.33}$$

to change the average over $\ln \mathcal{Z}$ to an average over n *replicated* partition functions

$$\mathcal{Z}^n[J] = \mathrm{Tr}_{S^1, S^2, \ldots, S^n} \exp\left\{-\beta \sum_{\alpha=1}^{n} \mathcal{H}[S^\alpha, J]\right\}. \tag{1.34}$$

Of course, after taking the average over the disorder, one must somehow take the limit $n \to 0$. It is not at all intuitive how this should be accomplished and is an issue that inhibited a correct solution to the mean-field SK model for many years.

The disorder average of an EA model is obtained through

$$[\mathcal{Z}^n]_{av} = \mathrm{Tr}_{S^1, S^2, \ldots, S^n} \prod_{ij} \int dJ_{ij} P(J_{ij}) \exp\left(-\beta \sum_{\alpha=1}^{n} J_{ij} S_i^\alpha S_j^\alpha\right) \tag{1.35}$$

which is fairly easily evaluated with a Gaussian integral if P is taken to be Gaussian. For the SK model that we discussed above, this disorder average results in [26]

$$[\mathcal{Z}^n]_{av} = \mathrm{Tr}_{S^1,S^2,\ldots,S^n} \exp\left(\frac{\beta^2 J^2}{4N}\sum_{ij}\sum_{\alpha\beta} S_i^\alpha S_i^\beta S_j^\alpha S_j^\beta + \beta J_0 \sum_\alpha S_i^\alpha S_j^\alpha\right)$$
$$= \mathrm{Tr}_S \exp(-\beta \mathcal{H}_{\text{eff}}). \tag{1.36}$$

The disorder has been taken care of but the resulting effective Hamiltonian now includes 4-spin interactions between replicas. A sort of order parameter can be identified as

$$q = q^{\alpha\beta} = \langle S_i^\alpha S_i^\beta \rangle \tag{1.37}$$

and with some work (which we will not describe here), in a mean-field approximation, the SK equation [73] in zero magnetic field can be extracted:

$$q = \int \frac{dz}{\sqrt{2\pi}} e^{-z^2/2} \tanh^2(\beta J \sqrt{q} z). \tag{1.38}$$

This is a self-consistent equation for the order parameter q originally determined by Sherrington and Kirkpatrick [73] giving a spin glass transition T_g. It turns out that it is not correct, however, and it gives some unphysical results, in particular a negative entropy at $T = 0$. The error is in the $n \to 0$ limit and the assumption that there is replica symmetry. The assumption that all replicas are equal must be true for an integer number of replicas, but the $n = 0$ limit is highly non-intuitive and allows for the system to not be invariant under permutation of the replicas. The problems with the mean-field solution of the SK model were finally fixed by Parisi [74, 75] by introducing replica symmetry breaking. Instead of a single order parameter q, one is left with a distribution of order parameters $P(q)$. This concept of replica symmetry breaking is intimately connected with broken ergodicity [26].

Perhaps some of the best "theoretical" evidence of spin glass physics comes from Monte Carlo simulations [25]. A vast set of simulations have been performed on various spin glass models since the introduction of the EA model in 1975 [25]. These numerical simulations provide an important link between theory and experiment, but, like experiments on spin glasses, can also suffer from very slow dynamics and long equilibration times [26]. Many simulations, such as those of Ref. [76], have provided a standard by which to judge critical exponents and dynamics in spin glass experiments. A distinct advantage of Monte Carlo simulations is their ability to study the same model in different dimensions, hopefully permitting the determination of the lower critical dimension, for example [26]. Where it currently seems rather conclusive that there is a sharp, finite-temperature phase transition

in 3D Ising spin glasses [77], for Heisenberg systems the lower critical dimension is likely 3 or higher [26]. In real systems like the RKKY spin glasses, small anisotropies may become very important, however, and lead to Ising behaviour [26].

This brief discussion has barely scratched the surface of spin glass theory. It is an immense field of research with connections to diverse subjects such as structural glasses and neural networks. It is, however, sufficient to conclude that, after much theoretical and experimental effort, a true thermodynamic phase transition to a spin glass state is believed to exist in a great many systems. In this thesis we will consider two magnetic systems that show glassy physics. In Chapter 3 we consider a system, $LiHo_xY_{1-x}F_4$ in which the existence of a spin glass state has been put in doubt and is now a matter of considerable debate. And in Chapter 5, we consider a system, $Gd_3Ga_5O_{12}$, in which the spin glass physics has defied explanation for well over a decade.

1.2.4 Critical Exponents and Scaling

While unusual in nature, the spin glass transition is understood to be a continuous phase transition and should therefore have certain (possibly universal) critical exponents near the transition temperature [26, 25]. The main difference is that the order parameter of a spin glass is not as clearly observable as say the magnetization in a ferromagnet. The usual magnetic susceptibility is not the susceptibility of the order parameter so does not exhibit critical behaviour at T_g and does not show a sharp peak or divergence. Instead, theory shows that the nonlinear susceptibility χ_3 is directly related to the spin glass susceptibility χ_{SG} which characterizes fluctuations in the spin glass order parameter, just as χ_1 or χ is representative of fluctuations in magnetization [76]. Thus the scaling relation

$$\chi_3 \sim \chi_{SG} \sim t^{-\gamma} \tag{1.39}$$

is observed, where $t = (T/T_g - 1)$ is the reduced temperature. A number of works have investigated scaling of the nonlinear susceptibility experimentally, in some of the canonical spin glasses, including Refs. [61, 78, 79, 47]. The exponent γ is found in the range from 2 to 4, with most results sitting close to 3. One of these seminal results is shown in Figure 1.1(c) from Lévy [61]. This is well matched to simulations which find $\gamma = 2.9 \pm 0.3$ [76]. The higher harmonics or terms in the $M(H)$ expansion, χ_5, χ_7, etc. are also expected to diverge at the transition, though with modified critical exponents [61].

While, as in other continuous phase transitions, the specific heat is also predicted to exhibit a scaling relation

$$C \sim |t|^{-\alpha}, \tag{1.40}$$

the exponent α is generally found to be in the range -2 to -4 which makes for an extremely small signature at the glass transition, one not typically observable in experiments [26].

For example, from scale invariance and other critical exponents, $\alpha = -1.9 \pm 0.3$ is found in numerical simulations [76]. One particular experimental work claims to have discovered this signature by making careful heat capacity measurements, fitting spline curves and taking derivatives with respect to temperature until a small peak becomes noticeable [80]. This result is shown in Figure 1.2(c). Generally, however, the specific heat is not regarded as a dependable indicator of the position of T_g and is, rather, more representative of excitations above the transition. As a rule of thumb, the specific heat is found to show a broad maximum at a temperature roughly 20% above the glass temperature [25].

Other critical exponents should apply as well. The order parameter q, below the transition, should obey the law

$$q \sim |t|^{\beta} \tag{1.41}$$

The correlation function of the order parameter should behave as

$$G(r) \sim r^{2-d-\eta} e^{-r/\xi}, \tag{1.42}$$

with critical exponent η and spatial dimension d. The correlation length ξ should behave in temperature as

$$\xi \sim |t|^{-\nu} \tag{1.43}$$

A particularly important scaling relation in spin glasses that is not so often dealt with in other systems is scaling of the dynamics. Historically, several ways of parameterizing the behaviour of $T_f(\omega)$ have been tried. The Arrhenius law

$$\tau = \tau_0 e^{-E_0/k_B T_f} \tag{1.44}$$

(where $\tau = 1/\omega$) has been successful in some cases. It exhibits a divergence of time scales at zero temperature and so does not imply a finite temperature phase transition. Alternatively, the Vogel-Fulcher law

$$\tau = \tau_0 e^{-E_0/k_B(T_f - T_0)}, \tag{1.45}$$

drawn from the study of structural glasses, predicts a divergence of time scales at some temperature T_0. Currently, however, numerically and experimentally, spin glasses are understood to exhibit a power law divergence of the time constant τ at the glass temperature T_g:

$$\tau = \tau_0 (T/T_g - 1)^{-z\nu} = \tau_0 t^{-z\nu}, \tag{1.46}$$

where ν is the exponent applying to the correlation function and z is a new dynamical critical exponent [26].

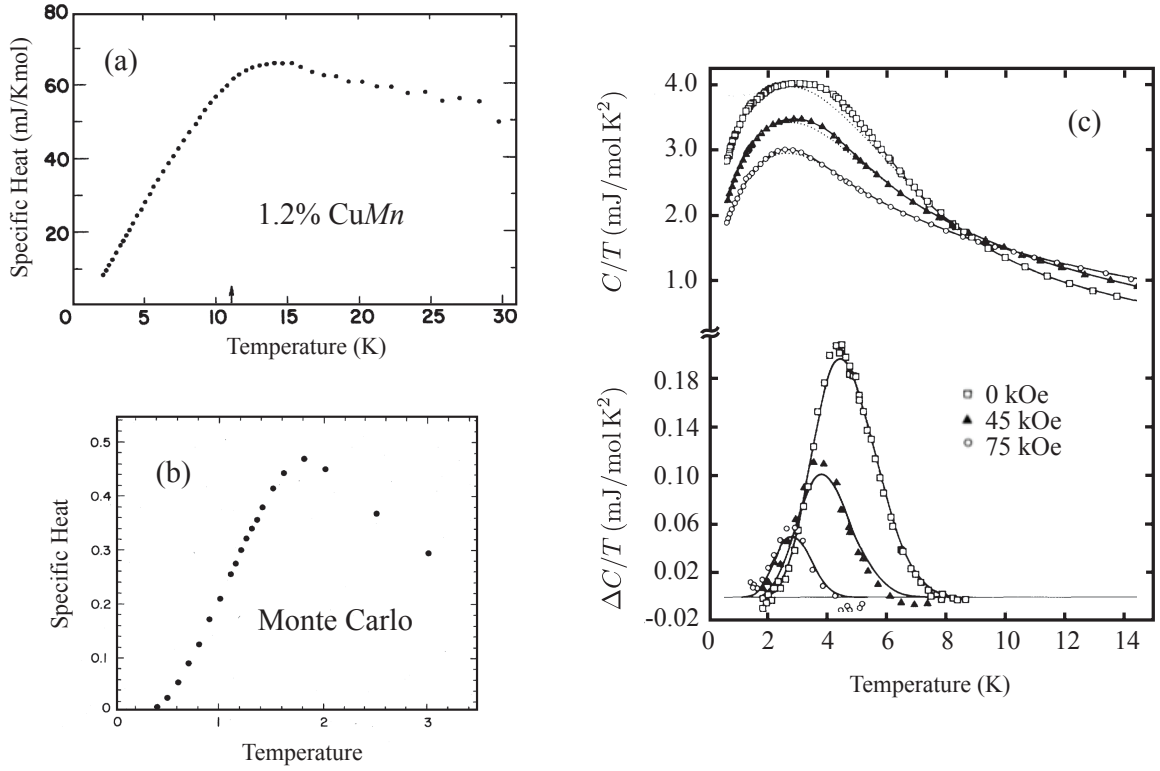

Figure 1.2: (a) The specific heat of the spin glass Cu*Mn* at 1.2% Mn from Ref. [49]. (b) Specific heat of a spin glass computed by Monte Carlo simulations from Ref. [76]. (c) Measurements of Fogle *et al.* [80] of the specific heat of Cu*Mn* taken at three different values of magnetic field. The lower curves, ΔC are an anomaly at the spin glass transition found from fitting spline curves to $C(T)$ and taking derivatives with respect to temperature.

The intricacies of how τ and z should be defined are quite complicated and have been discussed at length by Ogielski [76]. In numerical simulations, for example, one observes the relaxation of the autocorrelation function or order parameter q. The relaxation is characterized by a distribution of relaxation times $\rho(\tau)$. One then has different ways of parametrizing this distribution, such as

$$\tau = \int_0^\infty y^2 \rho(y) dy \Big/ \int_0^\infty \rho(y) y dy \tag{1.47}$$

or

$$\tau_{av} = \int_0^\infty y \rho(y) dy. \tag{1.48}$$

These two different ways of defining the intrinsic time constant should give rise to different critical exponents

$$\tau \sim |T - T_g|^{-z\nu} \qquad \text{and} \qquad \tau_{av} \sim |T - T_g|^{-z_{av}\nu} \tag{1.49}$$

In numerical simulations Ogielski finds $z\nu = 7.9 \pm 1.0$ and $z_{av}\nu = 7.0 \pm 0.8$ [76]. The critical exponent for the correlation length is $\nu \simeq 1.3$. Similar results are found in other numerical simulations [81].

Experimentally, the definition of τ or τ_{av} is somewhat ambiguous. The susceptibility should be defined as [25, 76]

$$\chi(\omega) = \chi'(\omega) - i\chi''(\omega) = \chi_0 \int_0^\infty \frac{d\tau' \rho(\tau')}{1 + i\omega\tau'} \tag{1.50}$$

Then, in principle, one can obtain the characteristic time constants by

$$\tau = \lim_{\omega \to 0} \frac{\chi_0 - \chi'(\omega)}{\omega \chi''(\omega)} \tag{1.51}$$

and

$$\tau_{av} = \lim_{\omega \to 0} \frac{\chi''(\omega)}{\omega \chi'(\omega)} \tag{1.52}$$

However, in practice, these limits are very difficult to take, as we shall see later in Chapter 3. Historically $T_f(\omega)$, given by the maximum in $\chi'(T)$, has often been used [44]. In other cases, researchers have used the peak or inflection point of χ'' [70]. We mention several experimental dynamical scaling results that have obtained good agreement with numerical simulations, determining critical exponents: $z\nu = 7.2$ [70], $z\nu = 8.2$ [82], $z\nu = 6.9 \pm 0.9$ [83] and $z\nu = 7.0 \pm 1.1$ [84].

With so many successful scaling studies performed either numerically or experimentally, particularly those observing a divergence of the nonlinear susceptibility, it seems very likely that there is indeed a sharp (though unusual) thermodynamic transition to a spin glass state. There is certainly a range of values of $z\nu$ found in experiment and theory, though considering the error bars and the complexities of how one defines $\tau(T)$, this is perhaps not surprising.

1.2.5 Glassiness and Percolation

Consider a system of spins on a lattice that are site diluted, so that the probability of a given site being occupied by a magnetic ion is x, where the spins are interacting via short range interactions. If we start from $x = 0$ and gradually increase x, the size of clusters that are completely connected by these short range interactions will grow. If the system size is taken to be infinite (the thermodynamic limit), there will be a critical $x = x_C$ at which the cluster size will diverge [28]. At this point and above, the entire system is connected by interactions.

The notion of a 'percolation' threshold comes from fluid flowing through a porous material. If the density of the pores in the material is too low, they will not all be connected together, hence inhibiting the flow of fluid. However, there is a critical density where the spaces in the material will form one large, interconnected space. At this point, the material will permit liquid to flow through it.

In the case of diluted spins on a lattice, the percolation threshold depends on the type of lattice and on the range of the interactions in the system. Take for example the system $Eu_xSr_{1-x}S$. The magnetic Eu^{2+} ions interact with a nearest-neighbour (n.n.) ferromagnetic interaction J_1 and a next-nearest-neighbour (n.n.n.) antiferromagnetic interaction J_2. At 100% Eu, the system is a ferromagnet. As Eu is diluted with non-magnetic Sr, the transition temperature T_C drops. At around $x = 0.5$ and below, there is sufficient random frustration resulting from the competition between n.n. and n.n.n. interactions, so that a spin glass transition results. However, at $x_C \simeq 0.1$, there is a percolation threshold. The interactions J_1 and J_2 no longer cover the entire system and it is broken up into finite clusters. At this point, the spin glass transition temperature seemingly drops to zero temperature (or at least drops well below the temperature that corresponds to the n.n. and n.n.n exchange interaction strengths) [47, 85]. The phase diagram of $Eu_xSr_{1-x}S$ is shown in Figure 1.3.

For a long range interaction such as the RKKY interaction or the dipole-dipole interaction, however, there is no percolation threshold. The magnetic moments are all connected to each other by some interaction strength, no matter how small. This means that we should expect critical behaviour to persist all the way to zero concentration, rather than

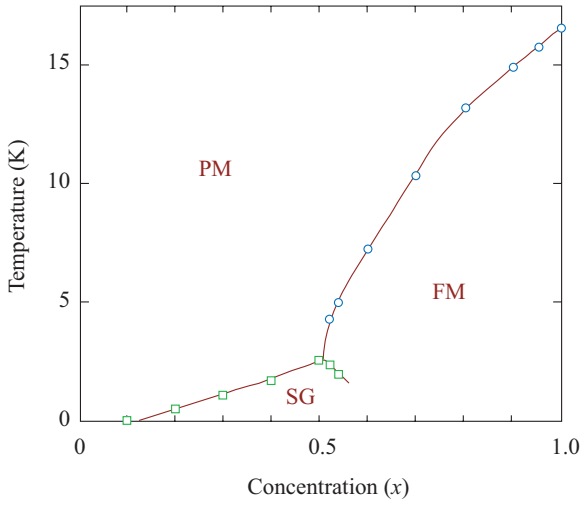

Figure 1.3: The phase diagram of the dilute Ising magnet $Eu_xSr_{1-x}S$. Data points are taken from Refs. [85, 47]. The square symbols are spin glass freezing transitions obtained from a dynamical scaling analysis and the circles are paramagnetic to ferromagnetic transition temperatures found from the position of the cusp in susceptibility.

drop to zero temperature at some critical x_C. This likely applies to $Eu_xSr_{1-x}S$ below the percolation threshold for short range interactions, where the dipolar interaction still connects the entire system.

Percolation with Long-Range Interactions

In this section, we will discuss the mean-field theory that was developed by Stephen and Aharony [29] which suggests that a spin glass should occur at low concentrations of magnetic moments in the presence of certain long range interactions, including the dipolar interaction. The bond distribution in this situation will be J_{ij} with a probability of p and 0 with a probability of $1-p$. Since we have a site-diluted system rather than a bond-diluted system, we should expect $p = x^2$. The Hamiltonian is

$$\mathcal{H}[S,P] = \sum_{\langle i,j\rangle} P_i P_j J_{ij} S_i S_j = \sum_{\langle i,j\rangle} P_i P_j J_0 \left(\frac{r_{ij}^2 - 3z_{ij}^2}{r_{ij}^5}\right) S_i S_j. \tag{1.53}$$

The z superscript is not written since we are only concerned with Ising spins. P_i can take on either 1 or 0, depending on whether the bond labeled by ij is occupied or not. Using

the replica trick, which was introduced earlier, one can write

$$[\mathcal{Z}^n]_{\text{av}} = \text{Tr} \prod_{ij} \left[1 + \nu \exp\left(\beta J_{ij} \sum_{\alpha=1}^{n} S_i^\alpha S_j^\alpha \right) \right] = \text{Tr} \exp(-\beta \mathcal{H}_{\text{eff}}) \tag{1.54}$$

where $\nu = p/(1-p)$. This effective Hamiltonian can be written as an expansion in higher-order spin interactions between the different replica indices, so

$$\mathcal{H}_{\text{eff}} = \sum_{ij} \sum_{k} \beta K_{ij}^k Q_{ij}^k \tag{1.55}$$

The index k labels the order of the expansion. K_{ij}^k must be determined from x, T and the J_{ij}'s. We will have terms containing interactions such as

$$Q_{ij}^k = \sum_{\alpha=1}^{n} S_i^\alpha S_j^\alpha, \qquad Q_{ij}^k = \sum_{\alpha<\beta} S_i^\alpha S_j^\alpha S_i^\beta S_j^\beta \tag{1.56}$$

This expansion then contains a number of competing order parameters. For example

$$m_i = \mu_i^\alpha = \langle S_i^\alpha \rangle \tag{1.57}$$

is the magnetization, so the order parameter for the ferromagnetic regime, whereas

$$q_i^{\alpha\beta} = \mu_i^{\alpha\beta} = \langle S_i^\alpha S_i^\beta \rangle \tag{1.58}$$

is the order parameter for the spin glass regime. The Fourier transforms of these order parameters are σ_q^α, $\sigma_q^{\alpha\beta}$, etc. Fourier transforming the effective Hamiltonian yields

$$\mathcal{H}_{\text{eff}} = -\frac{1}{2} \sum_{k} \sum_{q} (\hat{K}_q^k - 1) |\sigma_q^{\alpha_1 \ldots \alpha_k}|^2 + \mathcal{O}(\sigma^3) \tag{1.59}$$

The critical temperature at which a certain kind of ordering will take place is then found by

$$r_k = 1 - \hat{K}_0^k = 0 \tag{1.60}$$

For the ferromagnetic order parameter, this gives

$$r_1 = 1 - p\beta J_0 a_3 - p \sum_j (\tanh \beta J_{ij} - \beta J_{ij}) = 0. \tag{1.61}$$

The coefficient a_3 is defined [86], through a low-momentum expansion of the Fourier transform of J_{ij}:

$$\hat{J}(\boldsymbol{q}) = \sum_j \exp(i\boldsymbol{q}\cdot\boldsymbol{r}_{ij})J_{ij} \simeq J_0\left[a_3 + a_4 q^2 + a_2 q_z^2 - a_1(q_z/q)^2\right] \tag{1.62}$$

and therefore depends on the lattice in question. Alternatively, for the spin glass order parameter,

$$r_2 = 1 - p\sum_j (\tanh\beta J_{ij})^2 = 0 \tag{1.63}$$

gives the ordering temperature. The level of percolation is related to the ordering temperature T_g as

$$p = \frac{1}{\sum_j \left[\tanh(J_{ij}/k_B T_g)\right]^2} \tag{1.64}$$

If there are circumstances where $r_2 < r_1$, we should expect spin glass ordering. This, in fact, occurs at low values of p or x. What is important is that this spin glass ordering persists all the way to $x = 0$. There is no critical point $x_C \neq 0$ below which we lose the spin glass transition. As $T_g \to 0$, $p \to 0$. On the other hand, if there is a finite number, z, of exchange interactions in the system, it can be seen from Equation 1.64 that as $T_g \to 0$, $p \to 1/z$. Thus there is a percolation threshold at $p_C = 1/z$.

As we will see later in the thesis, this issue is very important to the system $LiHo_xY_{1-x}F_4$ which is dominated by dipolar interactions. As suggested earlier, this idea should also apply to $Eu_xSr_{1-x}S$ below its percolation threshold. At that point, it has been suggested that the long range dipolar interaction should take over from the short range interactions and continue to generate spin glass physics, albeit at a much lower temperature than the temperature at which the short range exchange interactions resulted in glassiness [87].

1.3 Geometric Frustration

Frustration is the inability of a system to minimize all pairwise interactions simultaneously. Geometric frustration, therefore, is frustration resulting purely from the geometric configuration of a crystal lattice. This could be contrasted with random frustration, which is generally at play in spin glasses, where random interactions or random site dilution result in competing interactions. As with spin glasses, the study of geometric frustration is a rather large topic and just a small summary of this area of research is given here, entirely in the context of geometrically frustrated magnets. There is considerable current interest in the subject, primarily as a result of the myriad of interesting and exotic states of matter

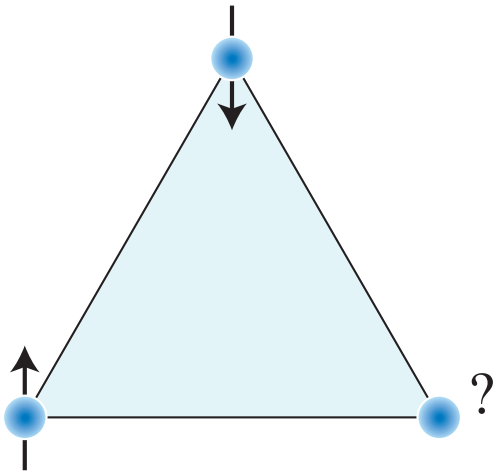

Figure 1.4: A simple example of geometric frustration: antiferromagnetically coupled Ising spins on an equilateral triangle. It is possible to satisfy one pair of bonds, but the third spin will always be frustrated.

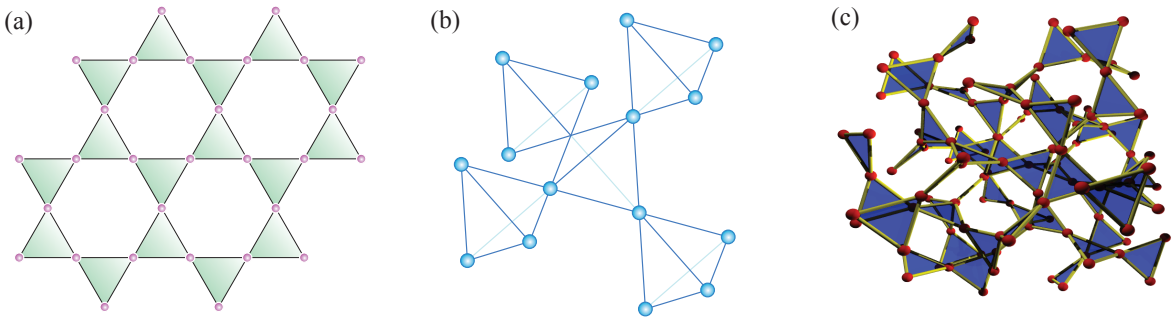

Figure 1.5: Three lattices that are networks of corner sharing simplexes. (a) The kagome lattice in 2-dimensions. (b) The pyrochlore lattice and (c) the hyperkagome garnet lattice, in 3-dimensions.

that have either been observed experimentally or predicted theoretically, resulting from this effect.

The simplest (and perhaps most often employed) illustration of geometric frustration is a triangle with Ising spins on the corners, as shown in Figure 1.4. If the spins are coupled antiferromagnetically, only two pairs, two bonds, can be satisfied completely. One of three spins is unable to choose its orientation. Indeed, the best way to realize geometric frustration in real-life materials, seems to be to use triangles, or their higher-dimension equivalents, tetrahedra. Three important lattices in the field are shown in Figure 1.5. The kagome lattice, in 2-dimensions, consists of a lattice of corner sharing triangles, named for a Japanese basket weaving pattern. In 3-dimensions, we have the pyrochlore lattice, which is based on corner sharing tetrahedra, and the garnet lattice, an example of a hyperkagome lattice of corner sharing triangles.

An often discussed situation is one of isotropic Heisenberg spins, antiferromagnetically coupled, on one of the lattices mentioned above. If we assume that these are purely classical spins, it can be seen that the ground state is one where the total magnetization $\mathbf{M}_s$ on each simplex s (triangle or tetrahedron) is 0. However, this is not just one ground state. The system is heavily underconstrained and there can be a macroscopic number of degenerate ground states available. The existence of this potentially macroscopic ground state degeneracy D can be argued with a simple Maxwellian counting argument [88]: $D = F - K$, where F is the number of degrees of freedom and K is the number of constraints. For spins on q-corner simplexes, each with n components (i.e. Heisenberg spins have $n = 3$), we have $D/N = [n(q-2) - q]/2$, where N is the number of simplexes in the system. This argument applies particularly well to the pyrochlore lattice, resulting in a macroscopic degeneracy $D = N$. This counting argument is too simplistic in the case of the kagome lattice, giving $D = 0$ when in fact it should be $D = N/9$ [88].

A macroscopic ground state degeneracy prevents the system from finding long range order, and thus it is left in some sort of 'spin liquid' or cooperative paramagnetic state. That is, until other interactions or order-by-disorder come into play. Generally speaking, other interactions beyond nearest-neighbour antiferromagnetic interactions will select, from that degenerate ground state manifold, a unique state of long range order. Dipolar interactions are particularly unavoidable for example. Even in the complete absence of other, symmetry-breaking interactions, an order-by-disorder mechanism may favor a certain ground state. There will inevitably be fluctuations around the degenerate manifold of ground states and often these modes will be particularly soft in the vicinity of a certain high-symmetry point on that manifold. Those soft excitations are more often occupied, thus more time is spent in that region of the manifold. This leads to a selection of that particular point, resulting in long range order [89].

In frustrated magnets, this long range order may occur at a temperature much lower

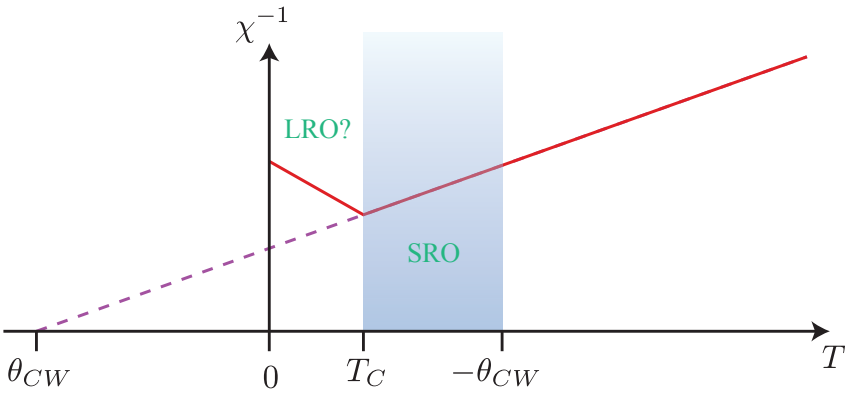

Figure 1.6: A cartoon of the behaviour of the magnetic susceptibility $\chi(T)$ in geometrically frustrated magnets. The temperature can often be decreased well below the Curie-Weiss temperature with only short range order (SRO). At some point, most systems still find a way to order at T_C, often with long range order (LRO), though sometimes with more exotic kinds of order.

than the magnitude of the Curie-Weiss temperature $|\theta_{CW}|$, which is representative of the strength of the nearest-neighbour interactions. This concept is shown in Figure 1.6. In the region between T_C and θ_{CW} there are often indications of short range order (SRO) or cooperative paramagnetism. The ratio

$$f = \theta_{CW}/T_C, \tag{1.65}$$

called the frustration parameter or frustration index [90], has been used as a representation of the degree of frustration in a system. Systems that exhibit such behaviour include several of the materials studied in Chapters 4 and 5 of this thesis.

The pyrochlore lattice is often regarded to be the one that is most likely to have a macroscopic ground state degeneracy and withstand order-by-disorder [88]. Consequently, materials with the pyrochlore lattice have received a great deal of attention and have also demonstrated a plethora of interesting ground states [91]. Without going into any level of detail, we will outline some of the more interesting varieties of highly frustrated magnets that have been observed to date.

Spin Ice

If spins on a pyrochlore lattice have a strong [111] easy-axis anisotropy (that is they prefer to point in or out of a tetrahedron) and are coupled ferromagnetically, a different sort of macroscopic ground state degeneracy can arise. In this case, the net spin on each tetrahedron should be maximized. This is accomplished by having two spins point out of the tetrahedron and two spins point into the tetrahedron. Again, this "two-in, two-out" state can be tiled about the lattice in a macroscopic number of ways [92]. It turns out that this problem is directly analogous to the problem of hydrogen bonds in water ice. There, the oxygen atoms reside on a diamond lattice and the hydrogen bonds between them cover a dual pyrochlore lattice. Each oxygen must have two hydrogen atoms close to it, and two hydrogen atoms more weakly connected, in direct analogy to the two-in, two-out state of what is therefore named spin ice. Hence these are referred to as the ice rules [91]. Pauling originally came up with the idea of a residual ground state entropy in water ice [93] and this same residual entropy, $S_0 = (Nk_B/2)\ln(3/2)$ has been found in spin ice, in the materials $Dy_2Ti_2O_7$ [94] and $Ho_2Ti_2O_7$ [95]. These materials are known as dipolar spin ice, because the nearest-neighbour ferromagnetic interaction is a result of dipolar interactions rather than exchange [95].

In addition to its cooperative paramagnetic ground state, spin ice exhibits a number of other exotic effects. Particularly important in recent years is the discovery of excitations analogous to magnetic monopoles. The ground states of spin ice, satisfying the ice rules, can be thought of as divergence-free, $\nabla \cdot \boldsymbol{M} = 0$, where $\boldsymbol{M}$ is the magnetization. However, flipping one of the spins effectively excites two magnetic monopoles, one with positive magnetic charge and the other negative. If one considers nearest-neighbour interactions only, these monopoles are able to move about on the diamond lattice of tetrahedra without any energy cost. With more distant dipole-dipole interactions included, however, the monopoles feel a Coulomb force between them. Applying magnetic field along the [111] direction allows one to tune the density of monopoles in the system and eventually results in a phase transition where there is no broken symmetry, comparable to a liquid-gas transition [96]. There has been a frenzy of activity on magnetic monopoles in spin ice in recent years, with several results confirming the idea [97, 98, 99].

Geometrically Frustrated Spin Glasses

Since the seminal paper of Villain [100], it has been understood that geometrically frustrated materials may be highly sensitive to the effects of small amounts of random disorder. Indeed, in recent years, the idea that a spin glass state can develop in such materials despite very small quantities of quenched randomness, has been put on more solid ground,

particularly in the context of pyrochlore antiferromagnets [101] and the anisotropic kagome Heisenberg antiferromagnet [102]. Several geometrically frustrated materials have shown stoichiometric or low-disorder spin glass states, including the pyrochlore $Y_2Mo_2O_7$ [103], the kagome hydronium jarosite [104] and the garnet $Gd_3Ga_5O_{12}$ (GGG) [7]. This idea will be discussed in more detail in Chapter 5, particularly for the case of GGG.

Spin Liquids

The idea of a spin liquid is a system that remains dynamic and disordered down to temperatures well below the Curie-Weiss temperature. Spin ice might also be referred to as a type of spin liquid or cooperative paramagnet, since it remains disordered at low temperature and does not undergo a spin glass freezing transition, but the dynamics certainly do slow appreciably as a result of significant energy barriers [105]. In quantum spin liquids, however, the spins can remain truly dynamic down to the lowest temperatures. Such systems possess ground states that exhibit a high degree of entanglement as a result of quantum fluctuations [105] and are more likely to manifest in systems with low spin, particularly spin-1/2, where quantum fluctuations can be as large as the spins themselves. Geometric frustration and low dimensionality are expected to aid in the development of a quantum spin liquid state. Originally proposed by Anderson, referred to as a resonating valence bond (RVB) state [106], quantum spin liquids may result in an exciting kind of fractionalized excitation known as the spinon: a pair of spin-1/2 excitations instead of the usual spin-1 magnon [107]. One of the hopes in this field of research is that it could lend insight to the pairing mechanism in high-T_C superconductors, which is thought to, at least partially, involve coupling with magnetic excitations, possibly from a RVB state [2].

In addition to spin ice, the pyrochlore lattice can also play host to the spin liquid $Tb_2Ti_2O_7$, a pyrochlore which remains disordered down to the lowest temperatures studied [108]. The pyrochlore $Yb_2Ti_2O_7$ [109] and garnet $Yb_3Ga_5O_{12}$ [110] show sharp phase transitions at ~ 250 mK and ~ 50 mK respectively, but appear to have disordered ground states, suggestive of another analogy to the liquid-gas transition. The hyperkagome system $Na_4Ir_3O_8$ [111] and the kagome system $ZnCu_3(OH)_6Cl_2$ (Herbertsmithite) [3], to name a couple, have received a great deal of attention as of late for their possible quantum spin liquid ground states.

Chapter 2

Experimental Methods and Apparatus

2.1 Cryogenics and Thermometry

2.1.1 The Dilution Refrigerator

The most conventional method of refrigeration is to make use of the latent heat of cooling of an evaporating liquid. This method applies for normal kitchen appliance refrigerators to progressively lower temperatures that require more exotic cooling fluids. By the time one obtains a temperature of 20 K or so, one is forced to turn to helium, as all other compounds and elements will be frozen. Liquefying helium allows one to obtain a stable bath of liquid at 4.2 K. From there, one may pump on ^{4}He to get to just above 1 K (in a so called 1K pot). The reason for this temperature limit is that the cooling power is directly related to the vapour pressure of the liquid, which becomes infinitesimally small by 1.2 K or so. In order to go to lower temperatures with cryogenic fluids, one needs to use the lighter and much rarer isotope ^{3}He, which has a lower vapour pressure than ^{4}He. Pumping on ^{3}He allows one to obtain temperatures just under 250 mK, with an apparatus therefore referred to as a ^{3}He refrigerator.

Finally, to achieve any lower temperatures with a continuous cycle, one uses a very different mechanism, that is a circulating mixture of ^{3}He and ^{4}He in what is known as a dilution refrigerator. This is the cryogenic device that was used for the experiments embodied in this thesis and which I will now briefly describe, drawing from Ref. [42]. The dilution refrigerator depends on two critical properties of ^{3}He-^{4}He mixtures. First, there is a higher enthalpy H for ^{3}He diluted in ^{4}He, than for pure ^{3}He. Second, at temperatures below ~ 0.7 K, a ^{3}He-^{4}He mixture phase separates into dilute and concentrated ^{3}He phases. At

zero temperature the dilute phase will contain a finite concentration (6.6%) of ^{3}He whereas the concentrated phase, at absolute zero, will consist of pure ^{3}He.

The first property is that which is used to generate cooling power. In the mixing chamber of the dilution refrigerator, ^{3}He is absorbed into mostly ^{4}He, resulting in an increase in enthalpy H and therefore cooling. When the dilute and concentrated phases are in chemical equilibrium, their chemical potentials are equal, $\mu_D = \mu_C$. Since $\mu = H - TS$, we can obtain ΔH through

$$\Delta H = T \int_0^T \left(\frac{C_D}{T'} - \frac{C_C}{T'} \right) dT' \tag{2.1}$$

Since the specific heat of ^{3}He diluted in ^{4}He, $C_D \simeq (106\,\mathrm{J/K^2\,mol})T$ is much larger than the specific heat of pure ^{3}He, $C_C \simeq (22\,\mathrm{J/K^2\,mol})T$, there is a $\Delta H \simeq (84\,\mathrm{J/K^2\,mol})T^2$ between the two phases (in the low temperature limit, below approximately 40 mK, where C/T is largely constant) [42].

If one were to imagine liquid helium as a classical liquid, one would expect that at zero temperature, the third law of thermodynamics would require that the two isotopes of helium should separate entirely in order to have $S = 0$. The cooling power of the dilution refrigerator is given by $\dot{Q} \propto x\Delta H \propto xT^2$. If x (the concentration of ^{3}He) were ever decreasing, for example exponentially as does the vapour pressure of helium, the fridge would be fighting a losing battle. However, there is in fact a finite solubility of ^{3}He in ^{4}He even at zero temperature, thus the cooling power drops out as T^2, quite a shallow temperature dependence compared to other processes such as evaporative cooling.

This finite solubility at absolute zero does not violate the third law because these isotopes of helium form quantum fluids at such low temperatures. ^{4}He is a Boson and is basically completely Bose condensed into a single superfluid ground state at temperatures well below 0.5 K. ^{3}He is a Fermion, so will not form a superfluid until lower temperatures than even a dilution refrigerator can provide. It can, however, fill up all the lowest lying states available to it quite independently of whether there is a ^{4}He superfluid surrounding it, thereby having 0 entropy. The reason that ^{3}He 'wants' to mix with ^{4}He is that there is an increased binding energy – with less zero point motion, ^{4}He atoms are, in some sense, easier to get close to than ^{3}He atoms, making them more attractive. Thus the first ^{3}He atom to enter ^{4}He is at an energy $\varepsilon_{3,d}$ lower than the chemical potential of pure ^{3}He. As more Fermions enter the dilute phase, however, they must pile on top of each other, unable to occupy the same energy levels. They will pile up to the Fermi temperature, which depends on concentration x. Then once $\varepsilon_{3,d} = k_B T_F(x)$ and the highest occupied energy levels have reached the chemical potential of the concentrated phase, there is no reason for the concentration to continue to increase (except for thermal fluctuations). This limiting fraction is found to be $x = 6.6\%$.

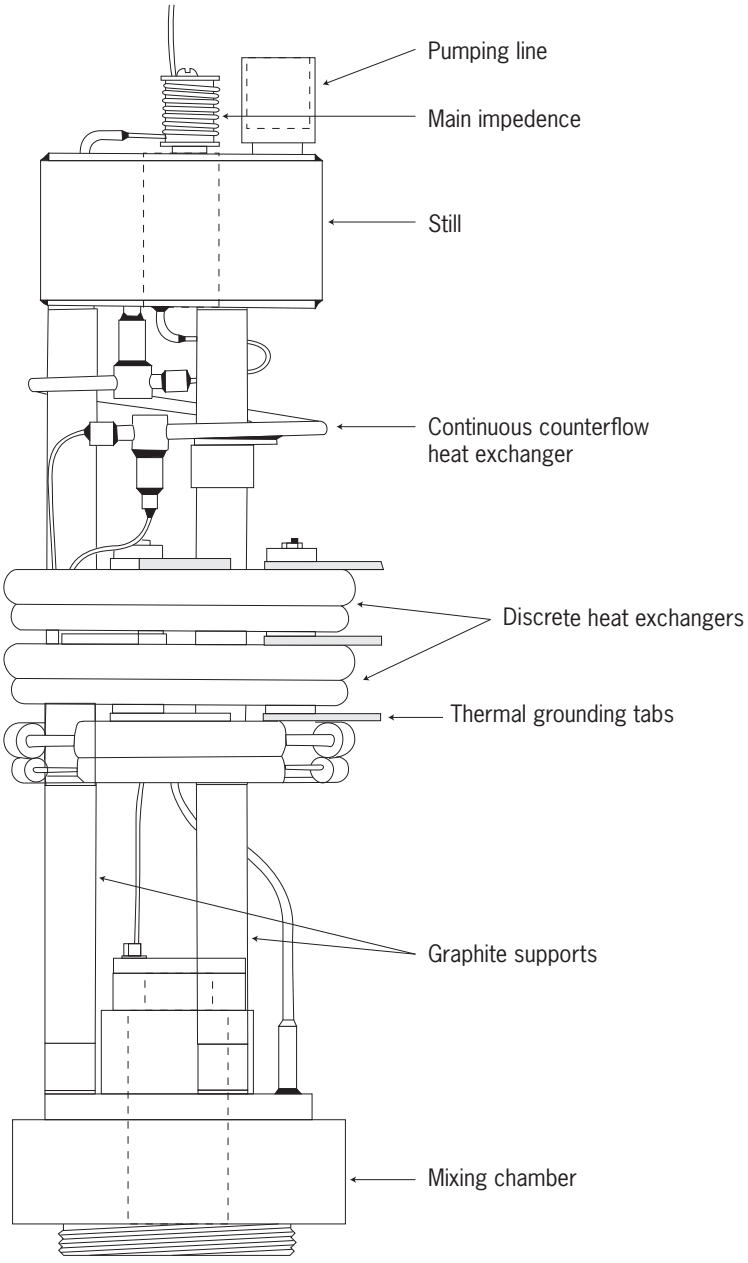

Figure 2.1: A diagram of the dilution unit from the S. H. E. dilution refrigerator used for the measurements contained in this thesis, taken from Ref. [112]. The base temperature is roughly 13 mK, depending on heat load.

The way that a dilution refrigerator is implemented can be very roughly thought of as a U-tube. The system pumps on one side of the U-tube (the side known as the still) and returns what was pumped away into the other side (the mixing chamber). When the mixture phase separates, the lighter concentrated phase floats on top of the dilute phase. Quantities of the different isotopes should be adjusted such that the phase separation line is inside the mixing chamber. Since the vapour pressure of ^{3}He is so much larger than that of ^{4}He, predominantly ^{3}He is pumped away at the still. This removal of ^{3}He at the still creates an osmotic pressure that pulls ^{3}He from the mixing chamber toward the still. This then makes 'space' in the mixing chamber for more ^{3}He to be returned into the dilute phase. This results in cooling because of the enthalpy difference ΔH between the concentrated and dilute phases.

While this description sounds very simple, much of the challenge to making a good dilution refrigerator comes from properly precooling the returning ^{3}He. It is first precooled with a 1K pot and condensed into liquid (this must be followed by a high impedance line to build up suitable pressure). It is then further cooled with the still, which is generally run at around 0.7 K. Finally it is run through heat exchangers with the dilute phase, so that when it enters the mixing chamber, it is already very cold and does not waste valuable cooling power. It is the manufacture of very effective heat exchangers that makes for a high performance dilution refrigerator, with the most successful reaching a base temperature of ~ 2 mK [42].

The particular dilution refrigerator used for this work, is a *S. H. E. Corporation* DRP-36 system from 1975. It can circulate at 200 μmoles/s per second and is capable of reaching a base temperature of just under 13 mK. In its current configuration, its minimum temperature is just over 20 mK, a likely result of increased heat load from a large amount of wiring for various experiments. In any case, a base temperature of 20 mK is more than adequate for the work contained in this thesis. A diagram of the dilution unit of the S.H.E. refrigerator is shown in Figure 2.1.

2.1.2 Thermometry

Thermometry is one of the most challenging aspects of low temperature physics, often requiring several different methods for different temperature ranges or applications. Resistive thermometry is by far the most convenient technique. For the main thermometer on the cryostat, we employ a commercial *LakeShore* germanium resistance thermometer (GRT). This thermometer is contained inside a small copper container filled with ^{4}He to create a strong thermal link while being carefully strain relieved so that it will be largely insensitive to thermal cycling and will have excellent reproducibility from one cool-down to the next. This thermometer comes calibrated down to a temperature of 50 mK.

At very low temperatures, 50 mK and below particularly, resistive thermometry can become quite difficult due to noise pickup. This 'self-heating', as it is known, can make resistive thermometers unpredictable and impossible to work with at the lowest temperatures. Careful attention must be paid to avoiding noise pickup by shielding and filtering signal lines. At the feedthroughs to our cryostat, we employ π-filters (an inductor in line with capacitors to ground on either side of it) to reduce high frequency noise. Furthermore, the pairs of voltage or current leads are run in twisted pairs, which also assists in noise cancellation.

In order to measure the temperature of the fridge below 50 mK (where the commercial GRT is no longer calibrated) we have employed two other thermometry techniques: CMN thermometry and nuclear orientation thermometry. The material $Ce_2Mg_3(NO_3)_{12} \cdot 24H_2O$ is a paramagnetic salt that does not order magnetically down to about 2 mK. Its susceptibility can be well approximated by a Curie-Weiss law $\chi \propto 1/(T-\theta)$ with $\theta = -0.004$ mK in the temperature range of 7 to 200 mK [42]. Our CMN thermometer consisted of a SQUID susceptibility measurement, similar to the one described in Section 2.3.1, using silver foil as a heat sink for the CMN. Since no leads are affixed to the sample, a CMN thermometer does not suffer the same self-heating problems as resistive thermometers. However, the apparatus required for this thermometer is much bulkier and significantly more complex than a 4-wire resistance measurement.

Nuclear orientation thermometry [42] makes use of a cobalt single crystal containing radioactive ^{60}Co. One particular decay process of ^{60}Co involves anisotropic emission of a gamma ray, predominantly away from the axis of orientation of the nuclear magnetic dipole moment. The electronic moments in a Co crystal are ferromagnetically aligned and below 50 mK, the nuclear moments begin to align with the electronic moments. As this happens, the gamma ray emission becomes anisotropic. One can place a detector outside the cryostat, aligned with the ferromagnetic axis of the crystal and monitor the count rate referenced to the isotropic, high-temperature count rate. As the temperature drops below 50 mK, this count rate drops, providing a indicator of the temperature. Once again, there are no leads attached to this sample so no self-heating occurs. The main downside to this type of thermometry is the long integration time required to get a precise measurement of the temperature. It also has very little applicability above 50 mK.

Nuclear orientation thermometry has a particular advantage in that it is a primary thermometer. It requires no predefined fixed temperature points. Calibration of the thermometer is accomplished by measuring the count rate at high temperatures $\gg 50$ mK, where the emission of radiation is completely isotropic. The count rate relative to this high-temperature, isotropic count rate then has a well-defined temperature dependence below 50 mK [42]. Nuclear orientation was used in conjunction with CMN thermometry (to provide overlap) to extend the calibration of the GRT to the base temperature of the

fridge. No self-heating was noticed in the GRT.

For specific heat measurements, we require a very portable thermometer with very little heat capacity. For this application, therefore, we employ thick film RuO_2 chip resistors, on alumina substrates manufactored by *Dale electronics*. Resistors of this kind are frequently used for such applications and their heat capacity has previously been characterized [113]. In a certain temperature range, from several hundred mK down to 50 mK, these thermometers have been fit by the simple form

$$R = R_0 \exp(T_0/T)^\beta \tag{2.2}$$

often with $\beta \simeq 1/4$, but in other cases choosing β to be as high as 0.345 [42]. This form is a reasonable approximation for our thermometers as well, though not sufficient to use as a calibration. It is, however, a good check that our thermometers are not self-heating in the temperature range of our data. A plot of $\log R$ versus $T^{-\beta}$ of our various thermometer calibration data, reveals good linear behaviour (with exponent $\beta \simeq 0.3$) to the lower temperature limit of our data and consistent slopes between various thermometers. A more reliable and universal fit is given [42] by

$$\ln T = \sum_{n=0}^{3} A_n (\ln R)^n \tag{2.3}$$

which has been used to calibrate our thermometers for specific heat experiments. These thermometers are not known for their reproducibility. It is expected that thermal cycling causes micro-cracks to form, which, over time, alter the calibration of the thermometers. However, in our applications, we use a new chip thermometer for each sample studied, calibrating it in place on the experiment. Thus each thermometer would only be exposed to a handful of thermal cycles and we generally do not notice significant changes in the calibration from one run to the next. There is much similarity between the calibrations of different resistors, but not enough to use one common $T(R)$ fit for all experiments – each new thermometer used, must be calibrated.

The GRT resistance is measured and the fridge temperature is controlled using a *LakeShore* 370 ac resistance bridge and temperature controller. The temperature stability is highly dependent on the temperature (therefore the heater resistance), the excitation used and the PID temperature control settings. However, some typical values of the temperature stability are ± 50 μK at 80 mK and ± 300 μK at 500 mK (relative stability of roughly 5×10^{-4}). The RuO_2 thermometers for specific heat experiments, on the other hand, were measured with a much lower noise *Linear Research* LR700 ac resistance bridge. For reasonable excitation voltages, a relative temperature resolution as good as 4×10^{-5}

was achieved, for example ± 10 μK at 250 mK. At lower temperatures, it is generally necessary to lower the excitation voltage in order to avoid heating the thermometer, which sacrifices some temperature resolution. For all resistive thermometers, the current and voltage leads were twisted pairs that were heat sunk at several points (at least at the 1K pot, still and mixing chamber). All leads were filtered with π-filters at the feedthroughs to the internal vacuum space of the cryostat (at room temperature).

2.2 Specific Heat Measurements

2.2.1 Design of Apparatus

As we are studying, in this work, insulating materials, some of which are polycrystalline samples, we must be ever cognizant of the potential for slow relaxation and thermal gradients within our samples and heat capacity apparatus. This has led us to implement a measurement scheme that, while more laborious to prepare, is much more reliable in such situations.

A typical heat capacity apparatus would consist of a substrate (often sapphire) on which a thermometer and heater are fixed and which is thermally linked with a known thermal conductance to the cryostat. Samples to be measured are then fixed with grease to the substrate. Such an apparatus, while enabling rapid switching of samples, makes for complicated heat flow and can lead to systematic errors. For example, if the sample is not well linked to the substrate, or has a particularly large heat capacity, much of the heat from a heat pulse may warm up the substrate then flow out through the thermal link, without possibly penetrating into the sample itself. This would likely lead to an overestimate of the sample temperature and therefore an underestimate of the heat capacity.

Our set-up, however, does away with the substrate. Thermometer, heater and weak thermal link are directly glued to the sample. This greatly simplifies the heat flow diagram and reduces systematic errors in temperature measurement, since heat flowing through the thermal link, must first flow through the sample. Unfortunately, this approach necessitates constructing a new heat capacity cell for each sample to be measured. Since an additional path for heat to flow is through the electrical leads to heater and thermometer, we have also made significant efforts to reduce the thermal conductivity of those leads.

An analysis of the potential effects of using a substrate for such measurements was performed in the author's M. Sc. thesis [114] and clearly illustrates that one can easily develop serious, systematic errors as a result of heat leaks. Such an analysis was performed assuming perfect thermal conductivity within the sample. Certainly adding a finite thermal conductivity to the sample, as discussed in Appendix C, could exacerbate these errors.

We are therefore confident that our apparatus, while cumbersome to make ahead of each experiment, is optimally designed to reduce systematic errors.

Specifically, our apparatus is made with the following design and materials. The outer support structure is a copper ring. This ring can be inserted into a hole on the inside of a copper box and held in place with a set screw. The copper box can be sealed up to block out blackbody radiation from higher temperatures, and screwed into the mixing chamber of the refrigerator. To support the sample without allowing it to be thermally linked to the cryostat, we use four, very thin nylon threads tied across the copper support structure. The sample is secured to these threads with *General Electric* (GE) varnish (an adhesive commonly used for low temperature physics applications).

For a thermometer, we use a 1 kΩ thick-film RuO_2 chip resistor on an alumina substrate from *Dale Electronics*. The heater is made from a metal-film chip resistor which has a largely temperature independent resistance, chosen to be in the range of 10 to 20 kΩ. The heater and thermometer are both fixed directly to the sample with GE varnish. No substrate is used.

A weak thermal link is made from either PtW (92% Pt, 8% W) or Manganin wire. It is connected to the sample on one side and the copper ring on the other, with silver epoxy. Manganin has a magnetic Schottky anomaly in its specific heat which can lead to a significant addendum if the sample's heat capacity is small. In that case, PtW is a better choice of weak link. The length and diameter of this link is chosen, with an estimate of the sample's heat capacity, to provide a time constant C/K, of our choosing. The thermal conductance K of the weak link can be calculated using the Wiedemann-Franz law knowing the resistivity of the wire. Since these metals are 'dirty' alloys, their residual resistance ratio (RRR) will be close to 1, thus their resistivities are not likely to change significantly from room temperature to 1 K and below. This will result in $K \propto T$. Of course, since we are typically dealing with insulating samples, there is also a Kapitza boundary resistance between the weak link and sample. This is difficult to predict and has a sharp temperature dependence T^3 or greater [42].

Electrical leads to the thermometer and heater are made with superconducting NbTi filaments that are roughly 6 μm in diameter. Such incredibly thin wires are obtained by etching the copper cladding away from multifilamentary NbTi magnet wire, with nitric acid. Contacts are made on either side of the leads with silver epoxy. Since these filaments are made from an alloy, and superconduct at $\sim$ 10 K, they are incredibly poor thermal conductors at 1 K and below. This allows for a well controlled heat flow in the system, with essentially all of the heat that enters the sample flowing out through the weak link and not through the electrical leads.

When performing a specific heat measurement, we apply quasi-adiabatic heat pulses of size Q (typically in the range of 10 nJ to 1 μJ) to our sample, via the heater, and

Figure 2.2: (a) A schematic diagram of the heat capacity cell used for these experiments. (b) A photo of a constructed heat capacity cell. This particular sample was single crystal $Yb_2Ti_2O_7$ although the construction of other heat capacity experiments was very similar with slight changes in sample geometry. The outer diameter of the copper support ring is 2.5 cm. (c) A diagram of relevant heat links and heat capacities in the system. Our apparatus design possesses a particularly simple version of such a diagram due to a lack of substrate.

monitor the change in sample temperature. For single crystal samples with very high thermal conductivity, it is often sufficient to perform linear fits to the data before the pulse and after the pulse and extrapolate to the mid point to find ΔT. The heat capacity is simply given by $C = Q/\Delta T$. The linear fits are reasonable if the period of time over which the fit is performed is much smaller than the time constant of relaxation to the cryostat temperature, τ_0. Since we choose to work with time constants of 1 hour or more, this is easily achieved.

Often there is some relaxation within the sample with a time constant τ_1. In single crystals, $\tau_1 \ll \tau_0$ and we can simply apply our fit after that internal relaxation has finished and extrapolate back to the heat pulse. In polycrystalline samples, however, the internal relaxation can become quite slow and we may even see more than one internal time constant, so τ_2, τ_3, etc. In that case, we have applied a double exponential fit to the τ_1 and τ_0 parts of the relaxation (avoiding the faster time constants). The longer exponential can then be extrapolated to the heat pulse to obtain ΔT. This double exponential fitting and internal time constants are discussed in more detail in Appendix C, where the error associated with poor thermal conductivity is analyzed and this method is justified.

A diagram and photo of one of our heat capacity cells is shown in Figure 2.2(a) and (b) respectively. In (c) we show the heat flow diagram of the experiment design. In a circuit diagram analogy, the thermal links may be thought of as resistors with heat capacities as

capacitors, temperature as voltage and heat flow as current. As can be seen in this heat flow diagram, our apparatus is quite simple and it is therefore very easy to understand where heat enters and exits the system. Whereas the thermometer-sample and heater-sample connections should be as good as possible (assisted by polishing down the alumina substrates of the chip resistors), the leads to the thermometer and heater should be as weak (thermally) as possible.

2.3 SQUID Magnetometry

The superconducting quantum interference device or SQUID is currently the most sensitive magnetic field sensor available. Use of a SQUID is a natural choice for studying glassy magnetic materials because of its high magnetic field sensitivity and because it responds directly to the magnetic field, rather than to the rate of change of the field, as in standard magnetic induction, so can therefore be used to very low frequencies. In Appendix D, an in-depth discussion of the theory of Josephson junctions and SQUIDs is presented. For a more detailed theoretical treatment of SQUIDs, see References [115, 116]. It is sufficient to mention here, that the dc SQUID (the variety used in this work) consists of a superconducting loop or washer interrupted by two tunnel junctions, known as Josephson junctions. Essentially the SQUID forms a Cooper pair interferometer and is, as a result, immensely sensitive to the flux threading the SQUID washer.

The SQUID is current-biased with a current I and the voltage V is amplified and measured. If biased at the correct current, the voltage varies sinusoidally with the external flux Φ_e, and therefore the applied magnetic field. The sinusoidal dependence of $V(\Phi_e)$ has a period of one flux quantum or $\Phi_0 = h/2e$, where h is Planck's constant and e is the charge of an electron [115]. Steep parts of the $V-\Phi$ curve allow for very high sensitivity, sometimes as good as 1 $\mu\Phi_0/\sqrt{\text{Hz}}$ [117]. More precisely, in order to handle such a severely non-linear gain, one must operate the SQUID in a feedback mode, which is also described in more detail in Appendix D. In the ensuing section is a detailed description of the construction and operation of our particular SQUID magnetometer. The SQUIDs and SQUID controller electronics used in this work were obtained from Michael Mück, *ezSQUID*.

2.3.1 Magnetometer design and operation

Our magnetometer has been designed, in particular, to study the susceptibility of glassy materials with slow magnetic relaxation. Thus, our aim was to create a magnetometer that would be sensitive to a wide range of frequencies. High sensitivity is also desirable, though for $LiHo_xY_{1-x}F_4$, for example, it is often not particularly necessary since the large magnetic

moment of Ho^{3+} ions provides a large signal. In order to achieve high sensitivity and a flat frequency response, we decided on a design using a SQUID and a superconducting flux transformer to input the signal to the SQUID. A superconducting flux transformer is simply a continuous loop of superconducting wire formed into the secondary or pickup coil on one side and the input coil to the SQUID on the other. The use of a SQUID and a flux transformer has two main advantages: flat frequency response and high sensitivity.

In standard inductive susceptometers (for example [118, 119, 58, 5]) one measures the electromotive force (emf) generated by inductive pickup in a coil. The resulting signal is unfortunately proportional to the rate of change of magnetic flux and will therefore drop off as the frequency of the excitation. A flux transformer, on the other hand, makes use of the Meissner effect, where the total flux through the superconducting loop is conserved. Thus if the flux in the pickup coil changes, so must the flux in the input coil near the SQUID. This effect is frequency independent so does not degrade the signal at low frequencies. Additionally, the high sensitivity of a SQUID permits the use of pickup coils that have few windings and therefore low inductance and will not exhibit resonances until very high frequencies, well above the frequency range in which we are working [117]. This flat frequency response over many decades of frequency is crucial to the study of glassy magnetic systems with slow dynamics and extremely broad frequency spectra (see for example Ref. [61] for the application of a similar device to the study of spin glasses).

Our work has been primarily concerned with measuring susceptibility at very low magnetic fields. This has allowed us to use a great deal of shielding to avoid noise pick-up and further increase our sensitivity. The SQUID itself is contained in a small superconducting lead (Pb) shield and the magnetometer apparatus as a whole is contained in a cylindrical lead shield. Beyond that, the radiation shield of the cryostat (which is attached to the 1 K pot) is plated with lead. A cryogenic μ-metal shield positioned in the liquid helium bath and another room temperature μ-metal shield placed around the dewar, are used to eliminate Earth's magnetic field and additional noise that might couple into the electrical leads.

To-scale diagrams of the apparatus that we designed and implemented are shown in Figure 2.4. The coils are built concentrically, on coil forms made of phenolic (bakelite). The primary coil consists of 375 turns of NbTi wire. Inside that is the secondary or pick-up coil, a second-order gradiometer. A first-order gradiometer would consist simply of two counter-wound coils, that would normally sum to zero signal in a uniform magnetic field. Placing a sample into one leg of the gradiometer perturbs the balance and results in a non-zero signal. A second order gradiometer, consists of three coils, the middle wound opposite to the others and with a larger inductance such that zero signal will result from both a uniform magnetic field and a linear gradient magnetic field, providing improved noise cancellation. Higher order gradiometers are conceivable. Our specific gradiometer

consists of 5-7-5 turn niobium coils, with the sample placed in the middle coil. A small niobium input coil is hand wrapped and fixed above the SQUID. The leads to this input coil are passed through a small hole in the lead shield and a superconducting contact to the secondary is made by embedding the bare wire ends in beads of PbSn solder.

The balance is never perfect on hand-wound coils and is further distorted by the superconducting shields, which are not symmetric about the secondary windings, thus we have added a 'trim' coil inside the far end of the pick-up coil consisting of 10 turns of NbTi wire which can be used to fine tune the balance. Otherwise, the system will have a significant frequency-independent offset signal which reduces the dynamic range and sensitivity of the measurement. The trim and primary coils are connected to the excitation voltage source in parallel, with current limiting resistors chosen such that the magnetometer is balanced.

The leads to the excitation and trim coils are twisted pairs, Manganin running from room temperature to the 1 K pot, and superconducting NbTi, clad with CuNi from the 1 K pot to the mixing chamber. These leads are filtered with π-filters at the feedthroughs to the internal vacuum space, to reduce high frequency noise that might impede the functioning of the SQUID. The lines for the SQUID bias current and feedback coil are rigid beryllium-copper coax for most of their length, but with a section of NbTi twisted pairs from the 1 K pot to the mixing chamber, to reduce heat load on the dilution refrigerator. The SQUID feedback coil is a small, 10-turn, hand-wrapped, copper coil placed behind the SQUID wafer.

Much effort has been made to reduce the amount of normal metal inside the magnetometer as it introduces a frequency dependent signal. The coil forms and structural supports for the magnetometer are made out of phenolic, or bakelite. Where screws are necessary near the coils, nylon screws are employed. The sample is heat sunk to the mixing chamber of the dilution refrigerator via a sapphire rod, one of the more thermally conductive options that is not metallic and will not affect the signal. The sapphire rod is clamped into a copper end cap which is fastened to the mixing chamber. The end cap and sapphire rod can be removed as one piece without taking apart the remainder of the apparatus, so as to quickly and easily change samples without perturbing the balance and calibration of the system. The sample is fixed to the sapphire rod with *General Electric* (GE) varnish.

The susceptibility measurements are performed by applying a sinusoidal current through the current limiting resistors and the excitation and trim coils with a *Stanford Research* 830 lockin amplifier's output. The SQUID controller is run in a flux locked loop (FLL) and the feedback signal is sent to the input of the lockin amplifier. Generally the cryostat is temperature controlled at a specific temperature for a long period of time (at least several hours) while the frequency of excitation is altered to obtain a frequency spectrum $\chi(\omega) = \chi'(\omega) - i\chi''(\omega)$. In other cases, the frequency has been held fixed and the cryostat temperature adjusted very gradually in steps. For every data point sampled, care is taken

to ensure that the sample and measurement have reached equilibrium. Often spectra are taken multiple times to ensure that the signal is not still evolving in time. Multiple excitation amplitudes are also tested and the results compared to ensure that a suitably small amplitude is chosen so that the sample or surrounding apparatus are not being heated.

Calibration of the magnetometer has been performed in two different ways. In some cases, the calibration was determined by measuring two samples of different geometries then choosing the calibration factor such that the results match when the demagnetization effect is taken into account. The demagnetization correction and this method of calibration will be discussed in more detail in Appendix A. In the most recent measurements, the magnetometer was calibrated by measuring the signal of a superconducting Pb prism in place of the sample, which should be perfectly diamagnetic thus will have a susceptibility of 1 (in SI units) or $1/4\pi$ emu/cm^3/Oe (in CGS units).

The primary success of our apparatus is its ability to measure signals at extremely low frequencies. Good temperature stability, low noise and flat frequency response are all required to achieve such a result. Specifically, measurements have been performed successfully down to a frequency of 1 mHz, with no loss of signal. In other words, we have a perfect flux transformer. Measurements of an empty and misbalanced magnetometer or of χ' at low frequency show that from several hundred Hz down to 1 mHz, there is no drop in the signal to *better* than one part in 2000.

Our frequency scans are limited at the high end by a frequency dependent background signal which comes primarily from phase shifts in the SQUID feedback electronics, and partly from capacitance in the lines and π-filters. This has led us to present data only up to a maximum frequency of 500 to 2000 Hz, depending on the configuration (gain setting) and therefore bandwidth of the system. This small background has therefore had no impact on the analysis of our data and the conclusions drawn. The high-frequency background is, for the most part, not inherent to the magnetometer design; the inductance of the primary and trim coils are small enough that they do not cause significant phase shifts below 100 kHz, with the chosen current limiting resistors. In future work, the π-filters can be removed and a higher frequency SQUID controller can be employed in order to extend the upper frequency limit of the system, if such a frequency range is useful or desirable. So far, we have been concerned with achieving the lowest possible frequencies of measurement rather than pushing to higher frequency.

The other main advantage to our apparatus is the possibility of working at very low magnetic fields and still obtaining ample signal strength. These extremely low fields (under 20 mOe) ensure that we are not heating the sample in any significant way. Furthermore, the samples that we study do not need to be extremely large, providing a better ratio of contact surface area to volume, again reducing the effects of heating.

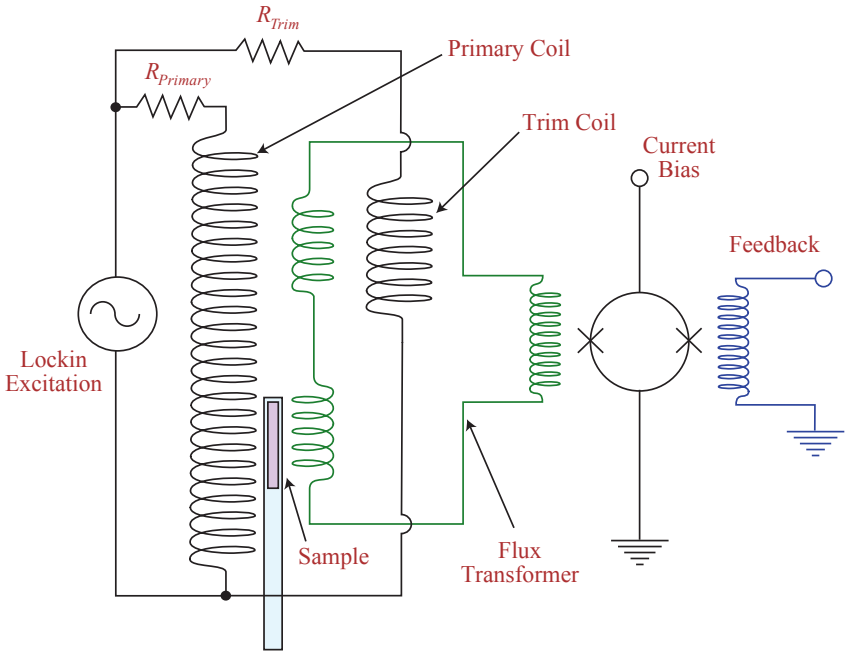

Figure 2.3: A circuit diagram of the magnetometer and balancing circuit. The sinusoidal excitation voltage is applied across current limiting resistors, chosen such that the magnetometer is balanced in the absence of a sample. The sample is placed in one leg of the secondary gradiometer which is placed concentrically inside the primary. The secondary is connected to the input coil of the SQUID by a superconducting link. There are also leads to the SQUID for bias current and voltage measurement and to the feedback coil, which is hand wrapped below the SQUID wafer. The current limiting resistors for both the primary and trim coils are ~ 30 kΩ. The primary coil has an inductance of approximately 600 μH. Thus the high frequency cut-off is above 1 MHz.

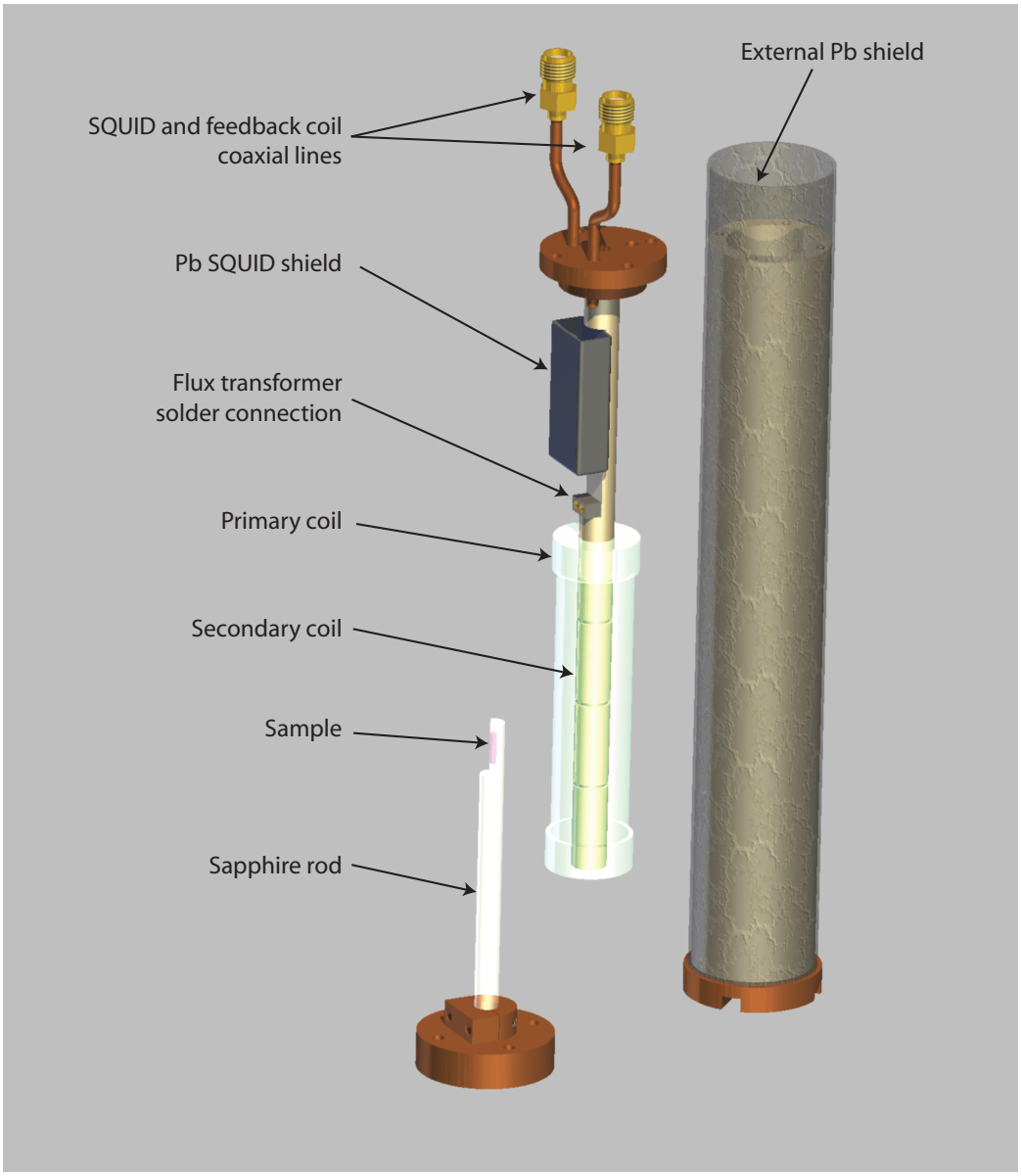

Figure 2.4: Diagram of the magnetometer apparatus used for this work. The magnetometer separates into three main parts: the external shielding, the sample mount and the interior including the coils, SQUID, signal lines, etc.

2.3.2 Future design considerations

While this magnetometer has served its purpose well, there is always room for improvement. Future designs of a similar magnetometer should incorporate several important ideas. First, the mechanical rigidity of the magnetometer structure is quite important. As pieces are pressed together in this initial model, the tolerances are not extremely high and when the magnetometer is taken apart and reassembled, the balance and calibration change.

Second, the flux transformer used here has been found to be vulnerable to thermal cycling. Even a small resistive contact breaking the superconducting loop will lead to a dramatic loss of signal, since the coils employed are of such low inductance. It is likely that thermal cycling causes the solder joints, most likely the interface between the niobium and the PbSn solder, to become Ohmic or even open circuited. It is possible that a different kind of solder, or perhaps pure lead, might be softer and more able to withstand thermal stresses and would be a more dependable method of making a flux transformer in future designs. It is most practical to use a material with a superconducting transition above 4.2 K so that the apparatus may be tested quickly and conveniently in a bath of liquid ^{4}He.

While a second-order gradiometer is, in principal, better at cancelling noise (that might manifest as a field with a linear gradient), it is much more difficult to balance – precise matching of inductances is not easy. With a first-order gradiometer, this task is made easier since one needs only to wrap two similar coils. It is not necessary to calculate the precise inductance for n turns of wire for example. It may be best in future designs to use a simpler and more robust first-order gradiometer, at least for similar applications. However, it is possible that applications requiring much higher sensitivity (for example the study of much smaller samples or samples with much lower susceptibility) would demand the improved noise cancellation provided by a second-order gradiometer. Pushing to higher frequencies (than those employed here) could also be inhibited by improperly canceling noise and thereby reducing the bandwidth of the SQUID. The use of a trim coil to adjust the balance is already, without a doubt, a detriment to noise cancellation. Allowing the primary coil to be translated relative to the secondary, sample and superconducting shields, would facilitate balancing of the magnetometer and might obviate the need for a trim coil.

Chapter 3

The Dilute Dipolar-Coupled Ising Magnet $\mathbf{LiHo}_x\mathbf{Y}_{1-x}\mathbf{F}_4$

The series of materials $LiHo_xY_{1-x}F_4$ has long been viewed as a "model magnet" whose Hamiltonian is simple and well understood[1] and allows one to experimentally test several very fundamental theories in condensed matter physics. The magnetic moments are well approximated as Ising moments, owing to the crystalline electric field and the interactions between the moments are overwhelmingly dipolar in nature, with only a small nearest-neighbour exchange interaction. Finally the magnetic Ho^{3+} ions may be diluted with non-magnetic Y^{3+} ions with out any significant change to the crystal structure, providing a mechanism to study the effects of chemical disorder [58].

At $x = 1$, or 100% Ho, the ground state of the material is ferromagnetic and has been studied extensively in transverse magnetic field, as a realization of the transverse field Ising model (TFIM), a simple model that exhibits a quantum phase transition [121]. As the moments are diluted, the transition temperature is reduced [122]. Below $x \simeq 0.25$, the material enters a glassy, disordered phase [58]. There is sufficient randomness and frustration resulting from competing dipolar interactions that one expects a spin glass state to occur here [29]. It is this disordered region that we primarily discuss here and that has been the subject of a tremendous amount of debate, both theoretically and experimentally, in the last few years [4, 5, 123, 65, 124, 125, 126, 127, 128].

There are two main components to this debate. The first is one that is largely theoretical; that is the question of whether idealized Ising spins coupled with the long range dipolar interaction, randomly placed on the $LiHo_xY_{1-x}F_4$ lattice, will exhibit a finite tem-

[1] The recent discovery of a persistent mismatch between theory and experiment in the parent compound $LiHoF_4$ has called into question the authenticity of the simple Hamiltonian that has been long held to apply to this material [120]

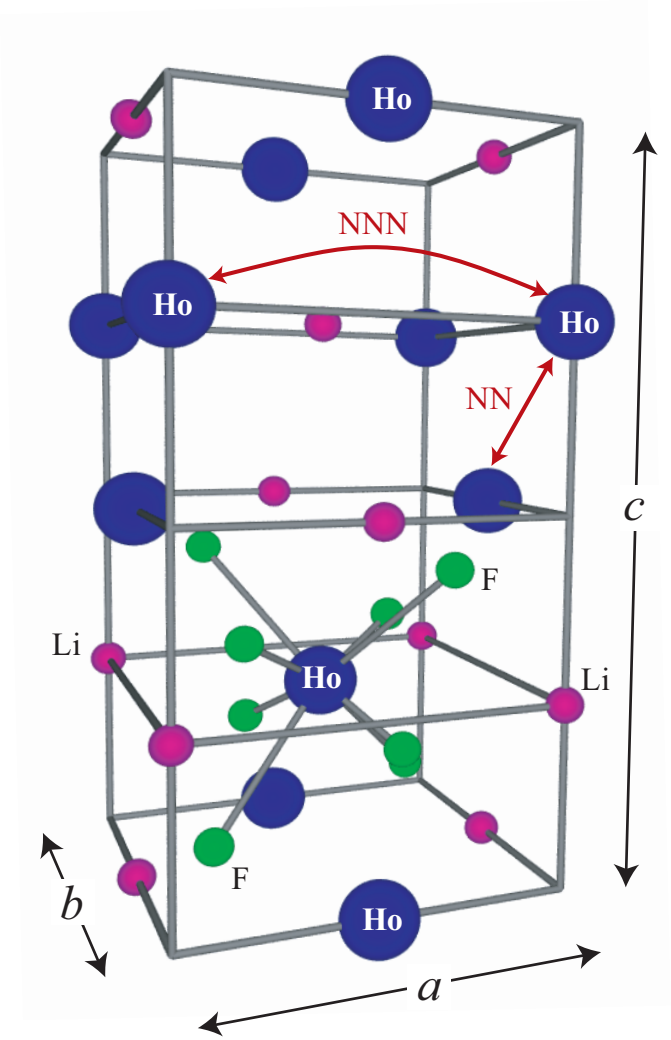

$$a = b = 5.176 \text{ Å}$$

$$c = 10.75 \text{ Å}$$

Figure 3.1: The crystal structure of $LiHo_xY_{1-x}F_4$.

perature glass transition [128]. The second question under debate is whether the real physical system $LiHo_xY_{1-x}F_4$ exhibits a spin glass transition and for what values of x. The real physical system, while uniquely close to ideal, is not a perfect toy model and does have other effects to consider such as off-diagonal interactions, nuclear moments, phonons, etc. Assuming that the toy model does give rise to spin glass behaviour, these material effects may preclude a spin glass state in the real system.

First we discuss the crystal structure and magnetic Hamiltonian of $LiHo_xY_{1-x}F_4$. Following that, we review some of the previous experimental and theoretical work that has been done on this series of materials, starting with the high x, ferromagnetic phase and working our way down to the surprising "antiglass" phase at $x = 0.045$. Finally, we introduce our specific heat and ac susceptibility results at low Ho concentrations and discuss them in the context of theoretical work on this material and other experiments.

3.1 Crystal Structure and Magnetic Hamiltonian

As discussed in Chapter 1, the $4f$-valence electrons in Ho^{3+} (and rare earth ions in general) have strong spin-orbit coupling, so that they prefer to be in states of total angular momentum $J = 8$. This leaves 17 degenerate states for the free ion. In the crystal structure, however, these energy levels will be split by the next most important term in the Hamiltonian, that is the crystal field, $\mathcal{H}_{CF}$. The crystal structure of $LiHoF_4$, shown in Figure 3.1, is of the $CaWO_4$ variety [58]. The point-group symmetry is S_4, which means that the structure is invariant under a rotation of 90 degrees about the c-axis followed by a reflection in the ab-plane. The crystal field, created principally by the surrounding F^- ions, can be written as [14]

$$\mathcal{H}_{CF} = \sum_{n\alpha} B_n^\alpha O_n^\alpha = B_2^0 O_2^0 + B_4^0 O_4^0 + B_4^{4C} O_4^{4C} + B_6^0 O_6^0 + B_6^{4C} O_6^{4C} + B_6^{4S} O_6^{4S}. \qquad (3.1)$$

There is some disagreement on the precise values of the B_n^α crystal field parameters. In a point-charge model, the crystal field parameters can be easily calculated, to within an overall proportionality factor (involving the size of the charges and the radial integral $\langle r^n \rangle$). However, the point-charge model is quite a large assumption – the charges on the F^- ions come from the nuclei and the surrounding screening electrons thus the potential is probably quite far from $\sim 1/r$. Generally speaking, one must turn to experimental data in order to accurately determine the crystal field parameters. Several different sets of crystal field parameters have been determined from various spectroscopic data [14, 129, 130, 131, 132], although the differences are unlikely to have significant effects on the physics of the material

Parameter	Ref. [14]	Ref. [130]	Ref. [133]
B_2^0 (K)	-6.96×10^{-1}	-7.54×10^{-1}	-6.09×10^{-1}
B_4^0 (K)	4.06×10^{-3}	4.94×10^{-3}	3.26×10^{-3}
B_4^{4C} (K)	4.18×10^{-2}	5.26×10^{-2}	4.30×10^{-2}
B_6^0 (K)	4.6×10^{-6}	1.2×10^{-6}	8.36×10^{-6}
B_6^{4C} (K)	8.12×10^{-4}	9.92×10^{-4}	8.18×10^{-4}
B_6^{4S} (K)	1.137×10^{-4}	1.96×10^{-4}	

Table 3.1: Crystal Field parameters from different references

below 1 K for example. For this work we will use those taken from Rønnow *et al.* [14]. Three example sets of experimentally determined B_n^α parameters are listed in Table 3.1.

The crystal field has the effect of splitting the $J = 8$ moments into a collection of doublets and singlets (since Ho^{3+} is a non-Kramers ion). Most important are the low lying states which consist of a doublet ground state and an excited singlet state at ~ 10 K. If the crystal field is diagonalized on its own (treating other parts of the Hamiltonian as a perturbation), the two ground states are given by

$$\begin{aligned} |\uparrow\rangle &= 0.7945e^{i105^o}|7\rangle + 0.6052e^{-i68.6^o}|3\rangle + 0.0411e^{-i3.13^o}|-1\rangle - 0.0295|-5\rangle \\ |\downarrow\rangle &= 0.0295e^{i105^o}|5\rangle + 0.0411e^{-i71.8^o}|1\rangle + 0.6052e^{-i6.41^o}|-3\rangle - 0.7945|-7\rangle \end{aligned} \tag{3.2}$$

It is easy to notice that these two states do not share any $|J_z\rangle$ components. Furthermore, all the J_z contained in $|\uparrow\rangle$ differ from the J_z in $|\downarrow\rangle$ by at least 2. And within the states $|\uparrow\rangle$ and $|\downarrow\rangle$, the J_z components are separated by 4. In other words, there are no matrix elements of J_+, J_-, J_x, J_y in the ground state manifold. Thus

$$\langle\uparrow|J_x|\uparrow\rangle = \langle\downarrow|J_y|\downarrow\rangle = 0. \tag{3.3}$$

and

$$\langle\uparrow|J_x|\downarrow\rangle = \langle\uparrow|J_y|\downarrow\rangle = 0. \tag{3.4}$$

Hence, if only these two states are considered, $LiHo_xY_{1-x}F_4$, is a perfect Ising model with magnetic moments only up or down along the c-axis with $\langle\uparrow|J_z|\uparrow\rangle = -\langle\downarrow|J_z|\downarrow\rangle = 5.15$. The effective g-factor of the Ho^{3+} (defined by its interaction with magnetic field) is

$$g_{\text{eff}} \equiv 2\langle J_z\rangle g_J = 13.8. \tag{3.5}$$

Reduction of the Ising character of the system occurs either through the introduction of coupling with the next excited state singlet $|\gamma\rangle$,

$$|\gamma\rangle = 0.575e^{-i43.4^\circ}|6\rangle + 0.411e^{i142.1^\circ}|2\rangle + 0.411e^{i174.6^\circ}|-2\rangle + 0.575|-6\rangle, \tag{3.6}$$

(most often accomplished with a magnetic field transverse to the z-axis of the material) or by reaching high enough temperatures such that the population of that excited level is not negligible. Much of the experimental work on $LiHo_xY_{1-x}F_4$ has revolved around understanding how the system behaves after introducing quantum fluctuations by applying a transverse magnetic field [121, 66]. Alternatively, one could break the symmetry of the lattice, for example with random strain which would introduce a B_2^2 term in $\mathcal{H}_{CF}$.

Now we turn to interactions between the magnet ions. There is a relevant nearest-neighbour antiferromagnetic exchange interaction $\mathcal{J}_{\rm Ex}\boldsymbol{J}_i \cdot \boldsymbol{J}_j$ where $\mathcal{J}_{\rm Ex} \simeq 0.1$ K as was determined by fitting to the high temperature $1/T^2$ tail of the specific heat of the parent compound, taking the dipolar contribution out to a distance of 200 Å [24]. In theoretical treatments it has been left as a free adjustable parameter, with similar results, such as $\mathcal{J}_{\rm Ex} = 0.12$ K obtained [127]. However, the most important interactions in this system are the dipole-dipole interactions. Quite simply, the magnetic field generated by one ion is felt by the dipole moment of all other ions. The dipole interaction takes the form

$$\mathcal{H}_D = \sum_{\langle i,j \rangle} \sum_{\alpha\beta} \mathcal{D}_{ij}^{\alpha\beta} J_i^\alpha J_j^\beta = \sum_{\langle i,j \rangle} \frac{\mu_0}{4\pi} g_J^2 \mu_B^2 \left[\frac{\mathbf{J}_i \cdot \mathbf{J}_j}{r_{ij}^3} - \frac{3(\mathbf{J}_i \cdot \mathbf{r}_{ij})(\mathbf{J}_j \cdot \mathbf{r}_{ij})}{r_{ij}^5} \right]. \tag{3.7}$$

If we are in the range of temperature and magnetic field where the system is a good Ising model, then we can simplify this expression to

$$\mathcal{H}_D = \sum_{\langle i,j \rangle} \frac{\mu_0}{4\pi} g_{\rm eff}^2 \mu_B^2 \left(\frac{r_{ij}^2 - 3z_{ij}^2}{r_{ij}^5} \right) S_i^z S_j^z \tag{3.8}$$

where the S_i^z quantities are taken as spin-1/2 entities and $g_{\rm eff}$ is given by Equation 3.5.

It is important to take into account two peculiarities of the dipolar interaction: its long range nature, and its angle dependence. The dipolar interaction presents somewhat of a challenge to theorists because of its $1/r^3$ decay and the fact that the distance of interaction cannot be safely truncated. It also makes the idea of a percolation threshold meaningless in this system, as discussed in Chapter 1. The angle dependence of the dipolar interaction results in interactions that can be either ferromagnetic (FM) or antiferromagnetic (AFM). For example, the nearest-neighbour spins in $LiHoF_4$ sit largely on top of each other along the c-axis, meaning that this interaction is ferromagnetic with an energy $E_{\rm NN} = -318$ mK. On the other hand, the second-nearest-neighbour spins are found in the same xy-plane thus the interaction is antiferromagnetic of strength $E_{\rm NNN} = +214$ mK. The nearest-neighbour (NN) and next-nearest-neighbour (NNN) sites are shown on the crystal structure in Figure 3.1. In the parent compound, the ferromagnetic interactions win out. This would not necessarily be true of a different crystal structure. As the moments are diluted, more

competition between FM and AFM interactions (frustration) is exposed and this random frustration is what may give rise to a spin glass state.

The holmium nucleus has an especially large magnetic moment of $4.173\mu_N$. Because of this and the fact that Ho^{3+} ions have $4f$ valence electrons which are tightly bound, the hyperfine interaction is very important. This interaction takes the form

$$\mathcal{H}_{HF} = \sum_i A\,\mathbf{I}_i \cdot \mathbf{J}_i. \tag{3.9}$$

Once again, if we are in an appropriate range of temperature and magnetic field, we can make the assumption that our electronic moments are fully Ising in nature and express our hyperfine Hamiltonian in the effective spin-1/2 model as

$$\mathcal{H}_{HF} = \sum_i A_{||} S_i^z I_i^z \tag{3.10}$$

where $A_{||} = 2\langle J_z \rangle A$. The nuclear spin is $I = 7/2$ thus there will be 8 electronuclear energy levels per electronic ground state corresponding to the m_I values of the nuclear spin.

Various values for A have been determined experimentally. One method used to determine this constant is electron paramagnetic (or spin) resonance (EPR/ESR). Resonances are found when the Zeeman energy $\mu_B g_J \mathbf{B} \cdot \mathbf{J}$ is equal to the energy of other interactions in the system. For every crystal field level, there are therefore 8 resonances associated with the 8 nuclear levels. The field splitting between these resonances can then give the energy of the nuclear hyperfine interaction: $A = \mu_B g_J \Delta H$. Assuming a $J = 8$, $L = 6$, $S = 2$ manifold, the Landé g-factor for Ho^{3+} is 5/4. For a free Ho^{3+} ion, EPR experiments find $A/k_B = 38.975$ mK [20]. For a Ho^{3+} ion in the $LiHoF_4$ lattice, EPR experiments find $A/k_B = 39.799$ mK [134] and for dilute ions in the $LiYF_4$ lattice, $A/k_B = 40.210$ mK [135]. Calculations here will use the latter value $A/k_B = 40.210$ mK as the lattice is most similar to that studied in this work.

Also important to consider is the nuclear quadrupole interaction with the electric field gradient at the nucleus. This interaction is described [20] by

$$\mathcal{H}_Q = \frac{eQV_{zz}}{4I(2I-1)}\left[3I_z^2 - I^2 + \frac{\eta}{2}(I_+^2 + I_-^2)\right] \tag{3.11}$$

where

$$\eta = \frac{V_{xx} - V_{yy}}{V_{zz}} \quad \text{and} \quad V_{\alpha\beta} = \frac{\partial^2 V}{\partial\alpha\partial\beta}. \tag{3.12}$$

Many of the parameters involved are difficult to calculate and we will just replace them with a single experimentally determined parameter P. The nuclear moments will be

strongly coupled to the up or down Ising spins so it is likely that the off-diagonal x and y components will have a small effect. Thus we will assume η to be 0 as is often done [24]. The quadrupolar interaction then becomes

$$\mathcal{H}_Q = \sum_i P(I_i^z)^2 \tag{3.13}$$

plus an irrelevant constant term. The value of P determined by EPR is only 1.7 mK [24], but since this term is dependent on the square of I_z, it is significant enough with respect to the hyperfine interaction energy that it will be just noticeable in calculations of the specific heat. Otherwise, this term is not expected to be important enough to have any impact on the physics of $LiHo_xY_{1-x}F_4$. Thus, aside from including it in the calculation of the non-interacting specific heat, we will herein ignore the quadrupole interaction.

As in any magnetic system, the application of a magnetic field, $\mathbf{H}$ is important, contributing the Zeeman energy

$$\mathcal{H}_Z = g_J \mu_B \mathbf{H} \cdot \mathbf{J}. \tag{3.14}$$

This is particularly important in the case of transverse (perpendicular to the c-axis or $\hat{z}$) magnetic field $H_\perp$, which introduces mixing with the excited state $|\gamma\rangle$ and therefore induces quantum fluctuations. Much of the work on $LiHo_xY_{1-x}F_4$ has been dedicated to understanding the impact of quantum fluctuations, as tuned by $H_\perp$, on the magnetic ordering. The coupling with the next excited state can be expressed as a term ΓS^x in the effective spin-1/2 Hamiltonian where Γ is the effective transverse field (as opposed to the real transverse field $H_\perp$) [18]. With the addition of this term, Equation (3.8) becomes the dipolar transverse field Ising model (TFIM):

$$\mathcal{H}_{\text{TFIM}} = \sum_{\langle i,j \rangle} J_{ij} S_i^z S_j^z - \Gamma \sum_i S_i^x. \tag{3.15}$$

Γ is not the real transverse field $H_\perp$, but is a splitting of the ground state doublet that is projected onto a spin-1/2 effective Hamiltonian as an effective transverse field.

To summarize, the important contributions to the total magnetic Hamiltonian of the material $LiHo_xY_{1-x}F_4$ are given by

$$\mathcal{H} = \mathcal{H}_{\text{CF}} + \mathcal{J}_{\text{Ex}} \sum_{\langle i,j \rangle_{nn}} \mathbf{J}_i \cdot \mathbf{J}_j + \sum_{\langle i,j \rangle} \sum_{\alpha\beta} \mathcal{D}_{ij}^{\alpha\beta} J_i^\alpha J_j^\beta + A \sum_i \mathbf{I}_i \cdot \mathbf{J}_i - g_J \mu_B \sum_i \mathbf{H} \cdot \mathbf{J}_i \tag{3.16}$$

consisting of crystal field, exchange, dipolar, hyperfine and Zeeman interactions, respectively. The crystal field gives us an excellent Ising model at low temperature. That Ising character can be degraded by the introduction of transverse magnetic field $H_\perp$. While

there is a small nearest-neighbour exchange, the dominant interactions in the system are dipolar in nature. Finally, the nuclear hyperfine coupling will be found to be an important component of the Hamiltonian in the vicinity of quantum critical points and in the physics of the low-x end of the phase diagram.

3.2 Previous Work on $LiHo_xY_{1-x}F_4$

3.2.1 Ferromagnetic Stoichiometries

Parent Compound: $LiHoF_4$

Pure $LiHoF_4$ is an excellent example of a dipolar coupled Ising magnet with a transition temperature of 1.53 K. Renormalization group (RG) theory finds that the upper critical dimension of a dipolar-coupled system is $d^* = 3$ instead of the usual 4 for short range interactions, so that the critical behavior at the transition is expected to have logarithmic corrections to mean-field critical behaviour, thus $\chi \sim t^{-1}|\ln t|^{1/3}$ or $C \sim |\ln t|^{1/3}$ [31, 32]. For higher dimensions above the upper critical dimension, the usual mean-field exponents are expected to apply. Since this is one of the rare cases where the upper critical dimension is physical, $LiHoF_4$ and the related compound $LiTbF_4$ have been studied in various ways as a test for these predicted corrections, in some cases successfully. Logarithmic corrections were observed successfully in the specific heat [33] and magnetization [34] of $LiTbF_4$ and later in the specific heat [36] and magnetization [35] of $LiHoF_4$. In other studies using neutron scattering [136] and measuring magnetic susceptibility [137], it was not possible to resolve the difference between logarithmic corrections and ordinary mean-field theory. In the case of Ref. [136], however, some universal amplitude relations also predicted with RG theory to apply at marginal dimensionality [138], were observed. Mean-field critical behaviour with logarithmic corrections has also been observed in Monte Carlo simulations [37, 38].

More recently, this material has been studied as an example of the transverse field Ising model (TFIM) whose effective Hamiltonian is given by

$$\mathcal{H} = \sum_{ij} J_{ij} S_i^z S_j^z - \Gamma \sum_i S_i^x. \tag{3.17}$$

The transverse field Ising model is one of the simplest models that exhibits a quantum phase transition. A quantum phase transition is a zero-temperature transition that occurs as some parameter of the Hamiltonian is adjusted, be it the dilution x, pressure P or magnetic field $\mathbf{H}$. In this case the parameter which is being tuned is the transverse magnetic

field Γ. Before the introduction of Γ, the Hamiltonian was diagonal in the $|\uparrow\rangle_i, |\downarrow\rangle_i$ basis. The transverse field, however, is an off-diagonal term ($\hat{S}^z$ and $\hat{S}^x$ do not commute). This allows tunneling events between the up and down Ising states or quantum fluctuations.

The quantum phase transition results from non-analytical behaviour of the ground state energy at a critical value of the parameter Γ, or at Γ_c [139]. For very low Γ and T the system is ordered ferromagnetically, but for very large Γ it is a quantum paramagnet as the dipolar coupling is weak compared to the transverse field term. In the ferromagnetic phase, the magnetization is gradually reduced by increasing Γ as quantum fluctuations allow spins to flip. At the transition Γ_c, the quantum fluctuations completely destroy the ferromagnetic order so that the longitudinal magnetization is 0, just as thermal fluctuations destroy order in a classical phase transition. For $\Gamma > \Gamma_c$ the system has an exponentially decaying correlation function $\langle S_i^z S_j^z \rangle \sim e^{-|x_i - x_j|/\xi}$ where ξ is the correlation length. As Γ is lowered towards Γ_c, this correlation length gets larger and diverges at the transition.

Quantum phase transitions in d dimensions may generally be mapped onto classical phase transitions in $d+1$ dimensions [139, 140]. Thus the quantum phase transition in the 3-dimensional dipolar TFIM is equivalent to the classical phase transition in the 4-dimensional dipolar Ising model.

In the case of $LiHoF_4$, a field $H_\perp$ applied perpendicular to the c-axis (easy axis) introduces coupling between the ground state Ising doublet and the next nearest excited state $|\gamma\rangle$. This leads to a splitting Δ in the ground state doublet, thus corresponding to an effective transverse field $\Gamma = \Delta/2$ in the transverse field Ising model [120]. This coupling leads to quantum fluctuations which eventually destroy or 'melt' the ferromagnetic order. At zero temperature, there is a quantum phase transition or quantum critical point at $H_\perp = 4.9$ T [121].

The critical behaviour of the material in transverse field was studied by Bitko *et al.* [121] by measuring the ac susceptibility of the material using a conventional susceptometer. In zero field, $\chi'(T)$ is found to diverge with the power law $t^{-\gamma}$ where $\gamma = 1$. In other words, it is very close to mean field theory as was seen previously [137] and the logarithmic corrections to scaling are not observed. At constant temperature, $\chi'(H_\perp)$ also shows a sharp cusp at the transition from ferromagnet to paramagnet. At all temperatures studied, the critical behaviour is $\chi \sim h^{-\gamma}$ where $\gamma = 1$ and $h = (H_\perp - H_\perp^C)/H_\perp^C$. There are no signs of logarithmic corrections in the quantum critical behaviour thus the $d = 3$ quantum transition appears to behave as a $d = 4$ classical transition, as is expected theoretically since quantum phase transitions can be mapped onto classical phase transitions in 1 higher dimension [63, 139].

This method also allows one to map out a $(T, H_\perp)$ phase diagram of the material which is shown in Figure 3.2. Bitko *et al.* present a theoretical phase diagram generated by

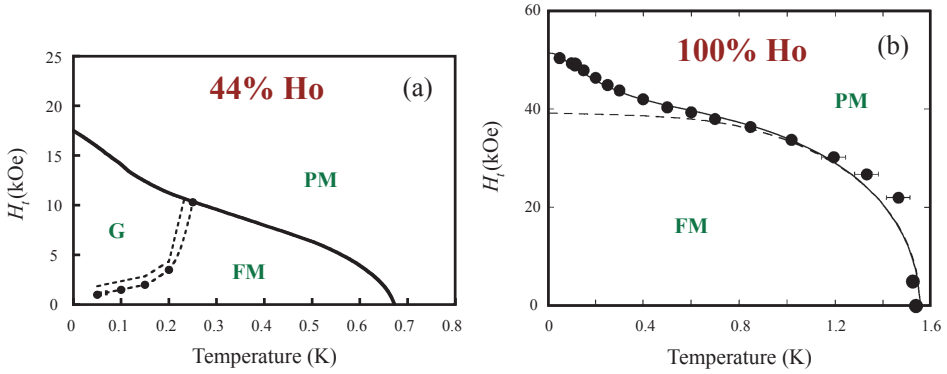

Figure 3.2: (a) The T-$H_\perp$ phase diagram of the 44% sample taken from Refs. [122, 141], showing paramagnetic (PM) and ferromagnetic (FM) phases, as well as a region found to exhibit glassy dyanmics (G). (b) The T-$H_\perp$ phase diagram of the parent compound $LiHoF_4$, taken from Ref. [121]. The dotted line is the expected behaviour without the nuclear hyperfine interaction.

solving the mean-field Hamiltonian

$$\mathcal{H}_{MF} = \mathcal{H}_{CF} + A\mathbf{I}\cdot\mathbf{J} - g_J\mu_B B_\perp J^x - 2J_0\langle J^z\rangle J^z \tag{3.18}$$

self-consistently. This phase diagram is found to fit the data well though only if J_0 is used as a fitting parameter. The nuclear hyperfine interaction is found to be fundamental to the low-temperature physics of this system near the quantum critical point.

Chakraborty *et al.* [18] are more rigorous in their treatment of the phase diagram. They develop the effective spin-1/2 Hamiltonian from the crystal field energies and then develop a mean-field theory and quantum Monte-Carlo simulations. Without leaving any fitting parameters, they reproduce qualitative features of the experiment but see a quantitative mismatch between theory and experiment as the critical field is much higher in experiment than in theory. Furthermore, even in the regime of small transverse field, near the classical critical point, theoretical results differ significantly from experiment [18]. The experimental results show a much shallower approach to the classical critical point, with $T_C(H_\perp)$ quite flat at $H_\perp < 0.5$ T [121].

This mismatch between experiment and theory has been further researched by Tabei *et al.* who have applied several varieties of perturbative Monte Carlo to the problem [142, 143]. All the theoretical methods agree roughly with one another, but do not accommodate the experimental data. Very recently, the experimental phase diagram of Bitko *et al.* [121]

at low transverse field was confirmed with dilatometry measurements [144]. To date this mismatch between experiment and theory remains an unsolved problem.

Inelastic neutron scattering studies of the quantum critical point reinforce the idea that the system is highly influenced by the nuclear hyperfine interaction, at least in certain regimes [145, 14]. As the 4.9 T quantum phase transition is approached, the energy gap to spin excitations gradually gets smaller. However, there is an incomplete softening of this mode (it never drops below 0.2 meV) which is directly attributed to the interaction with the nuclear moments. Rønnow *et al.* [145] relate this effect to the difficulties of attaining quantum coherence when coupled to a nuclear spin bath in quantum computing experiments.

Diluted Ferromagnetic Stoichiometries

Initially, dilution of the Ho moments simply seems to lower the T_C of the system. At $x = 0.44$, this material is found to be a ferromagnet with a sharp cusp in the ac susceptibility at 0.68 K [58]. This result was approximately reproduced by our research group [114], showing a phase transition at 0.68 K for an $x = 0.45$ sample (see Figure 3.3). In zero field, but at lower temperatures (~ 0.1 K) there is a peak in χ'' which may indicate some reentrant behaviour where degrees of freedom not locked away in ferromagnetic order freeze as a spin glass [146].

If a transverse field is applied, the system becomes much more complicated. There is a region where glassy dynamics are observed from the frequency response of the ac susceptibility [122, 141]. The system's behaviour shows a dependence on the way in which it is cooled. If it is cooled in a high transverse field where there are strong quantum fluctuations and the field is then turned off, the system is "annealed" quantum mechanically. If the system is cooled in zero field, on the other hand, the system is annealed classically. As a glassy system, it can be thought of as having a very complex free energy surface. Classically it must be thermally excited out of valleys in this free energy surface in order to find its ground state. Quantum mechanically, it can tunnel through barriers resulting in a very different end state. A proposed $(H_\perp, T)$ phase diagram is shown in Figure 3.2 [122, 141].

In a later reference [147], the primary conclusion is that the glassy dynamics stem from domain-wall tunneling. The ferromagnetic domain walls can be thought of as particles sitting in a potential energy surface. The transverse field tunes the mass of this particle and allows it to tunnel between minima in the potential energy surface. In zero field, thermal excitations are required to move the domain walls.

In a recent paper Silevitch *et al.* [148] compare results on $x = 1.0$, $x = 0.67$ and $x = 0.44$ samples in transverse magnetic field $H_\perp$. In the vicinity of the classical critical point, they

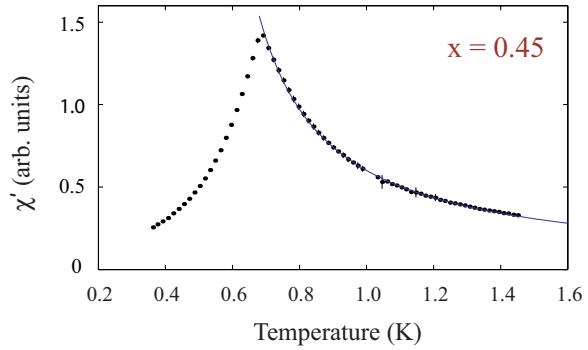

Figure 3.3: The magnetic susceptibility $\chi(T)$ of an $x = 0.45$ sample of $LiHo_xY_{1-x}F_4$ from Ref. [114].

find that the susceptibility is described by a modified Curie law:

$$\chi' \propto (\alpha' \mu_B |H_\perp| + (T - T_C) + \gamma' \Gamma)^{-1} \tag{3.19}$$

where Γ is the coupling with the next excited state $\propto H_\perp^2$ which controls quantum fluctuations. They suggest that this slightly unusual parametrization and the mismatch of the experimental phase diagram with theory are a result of Griffiths singularities.

3.2.2 The Spin Glass Regime

As the magnetic Ho^{3+} ions are diluted with non-magnetic Y^{3+} ions, random frustration begins to develop as a result of competition between the various ferromagnetic and antiferromagnetic interactions produced by the dipolar coupling. At sufficient levels of dilution, the system is found to lose its ferromagnetic order and a glassy state characterized by slow dynamics emerges [58]. This glassy state, particularly at the concentration $x = 0.167$, was assumed for some time, to have a finite temperature spin glass transition as predicted by theoretical work [29] and indeed experiments suggested that this was true [58]. With the zero-field physics of this stoichiometry seemingly well understood, much of the ensuing work on this assumed spin glass regime has been done in transverse magnetic field in an attempt to understand the effects of quantum fluctuations on a spin glass [149, 66].

At zero magnetic field, the frequency-dependent ac susceptibility has been measured in this sample for many frequencies and temperatures [58]. At a given frequency $\chi'(T)$ shows a rounded cusp at the temperature $T_f(\omega)$ which moves to lower temperatures as the measurement frequency is lowered. This cusp appears to obey an Arrhenius law over the

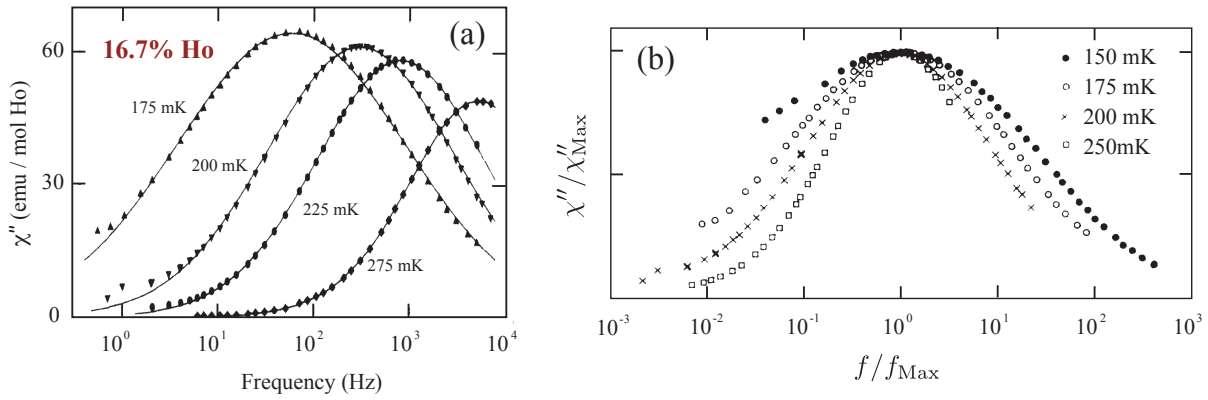

Figure 3.4: Results of Reich *et al.* [58] on an $x = 0.167$ sample of $LiHo_xY_{1-x}F_4$ in zero magnetic field. (a) Absorption spectra. (b) Absorption spectra superimposed by dividing by the peak frequency on the abscissa and dividing by the peak in χ'' on the ordinate. A clear broadening with lower temperature is observed.

temperature range studied in Ref. [58], which is in fact not generally indicative of a spin glass transition. A power law divergence at a finite T_g is now held to be a property spin glasses (see Chapter 2 or Section 3.4).

The absorption spectrum $\chi''(\omega)$ is a broad curve (several decades wide) as shown in Figure 3.4, which is well fit by a distribution of energy barriers to relaxation [58]. As the temperature is reduced, the spectrum shifts to lower frequency and the distribution of energy barriers becomes wider (so therefore the width of the absorption spectrum becomes wider). This is typical of other spin glasses and the dielectric susceptibility of structural glasses [150, 55]. The specific heat has also been measured, and after subtraction of the large nuclear component (which will be discussed in detail later), has been found to be a broad curve also typical of spin glasses [58].

In the work of Wu *et al.* [149, 66], it is found that application of a sufficiently large transverse field $H_\perp$ appears to destroy the spin glass ordering. The transverse field allows quantum fluctuations to occur (as in the pure material), opening up new routes to relaxation and basically preventing the spins from freezing. This apparent transition in $H_\perp$ has been measured in two ways: with the frequency dependence of χ'' [149] and with the non-linear susceptibility χ_3 [66].

Above the spin glass transition T_g, the effect of a transverse field is simply to narrow the absorption spectrum $\chi''(\omega)$ and to shift the maximum of the absorption spectrum

$f_{\rm Max}$ to higher frequencies as the quantum fluctuations allow the moments to relax more easily [149]. Below T_g, as $H_\perp$ is lowered, the low frequency behaviour of $\chi''(f) \sim f^\alpha$ is altered with α becoming smaller and eventually reaching 0 [149]. Theories have suggested that the spin glass state should be characterized by $\alpha = 0$ [151] and other experiments (on $Eu_xSr_{1-x}S$) have found a very small value < 0.1 for α in the spin glass regime [55]. Thus the point $(H_\perp, T)$ at which $\alpha \simeq 0$ is taken as the spin glass transition (H_c, T_g) [149].

Applying a larger, oscillating longitudinal field h (1.5 Hz and up to 150 Oe in this case), one can observer the field dependence of the susceptibility $\chi_{\rm tot}(h) = \partial M(h)/\partial h$. In a Taylor series expansion $\chi_{\rm tot} = \chi_1 - 3\chi_3 h^2 + \ldots$. Thus a quadratic fit to $\chi_{\rm tot}(h)$ will give the quantity χ_3 which is directly related to the spin glass susceptibility $\chi_{\rm SG}$.

In this system, $\chi_3(H_\perp, T)$ is found to be a maximum at the transition [66] which is found to be roughly at the same point as was seen using χ'' [149]. As one moves to lower temperatures, the peak in χ_3 becomes much smaller and very rounded. At a temperature of 25 mK, the maximum in χ_3 is found at a field $H_\perp \simeq 1.2$ T. Thus this suggests a critical transverse field (at zero temperature) that is equivalent to a ground state energy splitting of $\Gamma_c \simeq 1.0$ K. At zero transverse field, the spin glass temperature is $T_g \simeq 0.13$ K, thus, interestingly, the thermal fluctuations seem to destroy the spin glass order much more easily than quantum fluctuations.

In recent years, theorists have come to a good understanding of this portion of the $LiHo_xY_{1-x}F_4$ phase diagram in transverse magnetic field [152, 153, 154, 142, 155, 143]. In particular it is found that the nuclear hyperfine interaction and random fields are fundamentally important to this system. Taking into account nuclear hyperfine coupling (both transverse and longitudinal) and adding an adjustable parameter (the random transverse field coming from the dipolar interactions) allows the determination of an accurate theoretical $H_\perp$-T phase diagram. [152]. More rigorously incorporating induced random fields into the model results in an immediate destruction of the spin glass state at any non-zero transverse field $H_\perp$ [153, 154]. Thus, what was considered to be a quantum phase transition previously [149, 66], is actually a crossover from a state of spin glass ordered domains to a quantum paramagnet. The smearing of the peak in χ_3 is a natural consequence of the random fields and is well reproduced numerically [153]. This is shown in Figure 3.5.

One of the main effects of the nuclear hyperfine coupling is that it blocks quantum fluctuations since the two lowest lying electronuclear states $|\uparrow, I_z = -7/2\rangle$ and $|\downarrow, I_z = +7/2\rangle$ are not coupled by transverse magnetic field. The transverse part of the hyperfine interaction $A(I^+J^- + I^-J^+)$ must be included in order for quantum fluctuations to occur [155]. Schechter and Stamp [155] suggest that this effect leads to an increase in the critical transverse field $H_\perp^C$ (at which the crossover from spin glass-like state to quantum paramagnet occurs), particularly as x is *decreased*, a fact recently observed in experiments on $x = 0.167$ and $x = 0.20$ samples [125].

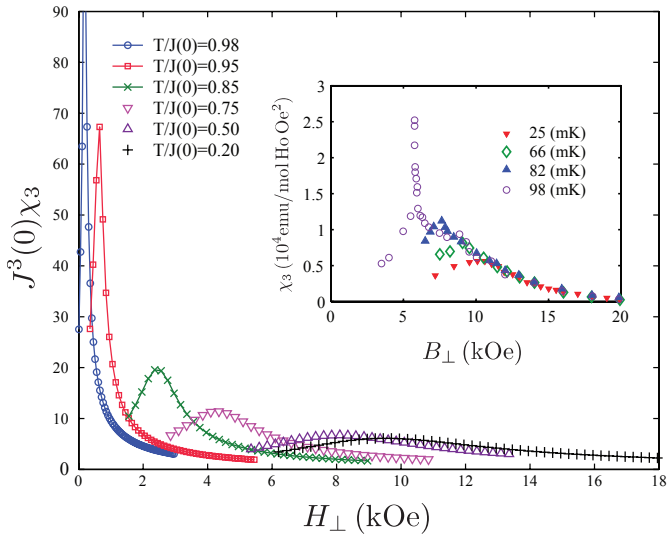

Figure 3.5: Numerical simulations of $\chi_3(T, H_\perp)$ considering induced random fields. Figure adapted from Tabei *et al.* [153]. Smearing of the peak in $\chi_3(H_\perp)$ is well reproduced. The experimental data [66] is shown in the top inset.

3.2.3 The "Antiglass" State

In many physical systems, at sufficient dilution of the magnetic moments, one will eventually reach what is known as the percolation threshold. The percolation threshold for a given system depends on the lattice structure and the extent of the interactions between the magnetic moments. Below that threshold, the system is essentially no longer macroscopic and is broken up into small disconnected domains. Above that threshold the system is, at least in some small way, completely connected by exchange interactions. A prime example is the system $Eu_xSr_{1-x}S$ [47, 85] which is dominated by a nearest-neighbour ferromagnetic interaction and a next-nearest-neighbour antiferromagnetic interaction. The system is ferromagnetic at high concentrations of Eu. As it is diluted, it enters a spin glass phase. The spin glass transition temperature gradually drops to zero temperature at the percolation threshold, below which there is no longer a finite temperature spin glass transition.

The dipolar interaction, however, is a long range interaction, dropping off as $1/r^3$. Thus there is no level of dilution at which the sample is broken up into disconnected domains, so no percolation threshold. One would expect, therefore, that the spin glass transition temperature in $LiHo_xY_{1-x}F_4$ would only go to zero temperature at zero concentration of

magnetic moments. Certainly this is the result of theory carried out many years ago by Stephen and Aharony [29] as described in Chapter 1. This is likely true of $Eu_xSr_{1-x}S$ below its percolation threshold, as well, but should take place at temperatures much lower than the energies of the exchange interactions in that system [87].

It was thus quite surprising that Reich *et al.* [58] and later Ghosh *et al.* [4, 5] discovered magnetic behaviour, summarized in Figure 3.6, that is quite far removed from that of spin glass phenomenology at $x = 0.045$. The first observed peculiarity of a 4.5% Ho sample, was a narrowing absorption spectrum $\chi''(\omega)$ as the temperature was lowered [58]. The specific heat, after subtraction of the nuclear component, was found to have unusually sharp peaks and accounted for only a very small portion of the expected $\ln 2$ entropy, roughly 15% [58, 5]. Later, even more exotic behaviour was found in the susceptibility. The absorption spectra were found to narrow appreciably and develop strong asymmetry at low temperatures, even exhibiting something resembling a low frequency gap [4]. The dc limit of the susceptibility was reported to obey the power law $\chi_{\rm DC} \sim T^{-0.75}$ [5].

Furthermore, Ghosh *et al.* performed some very interesting experiments to look for nonlinear dynamics [4]. Applying a fairly high power excitation up to 0.5 Oe, they found an eventual saturation of the signal at that frequency. Applying 'pump/probe' measurements where they apply a large 0.5 Oe pump excitation in addition to a variable frequency, small amplitude probe excitation (both along the c-axis), they found that the pump burns a hole in the spectrum as measured with the probe excitation. They also noted an overall frequency shift of the spectrum as a result of the high power pump excitation. Though a similar effect could be explained by heating of the sample from 110 mK up to 150 mK, a different shape to the spectrum is found, suggesting that it is not simply a result of heating [4].

Most unusually, Ghosh *et al.* observed slowly decaying coherent oscillations after the 0.2 Oe, 5 Hz excitation was turned off [4]. All of this exotic physics pointed to something very different from a spin glass state and in fact to a state that was fundamentally quantum mechanical. In Reference [5], a theory based on quantum entanglement of the magnetic dipoles is formulated and simulations show good agreement with the experiments. More recent investigations of this idea of hole burning and nonlinear dynamics have included the effects of transverse magnetic field [157].

It is worth mentioning now that the existence of this so-called "antiglass" has since been called into question and this is one of the central themes of this chapter. There is, in fact, a fair degree of inconsistency in the experimental papers proposing this novel state of matter at $x = 0.045$ [158, 58, 4, 5]. First and foremost, the dynamical measurements of Refs. [158, 58] show very different frequency dependence from those in Ref. [4], despite the fact that both sets of measurements were performed by the same research group and using the same single crystal of material [159]. While the peak frequency of the absorption

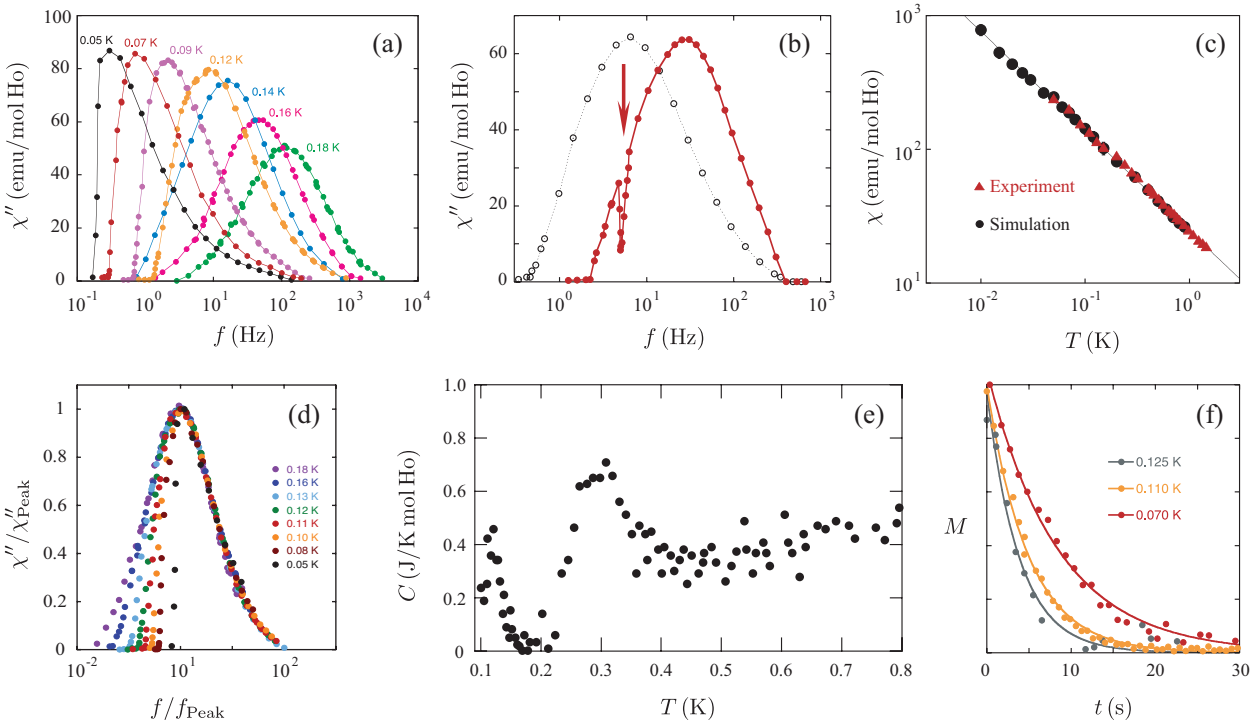

Figure 3.6: Summary of the "antiglass" physics observed by Ghosh *et al.* [4, 5]. (a) The absorption spectra as a function of frequency at different temperatures, showing an asymmetry developing at lower temperatures, taken from Ref. [4]. (b) A spectrum without a pump field and with a pump field applied, showing a hole being burnt into the spectrum [4]. (c) The temperature dependence of the dc susceptibility following a $T^{-0.75}$ law [5]. (d) Superimposed absorption spectra showing a narrowing of the spectrum as the temperature is lowered, opposite to what would be expected of a spin glass [156]. (e) The specific heat (after subtraction of the nuclear component) showing unusually sharp peaks [5]. (f) Coherent oscillations of the magnetization decaying after the probe is stopped [4].

spectrum f_{Max} roughly obeys an Arrhenius law in Refs. [158, 58], it takes on quite a different form in the later work Ref. [4]. The dc limit of the susceptibility is also found to be quite different between these articles. In particular, Reich *et al.* [158, 58] do not see a $T^{-0.75}$ dependence. The specific heat data of these works is also surprising, as it implies an extremely high residual entropy of 85% of $R \ln 2$. Thus, even before doing comparison experiments, the antiglass physics observed by Reich *et al.* and Ghosh *et al.* does not seem to be completely resolved experimentally. This point is discussed in more detail after presenting our own results on dilute $\mathrm{LiHo}_x\mathrm{Y}_{1-x}\mathrm{F}_4$.

3.2.4 Spin Glass, Antiglass or Superparamagnet?

As of 2003, it was established, largely by one research group [158, 58, 4, 5], that at a concentration $x = 0.167$, the material is a spin glass and that at a lower concentration of $x = 0.045$, the material becomes an exotic antiglass. However, in recent years, this has become a very contentious issue, with both experimental and theoretical groups debating the existence of the antiglass state and even a spin glass state.

Theoretical work has been largely dedicated to the determination of whether a perfect dipolar Ising model in zero magnetic field does or does not have a spin glass transition. As shown in the last section, mean-field theory suggests that there should be a spin glass transition and that it should persist all the way to zero concentration of magnetic moments [29]. However, Monte Carlo simulations should be a more authoritative method with which to tackle such a problem. Snider and Yu first suggested, theoretically that there might not be a spin glass transition in a dilute, dipolar Ising model, although their work was done on a simple cubic (SC) lattice [160]. Using the Wang Landau Monte Carlo technique, they found no spin glass transition for any concentration of magnetic moments.

Later Biltmo and Henelius applied Monte Carlo simulations directly to Ising spins on the $\mathrm{LiHo}_x\mathrm{Y}_{1-x}\mathrm{F}_4$ structure and found that the spin glass susceptibility χ_{SG} did not diverge and that the Binder ratio did not exhibit scale invariance at any temperature, again for any value of x [127, 161]. Most recently, however, Tam and Gingras have performed extensive computer simulations of the dilute dipolar Ising model on the appropriate lattice using parallel tempering and argue that there is indeed a spin glass transition, at 47 mK and 109 mK for values $x = 0.0625$ and $x = 0.125$ respectively [128]. Obtaining equilibrium in these experiments is found to be very challenging as the dynamics are very slow, and interpretation of the results are also complicated. In particular, it seems that a standard procedure of looking for a critical point by scale invariance of the Binder ratio B does not work here. However, the spin glass correlation length ξ_L/L (for different system sizes L) does show scale invariance at a finite temperature, strongly suggesting that there is a spin glass transition [128].

Thus, with the tentative conclusion that the ideal, dipolar, Ising model exhibits spin glass freezing, one is left wondering whether this is an accurate representation of the real system. One could imagine, for instance, that quantum effects would inhibit the formation of a spin glass state. The real system includes at least two additional effects: the nuclear hyperfine coupling (specifically the transverse part of that coupling) and transverse components of the dipolar interaction. Both of these effects have the potential to introduce coupling with the higher energy crystal field level $|\gamma\rangle$ and therefore induce quantum fluctuations. However, as analyzed by Schechter and Stamp [155], these terms in the Hamiltonian are not nearly strong enough to impinge upon the spin glass ordering that one should expect.

Another possibility to consider is the effect of strain in the crystal structure [143]. As discussed in Chapter 1, since the Ho^{3+} ion is a non-Kramers ion, the ground state doublet is not protected and is only present by virtue of the symmetry of the crystal field. Random strains that introduce a $B_2^2 O_2^2$ term to the crystal field Hamiltonian, for example, will split the ground state doublet. Such a random strain should therefore be equivalent to random transverse fields, which have been shown to theoretically destroy spin glass order [153]. Indeed such random strains have been observed in very dilute samples of $LiHo_xY_{1-x}F_4$ [162, 163] so we might expect that at some critical level of dilution, spin glass physics will be lost. However, the effects of a small transverse field on the dynamics of $LiHo_xY_{1-x}F_4$ have previously been found to be subtle and not strikingly different from spin glass phenomenology [149]. Thus it seems likely that random strains would also not give rise to such an exotic set of dynamics as seen in "anti-glass" physics [4]. Furthermore, the nuclear hyperfine interaction may block the quantum fluctuations created by random strains, restoring spin glass physics [152, 155].

From the experimental side of the debate, there are several view points. The first is that there is a spin glass state at 16.7% Ho [58] that gives way to an unusual antiglass state at 4.5% Ho [58, 4, 5]. The second view, recently suggested by Jonsson *et al.*, is that neither of those samples, 4.5% nor 16.7%, show a spin glass transition or an unusual antiglass state [65]. They find, in linear and nonlinear susceptibility measurements, that there is very little difference between those two stoichiometries, making the antiglass state unlikely. Furthermore, they argue that since the nonlinear susceptibility χ_3 does not show a true divergence, or even a very sharp peak, there must not be a spin glass transition. Instead, they parametrize their data with a model based only on thermal activation, rather than complicated many-body spin glass physics. Thus they seem to interpret the system to be a sort of superparamagnet – a disordered, glassy system with a $T = 0$ glass transition. Jonsson *et al.* [65] thereby opened a debate, largely dealing with the interpretation of experimental data [125, 126].

As discussed in more detail in presenting our results, we take a third distinct view:

that all samples with approximately $x < 0.25$ have finite temperature spin glass transitions. Specifically, we find evidence for glass transitions in samples of $x = 0.08$, $x = 0.045$ and $x = 0.018$. We find no evidence for the unusual antiglass state, in both ac susceptibility [124] and specific heat measurements [123]. Furthermore, we provide some insight as to why the experimental results of Refs. [58, 65, 125, 126] have not been easily and unambiguously interpreted as spin glass physics.

3.2.5 Very Dilute Limit

In samples of $LiHo_xY_{1-x}F_4$ with 0.1% Ho or less, the Ho^{3+} ions can be considered to be virtually isolated. Of course, they can never truly be isolated by virtue of the long range dipolar interaction, but the average interaction strength for such a sample is much smaller than that for the stoichiometries discussed above and interactions should not play a significant role until temperatures well below those obtained by a dilution refrigerator, for example. Such a very-dilute sample provides an ideal system in which to probe the single-ion physics of Ho^{3+} in the appropriate crystal field environment. Several very interesting experiments have been performed in such a configuration using SQUID magnetometry [129, 164, 165], μSR [166] and NMR [167, 168]. Here, we concentrate on describing the magnetometry experiments as they are likely most applicable to understanding our own results.

Hysteresis loops taken at different sweep rates and different temperatures show a great diversity of behaviour [129]. At temperatures above 200 mK, the loops tend to be rather smooth, with some small wiggles. At temperatures as low as 50 mK, however, pronounced steps in the magnetization are visible. The steps in the magnetization are understood to result from quantum relaxation (tunneling) at avoided level crossings or resonances. The magnetic field at which these steps occur can be connected to level crossings obtained by diagonalizing the single-ion Hamiltonian including the nuclear hyperfine interaction. Different amplitudes of the steps are indicative of different sizes of level crossings. Some of these crossings are directly caused by the transverse hyperfine coupling.

Faster sweep rates are found to result in an adiabatic process due to the long spin-lattice relaxation time [129]. If the field is swept too quickly, the nuclear spins are not able to relax and one is no longer just probing the lowest lying energy levels. As a result, many more resonances are observed in these adiabatic measurements. Additionally, application of a transverse magnetic field is found to assist tunneling, leading to large magnetization steps.

In a different work [165], ac susceptibility measurements are made on a very dilute sample above 1 K. χ' and χ'' are measured at 163 Hz while scanning the longitudinal magnetic field. The result is a set of peaks and dips once again corresponding to energy

level crossings where tunneling becomes easier. It is noticed that some of the peaks and dips are smaller than others. The large ones are assumed to be a result of single-ion relaxation whereas the smaller ones are a result of co-tunneling of pairs of interacting Ho^{3+} ions. Frequency scans of the susceptibility are also presented. At particular values of the longitudinal magnetic field $H_z = 80$ and 380 Oe, surprisingly slow relaxation is observed. Even at 1.75 K, the peak frequency in the absorption spectrum is under 200 Hz.

These experiments provide a great deal of information about the inner workings of a Ho^{3+} ion in the $YLiF_4$ lattice and may be very valuable for interpreting our results in much more concentrated samples. Clearly the hyperfine interaction is very important in controlling the rate of relaxation of the spins through quantum tunneling. As we shall discuss later, this may be seen in our experiments in a much less obvious way.

3.3 Experimental Parameters and Samples

AC susceptibility measurements were performed on three stoichiometries of the $LiHo_xY_{1-x}F_4$ series using the SQUID magnetometer apparatus described in Chapter 2. The measurements on the 4.5% sample are described in Ref. [124]. For $x = 0.018$, 0.045 and 0.080 frequency scans at various temperatures were obtained. Additionally, temperature scans at several different frequencies were obtained for the $x = 0.045$ sample. For the $x = 0.045$ and $x = 0.080$ samples, calibration of the magnetometer was achieved by matching data on different geometries of sample using the formulae described in Appendix A. The $x = 0.018$ sample was calibrated by measuring a superconducting (perfectly diamagnetic) Pb sample of the same dimensions mounted in precisely the same way. The various sample dimensions measured are listed in Table A.1.

Initially, frequency scans at constant temperature were performed. These measurements were performed with frequencies ranging from 1 mHz up to several kHz. The data presented here are limited to frequencies below which a background frequency dependence becomes significant. This background is also present in an empty magnetometer thus is not a property of the samples. Instead, it is the result of phase shifts in the excitation coil lines and in the SQUID feedback electronics and is dependent on the SQUID gain setting employed. In cases of lower SQUID bandwidth, where the background was more significant, data has been restricted to lower frequencies. The temperature ranges of our frequency scans were set so that we could always resolve the peak frequency in χ'' within our reliable frequency range. In some cases, the demagnetization correction ended up shifting the peak frequency out of our range of data, adding a further limitation to our accessible temperature range.

When temperature was changed, we waited for a period of an hour or more before

taking data. In many cases, at the lower temperatures, multiple scans were taken with a period of several hours in between to check for reproducibility and therefore thermal equilibrium of the sample.

We also checked for heating of the sample from our excitation field by varying the input power by more than an order of magnitude and checking for consistency between scans. All data presented here were taken using an excitation power at least four times lower than the excitation power where heating was observed (seen as a shift of the absorption spectrum to higher frequencies). The applied magnetic field was kept under 20 mOe in magnitude for all of the susceptibility measurements presented here. Even when much higher power was applied to look for heating effects, the result was uniform heating for all frequencies. This suggests that it was heating in the leads to the magnetometer rather than heating within the sample itself since we would expect the latter situation to depend on χ'' and change with frequency.

Temperature scans at fixed frequency were also performed at four frequencies: 0.001, 0.01, 0.1 and 1 Hz. These measurements are more time consuming as each temperature point sampled required thermal equilibration time. In fact, the time constant of thermal equilibration was found to be at most 350 s, at the lowest temperatures (around 70 mK). However, at the lower temperatures and frequencies we generally waited more than an hour at each temperature to ensure that both the temperature came into equilibrium and a suitable number of periods of the measurement frequency had passed. The results of temperature scans are found to be perfectly consistent with the results of frequency scans, further establishing the fact that our data are taken only once the system has obtained equilibrium.

We have also performed specific heat measurements on the $LiHo_xY_{1-x}F_4$ series. Most of our specific heat results (on $x = 0.018$, 0.045 and 0.080 samples) have been presented previously [123, 114]. However, this work contains one new specific heat result on an $x = 0.12$ sample. The specific heat measurements were performed with the quasi-adiabatic heat pulse method, with a very long time constant of relaxation (> 1 hour). Our specific heat measurement technique is described in detail in Chapter 2 and in Ref. [114].

Samples

The $LiR_xY_{1-x}F_4$ series of materials, also known as R:YLF, where R is a rare earth ion, are frequently used as laser crystals in optical physics. As a result, they are commercially available as very high quality single crystals. We have obtained samples of $LiHo_xY_{1-x}F_4$ or Ho:YLF from the company *Tydex, J. S. Co.* in St. Petersburg, Russia. The samples were grown by the Bridgeman technique and any ratio of Ho to Y is possible, with negligible change in the lattice parameter, as the Ho^{3+} and Y^{3+} ions have very similar ionic radii.

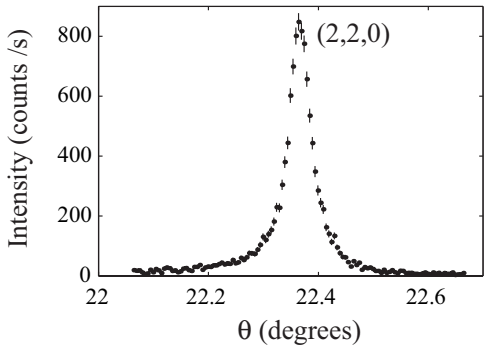

Figure 3.7: The 220 X-ray diffraction peak of the 8% $LiHo_xY_{1-x}F_4$ sample showing a width of less than 0.03 degrees, limited by instrument resolution, indicating extremely high sample quality.

Seven different stoichiometries were purchased to cover the more interesting regions of the phase diagram, with concentrations $x = 0.02$, 0.045, 0.08, 0.12, 0.25, 0.45 and 1.

Sample characterization on the 2%, 4.5% and 8% samples was performed in collaboration with Stefan Kycia and Ariel Gomez at the University of Guelph and with Jim Britten at McMaster University. Crystalline quality was verified by high resolution diffraction on a fine focus Cu rotating anode generator equipped with a high resolution Ge (220) four-crystal monochromator and a Huber 4-circle diffractometer. The measurements revealed extremely sharp Bragg peaks ($\theta_{\mathrm{FWHM}} < 0.015^\circ$) for all reflections, indicating high crystalline perfection. No twinning was observed. Extensive diffuse scattering measurements revealed no diffuse scattering near or away from the Bragg peaks or satellite peaks that could be associated with any disorder or short range ordering. Small ~ 100 μm fragments were taken from each sample, and crystallography data sets were measured using a molybdenum rotating anode, kappa diffractometer, and CCD area detector. All three data sets refined well with Ho substituting for Y in the expected tetragonal ($I4_1/a$) structure [2].

However, a precise determination of the holmium concentration (at the lower concentrations) with X-ray measurements was found to be prohibitively difficult. Instead, we found that the most precise way to establish the Ho concentration was through specific heat measurements (described in more detail in Section 3.5) and the contribution of the hyperfine coupling to the $I = 7/2$ nuclear moments. Fitting the specific heat to the 'high' temperature tail of the calculated hyperfine contribution around 1 K with a $1/T^2$ contribution from the electronic moments was more successful in precisely determining x. Specifically,

[2]Information communicated by Stefan Kycia, University of Guelph and contained in Ref. [123].

this was performed by adjusting the Ho concentration x such that, after subtraction of the nuclear hyperfine contribution, the high temperature tail of C was best fit by a $1/T^2$ power law. In the case of the nominally 2% sample, the specific heat showed the actual concentration to be closer to 1.8%. Such a change $\Delta x = 0.002$ is nearly impossible to resolve with X-ray spectroscopy whereas the nuclear contribution to the total specific heat is quite well understood and is proportional to the number of holmium ions. Determination of x could also have been accomplished using the high-temperature magnetic susceptibility, though susceptibility is a more challenging measurement to calibrate accurately than specific heat (especially given demagnetization effects for example). The samples with 4.5%, 8.0% and 12.0% Ho were found to have the correct, quoted stoichiometry.

3.4 AC Susceptibility Results on Dilute $\mathbf{LiHo}_x\mathbf{Y}_{1-x}\mathbf{F}_4$

Temperature Scans

Temperature scans of the susceptibility of a 4.5% sample are presented in Figure 3.8 along with results from other research groups. Seen is an increase in the susceptibility until a frequency dependent freezing temperature $T_f(\omega)$ at which point there is a sharp drop in the susceptibility. This freezing temperature moves to lower temperatures as the frequency of measurement is reduced. This behaviour is typical of spin glasses. As one approaches a spin glass transition, the dynamics of the moments slow down considerably. When the frequency of measurement is brought above the time constant of relaxation of these moments, the magnetization begins to lag behind the applied field, and eventually the magnetic susceptibility disappears entirely.

The temperature dependence of this sample is seen to match quite well with several other results. The results of Reich *et al.* [158, 58] are fairly close to our results. Certainly the differences could be explained by slight misbalance of a susceptometer or an incorrect demagnetization correction for example. Our results do not match the $T^{-0.75}$ power law proposed by Ghosh *et al.* [5], however.

The results of Jonsson *et al.* [65] match well with our results at temperatures above $\sim$ 200 mK (after applying a correction for demagnetization based on the geometry of their sample). Below roughly 200 mK, their results begin to deviate from ours. This is easily explained by the fact that, below that point, the measurements are no longer in the dc limit, so that the magnetization is lagging behind the applied magnetic field. They are using a method that involves linearly sweeping the magnetic field and tracking the magnetization and dividing to obtain the magnetic susceptibility χ. However, this is equivalent to measuring the susceptibility with a spectrum of probe frequencies, rather

than at a single probe frequency. Since their exact sweep rate and starting position are not explained, it is impossible to determine exactly what frequencies their measurement corresponds to and thus it is not possible to objectively compare with our data. Their sweep rate is cited as in the range of 1 to 50 Oe/s. The field range over which they analyze the magnetization data for obtaining χ' at 200 mK is roughly 25 Oe. Thus we can see that their measurement is corresponding to, at best, a measurement frequency of 40 mHz. While at first seemingly a very low frequency, it can be seen from our data that such a frequency can only be considered to be a "dc" measurement down to roughly 100 mK. Since Jonsson *et al.* are essentially measuring with a triangular wave probe, there are many higher harmonics that would be damped out at higher temperatures making it reasonable to see a deviation of their results and ours around 200 mK. Certainly we do not question the accuracy of the results of Jonsson *et al.*, but do disagree with the intimation that their results are taken in the dc limit over the entire range of their data.

Finally, we have also shown Monte Carlo simulation results from Biltmo and Henelius [161] in Figure 3.8 which appear to match very well with our results. Interestingly, the conclusions drawn from these Monte Carlo simulations was that there is no divergence of the spin glass susceptibility at finite temperature, thus that there is no spin glass transition in this material, for any value of x.

Frequency Scans

Initially, we pursued measurements on a 4.5% sample of Ho:YLF in hopes of reproducing and advancing the exotic and unusual antiglass physics that was seen by Reich *et al.* [158, 58] and Ghosh *et al.* [4, 5]. Since the main signature of the antiglass was a narrowing of the absorption spectrum $\chi''(\omega)$ with lower temperature, performing frequency scans of χ' and χ'' was an obvious choice of measurement. The results we obtained on a 4.5% sample are published in Ref. [124]. Since then, we have extended our measurements to two adjacent concentrations in our available series of samples: 8% and 1.8% Ho:YLF.

The resulting frequency scans on $LiHo_{0.045}Y_{0.955}F_4$ (see Figure 3.9) reveal broad features in the absorption spectra $\chi''(f)$ with a temperature dependent peak position defined to be $f_{\mathrm{Max}}(T)$. At a given temperature, the in-phase component of the susceptibility χ' is 0 at high frequencies (where the spins are too slow to respond to the perturbing magnetic field) and tends towards a constant value (the dc limit) at low frequency, which we will refer to as χ_{DC}.

Unsurprisingly, the peak frequency shifts to lower frequency with lower temperatures. χ_{DC} and χ''_{Max} both appear to be monotonically increasing with a decrease in temperature (at least in the range of our data). It is not immediately obvious in Figure 3.9 how the widths of the absorption spectra change with temperature. To facilitate this observation,

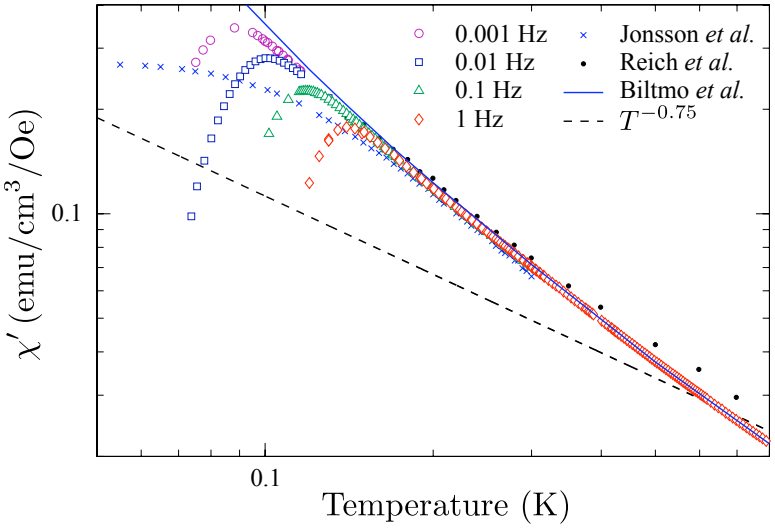

Figure 3.8: Temperature scans of the in-phase ac magnetic susceptibility χ' at different frequencies of an $x = 0.045$ sample. Shown for comparison is data from other experimental and theoretical research groups: experimental data from Reich *et al.* [158, 58] (black dots), experimental data from Jonsson *et al.* [65] (blue x's, corrected for demagnetization) and Monte Carlo data from Biltmo and Henelius [161]. Also shown is the proposed $T^{-0.75}$ power law of Ghosh *et al.* [5].

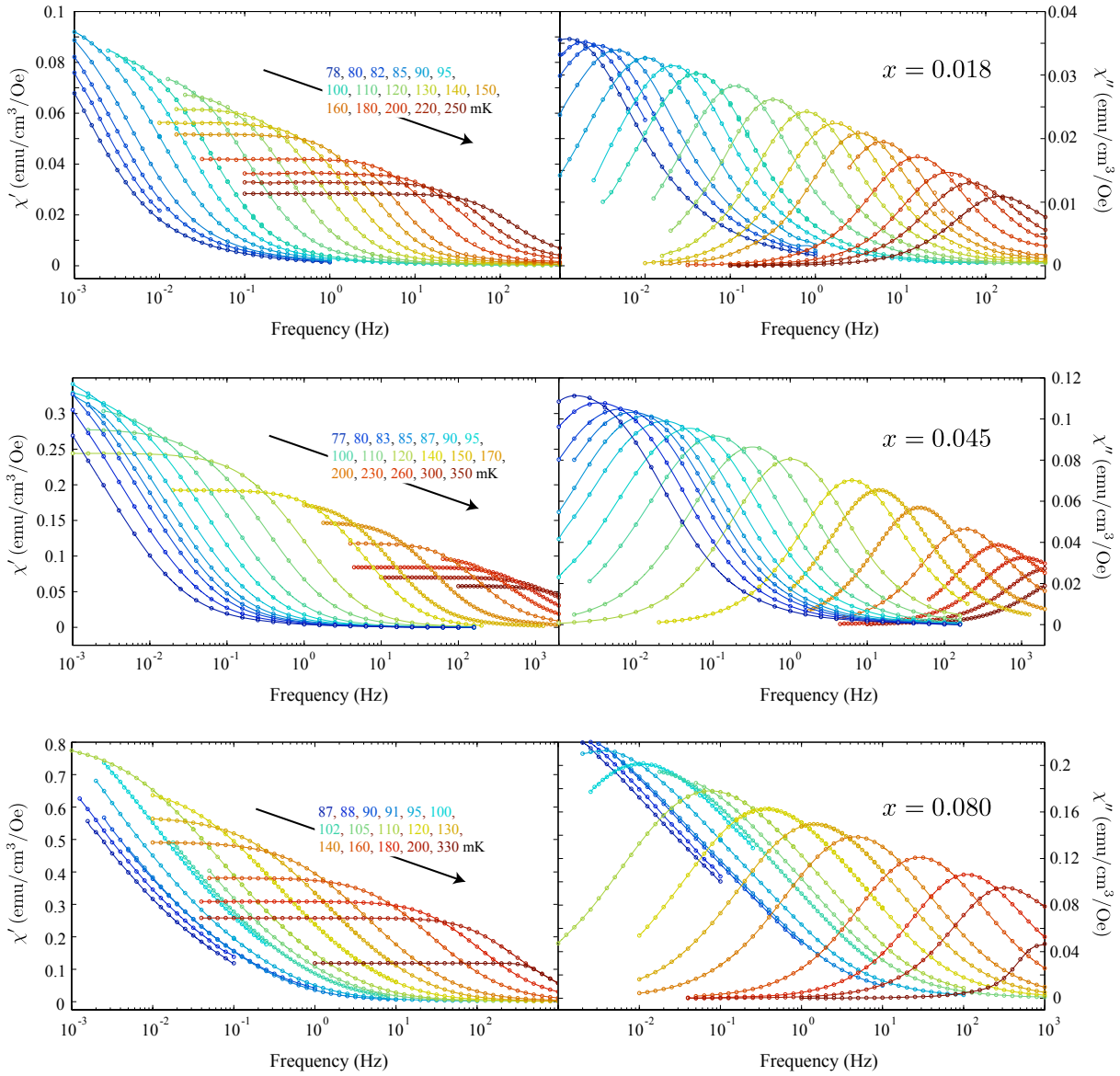

Figure 3.9: In-phase $\chi'(f)$ and absorption $\chi''(f)$ spectra at various temperatures for the concentrations $x = 0.018$, $x = 0.045$ and $x = 0.080$.

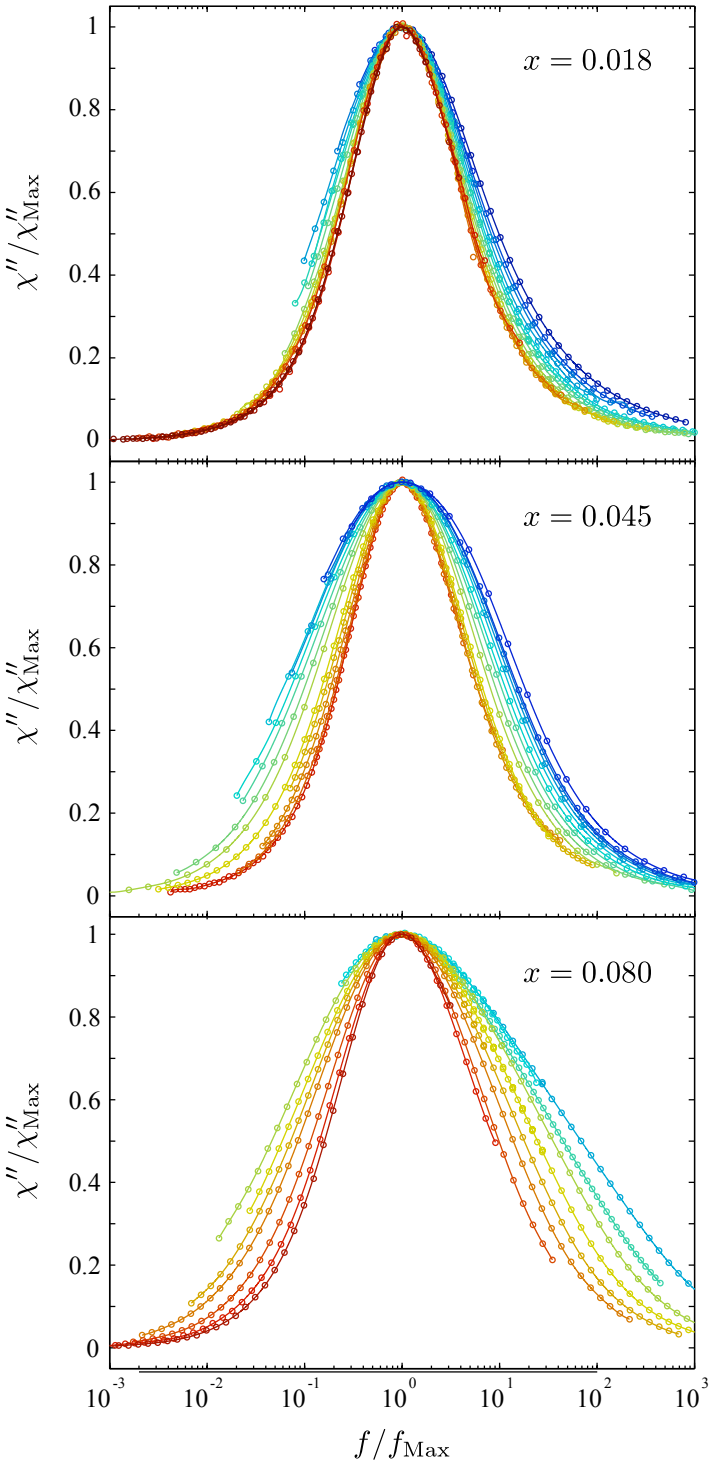

Figure 3.10: Superimposed absorption spectra.

we show a plot superimposing the spectra by plotting $\chi''(f)/\chi''_{\rm Max}$ against $f/f_{\rm Max}$. It then becomes obvious that the widths of the spectra are *increasing* with lower temperature. Additionally there is no development of a significant asymmetry in the spectra. Clearly, antiglass behaviour is not observed in our measurements and the results are, instead, consistent with spin glass physics.

In principle, a good but quick and simple analysis to determine whether a material is a spin glass or not is to calculate the ratio $\xi = \Delta T_f/(\tilde{T}_f \Delta \ln \omega)$, also known as the Mydosh parameter [44]. This is typically done from temperature scans of the susceptibility at different frequencies, taking T_f as the maximum in χ'. Then ΔT_f is the change in freezing temperature obtained by changing the measurement frequency by an amount $\Delta \ln \omega$. Here we normalize by $\tilde{T}_f$, the average of the values of T_f used. It is important to note that the parameter ξ is not well defined [44], and we might equally use T_g or the lowest achieved T_f instead of the average $\tilde{T}_f$. Essentially, this parameter expresses the fractional rate of change in freezing temperature with respect to the logarithm of the measurement frequency.

We could equally apply this analysis to frequency scans using $\tau_{\rm Max}$, thus writing the Mydosh parameter as $\xi = -\Delta T/(\tilde{T} \Delta \ln \tau_{\rm Max})$. This gives a value of $\xi \sim 0.138$ if we concentrate on the data near the bottom end of our temperature range. This is certainly higher than is typically expected of spin glasses. Canonical spin glasses have values of ξ around 0.005 to 0.06 [44]. As a counter example, a particular material, a-$(Ho_2O_3)(B_2O_3)$, that is known to be a superparamagnet or a kind of glassy material that does not have a finite temperature spin glass transition, has $\xi = 0.28$ [44]. With a value of ξ higher than other spin glasses studied, this simple analysis might suggest that our sample is a superparamagnet, or at least borderline between a superparamagnet and spin glass. However, this is merely a rough comparative analysis and as we shall see, not universally relevant. In fact the Mydosh parameter does not provide a good indication of whether there is a spin glass transition. Rather it provides a measure of how close one is to the spin glass transition (if it exists). It depends greatly on what temperature range is taken and, most importantly, how close to the glass transition one is able to measure in the frequency window accessible by a particular experimental probe. For example, if one were to measure the canonical spin glasses (such as CuMn and $Eu_xSr_{1-x}S$) with a measurement probe in the MHz or GHz frequency range, one would obtain much larger values of ξ.

Recently, our measurements of a 4.5% Ho sample, have been extended to two other stoichiometries in the series: 1.8% Ho and 8.0% Ho. Frequency scans of the susceptibility of all three materials are presented in Figure 3.9. The results are all qualitatively similar, again showing broad spectra, indicative of glassy relaxation and a trend toward lower frequencies as the temperature is reduced. Of course, the magnitude of the susceptibility is much larger for higher values of x, as there is higher density of magnetic moments and larger average interaction strengths.

Again, superimposing the absorption spectra for the 1.8% and 8.0% samples, there is clear broadening of the absorption spectra with lower temperatures, consistent with spin glass physics (see Figure 3.10). One can also see quite easily that the absorption spectra are generally broader for higher values of x. This could be explained simply by the temperature range of our measurements (which is similar for all three samples) being progressively closer to the spin glass transition temperature as x is increased and T_g is therefore increased. The lower end of our temperature range is actually defined not by cryogenics but by the characteristic frequency $f_{\mathrm{Max}}(T)$ reaching 1 mHz, which is the lowest frequency at which we have attempted measurements. The fact that this lower limit is at 77 to 80 mK for all three samples (before the demagnetization correction), where T_g should be roughly proportional to x, is quite surprising.

Thus far, we have shown a complete lack of "antiglass"-like behaviour in all three stoichiometries studied and instead qualitative spin glass behaviour, particularly a broadening absorption spectrum with lower temperature. However, the Mydosh parameter tends to suggest that these materials might be superparamagnets rather than true spin glasses. To rigorously and quantitatively demonstrate whether these materials are spin glasses or not, we must turn to a dynamical scaling analysis.

Dynamical Scaling Analysis

As discussed in Chapter 1, if the material is a spin glass, one expects to see a divergence of the dynamical exponent at the glass temperature, thus

$$\tau = \tau_0 \left(\frac{T - T_g}{T_g} \right)^{-z\nu} = \tau_0 t^{-z\nu} \tag{3.20}$$

where ν is the correlation function critical exponent, z is the dynamical critical exponent and t is the reduced temperature. Monte Carlo simulations [76] have found $z\nu \simeq 8.0$ and this has been roughly confirmed in various experimental spin glass systems (as discussed in Chapter 1).

Thus to state more assertively whether we are dealing with a spin glass, or not, we must perform such a dynamical scaling analysis. To do so, we have taken the peak frequency in χ'', f_{Max} and the corresponding time constant $\tau_{\mathrm{Max}} = 1/2\pi f_{\mathrm{Max}}$ as indicators of the relevant time scale of the material at a given temperature. We then use this time constant as a function of temperature τ_{Max} to search for critical behaviour that would prove or deny the existence of a finite temperature spin glass transition.

It is important to note that in other works, such as Refs. [70, 82, 83], the relevant time constant has been chosen differently. For example, in some cases, groups have looked at the freezing temperature, defined as the maximum in $\chi'(T)$ for a given measurement frequency

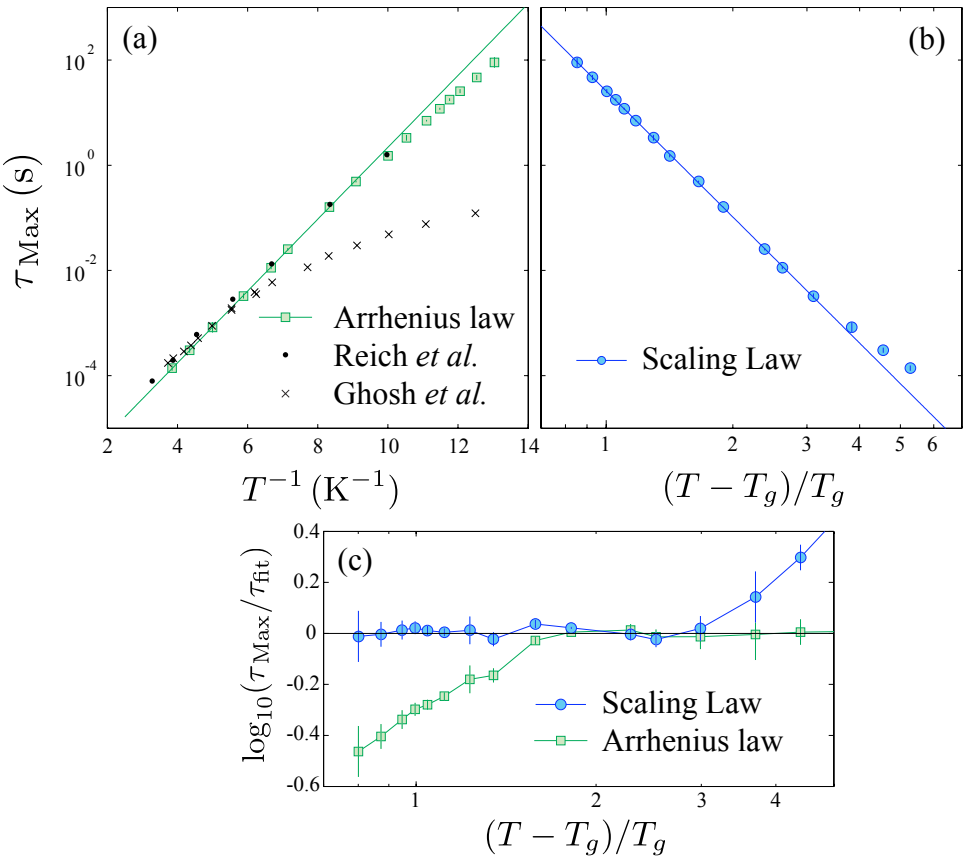

Figure 3.11: (a) An Arrhenius fit to $\tau_{\rm Max}(T)$ appears to work well for the higher temperatures studied here. However there is very noticeable deviation at the lower temperatures. The resulting fitting parameters are $\tau_{0A} = 0.32$ μs and $E_A = 1.57$ K. Shown for comparison are two different results from the same research group [158, 4]. (b) Fitting of a dynamical scaling law is very successful below 200 mK and gives a reasonable value of the critical exponent $z\nu = 7.8 \pm 0.2$ and glass transition temperature $T_g = 42 \pm 2$ mK. The $\tau_0 = 16 \pm 7$ s so obtained is surprisingly long, however. (c) Residuals (on a log scale) for the Arrhenius law and dynamical scaling law fits.

f, as a function of frequency so $T_f(f)$. This method has two major disadvantages. First, it is much more time consuming to change temperature than to change frequency, making it more difficult to narrowly pin down T_f as compared to $f_{\rm Max}$. Secondly, $T_f(f_{\rm Lower})$, where $f_{\rm Lower}$ is the lower bound on one's measurement frequency, is at a higher temperature than the temperature at which $f_{\rm Max} = f_{\rm Lower}$. Thus using $f_{\rm Max}$ allows us to move to lower temperatures, closer to the possible spin glass transition temperature, picking up more of the associated critical behaviour. Although the $T_f(f)$ method has been used quite often historically, there is no theoretical basis on which to favour it over the $f_{\rm Max}(T)$ method used here.

Alternatively, it has been theoretically proposed [76] that one should define the time constant as

$$\tau = \lim_{\omega \to 0} \frac{\chi''(\omega)}{\omega \chi'(\omega)}. \tag{3.21}$$

While potentially the most reliable choice of τ, this is highly impractical in experiment. The spectra are too broad and the frequencies too low to reach this limit for any useful temperatures (see Appendix B for more details and an illustrative plot). So, for the above reasons, we have employed $\tau_{\rm Max}$ in performing our dynamical scaling analysis.

For the 4.5% sample, the dynamical scaling has been performed by choosing a glass temperature T_g, applying a linear fit to $\ln \tau$ as a function of $\ln(T/T_g - 1)$ and evaluating the goodness of fit. This is done for many different possible glass temperatures and the temperature with the best fit is chosen (this method is outlined in further detail in Appendix B). While the fits are universally poor for the whole temperature range studied, restricting ourselves to temperatures below 200 mK, permits good agreement with a scaling law. Moreover, the exponent that is thereby determined, is $z\nu = 7.9$, which is very close to the value determined from Monte Carlo simulations of $z\nu = 8$ [76].

In all, the determined parameters in the case of $x = 0.045$, are $z\nu = 7.8 \pm 0.2$, $T_g = 42 \pm 2$ mK and $\tau_0 = 16 \pm 7$ s. While $z\nu$ is a very standard critical exponent and T_g is in the expected range of temperatures based on the T_g of other samples in the series, τ_0 is found to be many orders of magnitude larger than is seen in most spin glasses. For example, in $Eu_xSr_{1-x}S$ for $x = 0.4$, this intrinsic time constant is $\tau_0 \simeq 2 \times 10^{-7}$ s [70].

It can be seen from our data, that we are only able to resolve $f_{\rm Max}$ down to a temperature of 77 mK for the 4.5% sample (working at frequencies as low as 1 mHz). This is a temperature almost twice the glass temperature or a reduced temperature of just under 1. Clearly we are unable to successfully perform equilibrium measurements anywhere close to the transition temperature. Our dynamical scaling analysis holds up to about 200 mK, which is a reduced temperature of almost 4. It is not surprising that critical behaviour is lost above that point, as it is quite far from the critical temperature. The

higher temperature range of the data can be fit with an Arrhenius law

$$\tau = \tau_{0A} e^{-E_A/T} \tag{3.22}$$

with the parameters $\tau_{0A} = 0.32$ μs and $E_A = 1.57$ K. Fitting to the scaling and Arrhenius laws are shown in Figure. 3.11 as was published in Ref. [124].

This long τ_0 explains the unusually low Mydosh ratio, $\Delta \ln \tau / \Delta T$, in this system, which would surely be higher if we could move to much lower frequencies and therefore much closer to the glass transition. If one were to study the canonical spin glasses at frequencies in the MHz or GHz, for example, one would also expect an unusually low Mydosh parameter.

What is the explanation for such an unusually high τ_0? There are two possible (though not mutually exclusive) scenarios. First, it might be concluded that the many body physics of the dipolar, Ising spin glass leads to much slower relaxation when compared to other systems. Cluster glasses, for example, have been found to have higher time constants than spin glasses. Thus the answer could lie in the proximity of the system to ferromagnetism and the formation of large ferromagnetically correlated regions within the sample, for example. Alternatively, the explanation may come from single-ion physics. If the time to flip a single, isolated spin is already relatively long then the overall time constant must inevitably be very long as well. It turns out that the dynamics of the other stoichiometries studied may help provide a solution to this problem.

Concentration dependence

Dynamical scaling for the 8% sample is fairly straightforward and is just as successful as in the 4.5% sample. The result is a glass temperature $T_g = 65$ mK, critical exponent $z\nu = 7.8$ and intrinsic time constant $\tau_0 = 0.11$ s. Error bars are similar to the 4.5% fits, roughly ± 3 mK on T_g. One can notice immediately that τ_0 is more than two orders of magnitude *smaller* in the 8% sample. This dynamical scaling fit is shown in Figure 3.12 along with that of the other stoichiometries.

In the case of the 1.8% sample, the analysis is not so simple. With no free parameters, the results of the fit are $z\nu \simeq 7.3$, $T_g \simeq 41$ mK. The critical exponent is somewhat small and the glass temperature is extremely high, almost identical to that obtained for the 4.5% sample. On closer inspection (see Appendix B), it can be seen that the fit is highly unconstrained, so that a large range of critical temperatures and exponents are able to satisfactorily fit the data. With the exponent fixed at $z\nu = 8.0$, we obtain an adequate fit and a glass temperature of 35 mK. This is the result plotted in Figure 3.12. Thus for 1.8%, there remains quite a lot of ambiguity surrounding the transition temperature. This is likely related to the distance away from the glass temperature that we are measuring, making it much more difficult to extract critical behaviour. A reliable determination of T_g

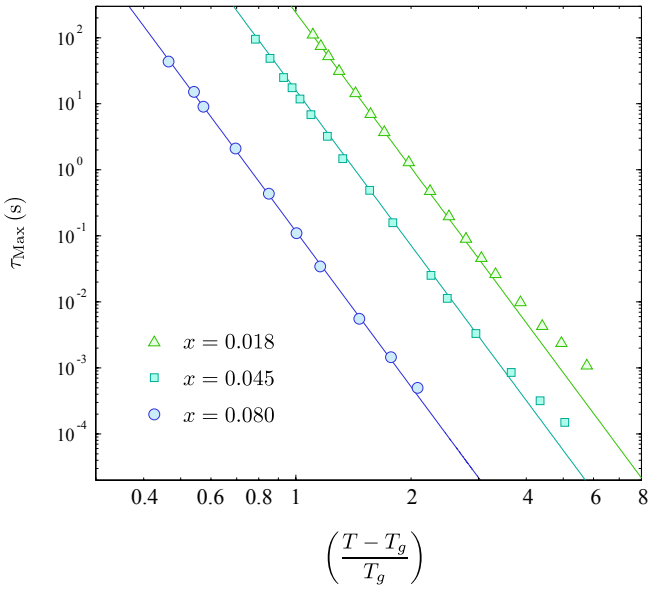

Figure 3.12: Dynamical scaling fits for all three stoichiometries studied.

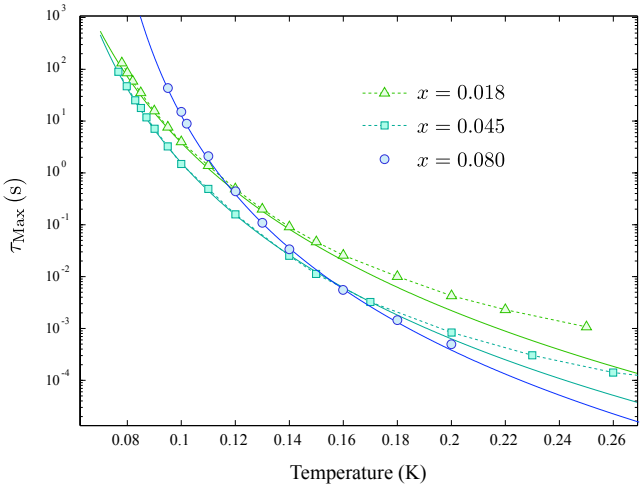

Figure 3.13: The time constant τ_{Max} plotted as a function of temperature T for three different stoichiometries. The solid lines are dynamical scaling law fits. At high temperatures, the time constant is inversely correlated with x.

for $x = 0.018$ may be impossible without much lower frequencies of measurement (which become prohibitively difficult).

Ambiguity aside, the 1.8% sample seems to exhibit a rather high glass temperature if we expect that, roughly, $T_g \sim x$. The mean-field model of Stephen and Aharony [29] predicts a $T_g(p)$ function that will be slightly steeper than linear, though that is a bond-diluted model and p is the bond dilution probability (see Section 1.2.5). Monte Carlo work of Tam and Gingras [128] on $LiHo_xY_{1-x}F_4$ suggests a $T_g(x)$ that scales close to linearly. The canonical RKKY spin glasses like Cu*Mn* are found to have a concentration dependence close to $T_g(x) \sim x^{0.7}$ [53]. The data here on our 1.8% sample does not appear consistent with any of those results or predictions.

For lower glass temperatures to fit the $x = 0.018$ data, higher values of the critical exponent $z\nu$ are required. We could speculate that there is some physical reason that $T_g(x = 0.018)$ is quite a bit higher than expected or that the exponent $z\nu(x = 0.018)$ is quite a bit larger than in other stoichiometries and simulations. Even with the underconstrained dynamical scaling fits, the glass transition (if it exists) of this 1.8% sample does seem to be at an anomalously high temperature and therefore more work is perhaps required to fully understand the behaviour of this particular sample. However with such a long time constant, this will not be an easy task.

What is quite clear is that $\tau_0(x = 0.018) \simeq 540$ s, is much larger than in the other samples. Clearly $\tau_0(x)$ is inversely correlated with x! Time constants as a function of temperature are shown in Figure 3.13 for the different stoichiometries studied. Toward the higher temperature limit of the data, the time constants (as with $\tau_0(x)$) are found to be *inversely* correlated with x. So at 150 mK, for example, the $x = 0.018$ sample is much slower than the $x = 0.045$ sample which is in turn slower than the $x = 0.08$ sample. When the temperature is lowered, to ~ 140 mK, the curves for 4.5% and 8.0% cross, as the time constant for the 8.0% sample begins to diverge. Presumably there would be a crossover for 1.8% and 4.5% as well, but it is not quite accessible in our measurements.

Above 200 mK or so, the dynamical scaling laws no longer seem to hold. Perhaps, in this regime, one is actually dominated by single ion physics rather than many body spin glass physics. Yet even in a temperature range where many body physics is not at play, the dynamics are very slow. Again, we ask the question, what could cause such a long time constant of relaxation? Furthermore, what is it that causes this inverse correlation of τ_0 with x?

Based on the above observations, a likely explanation involves largely single ion physics and the nuclear hyperfine coupling as suggested recently by Schechter and Stamp [155] and earlier by Atsarkin [169]. The nuclear hyperfine interaction splits the normally degenerate nuclear energy levels into 8 different energies that depend on whether the electronic moment is up or down, as is illustrated in Figure 3.14.

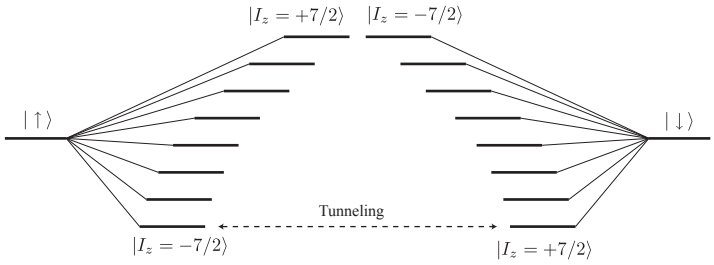

Figure 3.14: Adding the nuclear hyperfine interaction to the crystal field Hamiltonian has the effect of splitting the ground state doublet into 8 pairs of degenerate electronuclear states. Transverse field and transverse dipolar interactions relieve the degeneracy and allow for tunneling between these pairs.

The energy splitting between these levels is roughly 200 mK. Thus reducing the temperature appreciably below 200 mK depopulates all but the lowest energy electronuclear states leaving $|\uparrow, I_z = -7/2\rangle$ and $|\downarrow, I_z = +7/2\rangle$. The tunneling matrix element between the pairs of electronuclear states is 0 if one considers only the crystal field and nuclear hyperfine energies. This degeneracy will, in practice, be relieved by other perturbations, in particular by transverse magnetic field or transverse dipolar couplings. However, for the lowest energy levels, the degeneracy is not so easily lifted and remains small even for fairly large transverse fields [155]. With near-degeneracy of these energy levels comes a very slow transition rate between them, making it a very slow process to flip the electronic spins. Hence, the entire system is severely slowed down by this single-ion effect.

A possible scenario is that

$$\tau = \tau_{SI}(T) \times (1 + N_{SG}(T)) \tag{3.23}$$

where τ_{SI} is the time scale for flipping a single spin and N_{SG} is a dimensionless time constant, a number of spin flips required to get to a fraction $\exp(-1)$ away from equilibrium. If one imagines a Monte Carlo simulation on a spin glass, one would express the time constant as a dimensionless number, for example the number of metropolis algorithm trials required to reach equilibrium. The actual time the simulation took would depend on the processing time required of the computer to perform each spin flip times this dimensionless number. To get a physical time constant τ, one must take this single-ion spin flip time τ_{SI} and multiply by that dimensionless number N_{SG}. We could expect τ_{SI} to be somewhat Arrhenius-like, coming largely from thermal excitations, whereas N_{SG} should be a power

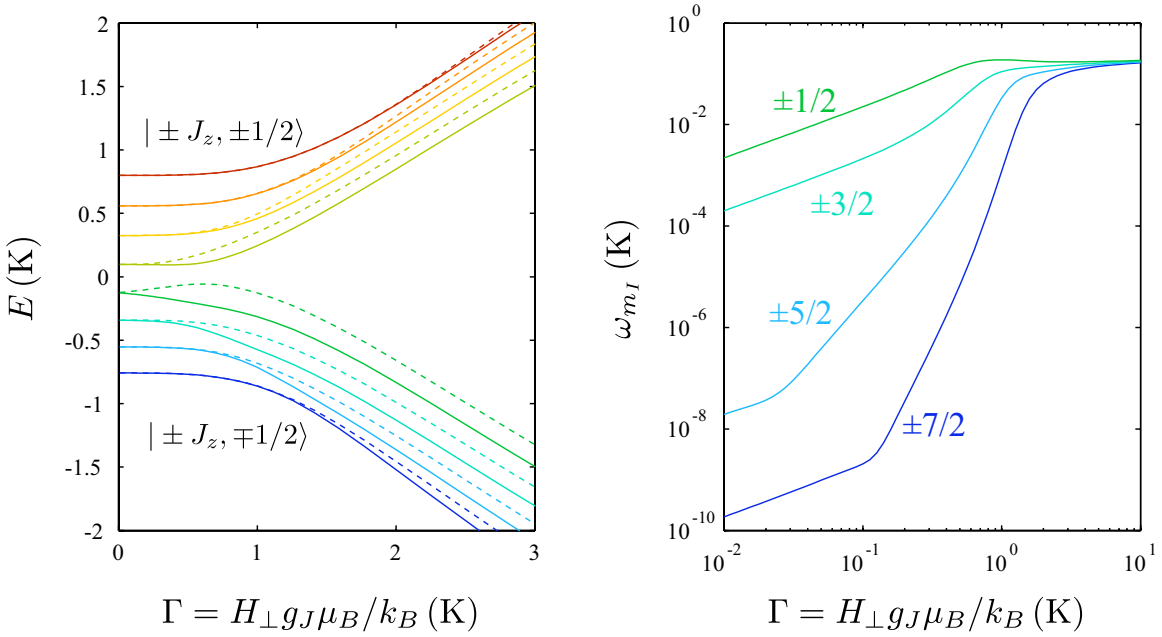

Figure 3.15: Following the work of Schechter *et al.* [155], calculations of the lower single-ion energy levels in transverse magnetic field $H_\perp$. (a) The lowest 16 energy levels in transverse field. Time reversed states are shown in the same colour, one solid and one dashed. (b) The energy splittings between the four lowest time reversed states, $m_I = \pm 7/2, \pm 5/2, \pm 3/2$ and $\pm 1/2$. The energy splitting for $m = \pm 7/2$ remains very small even out to relatively large transverse fields.

law divergence at the glass transition (the dynamical scaling fits we performed earlier). As we leave the range of critical behaviour, and N_{SG} gets very small, we cannot expect our dynamics to get infinitely fast. Rather, the single-ion relaxation time should take over at these higher temperatures.

We should expect two important things to be observed in the data from this proposed nuclear effect. (1) We should expect to see a large increase in τ_0 with lower dilution. Because T_g will be shifted down in temperature for lower x, the critical behaviour will kick in at lower temperatures where τ_{SI} will be longer, due to the depopulation of nuclear levels. (2) At higher temperatures, where critical behaviour is no longer observed, one should see a faster time constant in higher concentration samples. At higher x, the random transverse fields resulting from the transverse dipolar interaction terms will be stronger, leading to more significant tunneling matrix elements and therefore faster dynamics.

Indeed, this is exactly what we observe in the data, providing strong evidence that the hyperfine coupling is playing an important role in the dynamics. One could imagine other explanations for extremely slow dynamics, for example the idea of a cluster glass resulting from large ferromagnetic clusters resulting from proximity to the ferromagnetic phase. However, in this scenario it seems likely that larger x would have slower dynamics as it is closer to ferromagnetic and has on average stronger interactions.

Scaling and Shape of the Absorption Spectra

The slow dynamics in these materials make it prohibitively difficult to approach the glass transition. While this certainly makes these materials difficult to study, it in fact provides one important benefit. In all other spin glasses studied to date, the typical frequency window of an ac susceptibility experiment sits very close to T_g. As a result, the absorption spectra $\chi''(\omega)$ found are extremely broad and there is no way to discuss the shape of such spectra for example. However, in $LiHo_xY_{1-x}F_4$, that frequency window is far away from T_g making $\chi''(\omega)$ a manageable width (about 3.5 decades at most). This allows us to compare the widths at different temperatures and comment on the shape of the spectra

It is easy to see from Figure 3.10 that the width of the absorption spectra gets broader as the glass temperature T_g is approached. At higher temperatures, the absorption spectra approach a constant shape. We can speculate that the change in width of the spectra from the high temperature limit will be inversely proportional to the ratio T/T_g. Thus, we introduce a simple scaling law where we plot $\chi''/\chi''_{\text{Peak}}$ as a function of

$$(f/f_{\text{Peak}})^{1-T_g/T}$$

and we find that all the curves overlap on top of each other. There is some disagreement in the low and high frequency tails, though in the rest of the data the agreement is really

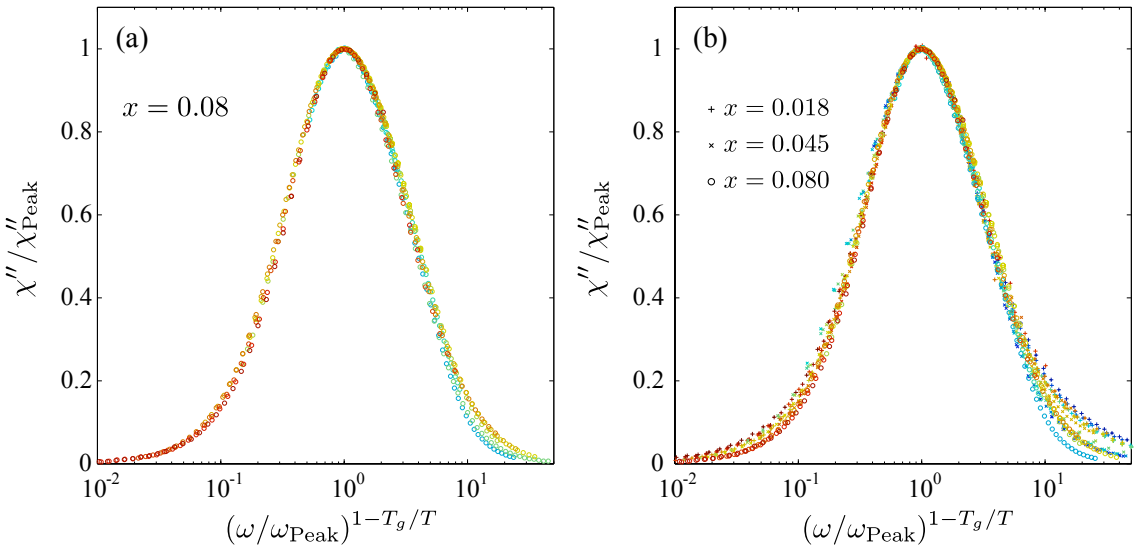

Figure 3.16: Universal scaling plots achieved by compressing the $\ln(f/f_{\mathrm{Max}})$ axis by an amount inversely proportional to the ratio T_g/T, or equivalently, raising f/f_{Max} to the exponent $1 - T_g/T$. This is shown for the 8% sample alone in (a) and for all three stoichiometries studied (b). For the 1.8% sample, $T_g = 30$ mK was used. There is some disagreement at the high and low frequency limits, but otherwise the scaling is quite successful.

quite good for the 4.5% and 8.0% samples. This scaling law is only successful with the 1.8% sample if we choose $T_g = 30$ mK, which is quite a bit lower than the results of the dynamical scaling best fit. However, a glass temperature of 30 mK is not obviously inconsistent with a dynamical scaling law (see Appendix B). Again, this highlights the difficulties of determining T_g when unable to measure at temperatures close to T_g. In the 4.5% and 8.0% samples, the overlap in such a scaling plot is optimized by choosing the same glass temperatures that were obtained in the dynamical scaling analysis (42 mK and 65 mK respectively), lending further evidence that those are the correct values of T_g.

Even more impressive is the fact that this simple scaling law applies to all three samples together. This is shown in Figure 3.16(b). To our knowledge, such a scaling law has not been previously proposed either theoretically or experimentally. Experimentally, this is not surprising, since other spin glasses do not have suitably slow dynamics necessary to undertake such a study, at least not with ac susceptibility.

Similarly, we plot the full-width and half-widths at half maximum in Figure 3.17 as a function of T_g/T (again taking $T_g = 30$ mK for the 1.8% sample) in the range of temperatures where it is possible to resolve enough of the spectrum. There is very little asymmetry seen from the comparing the width of the high frequency side $\log f_+/f_{\rm Max}$ with the width of the low frequency side $\log f_{\rm Max}/f_-$. There certainly is observable asymmetry in the spectra, but it seems to reside mostly in the tails of the spectrum.

We see that (Figure 3.18) in the high temperature limit of our data, the low frequency and high frequency tails tend to ω^1 and $\sim \omega^{-0.7}$ respectively. Thus there is already some noticeable asymmetry at higher temperatures. As the temperature is lowered, the spectra broaden and the power laws of these tails become less steep. The disagreement in the tails of the data shown in Figure 3.16 is a result of not properly accommodating this changing power law. Thus the scaling relation described above is unfortunately not quite perfect. The high frequency limit of the spectra becomes less steep as the temperature is lowered. At around 80 mK, for example, the power law appears to be roughly $f^{-0.65}$ (also shown in Figure 3.18).

As for the precise shape of the spectra, we have been so far unsuccessful in finding a satisfactory fitting form. A commonly employed method [58, 76, 170] for analyzing spectra of this variety is the Debye model

$$\chi(\omega) = \chi_0 \int_{-\infty}^{\infty} \frac{\rho(\tau) d\ln(\tau)}{1 - i\omega\tau} \tag{3.24}$$

If $\rho(\tau)$ is taken to be a δ-function, one has a single characteristic time constant. In general, this will result in too narrow a spectrum, especially in glassy systems. Thus a distribution $\rho(\tau)$ of relaxation times which broadens as the temperature is lowered can be employed. However, we have not been able to find a form of ρ that reliably fits the data.

Another fitting function that has been used in the case of structural glasses and spin ice [171], is the Davidson-Cole form [172, 173]:

$$\chi(\omega) = \frac{\chi_0}{(1 - i\omega\tau)^\beta} \tag{3.25}$$

This form is *almost* successful in fitting the highest temperature data with $\beta = 0.7$ (see Figure 3.18). However there is still a small discrepancy, which is not within the expected error bars of the measurement. The Davidson-Cole form can be generated from Equation 3.24 with an appropriate distribution of time scales:

$$\rho(\tau) = \begin{cases} \frac{\sin(\beta\pi)}{\pi} \left(\frac{\tau}{\tau_c - \tau}\right)^\beta & \tau < \tau_c \\ 0 & \tau \geq \tau_c \end{cases} \tag{3.26}$$

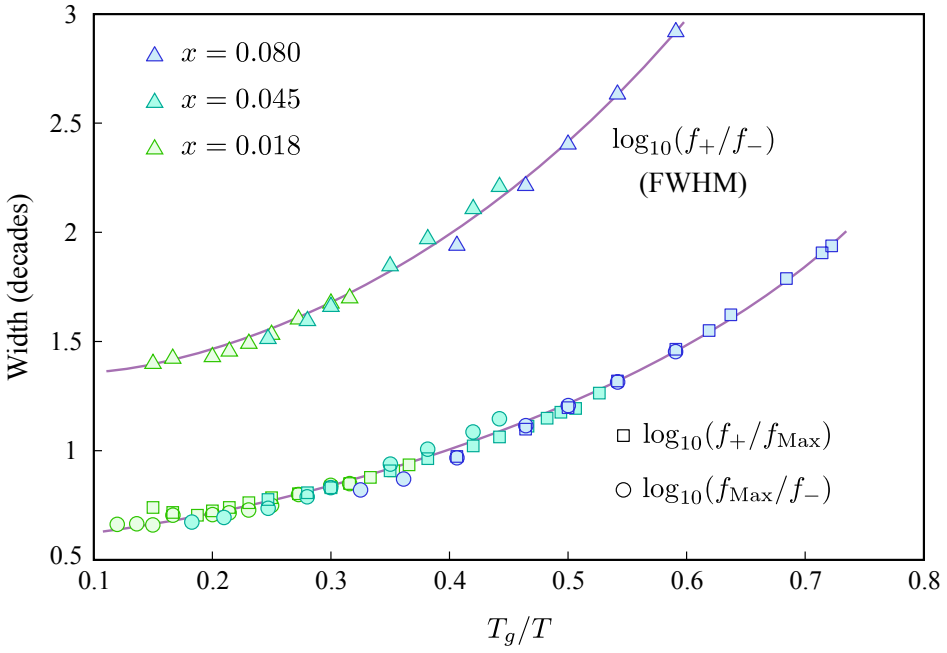

Figure 3.17: The full width at half maximum (FWHM) and half widths at half maximum of the absorption spectra (on a log scale) plotted against T_g for all three stoichiometries studied. The high frequency midpoint is f_+ and the low frequency midpoint is f_-. Triangles are the FWHM, whereas circles and squares are the widths of the low and high frequency sides of the spectrum, respectively. The solid lines are guides to the eye. Only a certain range of data could be accommodated because of the strong frequency dependence of χ''. Most of the asymmetry in the spectra is seen further out in the low and high frequency tails.

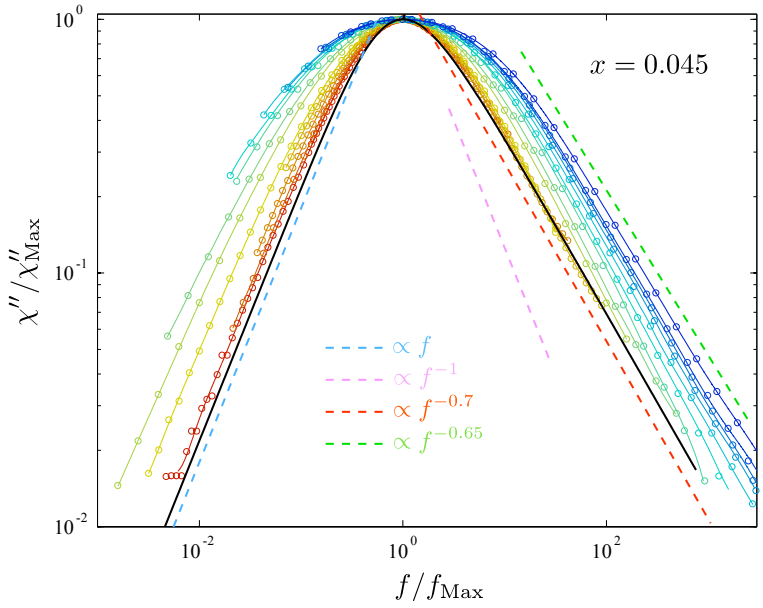

Figure 3.18: The superimposed absorption spectra of 4.5% sample shown on a log-log plot. The solid black curve is the Davidson-Cole form with $\beta = 0.7$, showing that it almost fits the high temperature limit of the data. The dashed lines are various power laws. The low frequency limit appears to be well fit by $\chi''(f) \propto f$ (blue). The high frequency tail varies from $f^{-0.7}$ (red) at high T to $f^{-0.65}$ (green) at low T. A $1/f$ power law (magenta) that would result from the Debye model with a single energy barrier to relaxation is far from fitting the data.

This distribution has a cut-off at τ_c and a long tail for short τ (high frequency). Thus even if the Davidson-Cole form is not a completely successful fit, we can at least see the importance of a long, high frequency tail in the distribution of relaxation times for this system.

3.5 Specific Heat of Dilute $\mathbf{LiHo_xY_{1-x}F_4}$

Much of our measurements of the specific heat of dilute $LiHo_xY_{1-x}F_4$ have been presented in an earlier thesis of the author [114]. Here we discuss those results on the concentrations $x = 0.018$, 0.045 and 0.080 and include a measurement of an additional stoichiometry $x = 0.120$. The low temperature specific heat is found to be dominated by a large nuclear

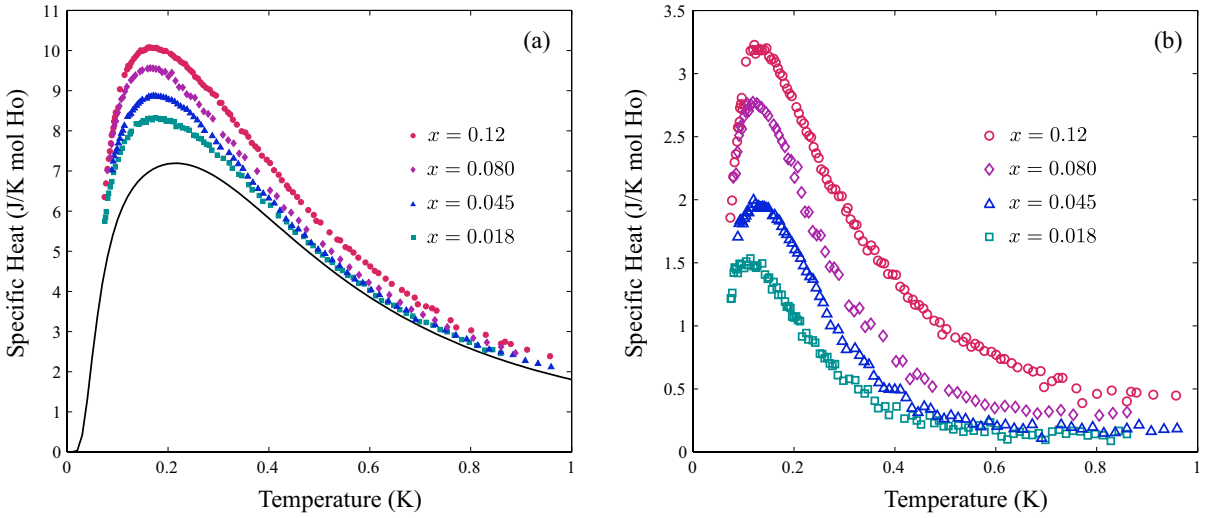

Figure 3.19: (a) The measured total specific heat of four different stoichiometries, $x = 0.018$, 0.045, 0.080 and 0.12, of $LiHo_xY_{1-x}F_4$. The solid line is the calculated single-ion specific heat. (b) The specific heat of those same four stoichiometries after subtraction of the single-ion specific heat.

component, resulting from the strong hyperfine coupling with the $I = 7/2$ Ho nuclear moments.

This specific heat is given roughly as

$$C_{\text{Nuclear}}/R = \left(\frac{\sum_m x_m e^{-x_m}}{\sum_m e^{-x_m}}\right)^2 - \frac{\sum_m x_m^2 e^{-x_m}}{\sum_m e^{-x_m}} \tag{3.27}$$

where

$$x_m = (A\langle J^z\rangle m_I + P m_I^2)/k_B T. \tag{3.28}$$

However, this makes the assumption that the moments are entirely Ising-like and includes no excited state at 10 K. A more accurate single-ion specific heat, C_{SI} can be calculated by diagonalizing the entire single-ion Hamiltonian including crystal field and hyperfine energies, a 136×136 matrix [123]. That calculation is shown as the solid line in Figure 3.19(a).

The measured specific heats are all broad features, slightly above this single ion specific heat, with their peaks at roughly the same position. To more carefully analyze these results, we have subtracted the underlying nuclear component of the specific heat. This

subtraction is justified to first order. If the moments are completely Ising, there is a symmetry between $|J_z, -I_z\rangle$ and $|-J_z, +I_z\rangle$ states which means that the nuclear specific heat can be separated from the electronic specific heat. However, if there is any admixing with the the next excited state at 10 K (which there is in small amounts), this symmetry no longer holds and the subtraction is not exact. We have performed this subtraction under the assumption that it is largely accurate and for better comparison with previous work from other groups in which such a subtraction was also assumed to be justified.

The results of the subtraction are shown in Figure 3.19(b) and show similar, broad features for all the stoichiometries studied. Broad features are consistent with spin glass behaviour, as the predicted specific heat critical exponent α is quite negative, in the range of -2 to -4 and would not present as a sharp feature. What is unusual about the specific heat is the lack of change of peak position with concentration. Typically in spin glass systems, the peak position of the specific heat scales linearly with T_g [44]. Here, the peaks all lie roughly on top of each other, where $T_g(x)$ is certainly not flat as seen in susceptibility measurements. For example, in Monte Carlo simulations, the peak in C is found to roughly scale with x [161].

Although the peak position is independent of x, the overall size of the "bump" in C is larger as x is increased. At higher temperatures it is easy to see that the specific heats should not line up on top of each other, even when normalized by the number of holmium atoms studied. The specific heat at high temperature should scale as E^2/T^2 and one would expect the energy scale of interactions E to be proportional to x. Thus we should expect the normalized specific heat (in units of $\mathrm{J/K\,mol\,Ho}$) to scale as x^2. This is roughly what is observed.

The entropy of a system can be obtained by doing a numerical integral of the specific heat:

$$S(T) = \int_0^T \frac{C(T')}{T'} dT' \tag{3.29}$$

At temperatures well above the Curie-Weiss temperature $\sim xT_c(x = 1)$ but still below 10 K, it is certain that the electronic moments will possess an entropy of $R \ln 2$. One would generally expect all of that $R \ln 2$ entropy to be released by zero temperature, although in some situations, namely spin ice [94], one sees a residual entropy S_0 at zero temperature. Such a numerical integral has been performed on our specific heat data (after subtraction of the nuclear component) and is shown in Figure 3.20. The results of the integral have been shifted so that they approach the necessary high temperature limit for an Ising system $R \ln 2$.

In order to fully capture the entropy in the material, one must do the integral from zero temperature, or at least from a temperature at which much of the specific heat has

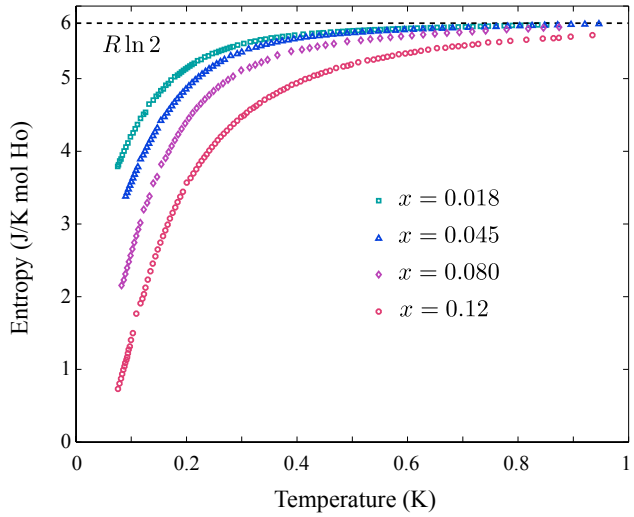

Figure 3.20: The entropy as a function of temperature, $S(T)$, of four samples of $LiHo_xY_{1-x}F_4$, obtained by performing a numerical integral of C/T from the lowest temperatures studied to T. The result is then shifted such that it tends towards the necessary $R \ln 2$ at the higher temperatures. Thus we can see the remaining entropy that has not been picked up in the range of our experiments. This quantity varies significantly from the 1.8% sample up to the 12% sample.

dropped away. Since our specific heat results extend down to 80 mK and much of the curve remains unexplored below that temperature, we cannot reliably determine the total entropy associated with the electronic moments. In the Ref. [123], we dealt with this problem by making a linear extrapolation to $T = 0$, based on the fact that spin glasses frequently show linear temperature dependence below T_g. With this extrapolation, we saw that there was an increasing residual entropy S_0 as the concentration x was lowered. At $x = 0.08$, the linear extrapolation gave $S_0 = 0$. This was connected to the simulations of Snider and Yu [160] where a lack of spin glass transition was seen in dipolar Ising moments in conjunction with a residual entropy.

Since then, it has come to light that these materials likely have spin glass transition temperatures *below* the lowest temperature that we have measured with specific heat. This makes it highly unlikely that we have observed all of the physics that there is to observe with our heat capacity measurements and that more is expected to happen at lower temperatures. Our recent measurements of a 12% sample (see Figure 3.19) shows an even larger specific heat than that of the 8% sample implying that the linear extrapolation cannot hold or there would be more than $R \ln 2$ entropy in the 12% sample, a physical impossibility. Finally, specific heat measurements may at some point succumb to the same problems of achieving equilibrium as susceptibility measurements. Although we have always done these experiments with very long time constants of relaxation, > 1 hour, as one approaches T_g the time constants diverge, so there will always be a point at which measurements may be out of equilibrium. It is seen in the susceptibility measurements that the intrinsic time constant in these materials is extremely long and that even by $T = 1.5T_g$, it becomes nearly impossible to obtain equilibrium measurements.

Our specific heat data is puzzling for two reasons. First, the peak in the specific heat is at a temperature much higher than the spin glass transition, where in most spin glass systems it is within 20% of T_g [25]. Second, the peak position is essentially concentration independent, where T_g is not independent of x. It has been proposed by Schechter *et al.* [155], that such a result is suggestive of the importance of single ion physics and the connection between the nuclear and electronic moments.

Past research on spin glasses has shown the specific heat to not be dominated by a feature at the spin glass transition [25]. The free energy landscape of a spin glass is very complex with many local maxima and minima and eventually, at low enough temperatures the system tends to get "stuck" in one of the valleys, eventually losing ergodicity altogether. The specific heat as one gets near to the transition is thus largely representative of the excitation spectrum of the material. In most spin glasses, it is reasonable to postulate that the height of energy barriers ΔE would scale proportionally to x. This would give rise to a heat capacity with a peak position that also scales roughly as x. However, in $LiHo_xY_{1-x}F_4$ at low temperatures, directly flipping a spin simultaneously with a nuclear moment is an

incredibly slow process. To flip a spin quickly, it must be excited into a higher energy nuclear spin state first. So, even if ΔE is very small, the specific heat maximum may be pinned to a temperature related to the nuclear hyperfine interaction. As x is increased, ΔE should eventually surpass the nuclear energy and at that point one would expect ΔE to be the dominant barrier to excitations and the peak in C might begin shifting to higher temperatures. However, the above argument is essentially a dynamic one and should depend on measurements being performed out of equilibrium. In our experiments, we see no evidence of such a loss of equilibrium. This is particularly true as high as 150 mK, where the dynamics are still quite fast compared to the time scales of our measurement. Below 70 mK or so, where the time constant is close to 1 hour or longer, a loss of equilibrium might occur.

Alternatively, we could speculate that the subtraction of the nuclear contribution might be incorrect. For the subtraction to be valid, the moments must be true Ising moments. Any transverse, off-diagonal contributions to the Hamiltonian break the degeneracy between the $|\uparrow, m_I\rangle$ and $|\downarrow, -m_I\rangle$ states, meaning that the nuclear specific heat is connected to the electronic states. There are such off-diagonal contributions to the Hamiltonian coming from the transverse dipole-dipole interaction and the transverse nuclear hyperfine interaction [155]. If the collective behaviour of the electronic moments in the system is somehow very sensitive to those off-diagonal components, then it could be difficult to differentiate between the nuclear and electronic contributions to the specific heat. Essentially, the system would consist of electronuclear objects interacting with one another rather than a set of interacting electronic spins, with an irrelevant nuclear moment following. It is important to note that these ideas are speculative. Our specific heat results remain poorly understood and a quantitative explanation is yet to be provided.

3.6 Comparison with Other Research Groups

Monte Carlo Simulations and Theory

For the most part, our results agree very well with the current theoretical understanding of $LiHo_xY_{1-x}F_4$. The temperature dependence of our susceptibility agrees well with Monte Carlo results [161]. Our glass transition temperatures $T_g(x)$ line up well with those determined in Monte Carlo [128] as can be seen from Figure 3.23. Furthermore, the notion of dynamics slowing with smaller x, related to the nuclear hyperfine coupling, matches the prediction of Schechter and Stamp [155].

One unresolved problem is the mismatch between Monte Carlo [161] and our specific heat experiments, as shown in Figure 3.22(a). While all theories developed so far suggest

that the peak in $C(T)$ should scale with x, our measurements show a concentration independent maximum at around 150 mK. We propose that this effect is somehow related to the importance of single-ion properties and the nuclear hyperfine interaction to the physics at large of this system. However, that conjecture remains to be proven and the behaviour of the specific heat of $LiHo_xY_{1-x}F_4$ remains a mystery.

Experimental Susceptibility and Specific Heat

Clearly, our results show no evidence of the exotic "antiglass" state that was proposed by Ghosh *et al.* [4, 5] and Reich *et al.* [158, 58]. This is indeed a major disagreement and it is important to at least suggest possible reasons for this discrepancy. Thus, we shall now analyze in further detail the differences between our data.

In fact, many of our results are quite consistent with the research performed by Reich *et al.* [158, 58]. Our $\tau_{\mathrm{Max}}(T)$ dependence for the 4.5% Ho sample is very similar to theirs (as shown in Figure 3.11). The $\chi_{DC}(T)$ behaviour presented in Ref. [58] is also fairly close to the dc limit of our data, shown in Figure 3.8. Both could be very roughly approximated by a similar power law around $T^{-1.2}$ as seen in Figure 3.8. There is some discrepancy at higher temperatures, but this may be related to an offset or phase shift for example, since the signal is much smaller in that range.

Our main disagreements with the susceptibility measurements of Reich *et al.* is their observation that the absorption spectrum narrows as T is decreased. Our results extend to lower temperatures and show clearly that it does not narrow. If we plot our data directly with that of Reich *et al.* [58], we see that our spectra agree remarkably well with theirs at 120 and 150 mK, the lowest temperatures at which Reich *et al.* measured $\chi(\omega)$ (see Figure 3.21(b)). Below those temperatures, our spectra broaden considerably. Surprisingly, it is at higher temperatures that our results differ: Reich *et al.* see their spectra start to broaden where we see the width remain roughly constant. It seems that, for the most part, the initial idea of the "antiglass" state came from an interpretation of data that was not extended to low enough temperatures (frequencies).

Our specific heat is also at odds with that of Reich *et al.* [58]. They find a fairly sharp peak at ~ 300 mK and later [5] lower temperature data is published that reveals another peak at roughly 100 mK. Our measurements, on the other hand, find one broad peak with a maximum at around 150 mK. We reproduce most of the expected entropy, whereas their specific heat accounts for only about 15% of $R \ln 2$. Our electronic specific heat approaches the noninteracting specific heat roughly as $1/T^2$ at temperatures close to 1 K, where very little in the way of collective behaviour should be expected. The electronic specific heat of Reich *et al.* continues to *rise* just above 1 K, without any clear cause. Furthermore, after measuring four different stoichiometries, we find a consistent trend with none of the

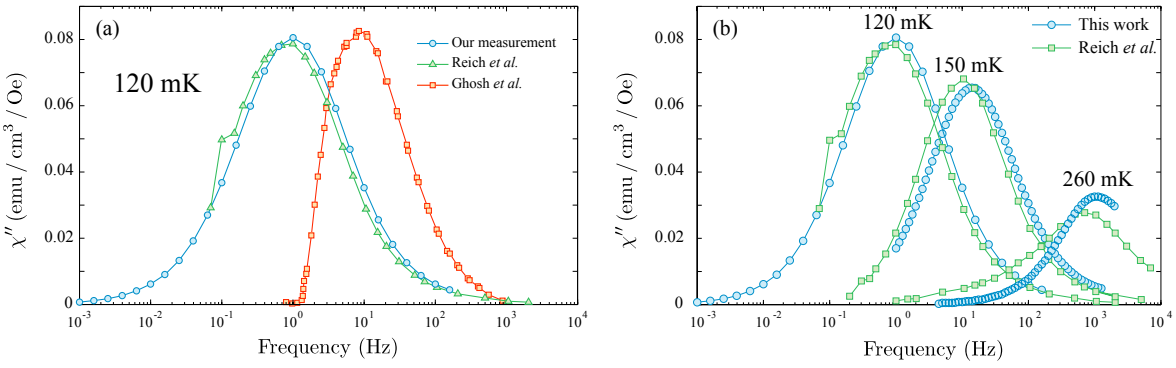

Figure 3.21: (a) Direct comparison of $\chi''(\omega)$ at 120 mK from our work (blue circles), Reich *et al.* [58] (green triangles) and Ghosh *et al.* [4] (red squares). Our agreement with Reich *et al.* is quite good in fact. Ghosh *et al.* disagree completely, however, not matching our results or results from their own research group [58]. (b) Comparison of our work with Reich *et al.* [58] at three different temperatures. Surprisingly, it is at the higher temperatures where disagreement is seen.

samples exhibiting anything close to what Reich *et al.* find. Note that thermal conductivity experiments also did not find any sharp features reminiscent of antiglass physics [174].

Disagreement with more recent results [4, 5] by that same research group is even more disconcerting however. The same research group has discovered rather more exotic physics in recent years that is inconsistent with their earlier work. The behaviour of $\tau_{\mathrm{Max}}(T)$ is very different, as shown in Figure 3.11(a), with much higher frequencies for a given temperature [4] and the temperature dependence of the dc limit of χ is very different: Ghosh *et al.* claim a $\chi_{dc} \sim T^{-0.75}$ power law [5] where Reich *et al.* have temperature dependence closer to $T^{-1.2}$ [58]. In Figure 3.21(a), we can see clearly that the spectrum of Ref. [4] is centred at much higher frequencies than in previous work, and also exhibits a very strong asymmetry that was not there in previous work.

We can say with certainty that we see no evidence of any "antiglass" physics. There is no narrowing or pronounced assymetry of the absorption spectrum. There is no $T^{-0.75}$ power law. Most importantly there is no dynamic ground state dominated by quantum entanglement. Instead we provide strong evidence of spin glass behaviour.

Many of the discrepancies between Ghosh *et al.* and our work, may possibly be explained by heating. Ghosh *et al.* show results that have higher frequencies at a given temperature than what we see, which can easily be explained by poorly heat sinking the

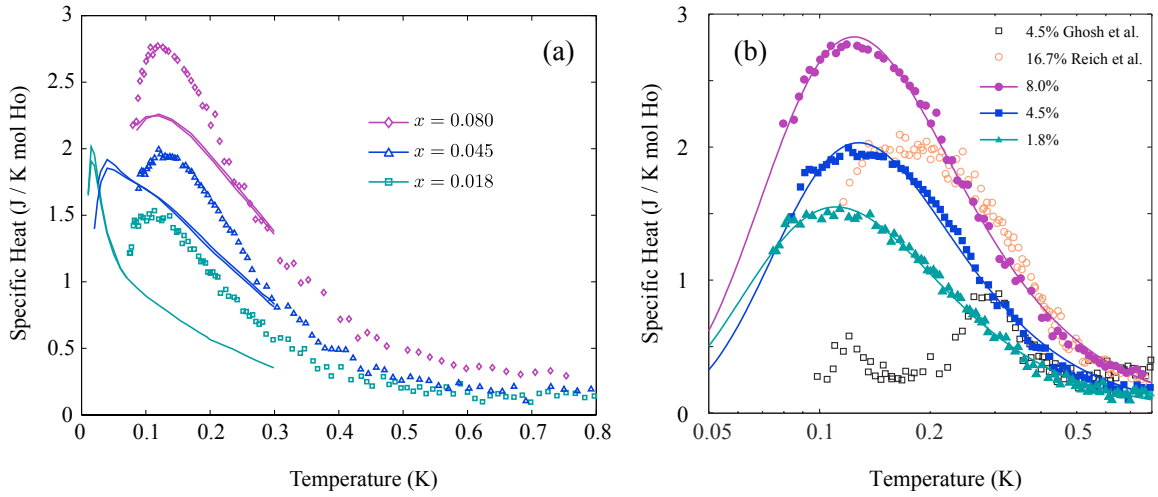

Figure 3.22: Specific heat of $LiHo_xY_{1-x}F_4$ measured by our research group [114, 123] on $x = 0.018$, 0.045 and 0.080 compared with (a) Monte Carlo simulations at the same value of x performed by Biltmo and Henelius [161] (lines) and (b) with the specific heat of an $x = 0.167$ sample measured by Reich *et al.* [58] and an $x = 0.045$ sample as published by Ghosh *et al.* [5]. There is very little agreement between any of our results and the 'antiglass' physics of Ghosh *et al.*. Monte Carlo simulations show a peak that scales roughly with the concentration x, where the peak position in our data is largely concentration independent.

sample, applying overly large excitations or not waiting sufficiently long to attain equilibrium. The pronounced asymmetry seen in their data, however, is not so easily explained. Although heating from an ac magnetic field should be proportional to χ'' and therefore will not be the same for all frequencies, it is not clear that this is a strong enough effect to create such an asymmetry in the data. Increasing the power as the frequency is lowered, to compensate for loss of signal in their conventional susceptometer, could certainly result in increased heating at low frequencies, causing χ'' to drop and making the spectrum appear asymmetric. Unfortunately, without more information, we can only speculate as to the explanation for the unusual results of Ghosh *et al.* [4, 5].

Most recently, Jonsson *et al.* also measured the susceptibility of a 4.5% Ho (and 16.7% Ho) sample. Instead of a sinusoidal probe field, they ramp the magnetic field linearly and track the magnetization with a SQUID magnetometer. Fitting $M(H)$ over a certain range of field ΔH allows them to extract χ and χ_3. This different method of taking data makes

it difficult to directly compare our results to theirs. As with our measurements, below a certain temperature, they are no longer taking equilibrium data. One can roughly approximate the effective frequency of their measurement by $f \sim (dH/dt)\Delta H$. From the range of parameters quoted in their article, this leads to frequencies of at least 40 mHz. While seemingly a very low frequency, it can be seen from Figure 3.8, that their measurement does eventually suffer from slow relaxation. Because ramping the field linearly should be equivalent to applying a range of frequencies, their susceptibility does not drop out at low T in precisely the same way that ours does. In the range of data where both of our sets of data can be considered to be in the dc limit, our data sets agree very well in fact, with only a slight, overall mismatch in susceptibility. Thus any disagreement between Jonsson *et al.* and our work [124], is related to the interpretation of experimental results, rather than mismatch of those experiments.

Implications of Slow Dynamics

While there is a large set of experimental signatures of spin glass behaviour, the ultimate proof of a spin glass transition is generally considered to be a divergence of the nonlinear susceptibility, χ_3. The question of whether χ_3 diverges at a finite T_g or not in a 16.7% sample of $LiHo_xY_{1-x}F_4$ has become the subject of much debate in recent publications [65, 125, 126]. While a peak at finite temperature is observed in $\chi_3(T)$, it has been argued by Jonsson *et al.* [65], that this peak is not representative of true spin glass behaviour. Certainly the data do not show a divergence. However, there is a very strong reason why the peak should be rounded, and that is to do with dynamics. There is no reason to believe that the nonlinear susceptibility should not respond to an increase in the frequency of measurement in a similar way to the linear susceptibility χ. In other words, one should expect that χ_3 should be a complex and frequency dependent quantity or $\chi_3' - i\chi_3''$.

Let us assume for the moment that χ_3 will have a similar frequency dependence to χ. In the regime where $f < 2\pi/\tau_{\rm Max}$, one would expect χ_3 to be saturated and frequency independent. Then in that regime, we would expect the scaling relation

$$\chi_3 \sim (T/T_g - 1)^{-\gamma} = t^{-\gamma} \tag{3.30}$$

However, when $f > 2\pi/\tau_{\rm Max}$, at constant temperature, the susceptibility scales roughly as $(f\tau_{\rm Max})^{-\lambda}$ where this new exponent λ falls in the range of 0.75 at low temperatures to 1 at higher temperatures. Thus in that range, we should expect the temperature dependence to be

$$\chi_3 \sim t^{-\gamma}(f\tau_{\rm Max})^{-\lambda} \sim f^{-\lambda}t^{-\gamma+\lambda z\nu} \tag{3.31}$$

Since $z\nu \simeq 8$ and $\gamma \simeq 3$ we should expect a crossover from the behaviour

$$\chi_3 \sim t^{-3} \tag{3.32}$$

at high temperatures to the rough behaviour

$$\chi_3 \sim t^5 \tag{3.33}$$

at low temperatures. The temperature at which this crossover takes place is when $f \simeq 1/2\pi\tau_{\mathrm{Max}}$. For most spin glasses, where $\tau_0 \simeq 10^{-7}$ s, this crossover will take place very close to the actual glass temperature T_g for typical frequencies of measurement (for example on the order of 1.5 Hz [125]). However, in the $LiHo_xY_{1-x}F_4$ system, as our measurements have shown, τ_0 is much longer and this crossover ought to take place much further from the glass temperature. With a measurement frequency of 1.5 Hz, in the 4.5% sample, the crossover should happen at $\sim$ 120 mK, almost three times the glass temperature! The 16.7% sample should be faster than the 4.5% sample, making this error somewhat less severe, but this idea should, in principal, explain the lack of a truly sharp peak or divergence in the nonlinear susceptibility.

This is precisely the reason why we have not yet worked towards measurements of χ_3 on the samples studied in this work. It is our opinion that the priority in studying these materials must be to understand the dynamics. As seen from the work of Jonsson *et al.* [65], interpretation of χ_3 measurements is very difficult without a complete understanding of the relevant time scales in this system, and in particular, without the realization that τ_0 is exceptionally long in these materials as compared to the canonical spin glasses.

μSR Experiments

It is important to mention recent μSR experiments which were performed by Rodriguez *et al.* [175, 176] on pieces of the same single crystals that were used for our work on $LiHo_xY_{1-x}F_4$. Surprisingly, the μSR experiments do not find typical spin glass physics in this system. The experiments were performed in the longitudinal field configuration, but note that this meant aligning the field parallel to the μ^+ polarization and *perpendicular* to the Ising axis of the Ho^{3+} moments.

These measurements discover that the relaxation rate λ increases below 20 K as the fluctuation rate slows down suitably, and λ continues to increase monotonically down to around 100 mK. A noticeable change in the relaxation rate around 200 mK, particularly in a 25% Ho sample, is attributed to the nuclear hyperfine interaction. They fit a stretched exponential with exponent β to their relaxation data and conclude that β does not drop below $\sim$ 0.8 where it would be expected to drop to $\sim 1/3$ in a spin glass. Furthermore, below 100 mK, where T_g is anticipated, there is very little change in the spectra. Determining the spin fluctuation rate ν based on a dynamical Kubo-Toyabe model, shows temperature independent fluctuations below $\sim$ 100 mK, also not consistent with spin glass physics.

One commonality between our measurements and those of Rodriguez *et al.* is the observation of slowing dynamics as the concentration x is decreased, again possibly highlighting the importance of random transverse fields. Otherwise, there is quite a surprising disagreement between the natural interpretations of the μSR data [176] and our ac susceptibility data. It is difficult to reconcile the clear observation of dynamics as slow as 1 mHz at ~ 80 mK observed in our experiments with fluctuation rates of 1 MHz or more seen in μSR. One of the main differences between our configurations is the application of magnetic field transverse to the Ising axis or lack thereof. The magnetic fields applied by Rodriguez *et al.* are all under 0.2 T, while the critical field, above which spin glass-like physics is lost in an $x = 0.167$ sample is $H_C \simeq 1.2$ T [66] and H_C might be expected to be similar or even higher as the concentration is reduced [155]. The question becomes: is a field of 0.2 T large enough to significantly alter the dynamics of the system? Certainly we should expect some acceleration of the dynamics in any transverse field. This question could be answered more quantitatively in future work with the application of a transverse field to our susceptibility measurements.

3.7 Conclusions

There are several conclusions that we would have the reader draw from the work presented in this chapter. First, it should be clear that at low concentrations x in the series $LiHo_xY_{1-x}F_4$, there is no exotic antiglass state as was proposed by Reich *et al.* [158, 58] and Ghosh *et al.* [4, 5]. None of our experiments have shown the slightest hint of antiglass physics. This is true of other experimental groups, who have found results that do not change qualitatively between the higher concentration spin glass regime and the supposed antiglass stoichiometry at 4.5% Ho [65, 176]. Theoretical work also shows that in an ideal dipolar Ising model, all that should result is a spin glass [128] and that quantum effects from random fields and the hyperfine interaction, are not sufficient to preclude such a spin glass [155].

The source of disagreement between our results and those of Ghosh *et al.* [4, 5], in particular, is not clear at this time. While sample quality has been considered as a possible explanation, the fact that Refs. [158, 58] and Refs. [4, 5], from the same research group on the same sample [159], are very inconsistent with each other points to an issue of experimental error.

Instead of an exotic "antiglass", we have shown that the physics of the $x = 0.018$, 0.045 and 0.080 samples is consistent with that of spin glasses. Our dynamical scaling analyses have provided a fair degree of evidence that there is a finite temperature spin glass transition in each of these samples (though T_g in the $x = 0.018$ sample is very

difficult to determine accurately). The spin glass transition temperatures that we have obtained match well with theory [128] and allow for a more complete picture of the phase diagram of $LiHo_xY_{1-x}F_4$ as is shown in Figure 3.23 and Table 3.2.

Despite the discovery of spin glass behaviour in these materials that was predicted to exist almost 30 years ago [29], this system has still managed to surprise us with some new and interesting physics. Unlike the canonical spin glasses, this system is found to be immensely slow. While this may simply be a property of Ising moments at very low temperatures, there is an interesting correlation between the intrinsic time scale τ_0 and the concentration x, with the low concentration materials slowing down immensely. We have proposed that this is a direct consequence of the nuclear hyperfine interaction and random fields generated by the off-diagonal part of the dipolar interaction, as suggested by Atsarkin [169] and by Schechter and Stamp [155].

This very slow behaviour makes for challenging measurements. Surprisingly it also brings an advantage in that the frequency window of our measurements corresponds to temperatures relatively far from T_g. This leads to relatively narrow absorption spectra and therefore allows us to resolve more information about the spectra than has been resolved in most spin glass systems. In other words, we can say a great deal more about the spectra than simply that they have a broad frequency dependence. This is highlighted by the very interesting, though not quite complete, scaling law shown in Figure 3.16. Certainly there is room for much conceptual work on understanding these spectra and the quantitative effects of the nuclear hyperfine interaction and random transverse fields. Additionally, the specific heat and its concentration independent maximum, remains a mystery that may also be solved through a better understanding of how single-ion physics affects this material.

Finally, we note that the results of this work may provide a valuable lesson. In some materials, it can be very important to take into account slow relaxation and not to fall into the trap of thinking that a measurement that seems slow on usual human time scales of seconds or minutes, is always sufficiently slow to be considered an equilibrium measurement in the dc limit. The uniquely slow dynamics in $LiHo_xY_{1-x}F_4$ make it incredibly difficult to achieve a successful nonlinear susceptibility measurement [65, 125, 126], for example. Just as theorists must worry about finite size scaling, experimentalists working in this area of research must worry about and take into account dynamical scaling.

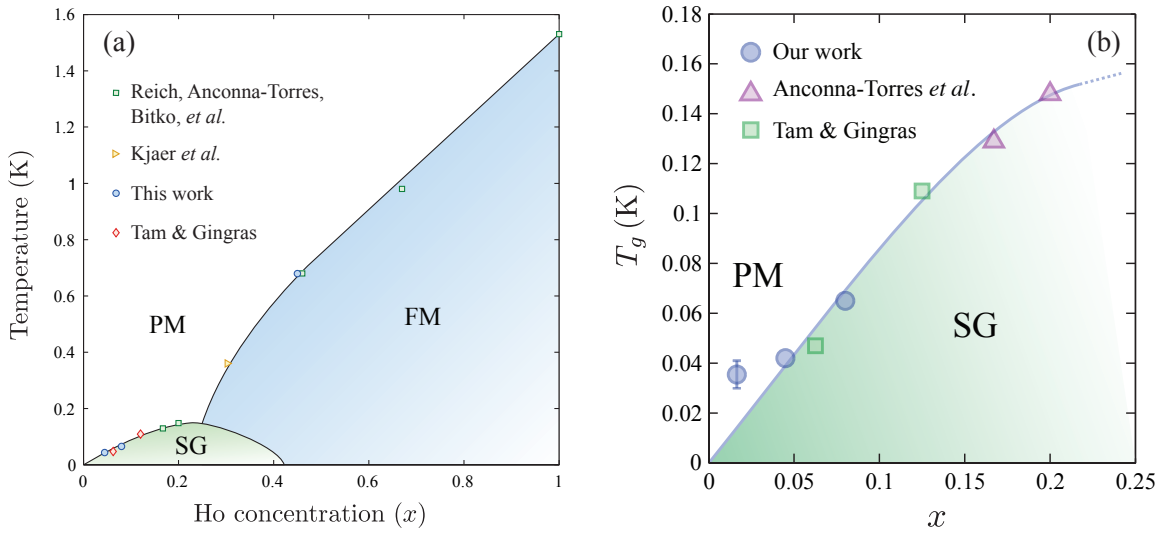

Figure 3.23: (a) The full x-T phase diagram of $LiHo_xY_{1-x}F_4$ as it is currently understood. Note however that the region of the phase diagram showing reentrance is only speculation and has not been studied at this point. (b) A zoomed-in view of the spin glass region of the phase diagram. Ferromagnetic data points are from Refs. [121, 58, 114, 177]. Spin glass transition points are taken from Refs. [125, 128] and this work. The 1.8% sample is included with an error bar reflecting the large uncertainty in T_g. For a detailed list of transition temperatures and corresponding references see Table 3.2. The solid lines are guides to the eye and are not fits based on a theoretical model. The region of reentrance from FM to SG, at $0.25 < x < 0.4$, is merely hypothesized [58], based on the behaviour of many other spin glass systems, and has not been demonstrated to exist in this particular series of materials.

Concentration	Transition Temperature	Reference
$x = 0.045$	$T_g = 42$ mK	This work, [124]
$x = 0.0625$	$T_g = 47$ mK	Tam and Gingras [128]
$x = 0.080$	$T_g = 65$ mK	This work
$x = 0.125$	$T_g = 109$ mK	Tam and Gingras [128]
$x = 0.167$	$T_g = 129$ mK	Anconna-Torres *et al.* [125]
$x = 0.20$	$T_g = 148$ mK	Anconna-Torres *et al.* [125]
$x = 0.30$	$T_c = 360$ mK	Kjaer *et al.* [177]
$x = 0.45$	$T_c = 680$ mK	Quilliam *et al.* [114]
$x = 0.44$	$T_c = 680$ mK	Reich *et al.* [58]
$x = 0.67$	$T_c = 980$ mK	Reich *et al.* [58]
$x = 1$	$T_c = 1.53$ K	Bitko *et al.* [121]

Table 3.2: Summary of transition temperatures for $LiHo_xY_{1-x}F_4$ as determined experimentally in this work and elsewhere [124, 125, 177, 114, 58, 121] and with Monte Carlo simulations [128].

Chapter 4

Gapped Spin Waves in $Gd_2Sn_2O_7$

In this chapter, we will discuss measurements of the specific heat of the geometrically frustrated material $Gd_2Sn_2O_7$, published in Ref. [178]. While from most points of view, this material appears to be the quintessential isotropic, dipolar, pyrochlore antiferromagnet, with the theoretically expected ground state ordering, the observation of spin dynamics persisting to the lowest temperatures studied makes for a puzzling situation. Here we show specific heat results that, when compared with linear spin wave calculations, paint a picture of a very conventional low temperature behaviour consisting of gapped magnon excitations that are at odds with the idea of a persistently dynamic ground state.

4.1 Persistent Spin Dynamics in Rare Earth Magnetic Pyrochlores

In the insulating, magnetic pyrochlores, $R_2M_2O_7$, the rare earth ions (R^{3+}) occupy a lattice of corner sharing tetrahedra. This geometric configuration results in strong frustration in some instances, for example in the case of antiferromagnetic nearest-neighbour exchange between Heisenberg spins [179, 88] and in the case of ferromagnetically coupled Ising moments with the easy-axis along the local [111] direction (in or out of the tetrahedra) [95]. As a result of this geometric frustration, a wide variety of magnetic behaviours, some very interesting and unusual, are observed in rare earth pyrochlores, ranging from long range ordered antiferromagnets to randomly frozen spin glass states to several varieties of cooperative paramagnet [91].

The cooperative paramagnets are perhaps the most exciting and exotic states observed. The ferromagnetically coupled [111] Ising systems tend to form what is known as spin ice [95]. Such a state consists of two spins in and two spins out on each tetrahedron,

but this is far from a unique configuration, exhibiting a macroscopic degeneracy of states. The system is therefore unable to find long range order (LRO) and remains a cooperative paramagnet. The name 'spin ice' is derived from a direct analogy to the hydrogen bonds in water ice. Specific materials that exhibit spin ice physics are $Dy_2Ti_2O_7$ [94], $Ho_2Ti_2O_7$ [95] and $Ho_2Sn_2O_7$ [180] as well as the more recently discovered $Pr_2Sn_2O_7$, a possible dynamic spin ice [181].

The material $Tb_2Ti_2O_7$, meanwhile, avoids ordering down to the lowest temperatures studied, maintaining a dynamic spin liquid state [108]. $Yb_2Ti_2O_7$, while exhibiting a sharp, first-order transition at $\sim$ 250 mK, does not show any signs of a conventionally ordered state at low temperatures [109], suggesting that it too possesses a spin liquid ground state or at least some kind of "hidden order". This material will be discussed in more depth in Appendix E.

Surprisingly, several stoichiometric magnetic pyrochlore oxides have shown a tendency to develop a spin glass state. Such materials include $Y_2Mo_2O_7$ [103] and $Tb_2Mo_2O_7$ [182], which were originally thought to be largely free of quenched randomness. It has since been realized that these materials do possess a certain level of disorder (on the order of 5%) in the bond lengths between magnetic ions. While this is a small level of disorder relative to what is required for many other spin glasses [47, 85], it has become understood that geometrically frustrated materials can be very sensitive to quenched randomness and the formation of a spin glass state [100, 101].

There is also a set of rare earth pyrochlores that show much more conventional behaviour, that is a transition to long range antiferromagnetic order. Materials in this class include $Gd_2Ti_2O_7$ [183, 184], $Gd_2Sn_2O_7$ [6, 185] and $Er_2Ti_2O_7$ [186]. Typically these materials have a critical temperature T_C that is depressed relative to their Curie-Weiss temperature θ_{CW}, by the effects of geometric frustration. The level of frustration is often parametrized by the frustration index $f = \theta_{CW}/T_C$.

A common trend that has been observed in essentially all of these systems, is an apparent persistence of spin dynamics down to the lowest temperatures [187, 188, 189, 190, 109, 183, 191, 192, 193]. Low temperature fluctuations in these sytems were discovered by three experimental techniques that are often used to differentiate between static and dynamic spins: muon spin relaxation/resonance (μSR), Mössbauer spectroscopy and neutron spin echo (NSE) experiments. Together, these measurements are able to cover a range of time scales from more than a THz down to 100 kHz or lower [194] and are therefore very well suited to differentiating dynamic magnetism (expected in paramagnets and spin liquids) from frozen ground states (as would generally be seen in spin glasses and long range ordered magnets such as ferromagnets and antiferromagnets).

μSR is a local probe that works in a similar way to NMR. Instead of using one of the nuclear isotopes found in the sample, however, μSR experiments deposit a polarized muon

(μ^+) inside the sample (it will come to rest in sites of low electric potential) and await its decay and the emission of a β-particle. The angle and time at which the positrons are emitted gives information on the precession of the muon, which gives information on the local fields inside the material. The relaxation rate of the muon precession can be used to determine the fluctuation rate of the magnetic moments inside the material in a wide range of frequencies, in principal from over 100 GHz to less than 100 kHz [194].

Mössbauer spectroscopy takes advantage of the Mössbauer effect, where, for select isotopes, absorption and emission of a gamma ray (through certain nuclear events) can be recoil-free, permitting resonance to occur [45]. The recoil energy of emitted photons from the source must be smaller than the linewidth of the relevant nuclear event or else there will be no reabsorption of the gamma rays by the isotopes in the sample. The photons can be Doppler shifted by oscillating the source to allow these resonances to occur. The transition will occur between the ground state of a nuclear isotope (with spin I_g, nuclear magnetic dipole moment μ_g and nuclear electric quadrupole moment Q_g) and a metastable excited state (with different spin I_e and moments μ_e and Q_e). The nuclear spin states will be split in energy by the interactions with their environment and these must be matched by the Doppler shift in order to meet the resonance condition and for absorption to occur. Thus a Mössbauer spectrum can be used to determine these energy splittings. Hyperfine splittings indicate "static" magnetic order, or at least that fluctuations are slower than the lower frequency limit of Mössbauer spectroscopy (the Larmor frequency of the particular nuclear isotope used). When fluctuations are faster, the hyperfine couplings can be "motionally narrowed", giving a measure of the fluctuation rate of the surrounding spins. The typical frequency range of applicability of Mössbauer spectroscopy covers roughly 100 MHz to 10 GHz [194].

Finally neutron spin echo experiments use polarized neutrons and magnetic fields to greatly enhance the energy resolution of inelastic neutron scattering. This permits the observation of relatively low frequency (therefore low energy) spin excitations.

Perhaps it is not too surprising to discover PSDs in a spin liquid ground state like that of $Tb_2Ti_2O_7$ or in the hidden order ground state of $Yb_2Ti_2O_7$, as there is no reason to believe that these are not reasonably dynamic ground states. The spin ice materials are also cooperative paramagnets, though the observation of glassy relaxation on much slower time scales [195] (with ac susceptibility) makes the observation of low temperature spin fluctuations fairly surprising [196, 193]. Still more unusual is the discovery that the spin glass ground states of $Tb_2Mo_2O_7$ (TMO) and $Y_2Mo_2O_7$ (YMO) possess PSDs [187]. A spin glass ground state typically has temperature dependent fluctuations and is eventually, at low enough temperatures, static on the time scale accessible by μSR. Yet, the pyrochlore spin glasses YMO and TMO show evidence (more pronounced in TMO), of a temperature independent relaxation rate in μSR, well below the glass transition temperature [187]. It

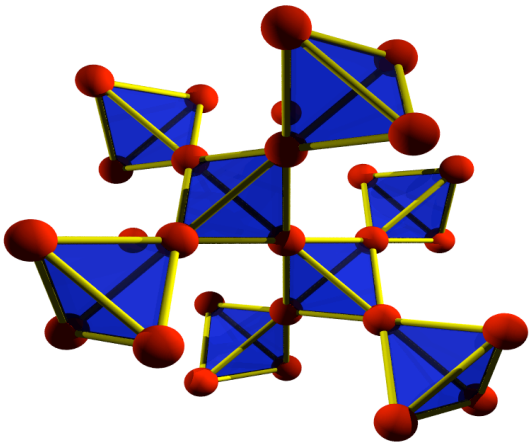

Figure 4.1: The magnetic ions of the pyrochlore lattice sit on a network of corner sharing tetrahedra.

would not be inconceivable to imagine that while much of the system is freezing randomly below the spin glass transition temperature, there are regions that remain dynamic down to the lowest temperatures.

The observation of PSD's in some pyrochlores such as $Gd_2Ti_2O_7$ (GTO) [190, 183], $Gd_2Sn_2O_7$ (GSO) [192, 6, 191] and $Er_2Ti_2O_7$ (ETO) [186] is most perplexing as these materials have been found in neutron scattering measurements [184, 185, 197] to display long range magnetic order below temperatures of 1.0 K, 0.74 K and 1.1 K, respectively. Conventional wisdom suggests that collective spin wave excitations, hence spin dynamics, should freeze out in the limit of zero temperature in such magnets, particularly in the presence of single-ion anisotropies and the long range dipolar interaction. The origin of the persistent spin dynamics (PSDs) in these ordered materials remains a major open question in the study of highly frustrated insulating magnetic oxide materials [6].

While not a pyrochlore, it is worth noting that the antiferromagnetic garnet $Gd_3Ga_5O_{12}$ (GGG), which shows spin glass physics [7] as well as rather extended magnetic correlations below 140 mK [8] that are now theoretically rationalized [198], also exhibits PSD's below 100 mK [199]. Much more of the physics of GGG will be discussed in Chapter 5.

The material $Gd_2Sn_2O_7$ (GSO) seems an obvious system in which to investigate these unusual spin dynamics as it has shown *mostly* conventional behaviour. It is seen to be a

good realization of a Heisenberg antiferromagnet on the pyrochlore lattice, with relatively small single-ion anisotropy [200]. It shows a single phase transition [6, 188] to a long range ordered state found in neutron scattering experiments [185] to be the theoretically predicted Palmer-Chalker (PC) ground state [201]. Nonetheless, the observation of PSDs in GSO calls into question this simple picture. Furthermore, previous measurements of the magnetic specific heat $C_m(T)$ on this material between 350 mK and 800 mK (see Fig. 4.6) were found to be parametrized by a $C_m(T) \sim T^2$ law [6]. Such a temperature dependence of C_m is unusual since conventional antiferromagnetic magnon excitations, with or without an anisotropy energy gap Δ, lead to $C_m(T) \sim T^3$ or $C_m(T) \sim \exp(-\Delta/T)$ respectively for $T < T_c$. Such an unconventional $C_m(T)$ behaviour further argues for the existence of unusual low-energy excitations in GSO. Quite interestingly, the related material $Gd_2Ti_2O_7$, which also exhibits PSD's, displays $C_m(T) \sim T^2$ for 100 mK $< T <$ 500 mK [183].

In contrast, del Maestro and Gingras [27] argue that the lowest temperature $\sim$ 350 mK considered in Ref. [6] for GSO corresponds to the *upper* temperature limit above which multi-magnon excitations become important. Their calculations show that in the temperature range where the specific heat was measured by Bonville *et al.* [6], multi-magnon excitations obscure the true low temperature limit of the specific heat. Calculations using the microscopic spin Hamiltonian [201, 185, 27] that describes the experimentally observed ground state of GSO [185] predict that C_m should begin to drop away exponentially exactly at or just below 350 mK as gapped magnetic excitations are quenched with lower temperature [27].

Here we discuss an investigation of the nature of the low-energy spin excitations in GSO through measurements of specific heat down to 115 mK. The results show an exponentially dropping specific heat at low temperature and, when compared with theoretical calculations [27, 178], confirm the picture of conventional, gapped antiferromagnetic magnons in $Gd_2Sn_2O_7$.

4.2 Previous Work on Gd Pyrochlores

Because the Gd^{3+} ion has a half filled $4f$ shell, Hund's rules imply that it will have maximized the spin to $S = 7/2$ and it will therefore have zero orbital angular momentum $L = 0$. Of course this only applies as a first approximation. In reality, there will be some intermixing with other states of finite orbital angular moment as a result of intra-orbital spin-orbit coupling. However, the Gd^{3+} moments do have very little orbital angular momentum and they are therefore only weakly affected by the surrounding crystalline electric field. This makes the moments largely isotropic $S = 7/2$ (large spin) moments with a rather small single ion anisotropy, hence well approximated as classical Heisenberg

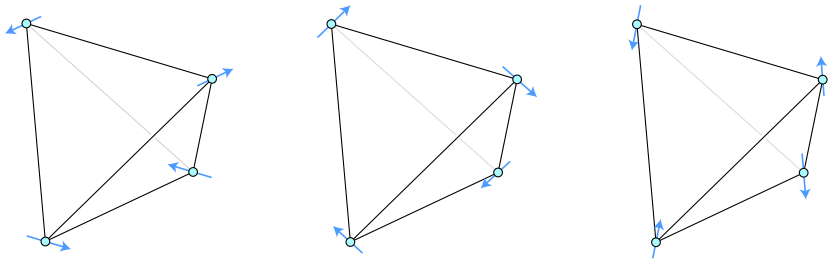

Figure 4.2: Three equivalent manifestations of the Palmer-Chalker ground state [201] (three others are obtained by flipping all the spins), a 4-sublattice Néel state which is understood to be the magnetic ground state of $Gd_2Sn_2O_7$ [185].

spins.

The nearest-neighbour exchange is found to be antiferromagnetic in these systems. Dipolar interactions are very significant and further exchange interactions such as J_2 and J_{31} are generally assumed to be important [27]. The theoretically predicted behaviour of the dipolar Heisenberg pyrochlore antiferromagnet has been an issue of much debate. One of the main contenders is a single transition to the $k = 0$ Palmer-Chalker (PC) state [201]. Other behaviours have also been proposed [202, 203, 204, 205]. Notably, a $\boldsymbol{k} = \left[\frac{1}{2}, \frac{1}{2}, \frac{1}{2}\right]$ or $k = \pi$ state has been proposed to be important and possibly to exist in certain situations, though calculations often indicate that the eventual ground state should be the Palmer-Chalker state [204, 203].

The M^{4+} ion in the $Gd_2M_2O_7$ materials can take several different forms. Here we will discuss four variants, all with non-magnetic M-ions: Ti^{4+}, Sn^{4+}, Hf^{4+} and Zr^{4+}. While $Gd_2Ti_2O_7$ appears to be the most exotic of these materials, we are concentrating primarily on $Gd_2Sn_2O_7$ in this work. In all four compounds, there are transitions to long range order, though the case of $Gd_2Ti_2O_7$ is a fair bit more complicated. These transitions are all at roughly 1/10 of the Curie-Weiss temperature giving a frustration index of $f = T_N/\theta_{CW} \simeq 10$.

4.2.1 $Gd_2Sn_2O_7$

The stanate pyrochlores $R_2Sn_2O_7$ are, as of yet, not available as good quality single crystals since the growth process tends to result in evaporation of tin. Thus all the work done on $Gd_2Sn_2O_7$ (GSO), including our own, has been performed with polycrystalline or powder samples. High temperature susceptibility measurements of $Gd_2Sn_2O_7$ give a Weiss constant

of $\theta_{CW} \simeq -10$ K. This can be used to determine a nearest-neighbour antiferromagnetic exchange interaction as

$$J_1 = \frac{3\theta_{CW}}{zS(S+1)} = -0.273\,\mathrm{K} \tag{4.1}$$

where $z = 6$ is the number of nearest neighbours (or coordination number of the lattice) [6].

Glazkov and coworkers performed ESR experiments on polycrystalline samples of very dilute GSO or $(Gd_{0.005}Y_{0.995})_2Sn_2O_7$ in order to probe the single ion or crystal field Hamiltonian [200]. Using the single ion Hamiltonian

$$\mathcal{H}_{\mathrm{SI}} = g\mu_B \boldsymbol{H} \cdot \boldsymbol{S} + B_2^0 O_2^0 + B_4^0 O_4^0 + \ldots \tag{4.2}$$

they were able to effectively simulate the ESR spectra and determine crystal field parameters. This is clearly an oversimplified Hamiltonian as symmetry allows for O_4^3, O_6^0, O_6^3 and O_6^6 terms to exist as well. It is likely, however, that those two crystal field terms are dominant and apparently sufficient. They determined $B_2^0 = 47 \pm 1$ mK and $B_4^0 = 0.05 \pm 0.02$ mK. The second term in equation 4.2 may also be written, more transparently, as DS_z^2, with $D = 3B_2^0$. Then the single ion anisotropy is $D = 140$ mK.

$Gd_2Sn_2O_7$ is characterized by a large and very sharp peak in C indicative of a first-order phase transition [188]. This transition is superimposed on a large, broad feature in the specific heat, which could signal the onset of short-range correlations, as is common in geometrically frustrated materials [188]. Alternatively, it may be related to the crystal field energies. This broad feature is responsible for a large part of the entropy in the system, with only 40% of the total $R \ln 8$ entropy accounted for by the transition and below.

Below the phase transition, Bonville *et al.* found a specific heat that drops out as T^2 [188]. This is to be contrasted with the T^3 behaviour expected of spin waves in a short range antiferromagnet, $T^{3/2}$ expected of ferromagnetic magnons or exponential behaviour that should be expected when the long range dipolar interaction is predominant, making T^2 a fairly unexpected temperature dependence. At the lower end of their data, a downturn is visible, though they have attributed this to experimental uncertainty (specifically thermometry issues). The specific heat data of Bonville *et al.* is shown in Figure 4.6.

The results of Mössbauer spectroscopy and μSR experiments, also call into question the notion of a conventionally ordered ground state in $Gd_2Sn_2O_7$ [192, 188]. A Mössbauer spectrum taken by Bertin and coworkers [192] at a temperature of 27 mK is shown in Figure 4.3(a). The four distinct nuclear energy levels, resulting from the hyperfine interaction $\mathcal{H}_{HF}$ and the nuclear quadrupole electric interaction $\mathcal{H}_Q$, are found to be at 0, 0.05, 12.1 and 15.9 mK. The spectrum taken at 27 mK, indicative of the population of different energy levels, is best fit with an effective hyperfine temperature $T_{HF} = 90$ mK, rather than the temperature of the sample itself. This suggests that the nuclear moments are out

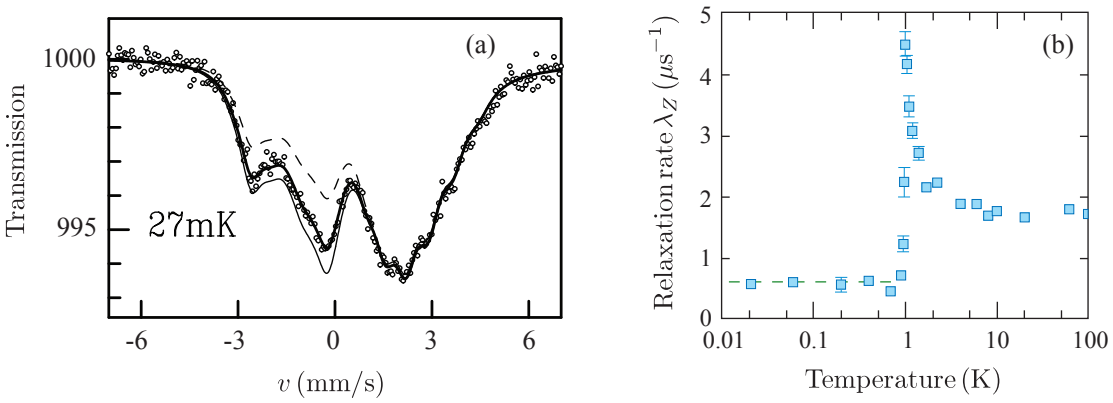

Figure 4.3: (a) Mössbauer spectrum of $Gd_2Sn_2O_7$. The solid line is the best fit employing an effective hyperfine temperature of 90 mK, whereas the sample is held at 27 mK [192]. (b) The μSR relaxation rate λ_Z as a function of temperature for $Gd_2Sn_2O_7$ showing a temperature independent relaxation rate of 0.6 MHz at low temperatures [6].

of equilibrium with the lattice. Bertin *et al.* [192] propose that the electronic spins are fluctuating on a time scale τ, and the nuclear moments relax on a time scale T_1 and that these two time scales are quite similar: $\tau \simeq T_1$. This makes it difficult for the nuclear spin to come into equilibrium with the lattice temperature and implies a dynamic magnetic ground state.

The μSR relaxation rate λ_Z, is also somewhat surprising. Above the transition temperature, the relaxation rate is roughly constant at 2 MHz. The relaxation rate peaks at around 1 K and then drops down to a temperature-independent value of 0.6 MHz [6] (data shown in Figure 4.3(b)). There are some oscillations in the μSR asymmetry at very short times which comes about from static order. However, it is the exponential relaxation, that likely results from interaction with spin waves, and its lack of temperature dependence which is most surprising. Bonville *et al.* suggest that this is likely explained by $Gd_2Sn_2O_7$ having an unusual spin wave spectrum possessing spin waves with a finite density of states at zero energy [188].

Thus the work of Bertin, Bonville and coworkers [192, 188], seems to imply a somewhat unusual ground state as characterized by PSDs and an unusual T^2 dependence of the specific heat. However, Wills *et al.* [185] have performed neutron diffraction experiments on $Gd_2Sn_2O_7$ and found that the results are perfectly refined to the Palmer-Chalker (PC) or $c\Gamma_{7+}$ state [201]. In the PC state, the spins sit in the local xy-plane (the local z-

axis points out of the tetrahedra) and are parallel to certain edges of the tetrahedra. For nearest-neighbour antiferromagnetic Heisenberg exchange on the pyrochlore lattice, one expects high frustration and a spin liquid ground state. However, when the dipolar interaction is included, the system is predicted to order in the PC state [201]. Thus $Gd_2Sn_2O_7$ appears, through neutron scattering, to be the quintessential dipolar Heisenberg pyrochlore antiferromagnet. The Palmer-Chalker state is also largely consistent with the Mössbauer results which suggest that the spins are oriented perpendicular to the electric field gradient along the local z-axis [192]

4.2.2 $Gd_2Ti_2O_7$

In the study of magnetic pyrochlore oxides, the titanates have generally been studied first, with the stannates receiving more recent attention [91]. This is likely a result of the problems with growing good single crystals of $R_2Sn_2O_7$ materials. Thus, $Gd_2Ti_2O_7$, available in single crystal and powder form, was the first material in which research groups attempted to study the ideal dipolar Heisenberg pyrochlore antiferromagnet [202]. As it turns out, $Gd_2Ti_2O_7$ exhibits more complicated physics than does $Gd_2Sn_2O_7$, suggesting that it is described by a more complex model.

Initially, only one transition was observed at ~ 1 K in a polycrystalline sample [202]. However, there were likely problems of sample quality, since, more recently, groups have observed two phase transitions at $T_{C1} = 1.02$ K and $T_{C2} = 0.74$ K in both polycrystalline and single crystal samples (see for example Refs. [206, 183] and data plotted in Figure 4.4). The lower transition is particularly sharp, likely a first-order phase transition, where the higher transition is consistent with a continuous or weakly first-order phase transition [183]. Below 0.7 K, the specific heat appears to follow a T^2 power law [206, 183].

Application of a magnetic field yields a rather complicated phase diagram, presumably with various ordering wavevectors [206, 207]. See Figure 4.4 for the phase diagram obtained on a powder sample [206]. For a given orientation of applied field there are three ordered phases [207], whereas in the polycrystalline case, it appears that there are four ordered phases in total [206]

Early neutron scattering studies of $Gd_2Ti_2O_7$ by Champion *et al.* found the ground state in zero field to be ordered with a $\boldsymbol{k} = \left[\frac{1}{2}, \frac{1}{2}, \frac{1}{2}\right]$ magnetic propagation vector [208]. They concluded that the spins are fully ordered in the (111) kagomé planes, with the spins at 120° angles to each other and tangent to the local [111] axes. The interstitial spins in between the kagomé planes, however, were found to have no net magnetic moment. In a later work, Stewart *et al.* have pointed out that the 1-k structure selected by Champion *et al.* cannot be distinguished from more complex multi-k structures (2-, 3- and 4-k) by Bragg diffraction [184]. They use diffuse neutron scattering to determine that the ordering is a

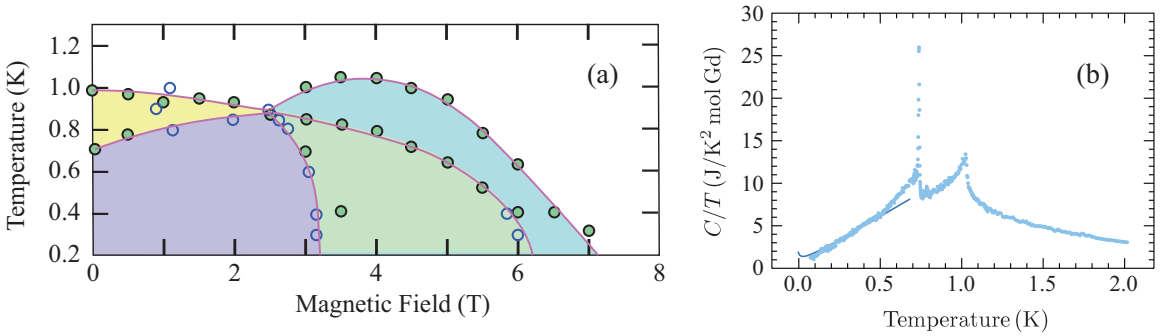

Figure 4.4: (a) The phase diagram of polycrystalline $Gd_2Ti_2O_7$ in magnetic field, taken from Reference [206]. (b) The specific heat of single crystal $Gd_2Ti_2O_7$ in zero field, showing transitions at 1.0 K and 0.7 K, taken from Reference [183].

4-k structure which can be constructed from all four symmetry related 1-k structures. In this 4-k structure, the disordered interstitial spins are combined into disordered tetrahedra. Furthermore, below ~ 0.7 K, a weak $\left[\frac{1}{2}, \frac{1}{2}, \frac{1}{2}\right]$ reflection indicates that the lower transition T_{C2} is the result of very weak ordering of those interstitial spins [184].

Clearly GTO does not order in the Palmer-Chalker state (a $k = 0$ ordering), suggesting that this material is not well modeled as an ideal dipolar Heisenberg pyrochlore antiferromagnet model. In between the two transitions a full 1/4 of the Gd^{3+} moments are completely disordered and below T_{C2} they are only partially ordered. It seems that there must be more at play, additional important interactions, for example.

μSR experiments performed by Yaouanc *et al.* on GTO, also show unusual behaviour [183]. At high temperature, as expected, the μSR spectra are found to be described by a single exponential decay at high temperature in the paramagnetic state. Approaching 1 K, the relaxation rate increases as fluctuations of the magnetic moments slow. Below T_{C1}, the relaxation is better described by a stretched exponential with exponent $\alpha \sim 0.75$ and below T_{C2}, $\alpha \sim 0.5$. Oscillations do develop below T_{C1}, indicative of static order, but a stretched exponential relaxation, largely temperature independent, persists to very low temperatures. The relaxation rate seems to plateau at about 0.4 MHz, a lower frequency than the 0.6 MHz seen in $Gd_2Sn_2O_7$ but nonetheless indicative of persistent spin dynamics (PSDs). Yaouanc *et al.* propose a phenomenological density of states of spin excitations to account for the μSR results as well as a T^2 specific heat [183].

In contrast to $Gd_2Sn_2O_7$, Mössbauer spectroscopy results on $Gd_2Ti_2O_7$ are quite well behaved. The effective hyperfine temperature that is obtained from fitting the spectrum at low temperatures matches well the temperature of the sample [192]. The Mössbauer ex-

periments show the existence of two distinct Gd^{3+} moments for $T_{C2} < T < T_{C1}$, consistent with 1/4 of the spins remaining disordered in that temperature range [6].

4.2.3 $Gd_2Hf_2O_7$ and $Gd_2Zr_2O_7$

The materials $Gd_2Zr_2O_7$ (GZO) and $Gd_2Hf_2O_7$ (GHO) have not received very much attention and Durand *et al.* [209] are one of very few groups to have investigated their magnetic properties at low temperature. The specific heat of each was found to exhibit a large, broad feature centred at about 1 K, giving way to a single sharp ordering transition at 0.769 K (in GZO) and 0.771 K (in GHO). Durand *et al.* [209] have extracted the nearest-neighbour exchange interaction (neglecting further neighbour interactions except for the dipolar interaction) in these two materials from the higher temperature specific heat and from susceptibility measurements. In the case of GZO, they obtain $J_1 = -112$ mK from specific heat and $J_1 = -122$ mK from susceptibility (which shows a Weiss constant of $\theta_W = -7.7 \pm 0.5$ K). In the case of GHO, they obtain $J_1 = -117$ mK from the specific heat and $J_1 = -116$ mK from the susceptibility ($\theta_W = -7.3 \pm 0.8$ K). In both these materials (and in GSO and GTO) the frustration index $f = T_N/\theta_W$ is roughly 10.

Thus the two materials are extremely close in behaviour. One notable difference between the two is that the peak in the specific heat of GZO is a fair bit larger than that of GHO. While these materials have ordering temperatures closer to that of $Gd_2Ti_2O_7$, there is no indication of a double transition, suggesting that the physics of these materials is more similar to that of $Gd_2Sn_2O_7$. The magnitude of the ordering transitions is also smaller in these systems so that the transitions could be continuous where GSO has a clearly first-order, discontinuous phase transition, with a very large specific heat peak. Lutique *et al.* also measured the specific heat of GZO, though they did not measure to low enough temperatures or with high enough resolution to observe the ordering feature around 1 K [210].

4.3 Spin Wave Theory

When magnetic materials are treated in mean-field theory, the spins are taken as essentially classical entities, and the ground state consists of spins fully magnetized along particular directions. However, spins are quantum mechanical and this classical picture is only accurate in certain situations. Take for instance, an antiferromagnetic chain, interacting via nearest-neighbour interactions. The classical ground state would be written as

$$|\uparrow\downarrow\uparrow\downarrow\uparrow\downarrow\uparrow\downarrow\ldots\rangle$$

However, acting on this state with the Hamiltonian

$$\mathcal{H} = J \sum_{\langle i,j \rangle} \boldsymbol{S}_i \cdot \boldsymbol{S}_j = J \sum_{\langle i,j \rangle} \left[S_i^z S_j^z + \frac{1}{2}(S_i^+ S_j^- + S_i^- S_j^+) \right] \tag{4.3}$$

does not return that classical ground state, as a result of the S^+ and S^- operators. Since this classical ground state is not even an eigenfunction of the Hamiltonian, it clearly cannot be the quantum mechanical ground state of the system. Essentially, the off-diagonal part of the Hamiltonian, the raising and lowering operators, have introduced quantum fluctuations. In the 1- and 2-dimensional cases, the Mermin-Wagner-Hohenburg theorem tells us that there is no spontaneous broken symmetry at some finite temperature. However, in 3-dimensions, there is a transition to long range order and the classical ground state will at least be a good approximation of what results. The system is divided into sublattices, each magnetized along a certain direction. For example, in a cubic lattice, there are two sublattices and the respective spins are either up or down along the z-direction. In the classical picture the sublattice magnetization would be maximized at zero temperature, but when quantum fluctuations are introduced, there is a deviation of the spins away from the z-axis and the thermal average of the sublattice magnetization is decreased [211].

In ferromagnetic systems, the classical ground state (all spins aligned or a single sublattice) is in fact an eigenstate of the Hamiltonian. Thus ferromagnets do not suffer the same reduction in magnetization due to quantum fluctuations at zero temperature. Nonetheless, in both ferromagnets and antiferromagnets, finite temperature results in excitations away from the ground state. Take for instance a ferromagnetic spin chain with ground state

$$|\uparrow\uparrow\uparrow\uparrow\uparrow\uparrow\uparrow\uparrow\ldots\rangle$$

Simply flipping one of the spins to obtain

$$|\uparrow\uparrow\uparrow\downarrow\uparrow\uparrow\uparrow\uparrow\ldots\rangle$$

does not result in an eigenstate of the Hamiltonian. Through the off-diagonal parts of the Hamiltonian $(S_i^+ S_j^- + S_i^- S_j^+)$, the flipped spin propagates through the lattice like a wave. Thus these excitations are known as spin waves, and they are quantized in units of energy, called magnons.

To treat such a problem exactly is generally impossible. The standard approach to defining the spin excitations in a magnetically ordered material [212] is to define Boson operators that represent excitations away from the ground state, via a Holstein-Primakoff transformation. It is then often necessary to perform an expansion of the Hamiltonian in linearized Boson operators. This is often justified provided that the spin quantum number

S is relatively high. The spin fluctuations must be small relative to S and one must be in a regime where magnon-magnon interactions are not important.

Let us take a lattice of spins where the spin at position $\boldsymbol{r}_i$ on a lattice is in spin state $|s_i^z\rangle$. The entire lattice can be represented by states of the form

$$\psi = \prod_i |s_i^z\rangle \tag{4.4}$$

though as mentioned above, such states will not always be eigenstates of the Hamiltonian. One such state will be our mean-field ground state. Spin wave theory consists of considering small deviations and fluctuations away from that "ground state". Essentially, the number of steps away from $s^z = S$ is given by a new quantum number

$$n_i = S - s_i^z \tag{4.5}$$

thus we can also define our basis states with

$$\psi = \prod_i |n_i^z\rangle. \tag{4.6}$$

Standard creation and annihilation operators can be defined as

$$\begin{aligned} c^\dagger|n_1 \dots n_i \dots n_N\rangle &= \sqrt{n_i+1}|n_1 \dots (n_i+1) \dots n_N\rangle \\ c|n_1 \dots n_i \dots n_N\rangle &= \sqrt{n_i}|n_1 \dots (n_i-1) \dots n_N\rangle \end{aligned} \tag{4.7}$$

Now it is practical to introduce the Holstein-Primakoff transformation [213] which consists of a mapping from the spin operators S^+, S^- and S^z to these new Boson creation and annihilation operators c and $c^\dagger$. The transformation is defined as

$$\begin{aligned} S_i^+ &= \left(2S - c_i^\dagger c_i\right)^{1/2} c_i \\ S_i^- &= c_i^\dagger \left(2S - c_i^\dagger c_i\right)^{1/2} \\ S_i^z &= S - c_i^\dagger c_i \end{aligned} \tag{4.8}$$

chosen to obey the correct commutation relations.

Particularly in the case of systems with large S, one may employ a $1/S$ expansion and linearize the Holstein-Primakoff transformation as

$$\begin{aligned} S_{\alpha i}^x &= \sqrt{S/2}(c_{\alpha i}^\dagger + c_{\alpha i}) \\ S_{\alpha i}^y &= \sqrt{S/2}(c_{\alpha i}^\dagger - c_{\alpha i}) \\ S_{\alpha i}^z &= S - c_{\alpha i}^\dagger c_{\alpha i} \end{aligned} \tag{4.9}$$

Here, I have added the subscript α to refer to the different sublattices of the magnetic order. For standard ferromagnetic ordering, for example, there would be only one sublattice. For an antiferromagnet on a square or cubic lattice, one would have two sublattices. In the case of the pyrochlore lattice and $Gd_2Sn_2O_7$, one will have a 4-sublattice Néel state [201]. This formulation now allows us to write the magnetic Hamiltonian formerly defined in terms of spin operators in terms of these Holstein-Primakoff Bosons. Finally, Fourier transforming the operators and diagonalizing the Hamiltonian permits one to discover the dispersion relations $\varepsilon(\boldsymbol{k})$ of different spin wave modes.

The remainder of this section will be a summary of the theoretical calculations done by Del Maestro *et al.* specific to $Gd_2Sn_2O_7$ and related systems, contained in References [214, 215, 27] and applied to our experiments in Ref. [178]. The magnetic Hamiltonian employed [27]

$$\mathcal{H} = \mathcal{H}_{ex} + \mathcal{H}_{dd} + \mathcal{H}_{cf} \tag{4.10}$$

incorporates exchange interactions J_1, J_2 and J_{31} (J_{32} is assumed to be negligible and is set to 0), the long range dipolar interaction and the crystal field anisotropy, using only the lowest-order, B_2^0 term [27].

The first step in the process of understanding the low temperature spin excitations in a magnetic system is to identify the ground state of the system. The Néel state of $Gd_2Sn_2O_7$ is known to be the Palmer-Chalker state [185, 201] shown in Figure 4.2. Thus the Hamiltonian is defined using four sublattices, each with a particular local coordinate system. The interacting part of this Hamiltonian is encapsulated in the interaction matrix $\mathcal{J}^{ij}_{\alpha\beta}(\boldsymbol{R}^{\mu\nu}_{\alpha\beta})$. The subscripts α, β are labels for the sublattices, i, j label the spins on those sublattices and μ, ν are the local cartesian coordinates.

Fourier transformed, linearized Holstein-Primakoff Bosons $c^\dagger_\alpha(\boldsymbol{k})$ and $c_\alpha(\boldsymbol{k})$ are defined through

$$\begin{aligned} c^\dagger_\alpha(\boldsymbol{R}^\mu) &= \frac{1}{\sqrt{N}} \sum_{\boldsymbol{k}} c^\dagger_\alpha(\boldsymbol{k}) e^{i\boldsymbol{k}\cdot(\boldsymbol{R}^\mu + \boldsymbol{r}_\alpha)} \\ c_\alpha(\boldsymbol{R}^\mu) &= \frac{1}{\sqrt{N}} \sum_{\boldsymbol{k}} c_\alpha(\boldsymbol{k}) e^{-i\boldsymbol{k}\cdot(\boldsymbol{R}^\mu + \boldsymbol{r}_\alpha)} \end{aligned} \tag{4.11}$$

where $\boldsymbol{r}_\alpha$ is the position of sublattice α and $\boldsymbol{R}^\mu$ is the position of the μ'th spin relative to $\boldsymbol{r}_\alpha$.

It is also necessary to take the Fourier transformation of the interaction matrix, which is a highly non-trivial process because of the long range nature of the dipolar interaction. This is accomplished [214, 215, 27] using the method of Ewald summation. For a given wavevector $\boldsymbol{k}$, one is left with a Hamiltonian that is defined in terms of pairs of Boson

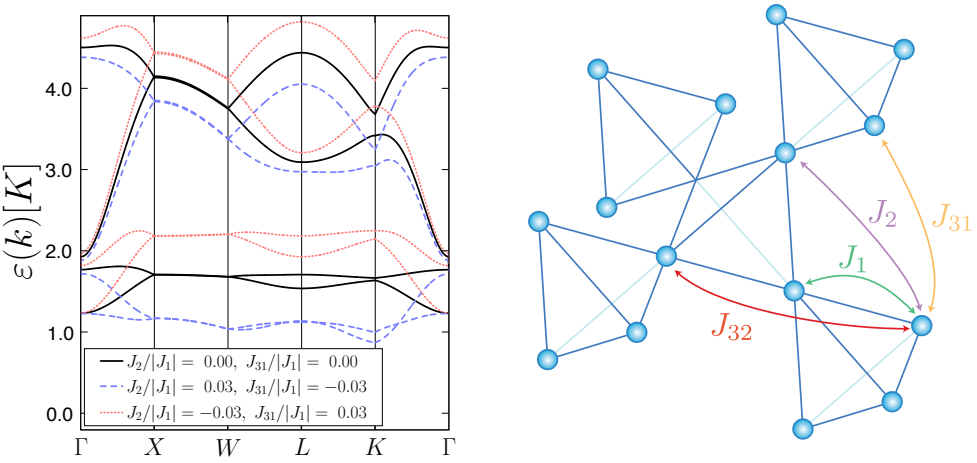

Figure 4.5: Dispersion relations $\varepsilon(\boldsymbol{k})$ calculated for different values of the exchange interactions (left), taken from del Maestro and Gingras [27]. A diagram of the pyrochlore lattice, with exchange interactions J_1, J_2, J_{31} and J_{32} labelled (also adapted from Ref. [27]).

operators. However, one would like, specifically to express the Hamiltonian as a collection of harmonic oscillators or as a Bose gas of noninteracting spin waves given by

$$\mathcal{H} + \mathcal{H}^{(0)} + \sum_{\boldsymbol{k}} \sum_{\alpha} \varepsilon_{\alpha}(\boldsymbol{k}) \left[\frac{1}{2} + a_{\alpha}^{\dagger}(\boldsymbol{k}) a_{\alpha}(\boldsymbol{k}) \right]. \tag{4.12}$$

These new Boson operators a_α and $a_\alpha^\dagger$ are obtained from the $c_\alpha^\dagger$ and c_α operators by diagonalizing the Hamiltonian using a generalized Bogoliubov transformation [214]. Once these dispersion relations have been calculated, the results may be used to calculate various thermodynamic (and dynamic) quantities in order to compare with experiment. The comparison of this model to our experimental results will be described in Section 4.5.

The specific heat resulting from spin-wave excitations is calculated with

$$C(T) = k_B \sum_{\boldsymbol{k}} \sum_{a} \left[\frac{\beta \varepsilon_a(\boldsymbol{k})}{e^{\beta \varepsilon_a(\boldsymbol{k})} - 1} \right]^2 e^{\beta \varepsilon_a(\boldsymbol{k})} \tag{4.13}$$

where $\varepsilon_a(\boldsymbol{k})$ is the dispersion relation for mode a and $\beta = 1/k_B T$. The denominator is the Bose-Einstein distribution function.

For short-range antiferromagnetic interactions, the low-temperature limit of the specific heat will be $C \sim T^3$. For a ferromagnet, the low temperature limit is $T^{3/2}$. An important

consequence of the dipolar interaction in this system is that it results in an anisotropy and this leads to gapped spin waves. The low temperature limit of the specific heat then becomes

$$C \sim \frac{1}{T^2} e^{-\Delta/T} \tag{4.14}$$

which at low enough temperatures, will drop out much more rapidly than T^3. This is indicative of spin waves 'freezing out' at low temperatures. With no soft modes available, spin waves become heavily depopulated as the system temperature gets well below the gap temperature Δ.

At much higher temperatures, one eventually finds that there is a high density of magnons excited in the system and thus they begin to interact with one another. Thus above a certain temperature, linear spin wave theory begins to lose its descriptive power.

4.4 Experiment

Polycrystalline samples of $Gd_2Sn_2O_7$ were obtained from Linton Corruccini at the University of California, Davis. They were prepared by solid state reaction as is detailed in Reference [216]. Gd_2O_3 and SnO_2 were mixed in stoichiometric ratio, pressed into pellets, and then fired in air for 48 hours at 1350°C. The pellets were then reground and the process repeated. Powder X-ray diffraction spectra taken after the two firings, were indistinguishable. All peaks were indexed to space group $Fd\bar{3}m$, with the size a of the cubic unit cell $a = 10.460$ Å, with no impurity peaks detectable at the 1% level. High temperature susceptibility measurements were also performed at UC Davis and yielded a magnetic moment of $7.95\mu_B$ for Gd^{3+} in GSO, close to the expected free-ion moment of $7.94\mu_B$.

Our specific heat measurements were performed at the University of Waterloo, using the quasi-adiabatic technique. A 1 kΩ RuO_2 resistor was used as thermometer and calibrated to a commercially calibrated, *LakeShore* germanium resistance thermometer (GRT). A 10 kΩ metal-film resistor was used as a heater. The sample was suspended from thin nylon threads and the heater and thermometer were fixed directly to the sample. Leads to the thermometer and heater were made from 6 μm diameter, 1 cm long NbTi wires. The sample was weakly heat-sunk to the mixing chamber of a ^{3}He/^{4}He dilution refrigerator with $Pt_{0.92}W_{0.08}$ wire, chosen for its insignificant contribution to the addendum. The addendum, due to other components such as heater and thermometer, was determined to be less than 2% of the sample's heat capacity in the worst case at around 120 mK and thus does not affect the results of our analysis.

Slow thermal relaxation within the sample was observed (with a relaxation time constant $\tau_{\rm Int} \sim 120$ s at 200 mK). The thermal link to the cryostat was chosen so that the relaxation time of the sample temperature to cryostat temperature, $\tau_{\rm Ext}$, would be much longer than $\tau_{\rm Int}$, thereby minimizing the temperature gradient within the sample. A double exponential form was fit to the sample's temperature as a function of time after a heat pulse and the longer exponential was extrapolated to zero time, giving a measure of the sample's heat capacity. The data presented here was taken using a long time constant $\tau_{\rm Ext} \simeq 20\tau_{\rm Int}$. Another experiment performed with $\tau_{\rm Ext} \simeq 5\tau_{\rm Int}$ resulted in a slightly noisier measurement, yet the specific heat in both measurements overlapped within the estimated error bars of the data, ruling out significant inaccuracies due to the slow thermal relaxation in the sample. More details on the experimental set-up and error analysis are given in Chapter 2 and Appendix C.

4.5 Results and Analysis

Our specific heat results, shown in Fig. 4.6, are largely consistent with previous work [6], though there is a 10 to 15% systematic discrepancy between the data sets. Our measurements, however, extend to considerably lower temperature (~ 115 mK) and allow us to test the proposal of gapped magnon excitations [27]. We observe below ~ 350 mK a deviation from the T^2 behaviour describing the data between 350 mK and 800 mK as previously reported [6]. The specific heat decreases also faster than the T^3 power-law expected for conventional gapless antiferromagnetic magnons. This already suggests that the specific heat may be dropping out exponentially, indicating a gapped spin-wave spectrum.

At the lowest temperatures an upturn in $C(T)$ becomes apparent and can be ascribed to a nuclear contribution, $C_N(T)$, stemming largely from the nuclear electric quadrupole interaction and, to a much lesser extent, to the nuclear hyperfine interaction. By properly parametrizing this term and subtracting it from the total specific heat, we can isolate the contribution from the electronic moments.

Our first attempt to understand this term is through a calculation based on ^{155}Gd Mössbauer spectroscopy experiments [43, 192]. Those experiments find a nuclear quadrupole electric splitting of -4.0 mm s^{-1} [43, 192]. More specifically, the four nuclear states (for this isotope, $I = 3/2$) are split with energies 0, 0.05, 12.1 and 15.9 mK as a result of both nuclear quadrupole and nuclear hyperfine interactions [192]. There is one other naturally occurring isotope of Gd that should also contribute to the nuclear specific heat, ^{157}Gd, which, like ^{155}Gd, has spin $I = 3/2$. The ratio of the nuclear dipole moments is $\mu_N^{157}/\mu_N^{155} \simeq 0.8$ and the ratio of quadrupole moments is $Q_N^{157}/Q_N^{155} \simeq 1.1$ [217]. The quadrupole interaction is expected to be proportional to $Q_N I_z^2$ where the local [111] z-direction points to the center

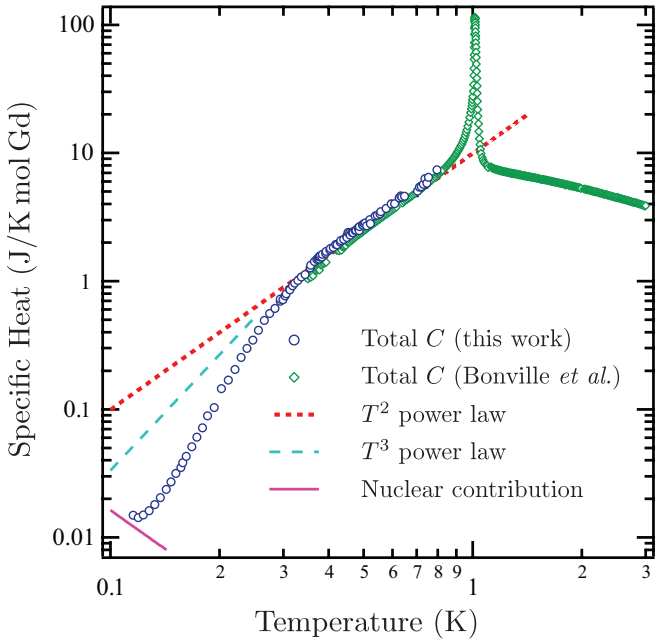

Figure 4.6: Specific heat of $Gd_2Sn_2O_7$ as a function of temperature from this work (blue circles) between 115 and 800 mK. Previously measured data at higher temperatures is plotted for comparison (green diamonds) [6]. The T^2 power law previously proposed (dotted red line) and a T^3 power law (dashed blue line) are also plotted for comparison. The upturn seen below 150 mK (solid line, see text) results from the nuclear electric quadrupole interaction.

of the Gd tetrahedra. While generally, the nuclear electric quadrupole Hamiltonian is

$$\mathcal{H}_Q \propto (3I^2 - I_z^2) + \eta(I_-^2 + I_+^2) \tag{4.15}$$

there are no I_x and I_y (or I_-, I_+) terms in the nuclear electric quadrupole interaction due to axial symmetry of the Gd magnetic site [43]. The component I^2 affects all energy levels equally since both ^{155}Gd and ^{157}Gd have $I = 3/2$.

The nuclear hyperfine interaction is proportional to $\mu_N \boldsymbol{I} \cdot \boldsymbol{J}$. However, in the Palmer-Chalker ground state of GSO [201], the electronic moments are ordered perpendicular to the local z-direction, so to a good approximation, we can simply write the nuclear hyperfine term proportional to $\mu_N I_x$. Thus the total nuclear Hamiltonian can be assumed to take on the simple expression

$$\mathcal{H}_N = a\mu_N I_x + bQ_N I_z^2 \tag{4.16}$$

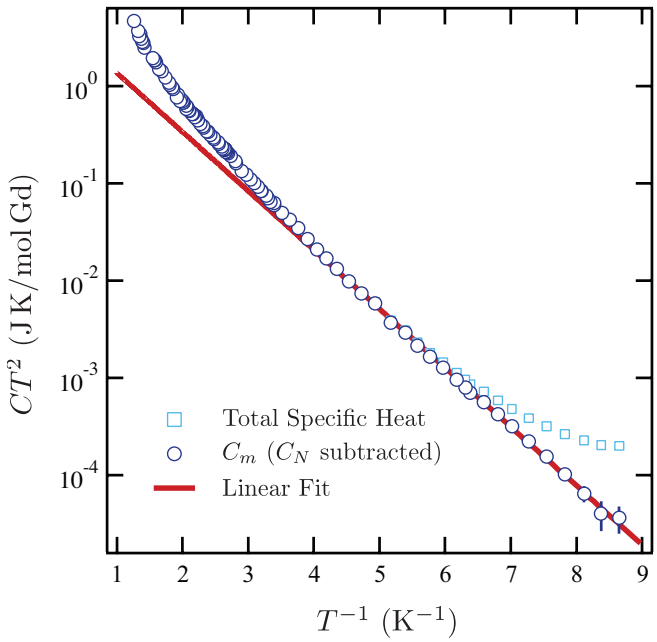

Figure 4.7: $\log(CT^2)$ plotted versus $1/T$. The low temperature limit of the magnetic specific heat is parametrized by a phenomenological form $C_m \propto (1/T^2)e^{-\Delta/T}$, which appear as a straight line on the above plot. The specific heat is plotted after a subtraction of a nuclear contribution A/T^2 where $A = 1.63 \times 10^{-4}$ JK/mol Gd (circles). The total specific heat before subtraction of the nuclear contribution is also shown (squares). The linear fit is performed between the lowest temperature measured and 250 mK and gives $\Delta = 1.40 \pm 0.01$ K.

which contains only two unknowns, a and b. We have calculated the nuclear contribution, $C_N(T)$, to the total specific heat by choosing coefficients a and b such that the resulting eigenvalues of $\mathcal{H}_N$ come closest to matching the above energy splittings for ^{155}Gd obtained by Bertin *et al.* [192]. The interactions are then scaled by the ratios of nuclear moments to obtain the coefficients for the nuclear Hamiltonian of ^{157}Gd. Thus, from the nuclear Hamiltonians for each isotope $\mathcal{H}_N^{155}$ and $\mathcal{H}_N^{157}$, we can obtain energy levels and specific heat contributions form each isotope, C_N^{155} and C_N^{157}. Finally, we multiply these specific heats by the respective natural isotopic abundances and add to obtain the total nuclear specific heat $C_N(T)$.

At temperatures much higher than 16 mK, the nuclear contribution $C_N(T)$ to C behaves as $C_N = AT^{-2}$ with, based on the calculation above, $A \simeq 1.35 \times 10^{-4}$ JK/mol Gd.

Perhaps due to uncertainties in the nuclear energy levels determined by Mössbauer spectroscopy [192], this value of A does not result in a good parameterization of the nuclear contribution to the specific heat. In an alternative analysis, we keep A as a free parameter. $C_N(T)$ can be quite reasonably subtracted from the total $C(T)$ at these temperatures since the hyperfine coupling between the nuclear and electronic moments is only a few mK. As a first rough indicator of a gapped excitation spectrum, we note that the electronic part of C can be parametrized at low temperature by

$$C_m(T) \propto (1/T^2)e^{-\Delta/T} \tag{4.17}$$

as in, for example, conventional colinear antiferromagnets with single ion anisotropy or compared with the low-temperature limit of the theory in Section 4.3.

A plot of $\log(CT^2)$ versus $1/T$ should then give a straight line and this appears to be the case if A is chosen to be 1.63×10^{-4} JK/mol Gd as shown in Fig. 4.7. This phenomenological value of A is quite close to the "calculated" value of 1.35×10^{-4} JK/mol Gd. The discrepancy is likely reasonable considering the uncertainty on the parameters in the calculation and the limited amount of data in the temperature range where the nuclear contribution becomes dominant. Alternatively, since the Mössbauer experiments on which this calculation was based are some of the same experiments that show persistent spin dynamics, this anomalous quadrupole splitting may be directly related to the effect of PSDs in this system, which remains to be explained.

The phenomenological "gap" Δ obtained from the linear fit of $\log(CT^2)$ to $1/T$ is $\Delta = 1.40 \pm 0.01$ K (see Figure 4.7). In order to quantitatively confirm that the specific heat measured here is consistent with gapped spin waves, a theoretical analysis of the magnetic excitations in $Gd_2Sn_2O_7$ as is described in Section 4.3 and Ref. [27] has been applied to our data[1]. This allows for refinement of the Hamiltonian of GSO, in particular the second- and third-nearest-neighbour interactions J_2 and J_{31}.

As stated previously, $Gd_2Sn_2O_7$, and the related material $Gd_2Ti_2O_7$, are well approximated as isotropic, Heisenberg antiferromagnets as the Gd^{3+} ions have half-filled shells ($L = 0$, $S = 7/2$). Neutron scattering experiments have identified a $\boldsymbol{k} = (0, 0, 0)$ ordered ground state [185] otherwise known as the Palmer-Chalker state [201]. Thus $Gd_2Sn_2O_7$ is particularly well suited to the standard protocol, described in Section 4.3, of computing the low-lying spin excitations (magnons) about a previously identified magnetic ground state [215, 27]. The nearest-neighbour exchange interaction is estimated from the Curie-Weiss constant $\theta_{\rm CW} = -8.6$ K by $J_1 = 3\theta_{CW}/zS(S+1) = -0.273$ K [6] where $z = 6$ is the number of nearest neighbours. The strength of the dipolar interaction is derived from the

[1]Spin wave calculations and fitting were performed by Adrian del Maestro and Michel J. P. Gingras for the manuscript [178]

size of the magnetic moments and the geometry of the lattice [201, 185, 215, 27]. Though the moments are fairly isotropic, there exists a small crystal field anisotropy resulting from second order admixing from the electronic $\mathbf{L}$=0 state to excited manifolds [200]). The crystal field parameter $B_2^0 = 47$ mK was used in this calculation as discussed in Ref. [27].

A general two-body spin interaction Hamiltonian was employed including interactions up to third nearest neighbours (J_1, J_2 and J_{31}), dipole-dipole interactions and single-ion anisotropy. The techniques of linear spin-wave theory [215, 27] were employed to express the Hamiltonian as a non-interacting Bose gas of magnons created and annihilated by operators $a_a^\dagger(\boldsymbol{k})$ and $a_a(\boldsymbol{k})$, respectively,

$$\mathcal{H} = \mathcal{H}^{(0)} + \sum_{\boldsymbol{k}} \sum_{\alpha} \varepsilon_\alpha(\boldsymbol{k}) \left[a_\alpha^\dagger(\boldsymbol{k}) a_\alpha(\boldsymbol{k}) + \frac{1}{2} \right], \tag{4.18}$$

where $\mathcal{H}^{(0)}$ is the classical ground state energy and $\varepsilon_a(\boldsymbol{k})$ are the spin-wave dispersion relations. The pyrochlore lattice can be viewed as a face-centred cubic lattice with a 4-site (the four corners of a Gd tetrahedron) basis. The summation runs over all wavevectors $\boldsymbol{k}$ in the first Brillouin zone of the FCC lattice and the subscript α labels the four sublattice sites. $C_m(T)$ is obtained from standard thermodynamic relations [215, 27]

$$C_m(T) = k_{\mathrm{B}} \beta^2 \sum_{\boldsymbol{k}} \sum_{a} [\varepsilon_a(\boldsymbol{k})]^2 \frac{\exp[\beta \varepsilon_a(\boldsymbol{k})]}{[\exp[\beta \varepsilon_a(\boldsymbol{k})] - 1]^2} \tag{4.19}$$

where $\beta = 1/k_{\mathrm{B}}T$, k_{B} the Boltzmann constant and T the temperature.

Using a maximum likelihood estimator as in Ref. [27], the specific heat is confirmed to fit quantitatively well by a model that includes weak ferromagnetic second-nearest-neighbour and antiferromagnetic third-nearest-neighbour interactions ($J_2/|J_1| = 0.01$, $J_{31}/|J_1| = -0.01$) as seen in Fig. 4.8. Qualitatively good fits are observed for a substantial region of the $J_2 - J_{31}$ plane, and there can be little doubt about the presence of a gap to spin excitations at low temperatures. With the above values of J_2 and J_{31}, the calculated dispersion relation shows a true spin wave gap, $\Delta_{\mathrm{SW}} \approx 1.24$ K, at the Γ point ($\boldsymbol{k} = 0$). The difference between this Δ_{SW} value and the $\Delta = 1.40$ K value above arises from the fact that Δ is obtained on the basis of a phenomenological parametric form $C_m(T) \propto (1/T^2)e^{-\Delta/T}$ while Δ_{SW} is a truly physical and microscopic gap. With the values of J_1, J_2, J_{31} above, the reduction of the classical order parameter $\langle S \rangle = 7/2$ due to quantum fluctuations is $\langle \delta S \rangle \approx 0.11$ [215, 27].

Later work of Sosin *et al.*, [218] has reproduced our result that the specific heat shows gapped magnon excitations below 350 mK or so. Above 200 mK, their data are found to match extremely well with our data. Below 200 mK, the agreement with our data is not

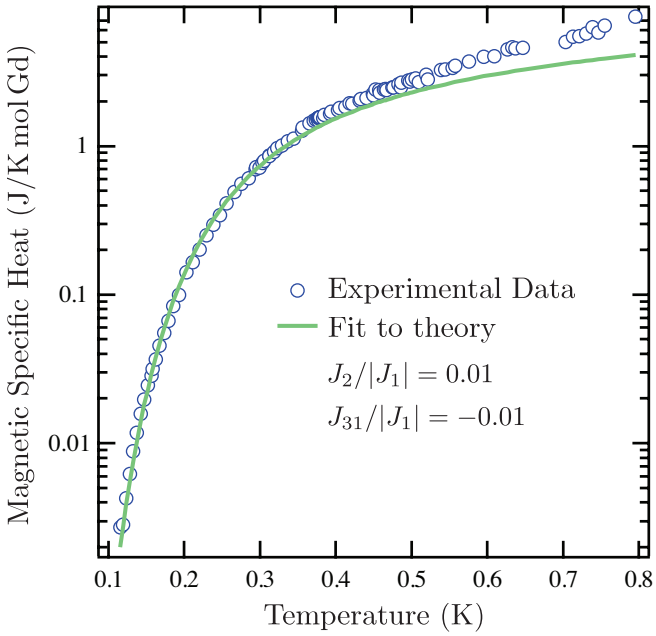

Figure 4.8: Theoretical curve predicted by linear spin-wave theory fit to experimental magnetic specific heat $C_m(T)$ ($C(T)$ with nuclear contribution subtracted) of $Gd_2Sn_2O_7$ with resulting values of the exchange interactions. The best fit gives $J_2/|J_1| = 0.01$ and $J_{31}/|J_1| = -0.01$. Deviation from the theoretical occurs at higher temperatures, close to the transition, where magnon-magnon interactions become important.

perfect with our specific heat appearing to drop out more quickly. The nuclear contribution in the data of Sosin *et al.* also seems to be somewhat different. If their data is used to determine the nuclear coefficient A, in the same way, it is found to be appreciably less than the calculated value of 1.35×10^{-4} JK/mol Gd. It seems that there may be an issue of long equilibration times in measuring the specific heat at those low temperatures that is leading to slightly conflicting results. Sosin *et al.* [218] present two different measurements of $C(T)$ with different rates, slow and fast. There is slight disagreement between these two data sets. The trend observed suggests that our measurements are slower than those of Sosin *et al.* making them likely very reliable. However, there is no quantitative measure of the speed of measurement given with which to directly compare our experiments [218].

Sosin *et al.* [218] also undertake a linear spin wave calculation, very similar to that carried out by Del Maestro and Gingras [27]. Their results are slightly different in that two of the four spin wave modes are degenerate in energy. They attribute this to a different treatment of the single-ion anisotropy. The conclusions, however, are the same, that there are fully gapped spin waves in $Gd_2Sn_2O_7$, that manifest as an exponential drop in $C(T)$. Electron spin resonance (ESR) data are also presented, finding further evidence of gapped spin waves and results consistent with their spin wave theory [218].

4.6 Conclusion

In conclusion, the experimental results presented here, in conjunction with those from a microscopic theoretical calculation that builds on a model that characterizes the long range ordered ground state of $Gd_2Sn_2O_7$ [201, 185, 215, 27], leave very little doubt that the bulk excitations in this system are conventional gapped collective magnons. The following question therefore arises: what is the microscopic origin of the temperature-independent μSR relaxation rate [188] and the higher than expected hyperfine temperature observed with Mössbauer spectroscopy [192]? Such gapped spin-wave excitations would typically be expected to lead to a sharply dropping spin relaxation rate.

The peculiar T^2 behaviour of the specific heat of GTO also remains a mystery for, in contrast to GSO, it does not exhibit a gap down to 100 mK [183] as might be naïvely expected. It would be valuable to investigate the possibility that the T^2 power law in GTO also gives way to an exponentially decaying specific heat at lower temperature. GSO and GTO are perhaps at this time the two pyrochlore materials most amenable to matching theory with experiment [215, 27]. Hence determining the cause of PSDs in these pivotal systems may provide insight into the cause of persistent spin dynamics in other more exotic, highly frustrated systems such as $Tb_2Ti_2O_7$ [189], $Tb_2Sn_2O_7$ [219], $Yb_2Ti_2O_7$ [109] and $Gd_3Ga_5O_{12}$ (GGG) [199].

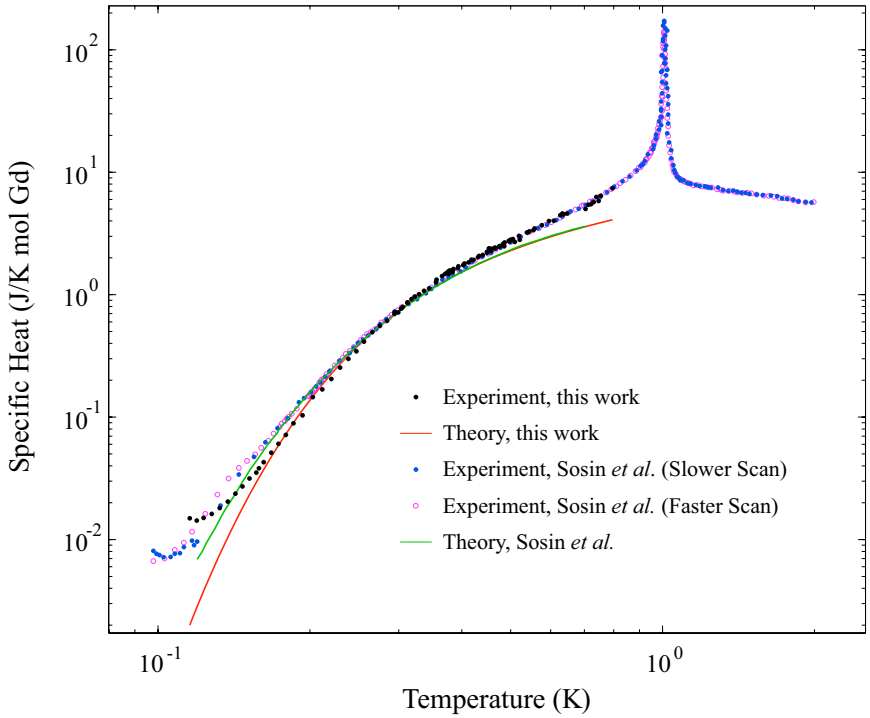

Figure 4.9: Specific heat versus temperature of $Gd_2Sn_2O_7$. More recent results of Sosin *et al.* [218] also find a clear exponential drop in $C(T)$, confirming our conclusion that the system possesses a long range ordered state with gapped spin waves. Two data sets from Ref. [218] are shown, taken with two different sweep rates as well as a theoretical fit using linear spin wave theory.

Chapter 5

Long Range Order and Glassiness in Gd Garnets

5.1 Disorder Free Spin Glasses

The question of whether a system can undergo a true finite temperature freezing transition *without* some degree of quenched random disorder, is one that that is fundamental to many diverse systems in condensed matter physics, including geometrically frustrated magnets, continuously frustrated Josephson junction arrays [220, 221], structural or orientational glasses [222] and even folding proteins [223]. As many magnetic systems are used as simple analogies for more complicated physical systems, spin glasses provide a simple and elegant starting Hamiltonian that results in a very unusual transition into a frozen random state, analogous to a non-crystalline, glassy material. It has long been thought that spin glasses require two ingredients to exist: frustration (an inability to minimize all pair-wise interactions) and some form of quenched randomness [26, 25]. However, in structural glasses, for example, the glass transition arrises out of a liquid that is largely free of imperfections, thus there is no quenched randomness. While much about the glass transition is still not fully solved, one important theory suggests that frustration is responsible for driving the freezing [222]. Similarly, Josephson junction arrays, for certain values of the applied flux, can be mapped onto a continuously frustrated XY-model and show a glass-like transition in experiment and theory, which does not appear to require disorder [220, 221]. Thus the discovery of a magnetic equivalent in a truly disorder-free spin glass has become a highly attractive problem in condensed matter physics. Most of the promising candidates for such a system have come in the form of geometrically frustrated magnetic systems.

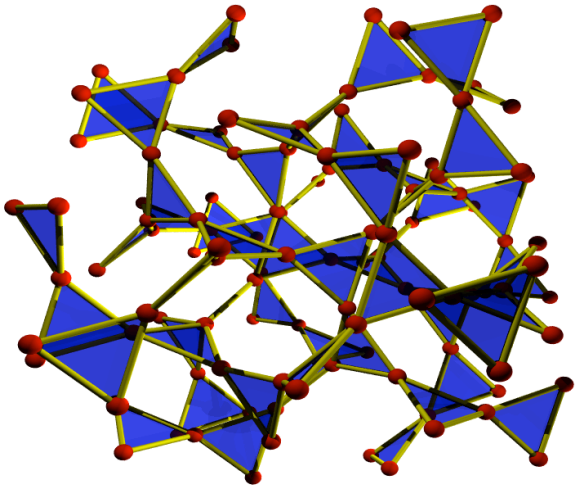

Figure 5.1: The garnet structure of GGG, GTLG and GAG consisting of two interpenetrating lattices of corner sharing triangles.

5.1.1 Theory

Theoretically, there is fairly limited evidence for truly disorder-free spin glasses. For some time, it has been recognized that geometrically frustrated materials should be quite sensitive to disorder and the formation of a spin glass [100]. Starting from a perfect nearest-neighbour Heisenberg exchange Hamiltonian $\mathcal{H}_0$ on a network of corner sharing triangles or tetrahedra, it is found that the system is fully frustrated. In other words, the bonds cannot be simultaneously satisfied pairwise. In a simple classical model, the lowest energy states are found by cancelling out the total magnetization $\boldsymbol{M}_s$ on each simplex s (triangle or tetrahedron), so that $\boldsymbol{M}_s = \sum_{i \in s} \boldsymbol{S}_i = 0$. However, this ground state is far from unique, possessing a macroscopic degeneracy. At the classical level, this prevents the system from finding a long range ordered ground state and leads to a sort of spin liquid [179]. The most famous lattice of this type is the two-dimensional network of corner sharing triangles known as the kagome lattice. In three dimensions, examples include the pyrochlore lattice of corner sharing tetrahedra and the garnet lattice (and other hyperkagome lattices) of corner sharing triangles.

Introduction of perturbing terms in the Hamiltonian $\mathcal{H}'$ will generally allow the system to fall into a long range ordered state. An order-by-disorder phenomenon where fluctuations select a preferred ground state may be necessary. The ensuing long range ordered

state is known to be very sensitive to quenched disorder, however. Villain anticipated the formation of spin glasses in geometrically frustrated systems with arbitrarily small amounts of disorder [100]. Recent theoretical work and numerical simulations have more firmly established the verity of this idea [101], particularly with regard to the pyrochlore lattice.

Thus very small amounts of quenched disorder have the potential to create an almost disorder-free spin glass in highly frustrated systems, but can a truly ideal, clean system freeze? There is one theoretical toy model, the anisotropic Heisenberg model on the kagome lattice, which has been shown to undergo a kind of finite temperature spin glass freezing transition without any quenched disorder necessary [102, 224, 225]. The Hamiltonian of this material

$$\mathcal{H} = J \sum_{\langle i,j \rangle} [S_i^x S_j^x + S_i^y S_j^y + (1+\epsilon) S_i^z S_j^z] \tag{5.1}$$

permits coplanar solutions either with staggered chirality (the $\sqrt{3} \times \sqrt{3}$ state) or uniform chirality (the $\boldsymbol{q} = 0$ state), which are favoured by the mechanism of order-by-disorder. These two ground states permit excitations known as spin folds, where either a closed loop of spins (weathervane modes) or an infinite line of spins rotate together out of the xy plane, respectively. Rotating by 180° (a π-fold) costs zero energy, but requires the system to overcome an energy barrier (because of the anisotropy). It turns out that as such a system is cooled, it cannot be annealed into one of the favoured ground states since in order to do so, it must create a thermodynamic number of π-folds, so traverse an infinite energy barrier. Thus, the system is locked into a disordered configuration by diverging energy barriers, as is the case for a spin glass. The freezing transition, a type of Kosterlitz-Thouless transition, occurs at a finite temperature, making this model a truly "disorder free" spin glass [102, 224]. This transition and glassy ground state have more recently been verified numerically [225].

It is important to distinguish between systems that simply get very slow to respond as the temperature is lowered and true spin glasses with a finite temperature glass transition. Spin ice, for example, also shows glassy relaxation, in that there is relaxation observed in the susceptibility on a scale that is "slow" by human standards [195]. However, there is not known to be a finite temperature at which the relevant time scales diverge. Aside from the anisotropic kagome Heisenberg model, no successful theoretical models of disorder free spin glasses exist at this point in time.

A tantalizing possibility is that a theory of spin glasses can be found that parallels the frustration-based approach to supercooled liquids and the glass transition [222]. This approach is based on the idea that locally preferred order in a liquid is frustrated in the long range by an inability to tile space. For example, one can see situations where the preferred

structure of small numbers of molecules is icosahedral. However those icosahedral bond angles cannot be built up into a periodic tiling of space, thereby introducing frustration. A simple toy model for such an approach, used for numerical simulations, is known as the Coulomb frustrated lattice model [222], the Hamiltonian of which is given by

$$\mathcal{H} = -J \sum_{\langle i,j \rangle} \boldsymbol{S}_i \cdot \boldsymbol{S}_j + \frac{Q}{2} \sum_{i \neq j} \frac{\boldsymbol{S}_i \cdot \boldsymbol{S}_j}{|\boldsymbol{r}_i - \boldsymbol{r}_j|}. \tag{5.2}$$

The summation over $\langle i, j \rangle$ refers to a summation over nearest neighbours whereas the long range Coulomb part of the Hamiltonian is taken over all spins. The spins $\boldsymbol{S}_i$ can be taken as different types of spins, be it XY, Ising or others. In the absence of the Coulomb interaction, these models would undergo ferromagnetic transitions. However, a finite Q prohibits a net magnetization which would lead to a diverging energy in the thermodynamic limit. Numerical simulations on such a model have shown behaviour reminiscent of glass-forming liquids, notably stretched exponential relaxation and super-Arrhenius $\tau(T)$ [226, 227].

The question becomes: is it possible that an analogous situation could occur in a geometrically frustrated material? One could imagine that such a scenario could occur in the case of corner sharing tetrahedra or triangles. The *local* Hamiltonian $\mathcal{H}_0$ consisting of nearest-neighbour antiferromagnetic Heisenberg exchange would be satisfied by spin liquid order with zero net magnetization on each tetrahedron or triangle. However, this locally satisfied order would be in competition, or frustrated, over long length scales by the long range dipolar interaction or $\mathcal{H}'$. The Hamiltonian of such an imaginary system, written in an analogous way, would be

$$\mathcal{H} = J \sum_{\langle i,j \rangle} \boldsymbol{S}_i \cdot \boldsymbol{S}_j + \frac{D}{2} \sum_{i \neq j} \frac{\boldsymbol{S}_i \cdot \boldsymbol{S}_j - 3(\boldsymbol{S}_i \cdot \hat{\boldsymbol{r}}_{ij})(\boldsymbol{S}_j \cdot \hat{\boldsymbol{r}}_{ij})}{r_{ij}^3} \tag{5.3}$$

We suggest, that a good candidate for such physics is the garnet $Gd_3Ga_5O_{12}$ or GGG, a material that is a good example of an isotropic Heisenberg antiferromagnet with an important dipolar interaction on a geometrically frustrated network of corner sharing triangles. The focus of this chapter will be to try to explain the unconventional glassiness that has been seen in GGG.

5.1.2 Experimental Systems

One of the best studied "disorder free" spin glasses is the pyrochlore $Y_2Mo_2O_7$. It is a stoichiometric material and initially seemed to be largely free of disorder, yet it demonstrates

completely conventional spin glass behaviour [103]. Though it has a Curie-Weiss constant of ~ -200 K, a spin glass transition is found at $T_g = 15$ K. Later work showed that there was in fact a rather high level of randomness in the Mo-Mo bond lengths [228, 229], on the order of 5% of the mean distance. While 5% seems a rather small percentage disorder compared to standard spin glasses (for example in $Eu_xSr_{1-x}S$, a dilution level of $x = 0.5$ is required to induce spin glass ordering [47, 85]), the high degree of geometric frustration is expected to make the system particularly sensitive to disorder [100, 230, 231]. The theory and simulations performed by Andreanov *et al.* have verified that such a small amount of disorder is indeed adequate to give rise to a spin glass state in $Y_2Mo_2O_7$ [101]. The pyrochlore material $Tb_2Mn_2O_7$ also shows a spin glass transition [182] and has been shown to have small amounts of bond length disorder [228]. There is a long list of other systems, for example URh_2Ge_2 [232], that have been suggested to be stoichiometric or disorder-free spin glasses at one time, but have later been found to possess important levels of quenched disorder.

Recently, the stoichiometric material $PrAu_2Si_2$ has been discovered to show spin glass physics without an appreciable amount of quenched disorder [233]. Irreversibility of the susceptibility, on typical time scales of a measurement, is seen at around 3 K [233]. The frequency dependence of χ would suggest a spin glass transition temperature closer to ~ 2.4 K. Most interestingly, *increasing* disorder, by substituting Ge for Si, leads to the opposite behaviour of what one might expect – that is, the spin glass transition is suppressed and gives way to antiferromagnetic ordering [234]. A more recent work, based on neutron scattering results, argues that the origin of the spin glass transition in this material is "dynamical frustration" [235]. They note that the magnetic ion, Pr^{3+}, does not have a magnetic ground state, but rather has a singlet ground state with an excited magnetic doublet. This makes these materials induced moment systems wherein there is a critical exchange interaction energy J_{ex} below which the system is a van Vleck paramagnet. It appears that the pure Si containing compound is quite close to this threshold, whereas $PrAu_2Ge_2$ clearly does have an induced moment, and therefore is able to order conventionally. Their final explanation for the spin glass freezing involves the relaxational broadening of the singlet to doublet transition which introduces a level of dynamical frustration [235].

Perhaps some of the the most promising candidates for true, disorder-free or topological spin glasses, are materials with large spin magnetic ions that sit on a kagomé lattice. As discussed above, with anisotropy, such materials are predicted to exhibit unconventional spin glass freezing [102, 224, 225]. A prime example is $SrCr_8Ga_4O_{19}$ which shows spin glass freezing at a temperature well below its Curie-Weiss temperature and an unconventional T^2 power law in the specific heat below the transition [236]. Additionally, introducing site dilution by creating $SrCr_{8-x}Ga_{4+x}O_{19}$, raises the glass temperature, despite reducing the average strength of interactions in the system [236].

Another example is hydronium jarosite or $(H_3O)Fe_3(SO_4)_2(OH)_6$ [104]. Here the magnetic Fe^{3+} ions have large spin $S = 5/2$ and sit on a kagomé lattice. Again, unconventional spin glass ordering is found, including a T^2 power law in the specific heat [237, 238, 239, 240]. Bisson and Wills [104] have shown that the distortion of the oxygen octahedra surrounding the iron atoms, represented by distortion parameter Δ, is linearly related to the spin glass freezing transition temperature. Under different crystal growth conditions, this parameter is varied and T_g can be tuned from roughly 12 to 18 K. They argue that this distortion parameter is related to the anisotropy energy felt by the Fe^{3+} ions and suggest that the spin glass ordering may be that theoretically predicted for the anisotropic, kagome system [102, 224, 225]. However, the exact origin of the anisotropy is not clear since Fe^{3+} is expected to have $S = 5/2$, $L = 0$. Various possible mechanisms for the generation of an anisotropy are suggested, including anisotropic exchange, the dipolar interaction and the Dzyaloshinsky-Moriya interaction [104].

Finally, the primary subject of this chapter, is the material $Gd_3Ga_5O_{12}$ or GGG. This geometrically frustrated material is known to exhibit exotic properties including unconventional spin glass behaviour [7], extended short range antiferromagnetic correlations [8] and persistent spin fluctuations [9]. The spin glass behaviour is surprising given the small amounts of disorder in the system, largely consisting of a 1-2% off-stoichiometry of Gd^{3+} ions on the Ga^{3+} sites.

One might jump to the conclusion that GGG, like $Y_2Mo_2O_7$, exhibits a sensitivity to small levels of disorder that results in a spin glass transition. However, $Y_2Mo_2O_7$ has been seen to possess rather conventional spin glass behaviour, where GGG has much more unusual properties. We would like to consider a more exciting possibility: that the glassiness in GGG may be intrinsic to the system and independent of quenched disorder. We consider that the glassiness might be a result of the locally favoured spin liquid order being frustrated at long length scales by the dipolar interaction in analogy to the frustration based approach to glass-forming liquids [222].

5.2 Past Work on GGG

The earliest low temperature measurements on GGG were performed by Kinney and Wolf [242]. From susceptibility measurements they estimated that the important exchange interactions in the system were $\mathcal{J}_1 = 0.107$ K, $\mathcal{J}_2 = -0.003$ K and $\mathcal{J}_3 = 0.010$ K. Of course, because these exchange interactions are small, yet the Gd^{3+} moments are quite large, there is a very significant dipolar interaction. Because Gd^{3+} has a half-filled valence shell, there is very little orbital angular momentum component to the moments, making it very insensitive to crystal field effects. In reality, there will be some mixing with states of

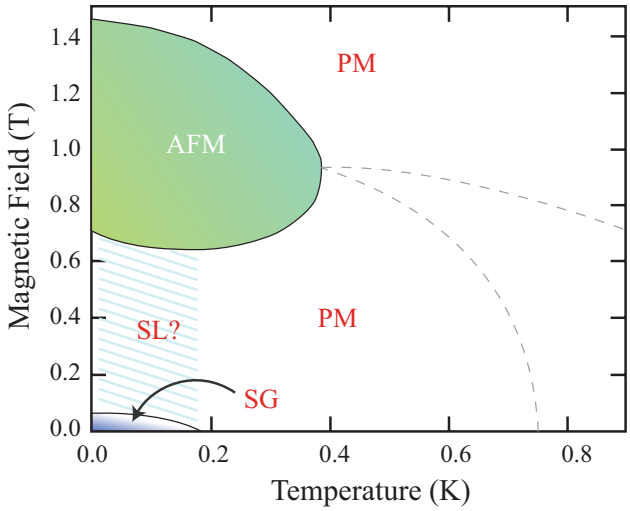

Figure 5.2: The phase diagram in magnetic field of GGG. Phase boundaries are taken from Ref. [241]. Shown are regions of paramagnetic (PM), spin glass (SG), spin liquid (SL) and antiferromagnetic (AFM) behaviour. The dashed lines are indicators of short range order from specific heat and susceptibility measurements [241].).

finite L resulting in some single ion anisotropy. This anisotropy is small and is thought to be fairly insignificant [243, 244]. Thus it has been accepted for some time that the relevant Hamiltonian of GGG is

$$\begin{aligned}\mathcal{H}_{\mathrm{GGG}} =& \mathcal{J}_1 \sum_{\langle i,j\rangle'} \boldsymbol{J}_i \cdot \boldsymbol{J}_j + \mathcal{J}_2 \sum_{\langle i,j\rangle''} \boldsymbol{J}_i \cdot \boldsymbol{J}_j + \mathcal{J}_3 \sum_{\langle i,j\rangle'''} \boldsymbol{J}_i \cdot \boldsymbol{J}_j \\ &+ \frac{\mu_0 g_J^2 \mu_B^2}{8\pi} \sum_{i\neq j} \frac{\boldsymbol{J}_i \cdot \boldsymbol{J}_j - 3(\boldsymbol{J}_i \cdot \hat{\boldsymbol{r}}_{ij})(\boldsymbol{J}_j \cdot \hat{\boldsymbol{r}}_{ij})}{r_{ij}^3}. \end{aligned} \tag{5.4}$$

In the specific heat, Kinney and Wolf [242] found no ordering feature down to a temperature of ~ 350 mK, only a broad feature centered at 800 mK, despite the fact that the Curie-Weiss temperature was $\theta_{CW} = 2.25$ K. Clearly the material exhibits a fair degree of frustration. Since then, no indication of a sharp ordering feature has been found down to temperatures as low as 50 mK [7].

Many of the low temperature bulk measurements taken on GGG in zero field point to some kind of unconventional spin glass transition. Schiffer *et al.* have measured ac susceptibility (χ), nonlinear susceptibility (χ_3) and specific heat [7]. The ac susceptibility shows glassy relaxation with a frequency dependent peak in χ'. If one fits a scaling law

of the form $f = f_0(T_f/T_g - 1)^{z\nu}$ to the peak (or freezing) temperatures T_f as a function of measurement frequency, assuming a dynamical exponent of $z\nu \simeq 8$, one obtains a glass temperature of roughly 140 mK. This quick analysis is based only on 3 data points and assumes a $z\nu$ that is found in many, but not all, spin glasses. The value of f_0 so determined is 4×10^5 Hz, which is fairly slow when compared to most conventional spin glass materials (see for example Ref. [70]).

The nonlinear susceptibility exhibits a reasonably sharp peak at 175 mK [7]. It is not surprising that this peak temperature is higher than the 140 mK determined from dynamical scaling as the nonlinear susceptibility was measured at a frequency of 36.7 Hz. Likely, with a lower probe frequency the peak would increase in height and shift to slightly lower temperatures. The nonlinear susceptibility, however, is slightly unconventional as it shows an additional smaller and broader feature at ~ 414 mK [7].

The specific heat was also found to be different from what one would typically expect of a spin glass. There is a very broad maximum at about 800 mK, below which the specific heat decreases monotonically [241, 7]. Rather than a "bump" in C near the spin glass transition, Schiffer *et al.* observe a maximum in C/T (or a maximum in the rate of entropy release) at roughly 120 mK. One can discern the presence of a broad feature in C/T near 400 mK which corresponds to the broad peak in χ_3 [7].

There are additional measurements by other groups that are quite inconsistent with spin glass physics. μSR measurements, for example, find persistent spin dynamics (PSDs) down to very low temperatures [9, 245]. Dunsiger *et al.* find a fluctuation rate of roughly 2 GHz at the lowest temperatures, ~ 25 mK, which is very inconsistent with static magnetic order [9]. Marshall *et al.*, also using μSR, find the Gd fluctuation rate to be linear in temperature until around 100 mK, below which point it is saturated at 1.5 GHz [245]. Finally Bonville *et al.*, using Mössbauer spectroscopy, find a quadratic temperature dependence of the Gd fluctuation rate [246] and significantly slower fluctuations below 100 mK than what were found in the μSR experiments [9, 245]. It is suggested [246] that this discrepancy is the result of assuming a constant root mean square, Δ, of the distribution of dipolar fields in analyzing the μSR data and that the data sets can be found to be consistent if Δ drops out significantly at low T with the development of spin correlations. Nonetheless, they suggest that the Gd fluctuation rate must saturate, though at a lower value of ~ 10 MHz where one is in a regime of quantum tunneling and below the lower frequency limit of the Mössbauer experiments [246].

Perhaps, the most conflicting results with the spin glass interpretation of GGG, are neutron scattering results [247, 8, 248, 249]. Studying Gd containing compounds with neutron scattering is made very challenging by the high neutron absorption of ^{157}Gd, one of the naturally abundant isotopes. Thus the neutron scattering experiments on GGG were carried out using polycrystalline samples grown with isotopically enriched ^{160}Gd,

which does not absorb neutrons [8].

The neutron powder diffraction data, so obtained, show quite complex and surprising behaviour. At higher temperatures, around 1 to 3 K, the spectrum is comprised of diffuse scattering peaks, attributed to the nearest-neighbour exchange interaction. As the temperature is lowered, these peaks increase in strength and a third diffuse peak is seen. Most strangely, below 140 mK, sharp peaks begin to appear, superimposed on the diffuse scattering. While not sharp enough to indicate true long range order, these peaks do indicate extended short range order with a correlation length on the order of 100 Å. Rather than spin glass freezing, this is suggestive of a change from a liquid-like phase to a solid-like phase [8]. It has also been suggested to be a sort of mixed liquid-solid state [8], perhaps a kind of "spin slush". Certainly it is difficult to reconcile the complete lack of an ordering transition in specific heat with the sudden onset of extended correlations.

Yavors'kii *et al.* have attempted to understand the neutron scattering peaks in the context of mean-field theory (MFT) [250, 198, 251]. Fixing the nearest-neighbour exchange strength and dipolar interaction (treated with Ewald summation), based on experimental data, they tuned the more distant interactions J_2 and J_3 and determined the MFT ordering and Gaussian fluctuations, thereby simulating the neutron scattering signal. For particular values of the interaction strengths, they were able to find excellent agreement between theory and experiment. A particular ordering wave-vector is selected, though a quasi-degeneracy of modes is observed where a large distribution of modes is very close to critical, making for a much more complex diffraction spectrum. Yavors'kii *et al.* suggest that this quasi-degeneracy of modes could lead to an increased sensitivity of the system to small amounts of disorder.

In magnetic field, a very complex phase diagram is observed [252, 241], as is shown in Figure 5.2. The paradoxical spin glass state does not survive well the application of a magnetic field, giving way to a spin liquid of sorts by 30 mT. At higher field (the specific value of which depends on the crystallographic orientation) a "bubble" of antiferromagnetic ordering is found. Above that bubble, one enters another, apparent cooperative paramagnetic state. The antiferromagnetic phase is quite interesting for the low field boundary exhibits reentrance. In other words, as the temperature is lowered at specific values of magnetic field, the material enters the antiferromagnetic phase and then exits back into a spin liquid phase. The analogy has been drawn to the ^{4}He melting curve [253, 254, 255, 256]. Petrenko *et al.* have recently discovered that the idea of one contiguous region of antiferromagnetism does not appear to be correct as neutron scattering shows very complex behaviour and multiple ordering wavevectors within that region [257].

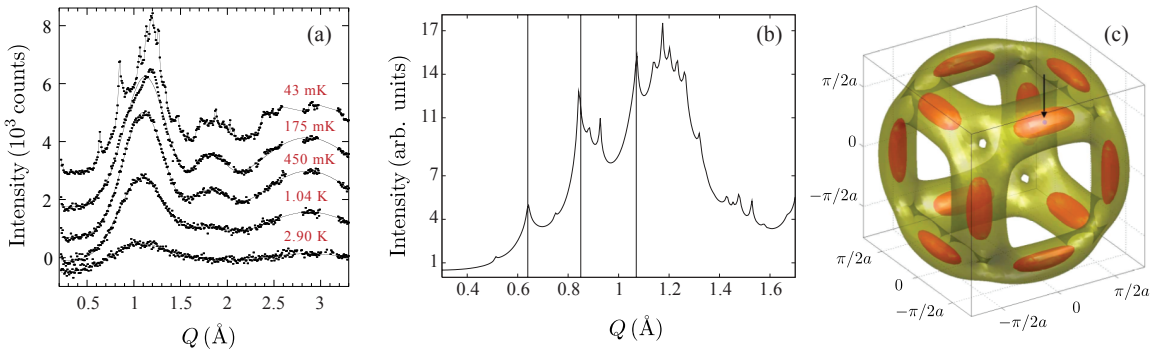

Figure 5.3: (a) The powder neutron diffraction spectra taken at different temperatures, taken from Ref. [8]. (b) Numerical simulations, from Ref. [198], of the powder diffraction intensity, $I(q)$, using mean-field theory and Ewald summation showing excellent agreement with experiment for particular values of exchange interactions J_2 and J_3. (c) The volume of quasi-critical modes that contribute to the calculated $I(q)$, at 3% (gold coloured surface) and 0.7% (orange coloured surfaces) above the MFT critical temperature. An arrow shows one of the MFT ordering wavevectors. Figure taken from Ref. [250].

5.3 Other Rare Earth Garnets

The rare earth garnets have received very little attention, compared to say the pyrochlore materials. This is perhaps because the bulk of them seem to exhibit fairly mundane behaviour, i.e. the expected long range order. There are however, exceptions, the most notable being $Gd_3Ga_5O_{12}$ or GGG. In many cases, experimental studies have failed to identify the ground state ordering simply for lack of suitable base temperature (see for example [258, 259]). A summary of three types of rare earth garnets that have been measured is given in Table 5.2. We have ignored several other types of rare earth garnets, particularly the rare earth iron garnets or $R_3Fe_5O_{12}$, since they should be expected to show rather different physics – for one, the iron ions are also magnetic. For the most part, those rare earth garnets studied to low enough temperatures exhibit antiferromagnetic ordering although there are a few cases that exhibit some fairly unique physics.

The in-field phase diagram of the material $Dy_3Al_5O_{12}$ received quite a bit of attention in the past [260, 261, 262]. It displays antiferromagnetic ordering in zero field, but also exhibits a phase of mixed antiferromagnetic and paramagnetic ordering between the fields along the [111] direction of roughly 0.4 T and 0.7 T (though this depends on the demagnetization factor of the crystal studied). The materials $Tb_3Ga_5O_{12}$ and $Ho_3Ga_5O_{12}$ have

been suggested to have antiferromagnetic order that is induced by the nuclear hyperfine coupling [263].

More recently, $Ho_3Ga_5O_{12}$ has been shown to have an exotic ground state with neutron scattering experiments [181]. As with many geometrically frustrated systems, there is a higher temperature onset of short range antiferromagnetic order, in this case around 0.6 K. Then at a lower temperature of 190 mK [264] or possibly as high as 300 to 400 mK [181], there is a transition to a state consisting of mixed short range order and long range order [181].

In close competition with GGG for the most unusual rare earth garnet is $Yb_3Ga_5O_{12}$. This material shows a sharp first-order phase transition at 54 mK [265]. Surprisingly, below this transition, no long range magnetic order is found, suggesting that it is a state of hidden order or a spin liquid [110]. Similar behaviour is observed in the pyrochlore material $Yb_2Ti_2O_7$ which shows a sharp transition at 214 to 250 mK [266] yet also does not exhibit long range magnetic order even at very low temperatures. The authors of Ref. [110] have noted that the first-order phase transitions in $Yb_2Ti_2O_7$ and $Yb_3Ga_5O_{12}$ account for a very small percentage (less than 20%) of the total entropy $R \ln 2$, with the remainder accounted for by the higher temperature short range ordering. In contrast, the materials $Gd_2Sn_2O_7$ and $Gd_2Ti_2O_7$ for example, which have LRO ground states, have transitions accounting for a much larger percentage of the total entropy, in that case $R \ln 8$. Thus Dalmas de Réotier *et al.* suggest that there is a direct correlation between the entropy of the transition in geometrically frustrated magnets and the ground state ordering, or lack thereof [110].

Finally, it is worth mentioning the material $Na_4Ir_3O_8$. While not a garnet, it consists of a related lattice of corner sharing triangles known as the hyperkagome lattice. This material has recently been found to possess a spin liquid ground state [267, 111].

5.4 Experimental Parameters

In order to further explore the unusual phenomenology of GGG, we have undertaken measurements of the specific heat, C, of three different Gd garnet compounds, which while similar in model, show very different magnetic behaviour. We have measured the specific heat of an isotopically pure sample of GGG to investigate two possible explanations for its paradoxical properties: first, that the formation of order might be unique to the isotopically pure sample which might therefore show an ordering transition in C where a non-isotopically pure sample would not and second that previous experiments might have missed a particularly small or narrow feature in C indicative of a phase transition. We have also measured the heat capacity of the materials, $Gd_3Te_2Li_3O_{12}$ (GTLG) and $Gd_3Al_5O_{12}$ (GAG) which possess the same lattice symmetry and magnetic ion as GGG, but naturally

Table 5.1: Ordering types and transitions for rare earth garnet materials.

R^{3+}	$R_3Ga_5O_{12}$	$R_3Al_5O_{12}$	$R_3Te_2Li_3O_{12}$
Pr^{3+}	? [258]		? [259]
Nd^{3+}	$T_C = 0.514$ K [268]		
Sm^{3+}	$T_C = 0.960$ K [268]		
Eu^{3+}	? [258]		
Gd^{3+}	Spin glass [7]	$T_C = 175$ mK $*$	$T_C = 243$ mK $*\dagger$
Tb^{3+}	? $T_C = 0.25$ K [264, 269] †	$T_C = 1.35$ K [270, 263, 271]	? [259]
Dy^{3+}	$T_C = 0.373$ K [272, 268]	$T_C = 2.53$ K [260, 261, 262]	$T_C \simeq 2$ K [259]
Ho^{3+}	Mixed LRO/SRO [181] $T_C = 0.19$ K [264]	$T_C = 0.839$ K [273] $T_C = 0.95$ K [263]	? [259]
Er^{3+}	$T_C = 0.79$ K [270, 268]		? [259]
Yb^{3+}	Hidden order [110] † $T_\lambda = 54$ mK [265, 272]		? [259]

Table 5.2: Compilation of results in zero field on various rare earth (R_3) garnets with either Al_5, Ga_5 or Te_2Li_3. If not otherwise stated, the ordering is found or assumed to be antiferromagnetic. Materials labeled with a question mark (?) have been studied but not to low enough temperatures to determine the ground state ordering (or lack thereof). Materials marked $*$ are results from this work. Materials marked † show clear first-order phase transitions observed whereas the others are either continuous phase transitions or weakly first-order.

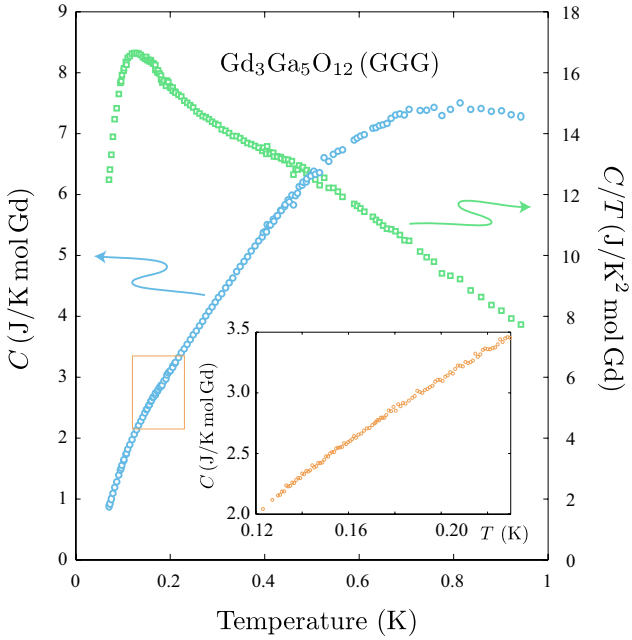

Figure 5.4: Specific heat (C) and C/T of isotopically pure GGG measured with coarse temperature resolution. Results match well with previous work [7]. The temperature region marked with a red box has been remeasured with a high temperature resolution shown in the inset and again does not find evidence of an ordering transition.

have different exchange interactions. The magnetic susceptibility of GTLG has been measured previously and an ordering transition was observed at around 250 mK [259]. Finally, in order to test the effects of chemical disorder on GTLG, we have measured a sample of GTLG where the Gd^{3+} ions have been slightly diluted with 2% non-magnetic Y^{3+} ions, or $Y_{0.06}Gd_{2.94}Te_2Li_3O_{12}$.

A single crystal of $Gd_3Ga_5O_{12}$ (GGG) was obtained from Oleg Petrenko at the University of Warwick. This material is somewhat unique in that it was made with isotopically enriched ^{160}Gd to avoid the high neutron absorption of other isotopes of Gd and to thereby enable neutron scattering studies.

The synthesis of the GGG sample is described in Ref. [257]. First, polycrystalline samples were grown by a solid diffusion reaction of Gd_2O_3 and Ga_2O_3 at a temperature of 1400°C for 12 hours then regrinding. The regrinding process was repeated until X-ray diffraction showed no impurity peaks. 99.98% isotopically pure ^{160}Gd (supplied by Oak Ridge National Laboratory) was used to create a sample that would have negligible

neutron absorption. The single crystal GGG that we have studied, was grown form the polycrystalline GGG with the floating zone method in a two mirror infrared image furnace.

The polycrystalline garnet samples that are studied in this work were obtained from Linton Corruccini at the University of California-Davis. Those samples include the garnets $Gd_3Te_2Li_3O_{12}$ (GTLG), $Gd_{2.94}Y_{0.06}Te_2Li_3O_{12}$ (dirty GTLG) and $Gd_3Al_5O_{12}$ (GAG).

The polycrystalline samples of GTLG and GTLG diluted with Y, were prepared through solid state reaction in air. The Te and Gd (Y) oxides and Li carbonate were mixed, pressed into pellets and fired at 850°C for 10 hours. They were then reground and fired a second time. Once again, powder x-ray spectra were taken and indexed to the expected space group $Ia\bar{3}d$, with no impurity peaks visible at the 1% level. The preparation of these samples is also described in Ref. [259].

The GAG sample was prepared using the sol-gel method, as described in Ref. [274]. It was heated to 1350°C for one hour, then removed from the furnace and rapidly quenched to room temperature, to minimize the formation of the perovskite phase $GdAlO_3$ [275]. In x-ray spectra taken on GAG, two impurity peaks were visible at the 3% level, which are attributed to $GdAlO_3$.

In the case of GGG, an initial measurement of the specific heat was made over a large temperature range (from 80 mK to 930 mK) using temperature steps of roughly 5 mK below 200 mK and temperature steps of 10 mK above 200 mK. A later measurement with a much higher temperature resolution of 1 mK was performed over the temperature range 130 mK to 230 mK to search for small or narrow features near where the neutron scattering peaks were discovered. This choice of resolution is based on scaling results of well characterized antiferromagnets (such as in Ref. [276]) to a transition temperature of 140 mK, suggesting one might expect a peak in C with a width of only several mK. GTLG and GAG were measured with variable temperature resolution, depending on the features observed.

5.5 Results

Results of our specific heat measurements on GGG, shown in Fig. 5.4, agree remarkably well with the previous specific heat measurement (on a single crystal containing naturally abundant Gd) of Schiffer *et al.* [7]. This suggests that the isotopically pure sample measured here exhibits the same physics as do naturally abundant Gd containing samples. We find a broad feature with a maximum at around 800 mK. This feature seems to drop out at lower temperature roughly as $T^{0.8}$ until around 125 mK, at which point there is a maximum in C/T and $C(T)$ becomes steeper. The high-resolution scan of C also did not reveal any anomalies that might be interpreted as an ordering transition, as shown in the inset of

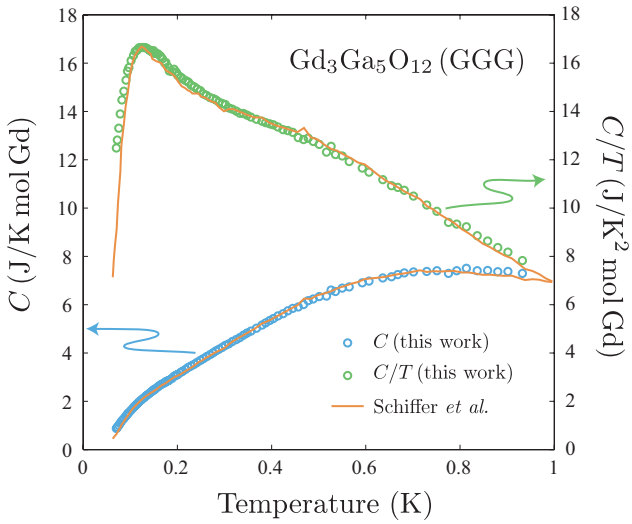

Figure 5.5: The specific heat measured in this work compared with that previously measured by Schiffer *et al.* [7]. The agreement is excellent for the most part. At the lowest temperatures, the specific heat of Schiffer *et al.* drops out slightly faster than our specific heat.

Fig. 5.4. The specific heat measurement of Dunsiger *et al.* on a naturally abundant Gd, powder sample is very similar, though the peak in C/T is found to be more pronounced [9].

Taking into account higher temperature data of other groups [9, 242], we can see that much, if not all, of the entropy ($R \ln 8 = 17.29$ J/K mol Gd) is accounted for in this system. Roughly 16 J/K mol Gd is picked up by integrating C/T from low temperature to about 2 K but more would be accounted for with an extension to higher temperature. Thus, if there is any residual entropy in this system, it is a very small fraction of the total $R \ln 8$ and would be quite difficult to precisely evaluate.

In stark contrast to GGG, GTLG shows a sharp ordering transition at 243 mK as shown in Fig. 5.6. The transition is clearly first-order, exhibiting a much larger feature in C than could be expected for a continuous phase transition and impossible to fit with any reasonable critical exponents. With a Curie-Weiss temperature $\theta_{CW} \simeq -2.7$ in GTLG [259], this ordering temperature gives a frustration index $f = \theta_{CW}/T_C = 11$. Below the transition, C drops out faster than T^3 suggesting that it is exponential and that there are gapped spin wave excitations, as would be expected from LRO with a strong dipolar interaction [178]. Gapped spin waves should result in the low temperature limit $C \propto T^{-2} e^{-\Delta/T}$, thus we have shown a plot of CT^2 vs. $1/T$ in inset (b) of Fig. 5.6 and the resulting fit which gives

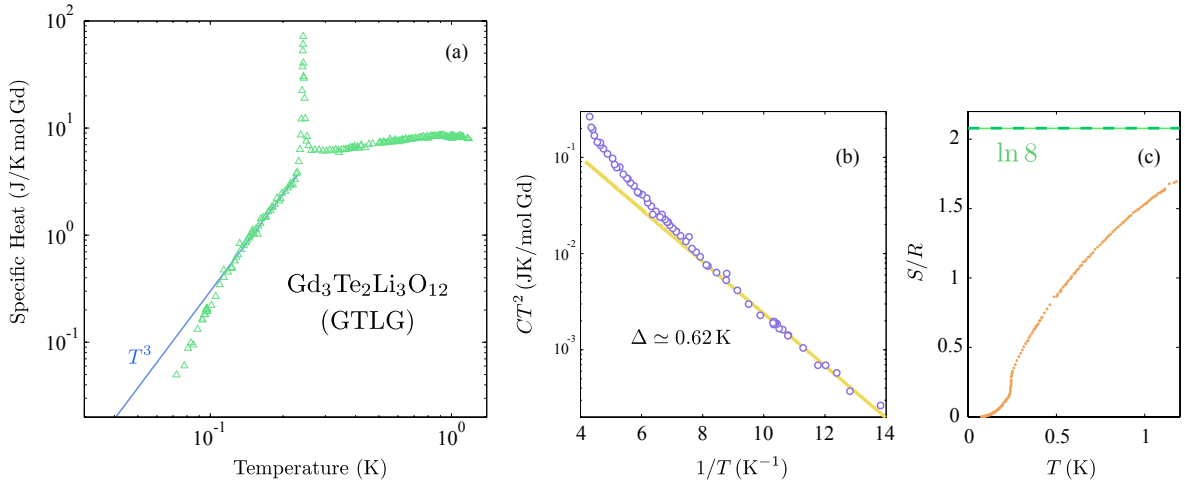

Figure 5.6: (a) Specific heat of GTLG showing a sharp first-order phase transition. The specific heat drops out more quickly than T^3 below T_c. (b) A plot of CT^2 as a function of T^{-1} and a linear fit suggestive of spin waves with a gap of $\Delta = 0.62$ K. (c) The entropy as a function of T compared with the total $R \ln 8$ entropy in the system.

$\Delta \simeq 0.62$ K.

For the material $Gd_2Sn_2O_7$ (GSO), discussed in Chapter 4, which shows a similar exponential drop in specific due to gapped spin waves, an upturn becomes noticeable at temperatures close to 100 mK, resulting from the nuclear electric quadrupole interaction. Why is that same upturn not seen in the GTLG data presented here? This can be easily explained by the fact that GTLG has a much lower transition temperature than GSO which orders at around 1 K. Thus by the time one reaches temperatures close to 100 mK, the exponentially dropping electronic specific heat of GSO has gotten very small, exposing the high temperature tail of the nuclear specific heat. In GTLG, 100 mK is not so much lower in temperature than T_C, thus the electronic specific heat is much larger at that point, obscuring the nuclear contribution.

Above the transition in GTLG, there is a broad feature centred around roughly 1.0 K, similar to the broad feature in GGG centred at $\sim$ 0.8 K. This is likely a signature of the development of short range correlations. Obtaining the entropy (S) from a numerical integral of C/T shows that only about 14% of the total $R \ln 8$ entropy in the system is accounted for by the transition, as shown in inset (a) of Fig. 5.6.

The third material studied here, GAG, may represent a point in between GGG and

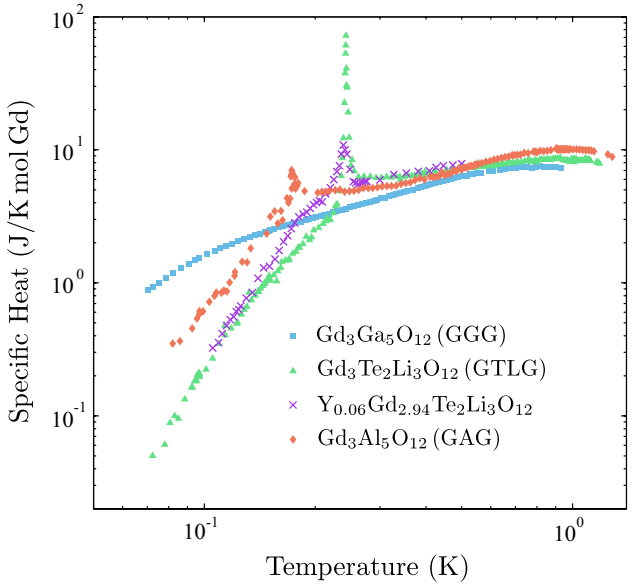

Figure 5.7: Comparison of the specific heat of GGG (blue squares), GTLG (green triangles), GAG (red diamonds) and a sample of 2% diluted GTLG (violet x's).

GTLG with a smaller and broader transition at a lower temperature of 175 mK (shown in Fig. 5.7). With $\theta_{CW} \simeq -3.0$ K [277], it is more antiferromagnetic than the other two garnets, but seemingly more frustrated than GTLG, with a frustration index $f = 17$. Otherwise, it shows similar features to GTLG, with a broad maximum centred around 1 K and a steeply dropping specific heat at lower temperatures. As in GTLG, the transition in GAG accounts for only a small percentage of the total $R \ln 8$ entropy in the system.

Lastly, the 2% diluted GTLG sample showed a significantly broadened peak at a slightly lower temperature than that of the pure material, as shown in Fig. 5.7. At temperatures well below and well above the transition, the heat capacities of the pure and diluted samples match up, and the transition accounts for the same amount of entropy in both systems, suggesting that the ground state ordering is not appreciably altered by the 2% impurity. A broadening of the peak in specific heat is an expected consequence of weak disorder.

5.6 Discussion

In conclusion, despite their similar models, we find GTLG and GAG to in fact behave entirely differently from GGG. The only commonality in all three systems is the broad

feature signaling short range correlations at around 0.8 K in GGG and 1.0 K in GAG and GTLG. The lower temperature of the broad feature in GGG is consistent with its smaller nearest-neighbour exchange interaction $\mathcal{J}_1 = 0.107$ K [242] as compared to $\mathcal{J}_1 = 0.126$ K for GTLG [259] and $\mathcal{J}_1 = 0.142$ K for GAG [277].

The sharp features observed in GTLG and GAG are in all likelihood signatures of transitions to long range order. As discussed above, the majority of insulating rare earth garnets studied [268, 261, 269] exhibit transitions to long range order. The notable exception is $Yb_3Ga_5O_{12}$, which, like $Yb_2Ti_2O_7$, has a sharp transition to some kind of spin liquid or "hidden order" ground state, perhaps analogous to a liquid-gas transition. Similar to those materials, the transitions in GTLG and GAG account for less than 14% of the total $R \ln 8$ entropy available. Thus the conjecture of Dalmas de Réotier *et al.* [110] mentioned in Section 5.3, would imply a spin liquid ground state for GTLG and GAG. However, indications of well-defined excitations below the transitions (characterized by an exponential drop in the specific heat) provide strong evidence of long range order. The Yb pyrochlore and garnet are most likely exceptions to the rule – a sharp peak in the specific heat of a magnetic material is almost universally an indication of a transition to an ordered state. These Gd garnets are very reminiscent of the Gd pyrochlore material $Gd_2Sn_2O_7$ which also shows a sharp first-order phase transition to a ground state exhibiting static magnetic order and well-defined excitations as seen by neutron scattering [185] and specific heat experiments [178], which is discussed in Chapter 4.

The materials GTLG and GAG clearly do not share the same glassy physics as GGG since spin glasses are universally found to *not* exhibit a sharp peak in C [25]. These results prove that the glassy physics of GGG is not a ubiquitous property of Gd garnets and we are therefore left with two possible conclusions. First, a very precise tuning of the parameters of the Hamiltonian may be required in order to produce the necessary competition between local and long range interactions to give rise to a magnetic analog of the glass transition, even without quenched disorder. GTLG and GAG may be outside this narrow "window" of required parameter space. However, in many glass forming liquids (see for example [278]) it is found that tuning interaction strengths, for instance by altering the substituents of molecules, without changing the overall symmetry of those molecules, does not tend to preclude a glass transition.

A strong and likely alternative is that it is indeed a sensitivity of the system to small levels of disorder that results in a spin glass transition in GGG. However, since the ordered ground state of GTLG appears to be robust against small levels of random dilution, it seems that the *type* of disorder may be the crucial ingredient in the exotic behaviour of GGG. In other words, the off-stoichiometry found in GGG may be a much more powerful way to introduce random frustration and trigger a spin glass transition than simple dilution of the magnetic moments. Certainly this would be a valuable hypothesis to investigate

theoretically and experimentally in future work. Obtaining a quantitative understanding of how the off-stoichiometric defects interact with the other spins would be key to determining how important that type of disorder truly is. Finding a way to eliminate the off-stoichiometry in GGG or introduce it to other Gd garnets would be ideal, though it is unclear at this time, how such results could be achieved.

Chapter 6

Conclusion

While this thesis may seem to be composed of three isolated results on disparate systems, as a whole it demonstrates just how many interesting and unusual results can come about in magnetic systems that are, at their core, some of the simplest materials possible. $LiHo_xY_{1-x}F_4$ is a nearly perfect Ising model and the Gd^{3+} containing compounds studied here are some of the best possible realizations of the isotropic Heisenberg model. Yet, numerous surprises have come about in studying these simple materials and much remains to be explained. These systems are exemplary demonstrations of the complexity that can arise from very simple building blocks, the understanding of which is one of the main goals of physics.

Much of the exotic antiglass physics of $LiHo_xY_{1-x}F_4$ may have been found to be erroneous through our measurements of the ac susceptibility and specific heat, but it has been replaced by a number of other interesting results and questions. What is the explanation for such long time scales and why do they increase at low concentration? What is the cause of a concentration independent peak in the specific heat? Why have experimental groups seen so many different results and made such different conclusions about this system? We have given qualitative arguments for what we think may be the origin of these effects, but hopefully quantitative explanations will arrive in the near future.

In $Gd_2Sn_2O_7$, our measurements show an excellent agreement with theory and portray a very simple picture of a classical Heisenberg system, with conventional long range order and gapped magnon excitations as a result of the dipolar interaction. However, this simple picture makes the observation of PSDs in Mössbauer and μSR measurements all the more confusing. How can a system that clearly exhibits gapped spin waves have temperature independent spin dynamics?

In studying GGG and related materials, we have reproduced physics of a very exotic material and found several others that behave completely conventionally. Again, the discovery

of fairly ordinary physics in these new Gd garnets makes the unconventional glassiness in GGG all the more puzzling. Specifically, the resilience of GTLG and GAG in the face of quenched disorder imply that the off-stoichiometry in GGG is a very special type of disorder, or that GGG is a very special material with the perfectly tuned Hamiltonian to give rise to intrinsic glassiness.

These three systems (chapters) have touched on some of the most important themes in the study of magnetism. We have dealt with strong disorder in the case of Ho:YLF and weak disorder in the case of the garnets. In fact, disorder may yet play a role in the eventual explanation of PSDs in GSO as it is becoming realized how important it can be in rare earth pyrochlore oxides (see Appendix E for example). Our second theme, geometric frustration, is at the heart of the physics of the pyrochlore GSO and the Gd garnets. Although GSO eventually overcomes its geometric frustration, with the aid of the dipolar interaction, the unusual ground state seen with local probes may be a remnant of those competing interactions. The physics of GGG is entirely dependent on frustration, either through a sensitivity to disorder or through a frustration induced glass state. Of course frustration of the random variety also plays an important role in spin glasses like $LiHo_xY_{1-x}F_4$.

Finally, we come to the theme of dipolar interactions, that could be more broadly defined as the issue of long range interactions. This theme applies quite significantly to all three problems that we have tackled in this thesis. Clearly, it is most essential to the physics of $LiHo_xY_{1-x}F_4$, which is, after all, a *dipolar* magnet. In the garnets studied, it is of comparable importance to the nearest-neighbour exchange interaction and we have hypothesized that it could be the frustrating influence that creates a glassy state analogous to that of structural glasses and supercooled liquids. In $Gd_2Sn_2O_7$, the dipolar interaction is also crucial, selecting the particular Palmer-Chalker ground state of the system and creating an anisotropy to spin wave excitations that we have indirectly observed.

6.1 Future Work

$\mathbf{LiHo_xY_{1-x}F_4}$

The work in this thesis has raised a number of conceptual questions regarding the low concentration limit of $LiHo_xY_{1-x}F_4$. The observation of very slow dynamics, the characteristic time constant of which is inversely correlated with x, has indicated the importance of single ion physics. While a number of theoretical works have delved deeper into understanding the impact of the hyperfine interaction and random fields in transverse field Ising models, there have not been many quantitative calculations regarding the low x limit

in zero field. It would be very useful, for example, to develop some quantitative understanding of relaxation time scales, even for small clusters or isolated ions. From a more phenomenological point of view, it would be exciting to be able to make use of the added information available in the relatively narrow absorption spectra of these materials, to test various ways of parametrizing the data.

Of course experimentally, there is still much exploring to do. On the x-axis of the phase diagram, we still have 12% and 25% Ho samples available for study. The 12% sample is not expected to present any qualitatively different physics from what we have already seen, but would certainly add a useful data point. The 25% sample, on the other hand, may show some very interesting physics indeed as it is uncertain whether it should be a spin glass or a ferromagnet. Even once that is discovered, it is likely that it will possess some exotic properties by virtue of its proximity to x_C. If it is to the left of x_C, for example, it may be more of a cluster glass than a spin glass. If it is on the FM side of x_C, it may still exhibit a fair bit of glassiness or even reentrance into a spin glass state at low temperatures.

Applying a transverse field to $LiHo_xY_{1-x}F_4$ has never failed to unearth very interesting physical problems, and could likely do so again. While the group of Rosenbaum and Aeppli [149, 121, 141, 148, 157] have left very few parts of the phase diagram unexplored, it seems that we could still make an impact with transverse field measurements in the low-concentration regime. One advantage of transverse field measurements is that they significantly speed up the dynamics [125], making experiments less time consuming.

Finally, we could consider in future work, cementing our conclusion that 1.8%, 4.5% and 8.0% samples have spin glass transitions, with measurements of the nonlinear susceptibility. Caution is merited, however. As discussed in Chapter 3, such a measurement would be very difficult to either achieve in the proper dc limit or to interpret correctly, owing to extremely slow dynamics.

$Gd_2Sn_2O_7$

As far as our measurement capabilities are considered, $Gd_2Sn_2O_7$ is largely resolved. It seems that a second look at the ground state of this material with those techniques that originally found PSDs, or a complementary technique, is warranted. The same analysis could be carried out on the related materials $Gd_2Ti_2O_7$, $Gd_2Zr_2O_7$ and $Gd_2Hf_2O_7$. GTO would be particularly interesting, but the experiment is more challenging as a T^2 dependence already persists to much lower temperatures. The last two Gd pyrochlores mentioned have not been studied with μSR or Mössbauer experiments to look for PSDs at this point in time.

It is worthwhile mentioning, as well, that GSO has not been studied in magnetic field. GTO has quite a rich H-T phase diagram, even powder samples, thus it would be inter-

esting to see if that is also the case for GSO.

Gd Garnets

Having studied a homologous series of Gd garnets and some of the effects of disorder, we are left with two possible conclusions: either the off-stoichiometry of GGG is a special kind of disorder or the Hamiltonian of GGG is perfectly tuned to give an intrinsic spin glass state or an increased sensitivity to disorder. Obviously we would suggest that future work on these materials should attempt to differentiate between these two possibilities.

In principle, it should be possible to analyze theoretically what the effects of an off-stoichiometry would be. However, it is likely that some additional information would be required: that is, how does a Gd ion interact with other Gd ions when it is residing on a Ga site? It is certainly reasonable to assume that the exchange interactions may be different and this information would be crucial to performing any calculations. The determination of such a number from 1% of the spins may be difficult though might be achievable with a probe such as ESR.

Otherwise, testing these conclusions might require finding a way to either eliminate the off-stoichiometry in GGG or introduce it to the other materials GTLG and GAG. There may be other Gd garnets available that might help clear up this problem. $Gd_3Sc_2Ga_3O_{12}$ (GSGG) certainly exists [279] and has not, to our knowledge, been studied at low temperatures. It might provide a slightly different off-stoichiometry or, even more interestingly, a similar ground state to GGG without any off-stoichiometry.

Appendix A

Demagnetization Correction and Effects of Sample Geometry

Measurements of the magnetic susceptibility are complicated by the so-called demagnetization effect [280]. Essentially, the magnetization of the sample is a result of both the external magnetic field and the demagnetizing field which is, somewhat cyclically, generated by the magnetization. Suppose we have a sample, which is magnetized with magnetization $\boldsymbol{M}$. This magnetization will lead to a magnetic field $\boldsymbol{B}_D$, known as the demagnetizing field, according to (in CGS units)

$$\boldsymbol{B}_D = -4\pi N \boldsymbol{M}$$

where N is the demagnetization factor of the sample. This demagnetizing field will only be uniform if the sample is an ellipsoid. Now the total magnetic field 'felt' by the sample is the sum of the external, applied magnetic field and the demagnetizing field, so $\boldsymbol{B}_{\text{Ext.}} + \boldsymbol{B}_D$. But if our applied magnetic field is relatively small and if we are not dealing with a ferromagnet which might have spontaneous magnetization, we can assume that the magnetization will be proportional to the total magnetic field in the sample, with a proportionality factor that is defined as the magnetic susceptibility χ. Thus, we have

$$\boldsymbol{M} = \chi(\boldsymbol{B}_{\text{Ext.}} + \boldsymbol{B}_D). \tag{A.1}$$

Our measurement apparatus is really measuring $\boldsymbol{M}$ and if we naively assume that there is no demagnetization effect, we would determine an apparent susceptibility χ_A given by

$$\chi_A = \boldsymbol{M}/\boldsymbol{B}_{\text{Ext.}} \tag{A.2}$$

Combining all these equations, we obtain the relation

$$\frac{1}{\chi} = \frac{1}{\chi_A} - 4\pi N \tag{A.3}$$

or

$$\chi_A = \frac{\chi}{1 + 4\pi N\chi}. \tag{A.4}$$

Thus it can be seen that if the demagnetization factor N is large and χ is large, then the apparent susceptibility will be reduced quite significantly. This effect will, for example, round peaks in the susceptibility at phase transitions. If χ is very large or diverges, the apparent susceptibility will asymptotically approach the demagnetizing limit of $1/4\pi N$.

The demagnetization factor, N, is dependent on sample geometry. For ellipsoids with semi-major axes of a, b and c, the demagnetizing field is constant throughout the sample and the demagnetizing factor can be related to the ratios a/c and b/c. There is no closed form expression for the demagnetization factor of an arbitrary ellipsoid. For a sphere, however, $N = 1/3$. As the z-axis of the crystal (the axis along which the magnetic field is applied) gets much longer than the other axes, $N \to 0$.

For rectangular prisms (which are used in this work) with sides of length a, b and c (the side along which the field is applied) and volume V, an analytic expression for the demagnetization factor is available [281]:

$$\begin{aligned}
\pi N = {} & \frac{b^2 - c^2}{2bc} \ln\left(\frac{V - a}{V + a}\right) + \frac{a^2 - c^2}{2ac} \ln\left(\frac{V - b}{V + b}\right) + \frac{b}{2c} \ln\left(\frac{A + a}{A - a}\right) \\
& + \frac{a}{2c} \ln\left(\frac{A + b}{A - b}\right) + \frac{c}{2a} \ln\left(\frac{\sqrt{b^2 + c^2} - b}{\sqrt{b^2 + c^2} + b}\right) + \frac{c}{2b} \ln\left(\frac{\sqrt{a^2 + c^2} - a}{\sqrt{a^2 + c^2} + a}\right) \\
& + 2 \arctan\left(\frac{ab}{cV}\right) + \frac{a^3 + b^3 - 2c^3}{3abc} + \frac{a^2 + b^2 - 2c^2}{3abc} V \\
& + \frac{c}{ab}\left(\sqrt{a^2 + c^2} + \sqrt{b^2 + c^2}\right) - \frac{(a^2 + b^2)^{3/2} + (b^2 + c^2)^{3/2} + (c^2 + a^2)^{3/2}}{3abc}.
\end{aligned} \tag{A.5}$$

The field distribution within the sample will, however, not be uniform. This is not expected to cause any problems in our measurements which are exclusively at low magnetic field, where the susceptibility is quite linear. Certainly, in spin glasses, as one approaches T_g, χ becomes quite nonlinear as χ_3 diverges. χ_3 only becomes significant relative to χ_1 very close to T_g or for large magnetic field. It is seen in our measurements that obtaining equilibrium near T_g requires extremely low frequencies. Thus in all of our measurements, our susceptibility is seen to be quite linear. In measurements of χ_3, the demagnetization effect may be quite important.

When studying glassy magnetic materials in particular, one must be concerned with the full complex susceptibility $\chi = \chi' - i\chi''$ which contains both the in-phase susceptibility $\chi'(\omega, T)$ and the out-of-phase susceptibility or dissipation $\chi''(\omega, T)$. The demagnetization

correction should now be written as

$$\frac{1}{\chi' - i\chi''} = \frac{1}{\chi'_A - i\chi''_A} - 4\pi N \tag{A.6}$$

The real and imaginary parts of this equation can be separated such that we should apply the following correction [57]:

$$\chi' = \frac{\chi'_A - 4\pi N(\chi'^2_A + \chi''^2_A)}{(1 - 4\pi N\chi'_A)^2 + (4\pi N\chi''_A)^2} \tag{A.7}$$

$$\chi'' = \frac{\chi''_A}{(1 - 4\pi N\chi'_A)^2 + (4\pi N\chi''_A)^2} \tag{A.8}$$

It can be see from the above equations that the demagnetization factor mixes the real and imaginary components of χ resulting in a phase shift. For glassy systems, $\chi'(\omega)$ is found to be 0 at high frequency and to saturate at some positive value at low frequencies. Meanwhile, $\chi''(\omega)$ shows a broad maximum around a frequency ω_{Max}. The apparent susceptibility will be altered by the demagnetization correction such that the peak in χ'' is pushed to higher frequencies and the overall magnitude of the susceptibility is lowered. This effect becomes more pronounced as the temperature is lowered and the overall susceptibility increases. Thus, it is clearly quite important to take into consideration the effects of demagnetization on the observed susceptibility of spin glasses if one is to attempt to pin down a glass temperature through dynamical scaling. It should be expected that demagnetization corrections should play just as significant a role, if not more, in measurements of the nonlinear susceptibility.

A.1 Calibration

For the 4.5% and 8.0% samples studied in this work, multiple sample geometries were studied. This was done partially to check for sample geometry effects beyond the expected demagnetization effect and partially to calibrate the susceptibility of the materials. For the 4.5% sample, temperature scans of two sample geometries were compared (shown in Figure A.1). The overall calibration factors used to determine the susceptibility for the two data sets were adjusted such that the two curves matched after correcting for demagnetization. The same method was used for the 8.0% sample, except that a frequency scan at a single temperature (120 mK) was used. Later modifications to the magnetometer made this labour intensive calibration procedure unnecessary. The magnetometer was changed so that the sample holder could be removed without taking anything else apart and

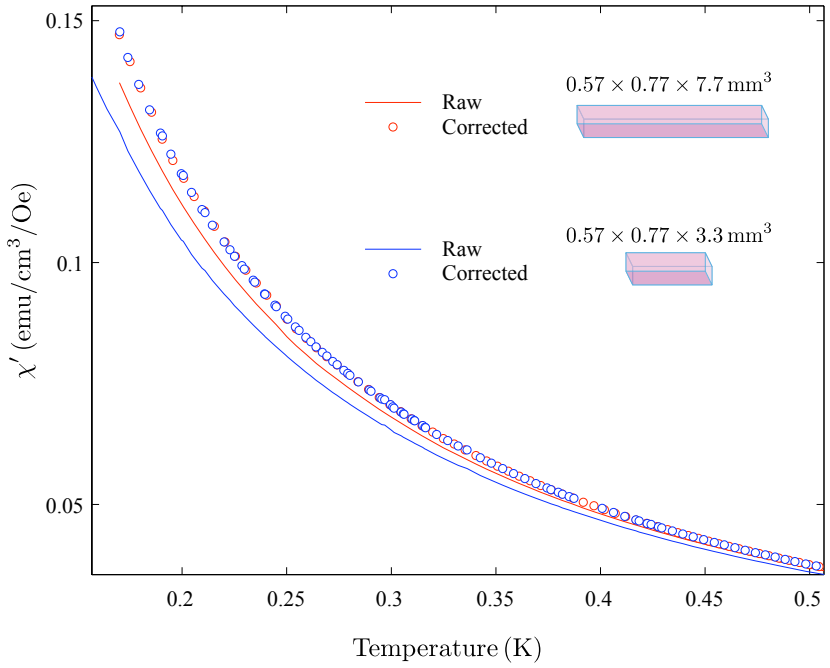

Figure A.1: The method of calibration used for the 4.5% sample. The susceptibility of two sample geometries was studied as a function of temperature, yielding two slightly different curves. The calibration factor was chosen such that the two curves matched after correcting for the demagnetization effect.

altering the calibration. Hence we could replace the sample with a perfectly diamagnetic superconducting Pb sample at 4.2 K in order to calibrate the system. This simpler method was performed for the 1.8% sample.

A third geometry of the 4.5% sample was studied to test the suggestion that differences between our data and those of Ghosh *et al.* could be a result of different sample geometries. Previously, we had worked with samples where $L_z > L_{x,y}$. This new sample was almost cubic: 1.2 mm on the c-axis, 0.57 and 0.77 mm on the other sides. Note the sample measured by Ghosh *et al.* [4] had a $2 \times 1 \times 1$ aspect ratio. Still, our results are very different from theirs, as shown in Figure A.2. Table A.1 shows the different sample geometries used in our work.

Reversing the demagnetization correction on the needle-shaped 4.5% sample to simulate what we should expect for our least elongated sample, we find that the results are very

x	L_z (mm)	L_x (mm)	L_y (mm)	$4\pi N$
0.080	7.44	0.94	0.66	0.60
0.080	2.59	0.94	0.66	1.61
0.045	7.7	0.77	0.57	0.49
0.045	3.3	0.77	0.57	1.11
0.045	1.2	0.77	0.57	2.68
0.018	5.84	0.89	0.61	0.71

Table A.1: Sample geometries of $LiHo_xY_{1-x}$ studied in this work.

close, but not perfect. This mismatch suggests that the overall calibration of our 4.5% data could be 10% too high. However, reducing the calibration by 10% does *not* impact the resulting glass temperature to within the error bars meaning that this slight mismatch does not affect the final analysis. Slight misalignment of the sample cut with respect to the c-axis could be responsible for the mismatch. The moments are very strongly Ising-like, thus the magnetization of the sample will always point along the c-axis. This means that rotation of the sample in the magnetometer, with respect to the applied magnetic field, will only reduce the overall signal, but will not affect the frequency or temperature dependence of the measured susceptibility. The overall signal would be dealt with in our calibration method so the alignment of the sample in the magnetometer is largely inconsequential. However, if the long axis of the sample is cut at an angle of several degrees away from the c-axis, the shape of the sample, relative to the magnetization axis, will be different resulting in a different (larger) demagnetization factor and leading to a mismatch between samples of different geometries.

A.2 Uncorrected Data

Since the calibration procedure described above, may not be perfect, we present here raw data that has not been corrected for demagnetization effects, shown in Figure A.4. We also show the change in the dynamical scaling analysis that results from not correcting for the demagnetization effect, in Figure A.3. For the 1.8% sample, there is very little change from the demagnetization correction, since the overall susceptibility is quite low. The 4.5% sample does have a noticeable change and different parameters are obtained in the dynamical scaling analysis: $T_g = 40$ mK, $z\nu = 7.9$ and $\tau_0 = 40$ s. Once the data is corrected, these values become $T_g = 42$ mK, $z\nu = 7.9$ and $\tau_0 = 16$ s. Thus there is a noticeable but not dramatic change in the results, with the exception of the time constant.

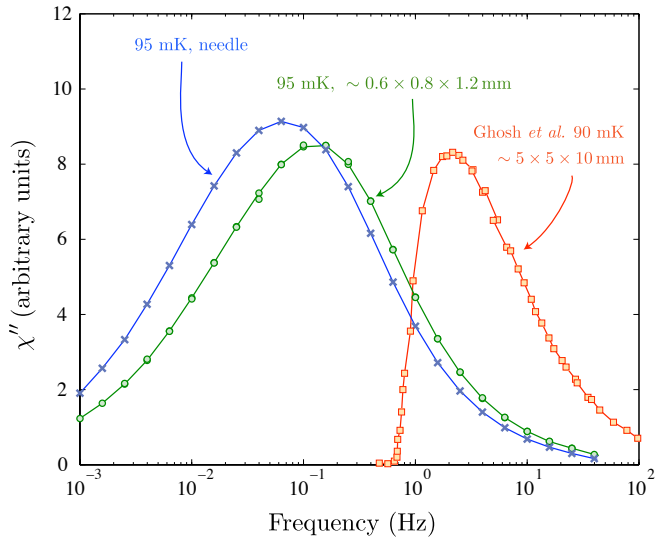

Figure A.2: The absorption spectrum $\chi''(f)$ at 95 mK for two different sample geometries measured by our group (raw data, not corrected for demagnetization). One sample (blue curve) is closer to needle-shaped, with dimensions $\sim 0.57 \times 0.77 \times 7.7$ mm^3, whereas the other sample (green curve) is less elongated with dimensions $\sim 0.57 \times 0.77 \times 1.2$ mm^3. A shift toward lower frequencies is observed as the sample geometry becomes more needle-like. Shown for comparison (red curve) is data from Ghosh *et al.* [4] on a sample with an aspect ratio of roughly $1 \times 1 \times 2$. The differences are remarkable and show that disagreement between our data sets are not related to sample geometry.

The error bars on the time constant are quite large to begin with (± 7 s) since the analysis is performed using $\ln \tau$. In fact the glass temperature is still the same within estimated error bars of ± 2 mK, and the exponent has not been altered. The shift in τ_0 is a result of the phase shift caused by the demagnetization effect.

The 8.0% sample is affected quite a bit more significantly. Without correction, the dynamical scaling analysis gives $T_g = 54$ mK, $z\nu = -8.2$ and $\tau_0 = 1.0$ s. These can be compared with the values $T_g = 65$ mK, $z\nu = -7.8$ and $\tau_0 = 0.12$ s obtained after correcting for demagnetization. The question becomes, just how dependent are we on the accuracy of the calibration and the demagnetization correction? Clearly for the 1.8% and 4.5% samples, there is very little change in the end results even if no demagnetization correction is considered. In the 8% sample, there is a significant change. To provide an idea of how sensitive the 8.0% sample is to demagnetization, increasing the overall magnitude of χ by

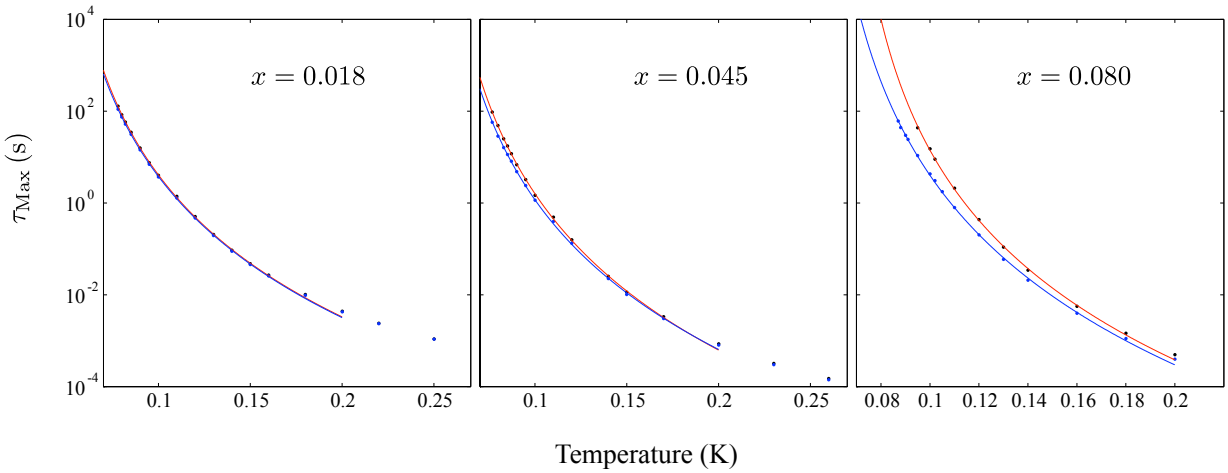

Figure A.3: The effect of the demagnetization correction on the peak positions τ_{Max} and therefore on the dynamical scaling analysis. Because of its small overall susceptibility, the 1.8% sample is barely affected by the demagnetization correction. The 4.5% sample shows a slight effect. The uncorrected data gives $T_g = 40$ mK and $\tau_0 = 40$ s, but with no change in exponent. The 8% sample shows quite a significant effect. The uncorrected data gives $T_g = 54$ mK, $z\nu = 8.2$ and $\tau_0 = 1.0$ s.

20% increases T_g by 5 mK and decreasing the magnitude of χ by 20% does not change the resulting T_g. Thus even the 8.0% results are fairly insensitive to errors in the calibration of the magnetometer. It is, nonetheless, very important to perform this correction as the raw data gives very different results.

It is clear that higher concentration samples must become very heavily affected by demagnetization. It is not clear whether Reich *et al.* [58] and Wu *et al.* [149] applied the same correction or not when measuring an $x = 0.167$ sample. It would certainly make a large difference in the determined glass temperature T_g.

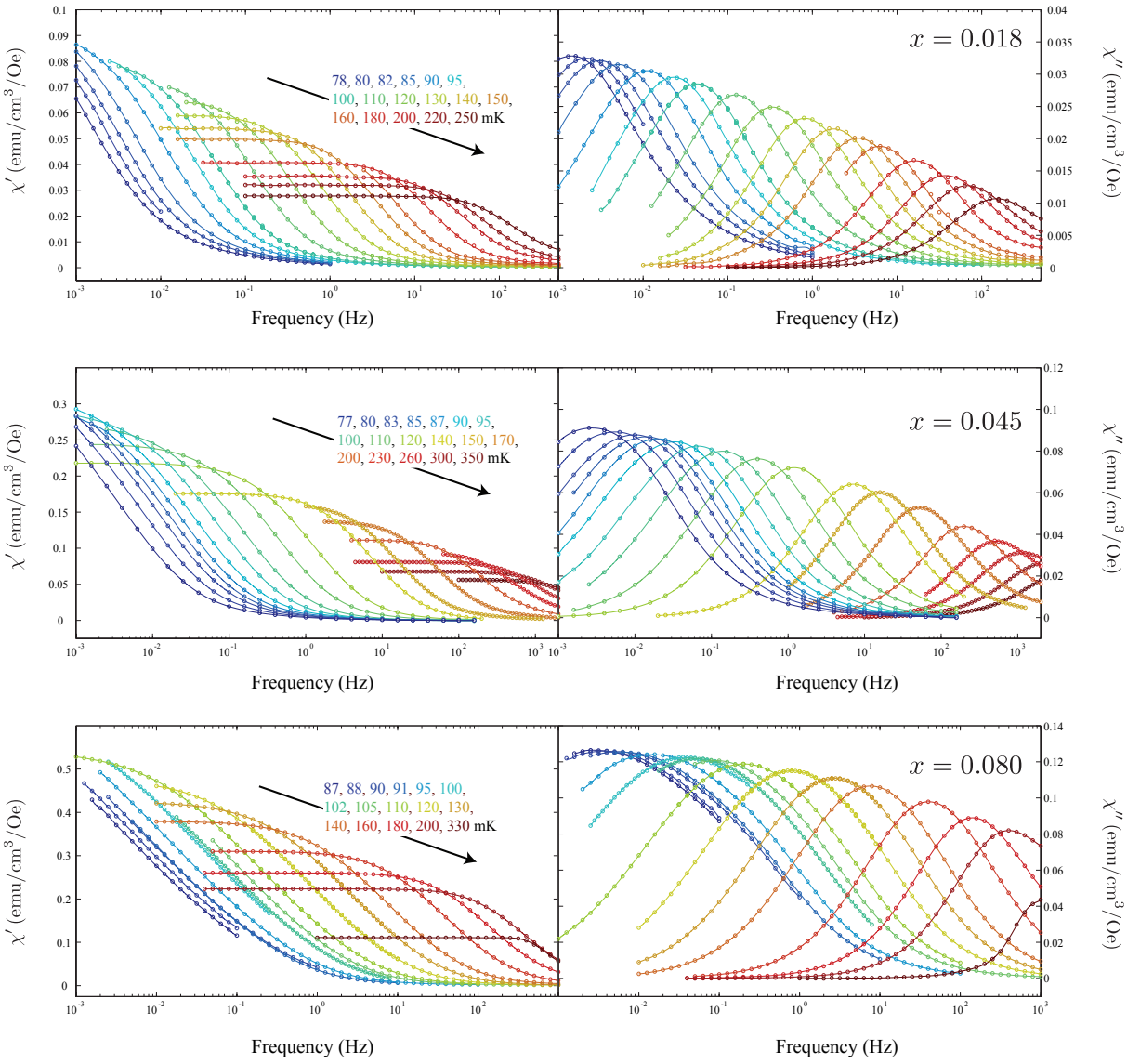

Figure A.4: Raw ac susceptibility data that has not been corrected for demagnetization (though does have the calibration applied as is described in the text). Note the 8% sample is close to reaching its demagnetizing limit, as seen by the leveling off of the maximum in χ''. The data shown here is taken on the samples that are close to needle-shaped.

Appendix B

Dynamical Scaling Fitting Procedure

The dynamical scaling analysis of $LiHo_xY_{1-x}F_4$ was performed using the peak frequency $f_{\rm Max}$ of the absorption spectrum $\chi''(f)$ to define the relevant time scale $\tau_{\rm Max} = 1/2\pi f_{\rm Max}$. An alternative method of choosing τ, suggested by Ogielski [76], is through the limit

$$\tau = \lim_{f \to 0} \frac{\chi''(f)}{f\chi'(f)}. \tag{B.1}$$

However, this limit is found to be very difficult to achieve for temperatures anywhere close to the glass transition. This is a result of the overall slowness of the dynamics in $LiHo_xY_{1-x}F_4$ as well as the breadth of the absorption spectra. In Figure B.1, we show $\chi''/f\chi'$ as a function of frequency, towards the low frequency end of our data (for a 4.5% sample). It is clear that to a frequency of 1 mHz, we are not able to obtain this limit for temperatures below 120 mK which is roughly $3T_g$. Using the $\tau_{\rm Max}$ method, we are able to approach to slightly lower than $2T_g$. This is still far from T_g, but significantly closer than with other methods.

More precisely, $f_{\rm Max}$ was obtained by fitting a quadratic curve to a 1 decade wide range of frequencies around the maximum sampled data point. This provides increased precision over simply choosing the maximum sampled value of χ'' (which would be only as precise as the data density, typically 1/10 of a decade).

Data 200 mK and below were used for the dynamical scaling fits. Above that temperature, $\tau_{\rm Max}(T)$ was no longer found to be adequately fit by a power law. This is perhaps not surprising given how far away from T_g it is. The fitting procedure involved defining an array of trial glass temperatures T_g. For each possible T_g, a linear least squares fit was performed to $\ln(\tau_{\rm Max}$ as a function of $\ln(T - T_g)$. This linear fit yielded τ_0 and $z\nu$ for a given T_g. The χ^2 statistic (not to be confused with the susceptibility) for each fit (each trial T_g) was determined, using error bars on the quadratic fits discussed above.

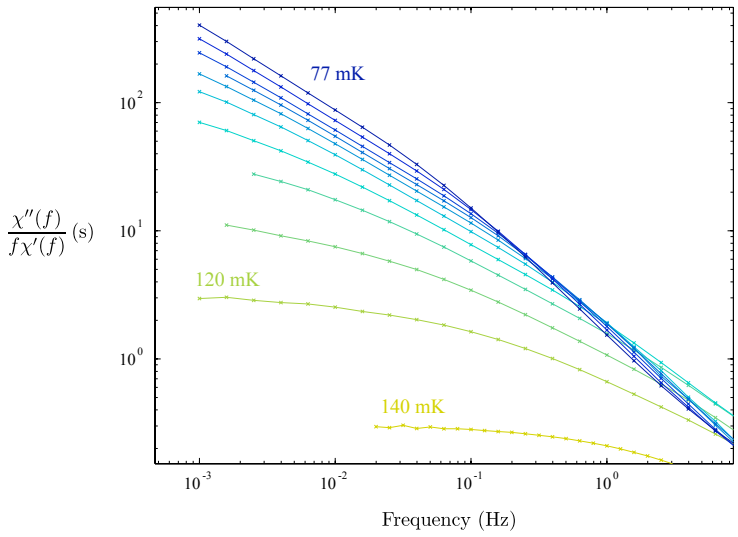

Figure B.1: A plot of $\chi''/f\chi'$ versus frequency for a 4.5% sample of $LiHo_xY_{1-x}F_4$. It can be seen that it is leveling off at the lowest frequencies studied only for temperatures above 120 mK.

The resulting $\chi^2(T_g)$ is plotted in Figure B.2 for the three different stoichiometries measured. Minimizing χ^2 allows us to choose the best fitting T_g, τ_0 and $z\nu$. The fit is, therefore, done with three free parameters. For the 4.5% and 8.0% samples, this gives an exponent $z\nu \simeq 8$, which is theoretically expected [76], and commonly observed in other spin glass experiments [26].

Using the values of χ^2 and the number of degrees of freedom permits estimation of the error bars on the fits. For the 4.5% and 8.0% fits, the error bars are similar, at around ± 2 mK and ± 3 mK on T_g, respectively (with a 68% or 1 σ confidence interval shown by the shaded regions). The 1.8% sample, however, results in a severely underconstrained fit, meaning that the data can be fit very well, but by a wide range of glass temperatures. This is clear from the plots in Figure B.2 given that the number of data points and therefore degrees of freedom are quite close between the different samples studied.

To further illustrate the fact that a dynamical scaling law is underconstrained in the case of the 1.8% sample, several fits to $\tau(T)$, constrained to different values of T_g, are shown in Figure B.3. The results are, at least visually, equivalently adequate. The reason that the 1.8% sample is so badly constrained may be related to curvature in the function $\tau_{\mathrm{Max}}(T)$. The more that function is curved, the closer one is to the glass temperature.

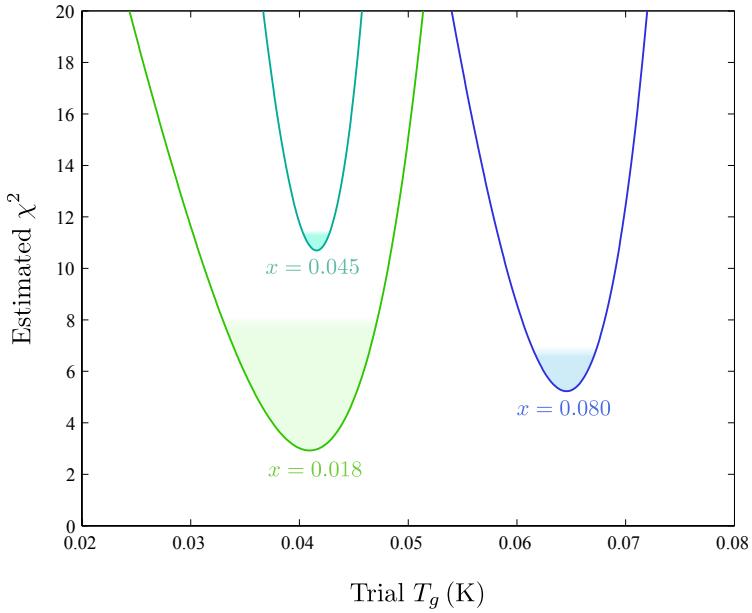

Figure B.2: The estimated χ^2 statistic as a function of trial glass temperature T_g. The glass temperature that minimizes χ^2 is chosen as the best fit T_g. The shaded areas correspond to the statistically relevant range of glass temperatures based on the number of degrees of freedom of the fits, choosing a confidence interval of 68% (roughly corresponding to 1 σ). Thus for the 4.5% and 8.0% samples, the error on T_g is roughly ± 2 mK and ± 3 mK, respectively. The 1.8% sample is much less constrained however, with a wide range of T_g adequately fitting the data (from perhaps 33 mK up to as high as 46 mK).

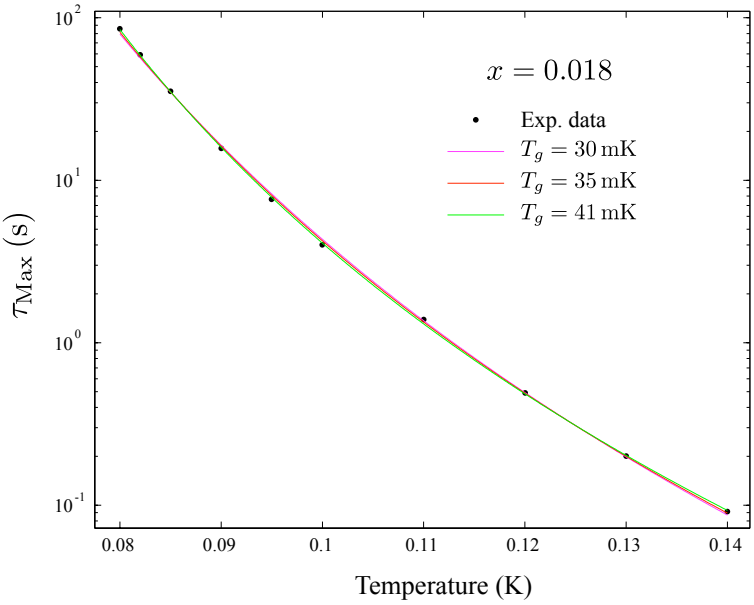

Figure B.3: The experimental data $\tau_{\mathrm{Max}}(T)$ is shown, along with several fits, constrained to different glass temperatures, T_g. $T_g = 41$ mK is the best fit, $T_g = 35$ mK is obtained by fixing $z\nu = 8.0$ and $T_g = 30$ mK is obtained from the best overlap of a scaling plot (Figure 3.16). In all cases, the fits are visually quite good, demonstrating that the best fit is rather unconstrained.

Thus if one is far from the glass temperature, there is less curvature and it is difficult to pin down a glass temperature. Even, given that argument, the range of acceptable glass temperatures for the 1.8% sample seems anomalously high, if one assumes that $T_g \propto x$. This is not necessarily a valid assumption. However with $T_g > 30$ mK for $x = 0.018$, it appears almost as if T_g will not go to 0 as $x \to 0$, an impossibility.

Appendix C

Modelling Thermal Relaxation in Powder Samples

When working with materials that have particularly poor thermal conductivity, as do polycrystalline insulators, and/or especially large heat capacity, it becomes important to consider heat diffusion [282] that manifests as thermal gradients and slow thermal relaxation within the sample. For example, one could simply imagine the sample to be a thin wire with one end weakly linked to the cryostat; as heat flows out of the sample, there will therefore be a gradient in the temperature from one end to the other. This is clearly a dramatic oversimplification. A sample with heat capacity density c (i.e. total heat capacity per volume) and thermal conductivity κ, will be governed by the heat equation [283]

$$\frac{\partial T}{\partial t} = \frac{\kappa}{c}\nabla^2 T \tag{C.1}$$

If the sample is isolated and so has no sources or sinks of heat, the sample's temperature distribution will behave in time as

$$T(\boldsymbol{r}, t) = \tilde{T} + \sum_{n=1}^{\infty} a_n e^{-t/\tau_n} f_n(\boldsymbol{r}) \tag{C.2}$$

where $\tilde{T}$ is the average temperature of the sample. The functions f_n are the various functions that satisfy the equation $\nabla^2 f_n = -(c/\kappa\tau_n) f_n$ and then the values of τ_n are determined based on boundary conditions. While the values of τ_n and the form of f_n are easily determined in certain shapes of sample, such as prisms and cylinders, more unusually shaped samples cannot be modeled analytically. What is clear, however, is that for a given geometry $\tau_n \propto c/\kappa$, illustrating the problems associated with samples of poor thermal

conductivity and high heat capacity. Furthermore, the τ_n's will increase roughly as $V^{2/3}$ where V is the volume of the sample, allowing the time constant to be significantly reduced by going to smaller sample size.

The parameter n is some arbitrary index chosen such that as n is increased, τ is decreased. Thus τ_n for large n will be very short and so fairly unobservable. Generally one will only notice at most, the first three or four time constants. When a heat pulse is given to the sample at $t = 0$, the shape of the heater and its location on the sample, roughly defines the initial temperature distribution and therefore selects the values of a_n. Again, for high n, a_n will be very small, unless the heater is tiny relative to the sample, since f_n will have a very small wavelength. The $n = 0$ eigenfunction could be thought of as simply constant or $f_0 = 1$, $a_0 = \tilde{T}$ with $\tau_0 = \infty$.

Connecting the sample to the cryostat via a weak thermal link, can be thought of as introducing a drain or sink. The power flowing through that drain, however, will be proportional to the temperature difference between the point on the sample to which it is connected and the cryostat. This will therefore alter the f_n's, the τ_n's and will make τ_0 finite therefore giving the sample an 'external' time constant of relaxation to the fridge temperature. There will also be an $f_0(\boldsymbol{r})$ distribution of temperature in the sample after all the faster relaxations have concluded. Finally the temperature will, as $t \to \infty$, approach the temperature of the refrigerator T_0. Thus the new behaviour of the sample will be

$$T(\boldsymbol{r}, t) = T_0 + a_0 e^{-t/\tau_0} f_0(\boldsymbol{r}) + \sum_{n=1}^{\infty} a_n e^{-t/\tau_n} f_n(\boldsymbol{r}) \tag{C.3}$$

In the limit $\tau_0 \gg \tau_1$, the function $f_0(\boldsymbol{r}) \simeq 1$ almost everywhere on the sample. In that case, $a_0 e^{-t/\tau_0}$ will be a good representation of the average temperature of the sample.

To see this more rigourously, let us write the heat equation including a source/drain

$$c\frac{\partial T(\boldsymbol{r}, t)}{\partial t} = \kappa \nabla^2 T(\boldsymbol{r}, t) + q(\boldsymbol{r}, t) \tag{C.4}$$

We can now say that the heat flow through the weak link ought to be proportional to the difference of the temperature of the sample where the link is connected and the fridge temperature T_0. For simplicity, T will just be considered relative to the cryostat temperature. Let us represent the contact of the link with the sample as occurring over a contact volume V_C and define a function $M(\boldsymbol{r})$ that acts as a mask so that it is equal to 1 inside that contact volume and 0 outside that volume. Then we can write the heat equation as

$$c\frac{\partial T(\boldsymbol{r}, t)}{\partial t} = \kappa \nabla^2 T(\boldsymbol{r}, t) + \frac{K}{V_C} M(\boldsymbol{r}) T(\boldsymbol{r}, t) \tag{C.5}$$

As usual, one can still apply separation of variables. The solution becomes the same as before, only the new spatial functions, call them g_n, are solutions of the equation

$$\mathcal{L}g_n(\boldsymbol{r}) = \left(\nabla^2 - \frac{KM(\boldsymbol{r})}{\kappa V_C}\right) g_n(\boldsymbol{r}) = -\frac{c}{\kappa\tau_n'} g_n(\boldsymbol{r}) \tag{C.6}$$

The most straightforward way to solve this equation is to take the f_n's, the solutions to the source-free heat equation in the relevant geometry, as our basis functions. We can then define matrix elements $\mathbf{L}_{mn} = \langle f_m|\mathcal{L}|f_n\rangle$ and diagonalize that matrix to obtain the eigenfunctions, the g_n's, and the eigenvalues, which will be equal to $-c/\kappa\tau_n'$. In the limit of an extremely poor connection to the cryostat, L will be diagonal with the entries $-c/\kappa\tau_n$. Introduction of a link of finite conductivity introduces the elements $-K\langle f_m|M(\boldsymbol{r})|f_n\rangle/\kappa V_C$. Thus, to first order, we end up with $\mathbf{L}_{00} = -K/\kappa V$ where V is the volume of the sample. This equates to a finite external time constant of

$$\tau_0 = \frac{C}{K} \tag{C.7}$$

where C is the total heat capacity of the sample. This is what we should expect to have for a perfectly conductive sample that is weakly linked to a heat bath with a link of thermal conductance K.

Now, depending on where the heater power is applied to the sample, where the weak link is positioned on the sample and where the thermometer measures the temperature of the sample, we can have different errors in our temperature measurement.

Our polycrystalline samples were cut as rectangular prisms, to a good approximation, so we shall model them as such. The prism will have sides L_x, L_y and L_z, taking one of the corners to be at $(0, 0, 0)$. We must replace our single subscript n with three indices $j, k, l = 0, 1, \ldots$. The unperturbed basis functions must satisfy the conditions that no heat can flow through the boundaries, thus

$$f_{jkl} = \cos(j\pi x/L_x)\cos(k\pi y/L_y)\cos(l\pi z/L_z) \tag{C.8}$$

The matrix elements of $\mathbf{L}$ and the initial condition a^0_{jkl} are then defined by the integrals over the regions where the weak link and heater are attached to the sample, respectively. Diagonalizing $\mathbf{L}$ gives the time constants τ_n' and the eigenstates, the g_n's. We will be most interested in g_0 since this will be the distribution of temperature within the sample after the other states have decayed. The form of g_0 will tell us how accurate our temperature measurement is by integrating it over a region where the thermometer is attached to the sample. If g_0 is close to f_{000}, i.e. almost constant, then our thermometer will be measuring something close to the average sample temperature. However, if g_0 has a large gradient,

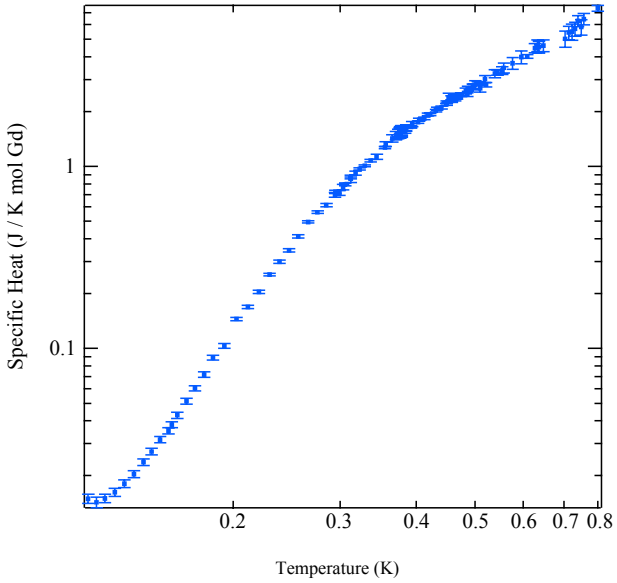

Figure C.1: A plot of the specific heat of $Gd_2Sn_2O_7$, including estimated error bars.

we may not have our thermometer optimally positioned to measure the average sample temperature.

This calculation has been performed for the sample geometry used for measuring a polycrystalline $Gd_2Sn_2O_7$ sample. For the PtW weak link that we employed, the external time constant τ_0 was approximately 20 times longer than the next longest time constant τ_1. This was determined through a double exponential fit of the data, ignoring earlier time data where faster time constants were significant. The sample was cut with sides of lengths $0.42 \times 0.52 \times 0.23$ cm^3. Using the positioning of the weak link and thermometer on the sample, and the procedure described above, we obtain the following results. When all of the internal time constants have subsided, leaving the distribution of heat in the sample well described by g_0 (the lowest eigenstate), the estimated, maximum temperature error can be expressed as

$$\frac{\sigma_T}{T - T_0} \simeq \zeta \frac{\tau_1}{\tau_0} \tag{C.9}$$

where ζ is dependent on the sample geometry. The temperature T_0 is the fridge temperature. In the case of this particular configuration, $\zeta = 0.53$. Alternatively, one can think of

the error in temperature measurement for a given cooling (heating) rate, so that

$$\sigma_T \simeq \zeta \tau_1 \frac{\partial T}{\partial t}. \tag{C.10}$$

This must be applied to our data before and well after heat pulses, to determine the error bars of our measurement. If the temperature is stable before a heat pulse and $\tau_0/\tau_1 \simeq 20$, a conservative estimated error on the specific heat will be about 2.5%. Estimated error bars for our $Gd_2Sn_2O_7$ measurement are shown in Figure C.1.

A large number of approximations have been made in the above error estimate. Furthermore, these errors are systematic, not random (although inconsistency in the sample temperature before the heat pulses can make the errors appear random). The result that the error due to thermal gradients is proportional to τ_1/τ_0 is quite clear, however. Thus a true test of whether our measurement is not being seriously affected by this issue is to repeat the measurement with a different ratio of time constants. This was performed with $Gd_2Sn_2O_7$, using the ratios $\tau_0/\tau_1 \simeq 5$ first and $\tau_0/\tau_1 \simeq 20$ later. The results of these two measurements were the same to within the scatter in the data. This served as a testing ground for our technique of measuring specific heat using powder samples. Since then, we have applied this method to other polycrystalline samples (discussed in Chapter 5), using a similarly high ratio of τ_0/τ_1.

If this error were a significant problem, one could, for example, mix the powder sample with silver powder and press it or encapsulate it in epoxy. This would improve the thermal conductivity of the sample, thereby greatly improving the ratio τ_0/τ_1. This would have the disadvantage of introducing an addendum that might be difficult to characterize. Since our measurement has been configured with a long τ_0, we have not found this to be necessary.

Appendix D

SQUID Theory and Practicalities

In this Chapter, we present a minimal overview of the theory of Josephson junctions and SQUIDs, followed by a discussion of how a SQUID is employed, particularly in our experiments. Much of the theory of the Josephson effect and SQUIDs is sourced from Refs. [116, 115] and we would refer the reader there for a much more in depth discussion. Value information on the practicalities of SQUIDs can be found in Ref. [117].

D.1 The Josephson Effect

Josephson was the first to derive some of the very interesting behaviour that occurs when Cooper pairs are allowed to tunnel from one superconducting electrode to another. The so-called Josephson effect, is described by two important equations known as the Josephson relations. Such a tunneling experiment can be set up in a variety of ways, but is most commonly implemented with either a narrow superconducting bridge or a thin insulating barrier in between bulk superconducting regions.

In the bulk superconducting electrodes, the wavefunction (at low enough temperatures) will simply be described as

$$\psi = \sqrt{\rho} e^{-i\varphi} \tag{D.1}$$

where φ will typically be an arbitrary value. However, when they are brought close together and tunneling is permitted, the phases become related. The Schroedinger equation for the two superconducting electrodes can be written simply as

$$i\hbar \frac{\partial \psi_1}{\partial t} = E_1 \psi_1 + K \psi_2 \tag{D.2}$$

$$i\hbar \frac{\partial \psi_2}{\partial t} = E_2 \psi_2 + K \psi_1 \tag{D.3}$$

where K describes the coupling between the superconductors as a result of Cooper pair tunnelling. If there is a voltage V between the electrodes, one can substitute $E_1 = eV$ and $E_2 = -eV$ (since Cooper pairs have charge $2e$). Incorporating the phase we obtain

$$\left[\frac{i}{2\rho_1}\dot{\rho}_1 - \dot{\varphi}_1\right]\hbar\sqrt{\rho_1}e^{i\varphi_1} = eV\sqrt{\rho_1}e^{i\varphi_1} + K\sqrt{\rho_2}e^{i\varphi_2} \tag{D.4}$$

$$\left[\frac{i}{2\rho_2}\dot{\rho}_2 - \dot{\varphi}_2\right]\hbar\sqrt{\rho_2}e^{i\varphi_2} = -eV\sqrt{\rho_2}e^{i\varphi_2} + K\sqrt{\rho_1}e^{i\varphi_1} \tag{D.5}$$

Now multiplying those equations by $\psi_1^\dagger$ and $\psi_2^\dagger$ respectively, we obtain

$$i\hbar\dot{\rho}_1/2 - \hbar\rho_1\dot{\varphi}_1 = eV\rho_1 + K\sqrt{\rho_1\rho_2}e^{i\Delta\varphi} \tag{D.6}$$

$$i\hbar\dot{\rho}_2/2 - \hbar\rho_2\dot{\varphi}_2 = -eV\rho_2 + K\sqrt{\rho_1\rho_2}e^{-i\Delta\varphi} \tag{D.7}$$

Subtracting the equations and taking the imaginary parts, we have the first Josephson relation as

$$\dot{\rho}_1 - \dot{\rho}_2 = \frac{2K\sqrt{\rho_1\rho_2}}{\hbar}\sin\Delta\varphi \tag{D.8}$$

or, since $\sqrt{\rho_1\rho_2}$ is largely constant, we can define a critical current I_0, such that

$$I_S = I_0\sin\Delta\varphi \tag{D.9}$$

Here, the current is written as I_S since this is the super current only. It is possible to have additional current flowing between the electrodes, but it will be dissipative or normal.

Taking the real parts instead, one obtains the second, ac Josephson relation:

$$\dot{\varphi}_1 - \dot{\varphi}_2 = \frac{2eV}{\hbar} \tag{D.10}$$

or

$$\frac{\partial\Delta\varphi}{\partial t} = \frac{2eV}{\hbar} \tag{D.11}$$

In fact, when discussing Josephson junctions and SQUIDs in magnetic field, one must work with the gauge-invariant phase difference γ defined as

$$\gamma = \Delta\phi - \frac{2\pi}{\Phi_0}\int \boldsymbol{A}\cdot d\boldsymbol{s} \tag{D.12}$$

where $\Phi_0 = h/2e$ is a flux quantum. Thus the Josephson relations may finally be written as

$$I_S = I_0\sin\gamma \tag{D.13}$$

$$\frac{\partial \gamma}{\partial t} = \frac{2eV}{\hbar} \tag{D.14}$$

A realistic Josephson junction, however, is more correctly modeled as a tunnel junction in parallel with a capacitor and possibly a resistor (often by design). In that case, one obtains the resistively and capacitively shunted Josephson junction model or RCSJ model, the circuit diagram of which is shown in the inset of Figure D.1(a). The total current I is given by

$$I = I_0 \sin\gamma + V/R + CdV/dt \tag{D.15}$$

Incorporating the ac Josephson relation, one obtains

$$I = I_0 \sin\gamma + \frac{\hbar}{2eR}\frac{\partial \gamma}{\partial t} + \frac{C\hbar}{2e}\frac{\partial^2 \gamma}{\partial t^2} \tag{D.16}$$

then transforming to dimensionless variables, we can write

$$\frac{\partial^2 \gamma}{\partial \tau^2} + \frac{1}{\beta_C}\frac{\partial \gamma}{\partial \tau} = \frac{I}{I_0} - \sin\gamma. \tag{D.17}$$

This equation can easily be compared to the equations governing a particle on a tilted washboard potential with mass $m = (\hbar/2e)^2 C$. The plasma frequency is $\omega_P = \sqrt{2eI_0/\hbar C}$ and the damping parameter is

$$\beta_C = \frac{2eI_0R^2C}{\hbar}. \tag{D.18}$$

This tilted washboard analogy allows one to easily visualize the behaviour of the phase γ. If there is a low current bias, or the washboard is slightly tilted, the phase particle will remain trapped in a local minimum. If the current exceeds the critical current, however, the particle will escape and tumble down the washboard, hence a voltage will develop across the junction. At this point, the behaviour of the phase particle depends heavily on the value of the damping parameter β_C. If $\beta_C < 1$, then the junction is overdamped or non-hysteretic. This means that the phase particle will reach a terminal velocity (or voltage) depending on the current bias. If the current is dropped back below I_0, the particle will be immediately retrapped and the voltage will go to zero. A hysteretic or underdamped junction, where $\beta_C > 1$, on the other hand, will not reach a terminal velocity. Instead, the voltage will increase until the gap voltage is reached and Cooper pairs are broken. On decreasing the current bias, a much lower current is required to slow down and trap the particle, thus there is hysteresis in the I-V curve. The behaviour of these distinct Josephson junctions is illustrated in Figure D.1.

In the design of SQUIDs, one generally wishes to use non-hysteretic junctions. If an insulating barrier is employed for the junction, R can end up being very large (thereby greatly reducing the damping). Often it is necessary to add a shunt resistor made of normal metal in parallel with the junction.

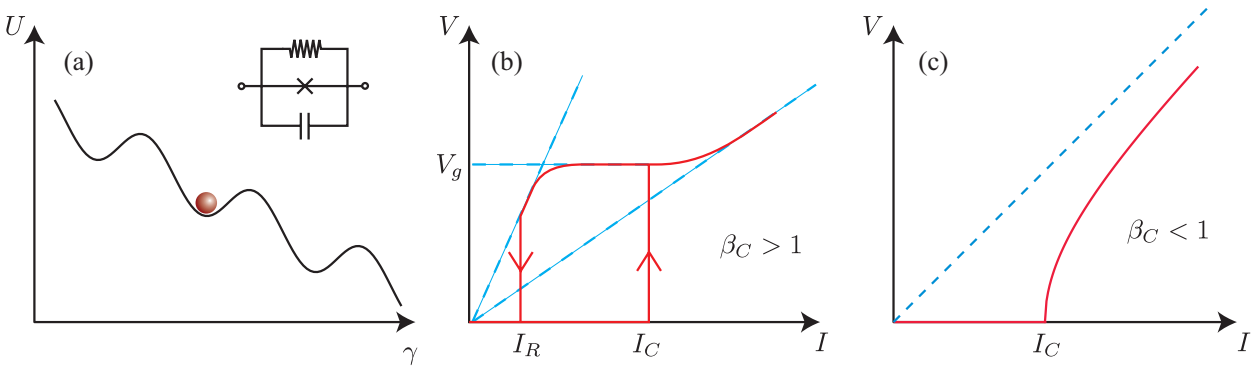

Figure D.1: (a) The tilted washboard potential and circuit diagram of the RCSJ model. (b) The I-V curve of a hysteretic or underdamped Josephson junction. (c) The I-V curve of a non-hysteretic or overdamped Josephson junction. Figure is based on Refs. [116, 115].

D.2 Physical Principles of SQUIDs

The superconducting quantum interference device (SQUID) is a device that makes use of Josephson junctions to make the superconducting equivalent of an interferometer that is an extremely sensitive magnetic field sensor. SQUIDs consist of a loop of superconducting material interrupted by one or two tunnel junctions, described as an rf-SQUID or dc-SQUID respectively. Historically, rf-SQUIDs were first employed as it was relatively easy to create one junction but is a technical challenge to create two, very similar junctions for a dc-SQUID [117]

In the rf-SQUID configuration, there is only one junction in the superconducting loop so there is always a superconducting shunt. Thus affixing leads to the rf-SQUID is quite ineffective. To read out the rf-SQUID one must couple it to a radio-frequency tank circuit (or LC resonator), hence the name. This makes for rather complicated read-out electronics.

The dc-SQUID consists of a loop with two junctions and leads can be connected between them. This is the type of SQUID used here, thus it is the one to which we will restrict our attention. Both SQUIDs are based on the idea of quantization of flux in a superconducting loop which results from the fact that the phase φ of the wavefunction must be single valued at any point. Thus if we take an integral of $\nabla\varphi$ around the loop, we must get an integer multiple of 2π.

$$\oint \nabla\varphi \cdot d\boldsymbol{l} = 2\pi n \tag{D.19}$$

In the Ginzburg-Landau theory of superconductivity [115],

$$\nabla\varphi = \frac{2\pi}{\Phi_0}\left(\boldsymbol{A} + \frac{m}{2e^2\rho}\boldsymbol{J}_S\right) \tag{D.20}$$

where $\Phi_0 = h/2e$ is the magnetic flux quantum, $\boldsymbol{A}$ is the magnetic vector potential, and $\boldsymbol{J}_S$ is the supercurrent density. The superconductor is assumed to be large enough that the integration can be constrained to the interior where the supercurrent density $\boldsymbol{J}_S$ should be almost nonexistent. Then we have, converting our loop integral into an integral over the surface area of the SQUID loop,

$$2\pi n = \frac{2\pi}{\Phi_0}\oint \boldsymbol{A}\cdot d\boldsymbol{l} = \iint_A \boldsymbol{B}\cdot\boldsymbol{\sigma} = 2\pi\frac{\Phi}{\Phi_0} \tag{D.21}$$

with $\boldsymbol{B}$ the magnetic field and Φ the corresponding flux through the SQUID. If we interrupt the superconducting loop with two Josephson junctions with phase differences $\Delta\varphi_1$ and $\Delta\varphi_2$, we will have

$$2\pi n = \Delta\varphi_1 - \Delta\varphi_2 + \int_\Gamma \boldsymbol{A}\cdot d\boldsymbol{l} \tag{D.22}$$

where Γ refers to the portion of the loop not taken up with junctions. Substituting the gauge invariant phase differences γ_1 and γ_2 completes the loop integral:

$$2\pi n = \gamma_1 - \gamma_2 + 2\pi\frac{\Phi}{\Phi_0}. \tag{D.23}$$

The current bias I is split between the two junctions, which we will assume have the same critical current I_0. This is certainly not always a good assumption. Incorporating the first Josephson relation, I is given by

$$I = I_0(\sin\gamma_1 + \sin\gamma_2) \tag{D.24}$$

The flux through the loop Φ consists of an applied or external portion Φ_e and a part that results from a screening current i_S, which is half the difference between the junction currents, thus

$$\Phi = \Phi_e + Li_S \tag{D.25}$$

$$i_S = \frac{I_0}{2}(\sin\gamma_1 - \sin\gamma_2) \tag{D.26}$$

where L is the inductance of the SQUID loop. So far, we have only considered the SQUID in the zero-voltage regime, but that is not the way a dc-SQUID is generally employed. There will be a critical I_C that depends on the applied flux Φ_e and in practice, one biases

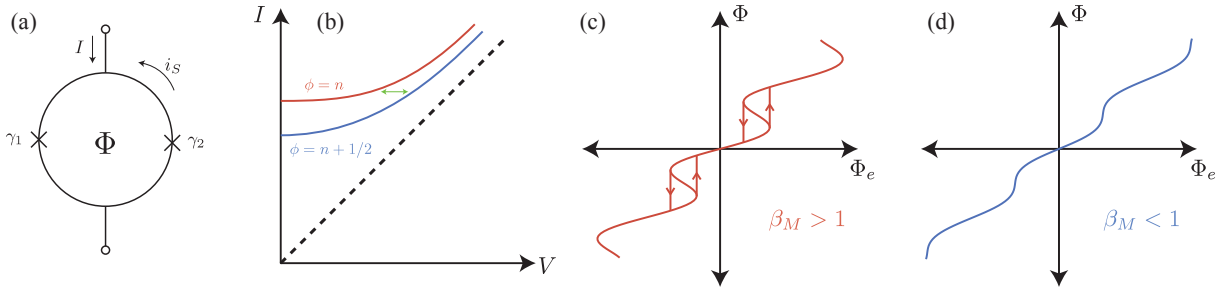

Figure D.2: (a) The circuit diagram of a SQUID showing the junctions with gauge invariant phases γ_1 and γ_2, the bias current I and the screening current i_S. (b) A sketch of the I-V curves at different values of flux Φ for an ideal SQUID. The green line shows modulation of the flux at constant bias current I. (c) A sketch of $\Phi(\Phi_e)$ for a hysteretic SQUID with $\beta_M > 1$. (d) A sketch of the single-valued $\Phi(\Phi_e)$ of a non-hysteretic SQUID with $\beta_M < 1$. Figure is loosely adapted from Refs. [116, 115].

the SQUID with a current I that is always above I_C. There will then be a non-zero voltage V across the SQUID leads which depends on I_C which in turn depends on Φ_0.

Thus it would be desirable to calculate I_C as a function of Φ_e, though because of the screening current i_S, this is quite challenging. If we make the approximation that L is very small, we can say that $\Phi = \Phi_e$ and ignore the screening current. Using this approximation, a simple trigonometric identity and letting $(\gamma_1 + \gamma_2)/2 = \gamma$, we can write

$$I = 2I_0 \sin(\gamma) \cos(\pi\Phi_e/\Phi_0 + n\pi) \tag{D.27}$$

Recall that this I is only supercurrent at this point. Thus to determine the critical current I_C for the dc-SQUID, we want to maximize I as a function of γ. Beyond that point, we will have exceeded the critical current and then normal electrons must flow to make up the difference, resulting in a finite voltage V across the device. Maximizing the above equation will result in

$$I_C = 2I_0 \left| \cos\left(\frac{\pi\Phi_e}{\Phi}\right) \right|. \tag{D.28}$$

Once we have exceeded the critical current, we must include the second Josephson relation $d\gamma/dt = 2eV/\hbar$. The current I will now be a sum of the supercurrent from before and a new normal current given by V/R from each junction (which we will assume to have the same resistances). We are ignoring the capacitance of the junctions at this point for

the sake of simplicity.

$$I = 2I_0 \cos(\pi\Phi_e/\Phi)\sin(\gamma) + \frac{\hbar}{eR}\frac{d\gamma}{dt} \tag{D.29}$$

For a given value of Φ_e, this looks rather similar to the equation of motion for a very overdamped junction, but with a critical current $I_C = 2I_0\cos(\pi\Phi_e/\Phi)$. This equation is analytically solvable and results in a time averaged voltage of

$$\bar{V} = (R/2)\sqrt{I^2 - [2I_0\cos(\pi\Phi_e/\Phi_0)]^2} \tag{D.30}$$

Thus, if we current bias our dc-SQUID above the critical current, we will have a sinusoidal dependence of $V(\Phi_e)$, with a periodicity of Φ_0, which provides a great deal of sensitivity to small changes in magnetic field.

If we now consider the case of zero applied current, implying that $\gamma_1 = -\gamma_2$ but allow for a non-negligible inductance L, we can see that

$$\Phi_e = \Phi - Li_S = \Phi - LI_0 \sin\left(\frac{\gamma_1 - \gamma_2}{2}\right)\cos(0) = \Phi - LI_0\sin(\pi\Phi/\Phi_0) \tag{D.31}$$

Using dimensionless values of flux $\phi = \Phi/\Phi_0$ and $\phi_e = \Phi_e\Phi_0$ we have

$$\phi_e = \phi + \frac{LI_0}{\Phi_0}\sin(\pi\phi) \tag{D.32}$$

$$\phi_e = \phi + \frac{\beta_M}{\pi}\sin(\pi\phi) \tag{D.33}$$

where we have introduced a new β-parameter

$$\beta_M = \frac{\pi LI_0}{\Phi_0} \tag{D.34}$$

If one plots ϕ against ϕ_e, it can be seen that for $\beta_M < 1$, $\phi(\phi_e)$ is single valued. However, for $\beta_M > 1$, it is multi-valued and hysteresis will result. These scenarios are depicted in Figure D.2(c) and (d). Thus just as β_C told us whether the I-V curve of a junction would be hysteretic, β_M tells us whether a SQUID will have magnetic hysteresis or not. For most practical purposes, it is best to choose SQUID parameters such that magnetic hysteresis does not occur.

Clearly, including both SQUID inductance and applied current, as well as erasing a number of other approximations such as perfectly symmetric junctions, negligible capacitance and magnetic field effects on the junctions themselves, makes for a very complex problem and equations that cannot be solved analytically. Nonetheless, the important

qualitative aspects of SQUID theory do not change. The parameters β_C and β_M must be chosen appropriately to avoid hysteresis. There is a critical current $I_C(\Phi_e)$ that is periodic in Φ_0. Biasing the device above that point results in a voltage $V(\Phi_e)$ which is also periodic in Φ_0. This periodic V-Φ curve provides a great deal of sensitivity to magnetic field, but also makes for tricky readout electronics as will be described in the next section.

D.3 Application of SQUIDs

While SQUIDs are the most sensitive magnetic field sensor currently possible, the readout of the SQUID is highly non-trivial and requires some complex electronics. The main challenges to overcome are (1) the small voltages on the SQUID that must be measured and (2) the very nonlinear V-Φ curve that one obtains.

For best results (lowest noise), the SQUID voltage should be amplified with a cryogenic transformer. However, this is certainly not the most convenient route to go as it is difficult to troubleshoot cryogenic apparatus. For many applications, including those in this work, it is sufficient to use a room temperature transformer (for impedance matching) followed by a room temperature semiconductor amplifier, both of which are incorporated into the SQUID controller [284].

To deal with the complicated V-Φ curve of the SQUID, it is necessary to either count the number of Φ_0 or linearize the transfer function. Counting flux quanta is dramatically less sensitive as the ideal sensitivity of a SQUID is on the order of 10^{-6} $\Phi_0/\sqrt{\text{Hz}}$. Linearizing the transfer function is performed with feedback or what is known as a flux-locked loop (FLL). Essentially the electronics are set up to feed back an additional flux, through the feedback coil, to keep the flux in the SQUID (and therefore the voltage) constant. Then the feedback voltage is used as the signal as it should be proportional to the flux created by the input coil.

In practice, the feedback system is more complicated than that and there are various schemes used. I will describe the scheme employed in the SQUID controllers used here [284][1]. In order to reduce errors caused by drift in the dc-voltages from the SQUID lines or amplifying electronics, a sinusoidal modulation is sent through the feedback coil in addition to the feedback current. This modulation is typically in the range of 100 kHz to several MHz in frequency and with an amplitude of approximately half of a flux quantum. In our specific apparatus, the modulation frequency is 100 kHz. The resulting modulation in the SQUID voltage is then amplified and read with a lock-in amplifier and phase-sensitive detector (PSD).

[1]SQUIDs and SQUID controllers were obtained from Michael Mück, ezSQUID

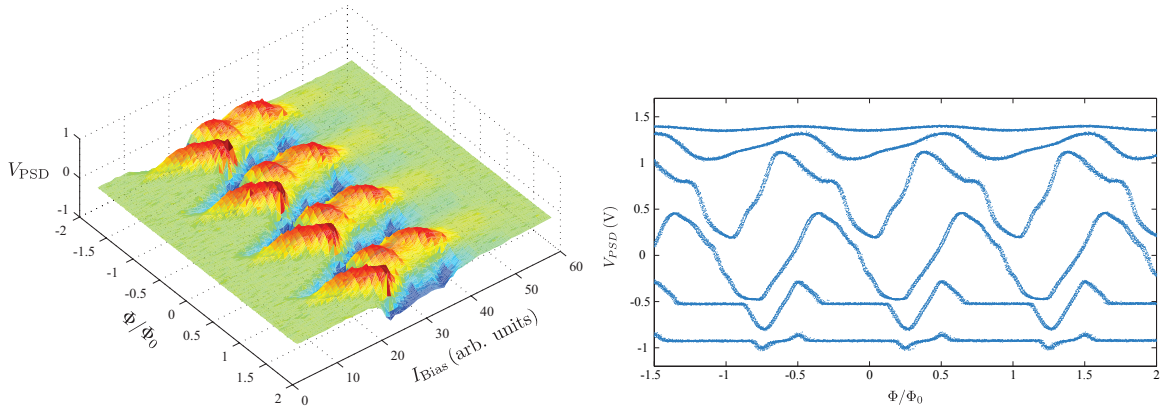

Figure D.3: Left: A surface plot of the different $V-\Phi$ curves obtained from tuning the bias current showing more complex behaviour than simple models of a SQUID would predict. While not perfect sine waves, the curves are nonetheless periodic in Φ and provide regions of steep gain on which to apply feedback. Right: selected V-Φ curves, shifted up with increasing bias current for ease of view.

In the simplest set-up, this signal is sent through an integrating circuit, compared with a voltage corresponding to the desired position on the V-Φ curve and then fed back to the feedback coil through a feedback resistor R_f such that it opposes any change in flux through the SQUID. The feedback resistor chooses the closed-loop gain of the system – larger R_f will result in larger gain since the voltage drop across R_f is taken as the signal. Higher gain can have consequences, however, in reducing the bandwidth of the apparatus and making it difficult to lock the feedback loop onto large signals. Smaller gain will have higher bandwidth, but can then become overly sensitive to noise feeding into the SQUID or electronics, making it difficult to maintain lock.

A slightly more complex approach, that is less sensitive to certain fluctuations, is employed in our SQUID electronics. Instead of fixing the amplitude of the modulation signal, the amplitude of the second harmonic of the modulated signal is *minimized*. This has the effect of maintaining the modulation about one of the steepest points of the V-Φ curve, thus providing the best open-loop gain. If the modulation was centred about the shallowest part of the V-Φ curve (at the maxima or minima of the sine wave) where the curvature is largest, the amplitude of the second harmonic would be largest. This feedback mechanism is insensitive to drifting offset voltages (since it uses an ac modulation). It also reduces the sensitivity to fluctuations in the critical current (these are already very small in magnitude) of the SQUID. Fluctuations in the amplitude of the V-Φ curve may change the amplitude

of the second harmonic, but the position of the minimum amplitude will not be shifted.

The SQUIDs employed here were made with thin-film technology using Nb-AlO-Nb tunnel junctions, with Pd shunt resistors. They include a lithographically patterned input coil on top of the SQUID washer, but we have used our own hand-wrapped input coil. While in theory, the V-Φ curve of a SQUID is close to a clean sine wave, in practice, it is often much more complicated, though still periodic in Φ_0. V-Φ curves at different bias currents for the SQUID used here are shown in Figure D.3. Clearly, these curves are quite a bit more complicated than the simple theory of Equation D.30. Because the feedback circuit linearizes the transfer function, these unusual curves do not result in any difficulties or errors.

In practice, the SQUID used for much of this work was found to have a noise floor of 9 to 12 $\mu\Phi_0/\sqrt{\text{Hz}}$. This is more than adequate for our applications here, as our signal is generally quite large. However, in some cases, SQUIDs may show a sensitivity as good as 1 $\mu\Phi_0/\sqrt{\text{Hz}}$ [117]. The bandwidth of the SQUID in lock can be as high as 10 kHz when a low value of feedback resistor (lower gain) is used and the frequency response is completely flat at low frequencies.

Appendix E

Specific Heat of $Yb_2Ti_2O_7$

While perhaps not a sufficiently in-depth study to stand as a full chapter, measurements on the material $Yb_2Ti_2O_7$ (YTO) are nonetheless important to mention and are thus presented in this appendix. YTO is expected to be described by the XY (easy local (111) plane anisotropy) model on a pyrochlore lattice [285]. In contrast with the case of local [111] Ising anisotropy with ferromagnetic interactions on the pyrochlore lattice which can lead to the exotic spin ice state [95], the case of XY anisotropy with ferromagnetic interactions has a non-degenerate classical ground state [286]. Nonetheless, this material has been observed to manifest a spin liquid or hidden order state at low temperatures and has eluded explanation to this point.

Here, we discuss specific heat measurements on both single crystal and polycrystalline samples of YTO. Though initially intended as a characterization study to complement neutron scattering experiments, the results are both dramatic and interesting, and will hopefully improve our understanding of this enigmatic material.

E.1 Background

As far back as 1969, Blöte *et al.* measured the specific heat of polycrystalline $Yb_2Ti_2O_7$ and found a sharp, first-order phase transition at 214 mK [266]. Above that was a broad feature centred around 2 K. With today's understanding of magnetism, this appears to be rather standard behaviour for a geometrically frustrated system in fact: a broad feature near the Curie temperature indicative of short range correlations and then a sharp ordering transition that has been pushed down to a lower temperature by the geometric frustration. Later experiments have found the transition temperature to be higher than that of Blöte *et al.*, in the range of 240 to 250 mK. This indicates a possible sample quality dependence.

Interestingly, much more recent neutron diffraction experiments (again on powder samples) found no indications of static magnetic order below the transition with no magnetic Bragg peaks visible [287, 109]. On the other hand, μSR and Mossbauer experiments found a very sudden, first-order, drop in the spin fluctuation rate at the transition. Below the transition, the system remains dynamic, with a temperature independent fluctuation rate of ~ 1 MHz [109], which is below the frequency window of Mössbauer measurements but within range of μSR. This transition, thus, is a very unusual kind of phase transition. It seems to be dynamical in nature, without any long range ordering. Excitingly, it bears many similarities to the liquid-gas transition – it is first-order, consists of a drop in relaxation rate (similar to an increase in viscosity) and does not appear to be associated with a broken symmetry.

This system is quite unique among magnetic materials, though the garnet material $Yb_3Ga_5O_{12}$ (YGG) does seem to be related, also showing some kind of spin liquid or hidden order state at low T [110]. In Ref. [110], it was noticed that both YTO and YGG have first-order phase transitions that account for only a small percentage ($\sim 20\%$) of the total entropy $R \ln 2$. This is because much of the entropy is already tied up in short-range correlations well above the transition temperature. However, other geometrically frustrated systems, such as $Gd_2Ti_2O_7$ and $Gd_2Sn_2O_7$ have first-order phase transitions that account for a larger percentage (40% or more) of their total $R \ln 8$ entropy. The authors of Ref. [110] propose that this low amount of entropy associated with the transition is somehow connected to the existence of an exotic, hidden-order ground state below the transition.

Neutron scattering experiments [6] performed on single crystal samples of $Yb_2Ti_2O_7$ have added richness to this problem, with the discovery of 'rods' of scattering. These rods, along the [111] and symmetry related directions, are indicators of 2-dimensional character. The rods increase in intensity with lower temperature (results are shown down to 1.4 K [6]) and seem to be connected to the broad feature in the specific heat. The question becomes, does this 2-dimensional character stem from strains in the crystal structure that locally destroy the 3-dimensional symmetry or is it possible for a perfect, 3D pyrochlore magnet to exhibit such 2D magnetic correlations?

Yasui *et al.* [288], have measured the ac susceptibility of and performed neutron scattering measurements on a single crystal of YTO. They find an anomaly at 240 mK in $\chi'(T)$ (near the specific heat peaks found by other groups), which they attribute to ferromagnetic ordering due to the large magnitude of the susceptibility which approaches the demagnetizing limit of their sample. Their neutron scattering measurements are reported to find extra magnetic scattering around the nuclear Bragg peaks consistent with a collinear ferromagnetic state, though with a greatly reduced magnetic moment. The polarized neutron-scattering measurements of Gardner *et al.* [289] are, however, inconsis-

tent with this picture of a ferromagnetic state, showing that the vast majority of the Yb moments remain dynamic and disordered below 240 mK.

It has been known for quite some time that the crystal field Hamiltonian of YTO leads to a planar anisotropy or a model close to XY-like [290, 285]. The ratio $g_\perp/g_\parallel$ is roughly 2.4 [285]. Recently, neutron scattering experiments [291] have been used to show that, even though the single-ions are XY-like, the dominant interaction between nearest neighbours is not an isotropic exchange but is in fact dominated by an $S_i^z S_j^z$ interaction. This may offset the planar anisotropy and make for a more isotropic, Heisenberg-like model.

Recently Ross *et al.* [286] have successfully observed these diffraction rods. They conclude that they are 2-dimensional correlations within the kagome planes of the crystal structure. Interestingly, at the lowest temperatures studied (30 mK), the rods have largely disappeared and given way to more 3-dimensional correlations. Thus, they have concluded that the transition seen in the specific heat and dynamics is a crossover from 2-dimensional to 3-dimensional correlations. Again, there are no indications of long range order down to the lowest temperatures studied.

Application of a suitably large magnetic field along $[1\bar{1}0]$ appears to induce long-range magnetic order, as evidenced by sharp spin waves. This transition takes place at $H_C \simeq 0.5$ T as the lowest temperatures studied. Complementing their neutron scattering measurements with SQUID magnetization measurements, Ross *et al.* define an $H-T$ phase diagram with the critical field at which LRO occurs, H_C, increasing as the temperature is increased. In low fields and below 240 mK, is situated a 3D short range ordered (SRO) region of the phase diagram and above that in temperature is a region of 2D SRO.

As a complement to the neutron scattering results of Ross *et al.* [286], we have performed specific heat measurements on single crystal and powder samples of $Yb_2Ti_2O_7$, taken from the same crystal growth used for the neutron scattering experiments.[1]

E.2 Specific Heat Results

Measurements of the specific heat of a single crystal of YTO have brought a significant surprise to this subject. Instead of a sharp peak, we observe a broad feature at a lower temperature around 180 mK. This seems unlikely to simply be a smeared phase transition as it is in fact at quite a different temperature from the transitions measured in the polycrystalline samples. This single crystal sample was from the same growth used for neutron scattering experiments in Ref. [286], which showed rods of scattering suggestive of 2D correlations. The fact that the rods of scattering are present at 200 mK and absent at 30 mK is consistent with a gradual crossover below 200 mK to more 3-dimensional correlations

[1] Samples were provided by Kate Ross and Bruce Gaulin at McMaster University

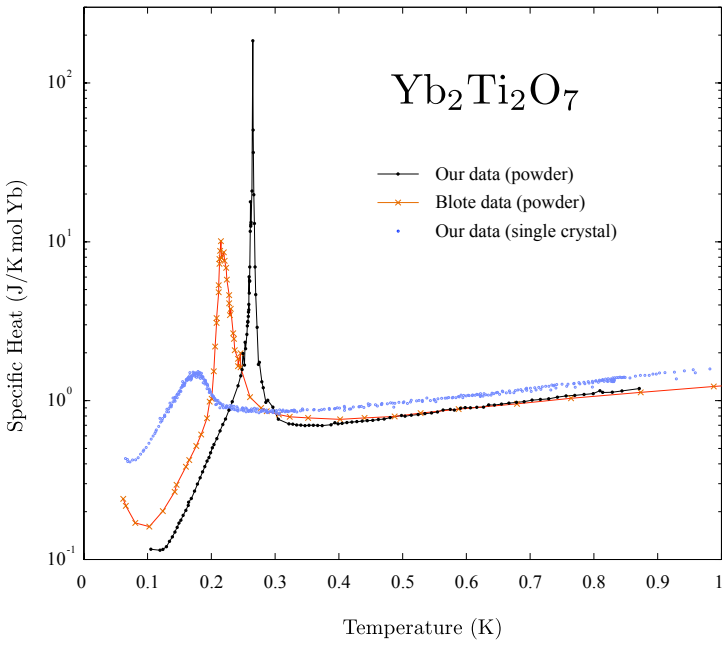

Figure E.1: A plot of measurements from this work of a single crystal of $Yb_2Ti_2O_7$ (blue), compared with measurements from this work on polycrystalline $Yb_2Ti_2O_7$ (black) and with previous measurements of a polycrystalline sample taken from Blote *et al.* [266].

and the loss of 2-dimensional correlations, signaled by this broad feature that we observe at 180 mK.

In contrast, the polycrystalline sample from which the single crystal was grown, shows a sharp phase transition as was seen previously [266, 292]. However, the transition temperature in our sample is slightly higher, close to 270 mK. This can be compared to the T_c of 214 mK from Blöte *et al.* [266] and 250 mK from de Réotier *et al.* [292]. This suggests that even in powder samples there is a significant sample quality effect.

At the lowest temperatures studied, one begins to observe an upturn in the specific heat, likely resulting from the nuclear moments of the various Yb isotopes. This contribution is expected to be a combination of the nuclear hyperfine coupling (from the nuclear magnetic dipole moment) and the nuclear electric quadrupole interaction with the electric field gradient in the vicinity of the nucleus. It is interesting to note that the nuclear contributions from the powder sample (similar to that of Blöte *et al.*) and the single crystal (near 100 mK) are not identical in magnitude. This is a likely indicator of different ground states

of the Yb^{3+} electronic moments in the powder and single crystal samples. Depending on whether the electronic moments are ordered or dynamic, and depending on the direction of the electric field gradient, we should expect different perturbing nuclear Hamiltonians and eigenvalues. This will give rise to different nuclear contributions to the specific heat. Thus in principle, the nuclear contribution to the specific heat can act as a microscopic probe of the magnetic fields inside the sample. Gd is reasonably amenable to calculation, as in Ref. [178], possessing only two isotopes with nuclear moments, both $I = 3/2$. It may be more challenging to do such an analysis here because of the likely dynamic ground states. It would also be severely complicated by the fact that the nuclear isotopes with magnetic moments are ^{171}Yb (with $I = 1/2$) and ^{173}Yb (with $I = 5/2$) and Mössbauer experiments are performed on ^{170}Yb [109].

Susceptibility measurements on a single crystal by Yasui *et al.* [288] do show a reasonably sharp feature around 240 mK, suggesting that a sharp phase transition is possible in single crystal $Yb_2Ti_2O_7$. Our specific heat measurements are the first reported on single crystals of YTO. Work is continuing, using neutron scattering, to try to explain the differences between these single crystals and the powder samples, both structurally and magnetically. It is clear, that the single crystal and polycrystalline samples are fundamentally different in their magnetic behaviour and it seems likely that there are important structural differences that cause such changes. As has been discussed in Chapter 5, geometrically frustrated materials (rare-earth pyrochlores in particular) are considered to be quite sensitive to small amounts of disorder.

References

[1] P. W. Anderson, Science **177**, 393 (1972).

[2] P. W. Anderson, Science **235**, 1196 (1987).

[3] F. Bert *et al.*, J. Phys.: Conf. Ser. **145**, 012004 (2009).

[4] S. Ghosh, R. Parthasarathy, T. F. Rosenbaum, and G. Aeppli, Science **296**, 2195 (2002).

[5] S. Ghosh, T. F. Rosenbaum, G. Aeppli, and S. N. Coppersmith, Nature **425**, 48 (2003).

[6] P. Bonville *et al.*, J. Phys.: Condens. Matter **15**, 7777 (2003).

[7] P. Schiffer *et al.*, Phys. Rev. Lett. **74**, 2379 (1995).

[8] O. A. Petrenko, C. Ritter, M. Yethiraj, and D. McK Paul, Phys. Rev. Lett. **80**, 4570 (1998).

[9] S. Dunsiger *et al.*, Phys. Rev. Lett. **85**, 3504 (2000).

[10] G. H. Dieke, *Spectra and Energy Levels of Rare Earth Ions in Crystals* (John Wiley and Sons, Inc., 1968).

[11] R. M. White, *Quantum Theory of Magnetism* (McGraw-Hill, Inc., New York, 1970).

[12] M. T. Hutchings, Solid State Phys. **16**, 227 (1964).

[13] K. W. H. Stevens, Proc. Phys. Soc. A **65**, 209 (1952).

[14] H. M. Rønnow *et al.*, Phys. Rev. B **75**, 054426 (2007).

[15] A. J. Freeman and J. P. Desclaux, J. Magn. Magn. Mater. **12**, 11 (1979).

[16] J. Phys.: Condens. Matter **1**, 755 (1989).

[17] M. J. P. Gingras *et al.*, Phys. Rev. B **62**, 6496 (2000).

[18] P. B. Chakraborty, P. Henelius, H. Kjonsberg, A. W. Sandvik, and S. M. Girvin, Phys. Rev. B **70**, 144411 (2004).

[19] M. Tinkham, *Group theory and quantum mechanics* (McGraw-Hill, Inc., New York, 1964).

[20] A. Abragam and B. Bleaney, *Electron Paramagnetic Resonance of Transition Ions* (Clarendon Press, Oxford, 1970).

[21] G. T. Trammell, Phys. Rev. **131**, 932 (1963).

[22] K. Andres, E. Bucher, S. Darack, and J. P. Maita, Phys. Rev. B **6**, 2716 (1972).

[23] R. W. Youngblood, G. Aeppli, J. D. Axe, and J. A. Griffin, Phys. Rev. Lett. **49**, 1724 (1982).

[24] G. Mennenga, L. de Jongh, and W. Huiskamp, J. Magn. Magn. Mater. **44**, 59 (1984).

[25] K. Binder and A. P. Young, Rev. Mod. Phys. **58**, 801 (1986).

[26] K. H. Fischer and J. A. Hertz, *Spin Glasses* (Cambridge University Press, 1991).

[27] A. Del Maestro and M. J. P. Gingras, Phys. Rev. B **76**, 064418 (2007).

[28] J. W. Essam, *Phase Transitions and Critical Phenomena* (Academic Press Inc., London, 1972), chap. 6, p. 197.

[29] M. J. Stephen and A. Aharony, J. Phys. C **14**, 1665 (1981).

[30] J. Zinn-Justin, *Quantum field theory and critical phenomena* (Oxford University Press, 2002).

[31] A. I. Larkin and D. E. Khmel'nitskii, Sov. Phys. JETP **29**, 1123 (1969).

[32] A. Aharony, Phys. Rev. B **8**, 3363 (1973).

[33] G. Ahlers, A. Kornblit, and H. J. Guggenheim, Phys. Rev. Lett. **34**, 1227 (1975).

[34] R. Frowein, J. Kötzler, and W. Assmus, Phys. Rev. Lett. **42**, 739 (1979).

[35] J. A. Griffin, M. Huster, and R. J. Folweiler, Phys. Rev. B **22**, 4370 (1980).

[36] J. Nikkel and B. Ellman, Phys. Rev. B **64**, 214420 (2001).

[37] H.-J. Xu, B. Bergersen, and Z. Racz, J. Phys.: Condens. Matter **4**, 2035 (1992).

[38] A. Biltmo and P. Henelius, Europhys. Lett. **87**, 27007 (2009).

[39] A. Aharony, Phys. Rev. B **8**, 3349 (1973).

[40] A. Kornblit and G. Ahlers, Phys. Rev. B **8**, 5163 (1973).

[41] A. Kornblit and G. Ahlers, Phys. Rev. B **11**, 2678 (1975).

[42] F. Pobell, *Matter and Methods at Low Temperatures* (Springer-Verlag, Berlin, 1992).

[43] W. A. Barton and J. D. Cashion, J. Phys. C **12**, 2897 (1979).

[44] J. A. Mydosh, *Spin Glasses An Experimental Introduction* (Taylor and Francis, 1993).

[45] D. P. E. Dickson and F. J. Berry, editors, *Mössbauer Spectroscopy* (Cambridge University Press, 1986).

[46] J. de Nobel and F. J. du Chatenier, Physica **25**, 969 (1959).

[47] H. Maletta and W. Felsch, Phys. Rev. B **20**, 1245 (1979).

[48] P. W. Anderson, B. I. Halperin, and C. M. Varma, Philosophical Magazine **25**, 1 (1972).

[49] L. E. Wenger and P. H. Keesom, Phys. Rev. B **13**, 4053 (1976).

[50] V. Cannella, J. A. Mydosh, and J. I. Budnick, J. Appl. Phys. **42**, 1689 (1971).

[51] V. Cannella and J. A. Mydosh, Phys. Rev. B **6**, 4220 (1972).

[52] J. L. Tholence, Solid State Commun. **35**, 113 (1980).

[53] C. A. M. Mulder, A. J. van Duyneveldt, and J. A. Mydosh, Phys. Rev. B **23**, 1384 (1981).

[54] C. A. M. Mulder, A. J. van Duyneveldt, and J. A. Mydosh, Phys. Rev. B **25**, 515 (1982).

[55] C. C. Paulsen, S. J. Williamson, and H. Maletta, Phys. Rev. Lett. **59**, 128 (1987).

[56] D. Hüser, L. E. Wenger, A. J. van Duyneveldt, and J. A. Mydosh, Phys. Rev. B **27**, 3100 (1983).

[57] C. Dekker, A. F. M. Arts, H. W. de Wijn, A. J. van Duyneveldt, and J. A. Mydosh, Phys. Rev. B **40**, 11243 (1989).

[58] D. H. Reich *et al.*, Phys. Rev. B **42**, 4631 (1990).

[59] S. Nagata, P. H. Keesom, and H. R. Harrison, Phys. Rev. B **19**, 1633 (1979).

[60] P. C. Hohenberg and B. I. Halperin, Rev. Mod. Phys. **49**, 435 (1977).

[61] L. P. Lévy, Phys. Rev. B **38**, 4963 (1988).

[62] Phys. Rev. B **26**, 5056 (1982).

[63] M. Suzuki, Prog. Theor. Phys. **56**, 1454 (1976).

[64] P. Monod and H. Bouchiat, J. Phys. (Paris) Lett. **43**, L45 (1982).

[65] P. E. Jönsson, R. Mathieu, W. Wernsdorfer, A. M. Tkachuck, and B. Barbara, Phys. Rev. Lett. **98**, 256403 (2007).

[66] W. Wu, D. Bitko, T. F. Rosenbaum, and G. Aeppli, Phys. Rev. Lett. **71**, 1919 (1993).

[67] M. Ocio, H. Bouchiat, and P. Monod, J. Magn. Magn. Mater. **54**, 11 (1986).

[68] L. R. Walker and R. E. Walstedt, Phys. Rev. Lett. **38**, 514 (1977).

[69] H. Maletta, W. Felsch, and J. L. Tholence, J. Magn. Magn. Mater. **9**, 41 (1978).

[70] N. Bontemps, J. Rajchenbach, R. V. Chamberlin, and R. Orbach, Phys. Rev. B **30**, 6514 (1984).

[71] C. Djurberg, P. Svedlindh, P. Nordblad, M. F. Hansen, and F. B. ad S. Morup, Phys. Rev. Lett. **79**, 5154 (1997).

[72] S. F. Edwards and P. W. Anderson, J. Phys. F **5**, 965 (1975).

[73] D. Sherrington and S. Kirkpatrick, Phys. Rev. Lett. **35**, 1792 (1975).

[74] G. Parisi, Phys. Rev. Lett. **43**, 1754 (1979).

[75] G. Parisi, J. Phys. A **13**, 1887 (1980).

[76] A. T. Ogielski, Phys. Rev. B **32**, 7384 (1985).

[77] W. L. McMillan, J. Phys. C **17**, 3179 (1984).

[78] M. A. Novak, O. G. Symko, and D. J. Zheng, Phys. Rev. B **33**, 343 (1986).

[79] H. Bouchiat, J. Phys. (Paris) **47**, 71 (1986).

[80] W. E. Fogle, J. D. Boyer, R. A. Fisher, and N. E. Phillips, Phys. Rev. Lett. **50**, 1815 (1983).

[81] R. N. Bhatt and A. P. Young, Phys. Rev. Lett. **54**, 924 (1985).

[82] N. Bontemps, J. Rajchenbach, R. V. Chamberlin, and R. Orbach, J. Magn. Magn. Mater. **54-57**, 1 (1986).

[83] E. Vincent, J. Hammann, and M. Alba, Solid State Commun. **58**, 57 (1986).

[84] J. A. Hamida and S. J. Williamson, Phys. Rev. B **34**, 8111 (1986).

[85] H. Maletta and P. Convert, Phys. Rev. Lett. **42**, 108 (1979).

[86] A. Aharony and M. E. Fisher, Phys. Rev. B **8**, 3323 (1973).

[87] J. L. Tholence, J. Appl. Phys. **50**, 7369 (1979).

[88] R. Moessner, Can. J. Phys **79**, 1283 (2001).

[89] J. T. Chalker, cond-mat/0901.3492 (2009).

[90] A. Ramirez, Ann. Rev. Mat. Sci. **24**, 453 (1994).

[91] J. S. Gardner, M. J. P. Gingras, and J. E. Greedan, Rev. Mod. Phys. **82**, 53 (2010).

[92] S. T. Bramwell and M. J. P. Gingras, Science **294**, 1495 (2001).

[93] L. Pauling, *The Nature of the Chemical Bond* (Cornell University Press, Ithica, New York, 1945).

[94] A. Ramirez, A. Hayashi, R. Cava, R. Siddharthan, and B. Shastry, Nature **399**, 333 (1999).

[95] S. T. Bramwell, M. J. Harris, B. C. den Hertog, and M. J. P. Gingras, Phys. Rev. Lett. **87**, 047205 (2001).

[96] C. Castelnovo, R. Moessner, and S. L. Sondhi, Nature **451**, 42 (2008).

[97] L. D. C. Jaubert and P. C. W. Holdsworth, Nature Phys. **5**, 258 (2009).

[98] T. Fennell *et al.*, Science **326**, 415 (2009).

[99] S. T. Bramwell *et al.*, Nature **461**, 956 (2009).

[100] J. Villain, Z. Phys. B **33**, 31 (1979).

[101] A. Andreanov, J. T. Chalker, T. E. Saunders, and D. Sherrington, Phys. Rev. B **81**, 014406 (2010).

[102] P. Chandra, P. Coleman, and I. Ritchey, J. Phys. I France **3**, 591 (1993).

[103] M. J. P. Gingras, C. V. Stager, N. P. Raju, B. D. Gaulin, and J. E. Greedan, Phys. Rev. Lett. **78**, 947 (1997).

[104] W. G. Bisson and A. S. Wills, J. Phys.: Condens. Matter **20**, 452204 (2008).

[105] L. Balents, Nature **464**, 199 (2010).

[106] P. W. Anderson, Mater. Res. Bull. **8**, 153 (1973).

[107] V. Kalmeyer and R. B. Laughlin, Phys. Rev. Lett. **59**, 2095 (1987).

[108] J. S. Gardner *et al.*, Phys. Rev. Lett. **82**, 1012 (1999).

[109] J. A. Hodges *et al.*, Phys. Rev. Lett. **88**, 077204 (2002).

[110] P. D. de Réotier *et al.*, Phys. Rev. Lett. **91**, 167201 (2003).

[111] Y. Zhou, P. A. Lee, T.-K. Ng, and F.-C. Zhang, Phys. Rev. Lett. **101**, 197201 (2008).

[112] S. H. E. Corporation, *Installation and Operation of the SHE Dilution Refrigerator and Gas Handling System*, 1975.

[113] Y. E. Volotikin, R. C. Thiel, and L. J. de Jongh, Cryogenics **34**, 771 (1994).

[114] J. A. Quilliam, *Specific Heat of the Dilute, Dipolar Coupled, Ising Magnet* $LiHo_xY_{1-x}F_4$, Master's thesis, University of Waterloo, 2006.

[115] A. Barone and G. Paterno, *Physics and Applications of the Josephson Effect* (John Wiley and Sons, Inc., 1982).

[116] M. Tinkham, *Introduction to Superconductivity*, 2 ed. (Dover Publications, Inc., 1996).

[117] J. Clarke and A. I. Braginski, editors, *The SQUID Handbook* (Wiley-VCH, 2004).

[118] A. Bajpai and A. Banerjee, Rev. Sci. Instrum. **68**, 4075 (1997).

[119] H. Ferrari *et al.*, Cryogenics **33**, 1037 (1993).

[120] S. M. A. Tabei, M. J. P. Gingras, Y.-J. Kao, and T. Yavors'kii, Phys. Rev. B **78**, 184408 (2008).

[121] D. Bitko, T. F. Rosenbaum, and G. Aeppli, Phys. Rev. Lett. **77**, 940 (1996).

[122] J. Brooke, D. Bitko, T. F. Rosenbaum, and G. Aeppli, Science **284**, 779 (1999).

[123] J. A. Quilliam, C. G. A. Mugford, A. Gomez, S. W. Kycia, and J. B. Kycia, Phys. Rev. Lett. **98**, 037203 (2007).

[124] J. A. Quilliam, S. Meng, C. G. A. Mugford, and J. B. Kycia, Phys. Rev. Lett. **101**, 187204 (2008).

[125] C. Ancona-Torres, D. M. Silevitch, G. Aeppli, and T. F. Rosenbaum, Phys. Rev. Lett. **101**, 057201 (2008).

[126] P. E. Jönsson *et al.*, cond-mat/0803.1357 (2008).

[127] A. Biltmo and P. Henelius, Phys. Rev. B **76**, 054423 (2007).

[128] K.-M. Tam and M. J. P. Gingras, Phys. Rev. Lett. **103**, 087202 (2009).

[129] R. Giraud, W. Wernsdorfer, A. Tkachuk, D. Mailly, and B. Barbara, Phys. Rev. Lett. **87**, 057203 (2001).

[130] P. E. Hansen, T. Johansson, and R. Nevald, Phys. Rev. B **12**, 5315 (1975).

[131] N. Karayianis, D. E. Wortman, and H. P. Jenssen, J. Phys. Chem. Solids **37**, 675 (1976).

[132] B. M. Walsh, G. Grew, and N. P. Barnes, J. Phys.: Condens. Mater. **17**, 7643 (2005).

[133] Gifeisman, Optics and Spectroscopy **44**, 68 (1978).

[134] J. Magarino, J. Tuchendler, J. P. D'Haenens, and A. Linz, Phys. Rev. B **21**, 18 (1980).

[135] J. Magarino, J. Tuchendler, J. P. D'Haenens, and A. Linz, Phys. Rev. B **13**, 2805 (1976).

[136] J. Als-Nielsen, Phys. Rev. Lett. **37**, 1161 (1976).

[137] P. Beauvillain and J.-P. Renard, Phys. Rev. B **18**, 3360 (1978).

[138] A. Aharony and P. Hohenberg, Phys. Rev. B **13**, 3081 (1976).

[139] S. Sachdev, *Quantum Phase Transitions* (Cambridge University Press, 1999).

[140] S. L. Sondhi, S. M. Girvin, J. P. Carini, and D. Shahar, Rev. Mod. Phys. **69**, 315 (1997).

[141] J. Brooke, *Quantum Fluctuations and Disorder in a Model Magnet*, PhD thesis, University of Chicago, 2000.

[142] S. M. A. Tabei, F. Vernay, and M. J. P. Gingras, Phys. Rev. B **77**, 014432 (2008).

[143] S. M. A. Tabei, *Interplay of Disorder and Transverse-Field Induced Quantum Fluctuations in the $LiHo_xY_{1-x}F_4$ Ising Magnetic Material*, PhD thesis, University of Waterloo, 2008.

[144] J. L. Dunn *et al.*, cond-mat/1005.1935 (2010).

[145] H. M. Ronnow *et al.*, Science **308**, 389 (2005).

[146] D. Bitko, *Order and Disorder in a Model Quantum Magnet*, PhD thesis, University of Chicago, 1997.

[147] J. Brooke, T. Rosenbaum, and G. Aeppli, Nature **413**, 610 (2001).

[148] D. M. Silevitch *et al.*, Nature **448**, 567 (2007).

[149] W. Wu, B. Ellman, T. Rosenbaum, G. Aeppli, and D. Reich, Phys. Rev. Lett. **67**, 2076 (1991).

[150] D. Hüser, L. E. Wenger, A. J. van Duyneveldt, and J. A. Mydosh, Phys. Rev. B **27**, 3100 (1983).

[151] D. S. Fisher and D. A. Huse, Phys. Rev. Lett. **56**, 1601 (1986).

[152] M. Schechter and P. C. E. Stamp, Phys. Rev. Lett. **95**, 267208 (2005).

[153] S. M. A. Tabei, M. J. P. Gingras, Y. J. Kao, P. Stasiak, and J.-Y. Fortin, Phys. Rev. Lett. **97**, 237203 (2006).

[154] M. Schechter and N. Laflorencie, Phys. Rev. Lett. **97**, 137204 (2006).

[155] M. Schechter and P. C. E. Stamp, Phys. Rev. B **78**, 054438 (2008).

[156] S. Ghosh, *Non-Linear Dynamics in Spin Liquids*, PhD thesis, University of Chicago, 2003.

[157] D. M. Silevitch, C. M. S. Gannarelli, A. J. Fisher, G. Aeppli, and T. F. Rosenbaum, Phys. Rev. Lett. **99**, 057203 (2007).

[158] D. D. H. Reich, T. Rosenbaum, and G. Aeppli, Phys. Rev. Lett. **59**, 1969 (1987).

[159] Private communication with D. M. Silevitch.

[160] J. Snider and C. C. Yu, Phys. Rev. B **72**, 214203 (2005).

[161] A. Biltmo and P. Henelius, Phys. Rev. B **78**, 054437 (2008).

[162] G. S. Shakurov *et al.*, Appl. Magn. Reson. **28**, 251 (2005).

[163] S. Bertaina *et al.*, Phys. Rev. B **74**, 184421 (2006).

[164] R. Giraud, W. Wernsdorfer, A. Tkachuk, D. Mailly, and B. Barbara, J. Magn. Magn. Mater. **242**, 1106 (2002).

[165] R. Giraud, A. M. Tkachuck, and B. Barbara, J. of Appl. Phys. **93**, 7077 (2003).

[166] M. J. Graf *et al.*, Phys. Rev. Lett. **99**, 267203 (2008).

[167] M. J. Graf *et al.*, Physica B **374**, 9 (2006).

[168] M. J. Graf, A. Lascialfari, F. Borsa, A. M. Tkachuk, and B. Barbara, Phys. Rev. B **73**, 024403 (2006).

[169] V. A. Atsarkin, Phys. Lett. A **130**, 492 (1988).

[170] P. Debye, *Polar Molecules* (Chemical Catalogue, New York, 1929).

[171] K. Matsuhira, Y. Hinatsu, and T. Sakakibara, J. Phys.: Condens. Matter **13**, L737 (2001).

[172] D. W. Davidson and R. H. Cole, J. Chem. Phys. **18**, 1417 (1950).

[173] D. W. Davidson and R. H. Cole, J. Chem. Phys. **19**, 1484 (1951).

[174] J. Nikkel and B. Ellman, cond-mat/0504269 (2005).

[175] J. Rodriguez *et al.*, Physica B **374**, 13 (2006).

[176] J. Rodriguez *et al.*, cond-mat/0910.5486 (2009).

[177] K. Kjaer, J. Als-Nielsen, I. Laursen, and F. K. Larsen, J. Phys.: Condens. Matter **1**, 5743 (1989).

[178] J. A. Quilliam *et al.*, Phys. Rev. Lett. **99**, 097201 (2007).

[179] R. Moessner and J. T. Chalker, Phys. Rev. Lett. **80**, 2929 (1998).

[180] K. Matsuhira, Y. Hinatsu, K. Tenya, and T. Sakakibara, J. Phys.: Condens. Matter **12**, L649 (2000).

[181] H. D. Zhou *et al.*, Phys. Rev. B **78**, 140406(R) (2008).

[182] B. D. Gaulin, J. N. Reimers, T. E. Mason, J. E. Greedan, and Z. Tun, Phys. Rev. Lett. **69**, 3244 (1992).

[183] A. Yaouanc *et al.*, Phys. Rev. Lett. **95**, 047203 (2005).

[184] J. R. Stewart, G. Ehlers, A. S. Wills, S. T. Bramwell, and J. S. Gardner, J. Phys.: Condens. Matter **16**, L321 (2004).

[185] A. S. Wills *et al.*, J. Phys.: Condens. Matter **18**, L37 (2006).

[186] J. Lago *et al.*, J. Phys.: Condens. Matter **17**, 979 (2005).

[187] S. R. Dunsiger *et al.*, Phys. Rev. B **54**, 9019 (1996).

[188] P. Bonville, J. A. Hodges, E. Bertin, and J.-P. Bouchaud, Hyperfine Interactions **156**, 103 (2004).

[189] J. S. Gardner *et al.*, Phys. Rev. Lett. **83**, 211 (1999).

[190] S. Dunsiger *et al.*, Phys. Rev. B **73**, 172418 (2006).

[191] P. Dalmas de Réotier, P. C. M. Gubbens, and A. Yaouanc, J. Phys.: Condens. Matter **16**, S4687 (2004).

[192] E. Bertin, Eur. Phys. J. B **27**, 347 (2002).

[193] G. Ehlers *et al.*, J. Phys.: Condens. Matter **16**, S635 (2004).

[194] A. Schenck, *Muon Spin Rotation Spectroscopy, Principles and Applications in Solid State Physics* (Adam Hilger Ltd., 1985).

[195] J. Snyder, J. S. Slusky, R. J. Cava, and P. Schiffer, Nature **413**, 48 (2001).

[196] M. J. Harris, S. T. Bramwell, T. Zeiske, D. F. McMorrow, and P. J. C. King, J. Magn. Magn. Mater. **177**, 757 (1998).

[197] J. D. M. Champion *et al.*, Phys. Rev. B **68**, 020401 (2003).

[198] T. Yavors'kii, M. Enjalran, and M. Gingras, Phys. Rev. Lett. **97**, 267203 (2006).

[199] S. R. Dunsiger *et al.*, Phys. Rev. Lett. **85**, 3504 (2000).

[200] V. N. Glazkov *et al.*, J. Phys.: Condens. Matter **18**, 2285 (2006).

[201] S. E. Palmer and J. T. Chalker, Phys. Rev. B **62**, 488 (2000).

[202] N. P. Raju, M. Dion, M. J. P. Gingras, T. E. Mason, and J. E. Greedan, Phys. Rev. B **59**, 14489 (1999).

[203] M. Enjalran and M. J. P. Gingras, cond-mat/0307152 (2003).

[204] O. Cépas and B. S. Shastry, Phys. Rev. B **69**, 184402 (2004).

[205] O. Cépas, A. P. Young, and B. S. Shastry, Phys. Rev. B **72**, 184408 (2005).

[206] A. P. Ramirez *et al.*, Phys. Rev. Lett. **89**, 067202 (2002).

[207] O. A. Petrenko, M. R. Lees, G. Balakrishnan, and D. McK Paul, Phys. Rev. B **70**, 012402 (2004).

[208] J. D. M. Champion *et al.*, Phys. Rev. B **64**, 140407 (2001).

[209] A. M. Durand, P. Klavins, and L. R. Corruccini, J. Phys.: Condens. Matter **20**, 235208 (2008).

[210] S. Lutique *et al.*, J. Chem. Thermodyn. **36**, 609 (2004).

[211] P. W. Anderson, Phys. Rev. **86**, 694 (1952).

[212] C. Kittel, *Quantum Theory of Solids* (John Wiley and Sons, Inc., 1963).

[213] T. Holstein and H. Primakoff, Phys. Rev. **58**, 1098 (1940).

[214] A. G. Del Maestro, *Quantum Spin Fluctuations in the Heisenberg-Like Pyrochlore Antiferromagnet Gadolinium Titanate*, Master's thesis, University of Waterloo, 2003.

[215] A. G. Del Maestro and M. J. P. Gingras, J. Phys.: Condens. Matter **16**, 3339 (2004).

[216] G. Luo, S. T. Hess, and L. R. Corruccini, Phys. Lett. A **291**, 306 (2001).

[217] D. R. Speck, Phys. Rev. **101**, 1725 (1956).

[218] S. S. Sosin, L. A. Prozorova, P. Bonville, and M. E. Zhitomirsky, Phys. Rev. B **79**, 014419 (2009).

[219] F. Bert *et al.*, Phys. Rev. Lett. **97**, 117203 (2006).

[220] T. C. Halsey, Phys. Rev. Lett. **55**, 1018 (1985).

[221] P. Gupta, S. Teitel, and M. J. P. Gingras, Phys. Rev. Lett. **80**, 105 (1998).

[222] G. Tarjus, S. A. Kivelson, Z. Nussinov, and P. Viot, J. Phys.: Condens. Matter **17**, R1143 (2005).

[223] H. Frauenfelder, S. G. Sligar, and P. G. Wolynes, Science **254**, 1598 (1991).

[224] I. Ritchey, P. Chandra, and P. Coleman, Phys. Rev. B **47**, 15342 (1993).

[225] S. Bekhechi and B. W. Southern, Phys. Rev. B **67**, 144403 (2003).

[226] M. Grousson, G. Tarjus, and P. Viot, J. Phys.: Condens. Matter **14**, 1617 (2002).

[227] M. Grousson, G. Tarjus, and P. Viot, Phys. Rev. E **65**, 065103(R) (2002).

[228] C. H. Booth *et al.*, Phys. Rev. B **62**, R755 (2000).

[229] A. Keren and J. S. Gardner, Phys. Rev. Lett. **87**, 177201 (2001).

[230] L. Bellier-Castella, M. J. P. Gingras, P. C. W. Holdsworth, and R. Moessner, Can. J. Phys. **79**, 11 (2001).

[231] T. E. Saunders and J. T. Chalker, Phys. Rev. Lett. **98**, 157201 (2007).

[232] S. Süllow *et al.*, Phys. Rev. Lett. **78**, 354 (1997).

[233] A. Krimmel, J. Hemberger, M. Nicklas, G. Knebel, and W. Trinkl, Phys. Rev. B **59**, R6604 (1999).

[234] A. Krimmel *et al.*, J. Phys.: Condens. Matter **11**, 6991 (1999).

[235] E. A. Goremychkin, R. Osborn, B. D. Rainford, and R. T. Macaluso, Nature Phys. **4**, 766 (2008).

[236] A. P. Ramirez, G. P. Espinosa, and A. S. Cooper, Phys. Rev. Lett. **64**, 2070 (1990).

[237] A. S. Wills and A. Harrison, J. Chem. Soc. Faraday T **92**, 2161 (1996).

[238] A. S. Wills, A. Harrison, S. A. M. Mentink, T. E. Mason, and Z. Tun, Europhys. Lett. **42**, 325 (1998).

[239] A. S. Wills, V. Dupuis, E. Vincent, J. Hammann, and R. Calemczuk, Phys. Rev. B **62**, R9264 (2000).

[240] V. Dupuis, E. Vincent, J. Hammann, J. E. Greedan, and A. S. Wills, J. Appl. Phys. **91**, 8384 (2002).

[241] P. Schiffer, A. Ramirez, D. Huse, and A. Valentino, Phys. Rev. Lett. **73**, 2500 (1994).

[242] W. I. Kinney and W. P. Wolf, J. Appl. Phys. **50**, 2115 (1979).

[243] J. Overmeyer, E. A. Giess, M. J. Freiser, and B. A. Calhoun, *Paramagnetic Resonance I* (Academic, New York, 1964), .

[244] O. A. Petrenko and D. McK Paul, Phys. Rev. B **63**, 24409 (2000).

[245] I. M. Marshall *et al.*, J. Phys.: Condens. Matter **14**, L157 (2002).

[246] P. Bonville, J. A. Hodges, J. P. Sanchez, and P. Vulliet, Phys. Rev. Lett. **92**, 167202 (2004).

[247] O. A. Petrenko, C. Ritter, M. Yethiraj, and D. McK Paul, Physica B **241**, 727 (1997).

[248] O. A. Petrenko, D. McK Paul, C. Ritter, T. Zeiske, and M. Yethiraj, Physica B **266**, 41 (1999).

[249] O. A. Petrenko, G. Balakrishnan, D. McK Paul, M. Yethiraj, and J. Klenke, Appl. Phys. A **74**, 760 (2002).

[250] T. Yavors'kii, M. Enjalran, and M. Gingras, cond-mat/0511403 (2005).

[251] T. Yavors'kii, M. Gingras, and M. Enjalran, J. Phys.: Condens. Matter **19**, 145274 (2007).

[252] S. Hov, H. Bratsberg, and A. T. Skjeltorp, J. Magn. Magn. Mater. **15-18**, 455 (1980).

[253] Y. Tsui, C. Burns, J. Snyder, and P. Schiffer, Phys. Rev. Lett. **82**, 3532 (1999).

[254] Y. Tsui, N. Kalechofsky, C. Burns, and P. Schiffer, J. Appl. Phys. **85**, 4512 (1999).

[255] Y. Tsui, J. Snyder, and P. Schiffer, Phys. Rev. B **64**, 12412 (2001).

[256] Y. Tsui, J. Snyder, and P. Schiffer, Can. J. Phys **79**, 1439 (2001).

[257] O. A. Petrenko *et al.*, Journal of Physics: Conference Series **145**, 012026 (2009).

[258] D. P. Goshorn, D. G. Onn, and J. P. Remeika, Phys. Rev. B **15**, 3527 (1977).

[259] R. P. Applegate, Y. Zong, and L. R. Corruccini, J. Phys. Chem. Solids **68**, 1756 (2007).

[260] B. E. Keen, D. Landau, B. Schneider, and W. P. Wolf, J. Appl. Phys. **37**, 1120 (1966).

[261] D. P. Landau, B. E. Keen, B. Schneider, and W. P. Wolf, Phys. Rev. B **3**, 2310 (1971).

[262] W. P. Wolf, B. Schneider, D. P. Landau, and B. E. Keen, Phys. Rev. B **5**, 4472 (1972).

[263] J. Hammann and P. Manneville, J. Phys. France **34**, 615 (1973).

[264] J. Hammann and M. Ocio, Physica B **86**, 1153 (1977).

[265] J. Filippi, J. C. Lasjaunias, B. Hebral, J. Rossa-Mignod, and F. Tcheou, J. Phys. C **13**, 1277 (1980).

[266] H. W. Blöte, R. F. Wielinga, and W. J. Huiskamp, Physica **43**, 549 (1969).

[267] Y. Okamoto, M. Nohara, H. Aruga-Katori, and H. Takagi, Phys. Rev. Lett. **99**, 137207 (2007).

[268] D. G. Onn, H. Meyer, and J. P. Remeika, Phys. Rev. **156**, 663 (1967).

[269] K. Kamazawa *et al.*, Phys. Rev. B **78**, 064412 (2008).

[270] A. H. Cooke, T. L. Thorpe, and M. R. Wells, Proc. Phys. Soc. **92**, 400 (1967).

[271] A. Gavignet-Tillard, J. Hammann, and L. de Seze, J. Phys. France **34**, 27 (1973).

[272] J. Filippi, J. C. Lasjaunias, B. Hébral, J. Rossa-Mignod, and T. Tchéou, J. Magn. Magn. Mater. **15**, 527 (1980).

[273] S. Nagata, H. Sasaki, K. Suzuki, J. Kiuchi, and N. Wada, J. Phys. Chem. Solids **62**, 1123 (2001).

[274] A. L. Costa, L. Esposito, V. Medri, and A. Bellosi, Adv. Eng. Mater. **2007**, 307 (2007).

[275] C.-C. Chiang, M.-S. Tsai, and M.-H. Hon, J. Electrochem. Soc. **154**, J326 (2007).

[276] C. Holm and W. Janke, Phys. Rev. B **48**, 936 (1993).

[277] W. P. Wolf, M. Ball, M. T. Hutchings, M. J. M. Leask, and A. F. G. Wyatt, J. Phys. Soc. Japan **17 (Suppl. B-I)**, 443 (1962).

[278] C. Alba-Simionesco, J. Fan, and C. A. Angell, J. Chem. Phys. **110**, 5262 (1999).

[279] X. Chen and B. Di Bartolo, J. Luminescence **54**, 309 (1993).

[280] A. Aharoni, *Introduction to the Theory of Ferromagnetism*, 2 ed. (Oxford University Press, 2000).

[281] A. Aharoni, J. Appl. Phys. **83**, 3432 (1998).

[282] N. O. Birge, Phys. Rev. B **34**, 1631 (1986).

[283] R. Haberman, *Elementary Applied Partial Differential Equations With Fourier Series and Boundary Value Problems*, 3rd ed. (Prentice Hall, 1998).

[284] M. Mück, *Operator's Manual for the dc SQUID electronics type ez SQUID SQE-DC 100k*.

[285] J. A. Hodges *et al.*, J. Phys.: Condens. Matter **13**, 9301 (2001).

[286] K. A. Ross *et al.*, Phys. Rev. Lett. **103**, 227202 (2009).

[287] J. A. Hodges, P. Bonville, A. Forget, and G. André, Can. J. Phys **79**, 1373 (2001).

[288] Y. Yasui *et al.*, J. Phys. Soc. Japan **72**, 3014 (2003).

[289] J. S. Gardner, G. Ehlers, N. Rosov, R. W. Erwin, and C. Petrovic, Phys. Rev. B **70**, 180404R (2004).

[290] A. Sengupta, J. Jana, and D. Ghosh, J. Phys. Chem. Solids **60**, 331 (1999).

[291] H. Cao *et al.*, Phys. Rev. Lett. **103**, 056402 (2009).

[292] P. Dalmas de Réotier *et al.*, Physica B **374**, 145 (2006).